Experimental and Numerical Modelling of Scour Around Walls due to Turbulent Bores

Seyed Abbas Jazaeri

Thesis submitted to the University of Ottawa in partial fulfillment of the requirements for the
Doctorate in Philosophy Civil Engineering

Academic Advisors:
Dr. Ioan Nistor, Dr. Abdolmajid Mohammadian, Dr. Xin Liu

uOttawa

Department of Civil Engineering
Faculty of Engineering
University of Ottawa

Abstract

Tsunamis are large and powerful waves typically generated by earthquakes, landslides, or volcanic eruptions in the ocean, propagating toward coastal areas with immense energy. Upon reaching shallow coastal regions, tsunami waves undergo rapid transformation, leading to inundation flows characterized by high velocities, strong accelerations, and complex hydrodynamic interactions with coastal infrastructure. Post-event field surveys conducted in the aftermath of recent tsunamis, such as the 2004 Indian Ocean, 2010 Chile, 2011 Tohoku, and 2018 Indonesian tsunamis, have consistently identified local scour around structures as a dominant mechanism of infrastructure failure. Despite the critical importance of this phenomenon, its influence on foundation design is often neglected in existing engineering standards and guidelines. Chapter 6 of ASCE 7-22 (2022) represents the only design standard that systematically addresses tsunami loading, with a section dedicated to local scour considerations. However, the provisions in this standard are derived from a limited body of research, and the effects of essential parameters, such as wall width and wall orientation relative to the flow direction, remain largely unexamined. This limitation highlights the need for controlled experimental data and physics-based numerical modelling to improve the understanding of tsunami-induced scour processes around coastal structures.

The literature on local scour around columns is extensive. However, to the best of the authors' knowledge, no prior study has specifically investigated tsunami-induced local scour around walls subjected to unsteady tsunami-like dam-break bores. Such structures are more representative of coastal infrastructure such as building facades, yet their interaction with highly transient tsunami-like flows has received comparatively limited attention. Therefore, the primary objective of this study was to fill this knowledge gap through a comprehensive series of laboratory experiments. Among the influential parameters, wall width and orientation relative to the flow were selected for detailed examination regarding their effects on local scour development. The generating impoundment depth was varied to produce tsunami-like dam-break bores with different flow depths and velocities, enabling assessment of scour behaviour under a range of hydraulic loading conditions. Furthermore, two numerical models, MIKE3 HD/ST and FLOW-3D, were employed to evaluate their capability in reproducing this complex process.

The laboratory experiments were conducted in the large dam-break flume at the University of Ottawa, allowing for detailed measurements of free-surface evolution, flow velocities, and bed morphology during and after bore impact. Scour development was monitored both spatially and temporally, with particular attention given to the formation of scour holes at the upstream corners and front face of the wall, where flow separation and vortex structures are most intense. The experimental findings demonstrated that wall orientation has a significant influence on the local scour depth by controlling the formation and intensity of horseshoe vortices. Walls oriented perpendicular to the flow consistently produced the deepest scour holes, whereas wall width exhibited a relatively minor effect. Comparisons with the envelope prescribed in ASCE 7-22 (2022) for estimating scour depth indicated that normalizing scour depth by projected width may misrepresent structural vulnerability. In several cases, walls parallel to the flow direction, i.e. having smaller projected widths, exhibited greater normalized scour depths despite shallower absolute values. These findings suggest that existing design approaches may underestimate scour-related risk for certain structural configurations.

The numerical simulations showed that both models reproduced the scour depth with reasonable accuracy. Although minor differences were observed in the temporal evolution of scour depth, both models successfully captured the key characteristics of the scouring process,

including the maximum erosion occurring at the upstream corner of the wall. Refinement of model configurations, such as selecting an appropriate turbulence closure scheme to resolve vortical structures around the wall and refining near-bed vertical mesh resolution, significantly improved the accuracy of the results without altering sediment transport calibration parameters such as bedload and suspended load factors, which are commonly adjusted in numerical sediment transport modelling.

The results of this study provide new experimental data and numerical insights into tsunami-induced local scour around walls, addressing a significant gap in the existing literature. The findings have direct implications for tsunami-resistant design and highlight the need for revisiting current design guidelines and standards related to scour depth estimation. Ultimately, this work contributes toward improving the resilience of coastal infrastructure subjected to extreme tsunami loading conditions.

Acknowledgment

I would like to express my sincere gratitude to my supervisors, Professor Ioan Nistor, Professor Majid Mohammadian, and Professor Xin Liu, for their continuous support, guidance, and encouragement throughout the course of my research. Their expertise, constructive feedback, and commitment to excellence have been instrumental in shaping this work and helping me grow as a researcher.

I am also deeply thankful to everyone who supported me during my laboratory work. I would like to express my appreciation to my friends from France, Agathe, Candice, Nathan, and Jules, whose enthusiasm, teamwork, and positive spirit made the experimental phase both productive and enjoyable. I also wish to thank my friend Shahrzad for her help, companionship, and support during long days in the lab. In addition, I am sincerely grateful to the laboratory technicians, Mark Lapointe and Leo Denner, for their invaluable technical assistance and dedication throughout the experiments.

I am furthermore grateful to my colleagues at DHI, whose understanding and encouragement made it possible for me to balance full-time work with my graduate studies. Their support and flexibility played an important role in helping me manage both responsibilities. I would like to especially thank Jordan Matthieu and Danker Kolijn for their continued support, guidance, and patience during this demanding period.

Above all, I am profoundly thankful to my family. I owe my deepest gratitude to my parents for their unwavering love, prayers, and encouragement throughout my life. I am especially grateful to my wife, Zeinab, whose patience, strength, and exceptional support carried me through the most challenging stages of this journey. She remained understanding and supportive while I managed significant commitments to both my work and my studies, and her constant belief in me made this accomplishment possible. I am also grateful to my son, Amirali, whose presence brought joy, purpose, and motivation during even the most difficult moments.

Table of Contents

Abstract . . . . . **ii**

Acknowledgment . . . . . **iv**

List of Figures . . . . . **viii**

List of Tables . . . . . **xii**

List of Acronyms . . . . . **xiii**

List of Symbols . . . . . **xiv**

1 Introduction **1**
1.1 Research Context 1
1.2 Research Questions 2
1.3 Objectives 3
1.4 Scope and Limitations of the Study 3
1.5 Novelty 4
1.6 Publications 4
1.6.1 Journal Publications 4
1.6.2 Conference Publications 5
1.7 Outline of the Thesis 5

2 A Critical Review on the Tsunami-Induced Scour around Structures **7**
2.1 Introduction 7
2.1.1 Post Tsunami Field Surveys 8
2.1.2 Tsunami Design Guidelines and Standards 10
2.1.3 Tsunami Inundation 11
2.1.4 Scour-Induced Failure Modes of Structures due to Tsunami Inundation . 11
2.1.5 Different Types of Scouring Induced by Tsunami Inundation 12
2.1.6 Numerical and Experimental Modeling of Tsunami-Induced Scour . . . 13
2.1.7 Scaling and Similarity in Tsunami Scour Studies 13
2.1.8 Objectives 13
2.2 State of the art in Tsunami-Induced Scour around Structures 15
2.2.1 Tsunami Generation Methods in Laboratory 15
2.2.2 Effects of Structure's Geometry on Local Scour 23
2.2.3 Effect of Structures' Arrangement on Local Scour Pattern 27
2.2.4 Numerical Modeling of Tsunami-Induced Scour 31
2.3 Research Needs and Future Possible Directions 35
2.4 Conclusion 38

3 Experimental Investigation of Structural Width Effects on Bore-Induced Scour Depth Around Walls . . . 39
3.1 Introduction . . . 39
3.2 Methodology . . . 41
3.2.1 Experimental Setup and Test Matrix . . . 41
3.2.2 Instrumentation . . . 42
3.2.3 Test Procedure . . . 43
3.2.4 Scaling Considerations . . . 43
3.3 Results . . . 46
3.3.1 Hydrodynamics . . . 46
3.3.2 Effect of the Impoundment Depth on the Scour Depth . . . 53
3.3.3 Effect of Width of Structure on Scour Depth . . . 53
3.4 Discussion . . . 63
3.5 Conclusion . . . 65

4 Experimental Investigation of Tsunami-Induced Local Scour Around Walls: Effects of Bore Depth and Structure's Geometry . . . 67
4.1 Introduction . . . 67
4.2 Flume Setup and Test Matrix . . . 68
4.3 Results . . . 70
4.3.1 Data Validation and Preprocessing . . . 70
4.3.2 Dam-Break Hydrodynamic Validation . . . 71
4.3.3 Temporal Evolution of Scour Depth . . . 74
4.3.4 Parametric Analysis of the Maximum Scour Depth . . . 76
4.3.5 Residual Scour Depth . . . 79
4.3.6 Comparison with ASCE 7-22 ASCE-7-22 (2022) Standard . . . 79
4.4 Discussion and Conclusions . . . 81
4.4.1 Key Finidings . . . 82
4.4.2 Limitations and Future Work . . . 82

5 Numerical Simulation of Local Scour Around Walls Under Unsteady Dam-Break Bores: Benchmarking MIKE3 HD/ST and FLOW-3D with MCDA . . . 84
5.1 Introduction . . . 84
5.2 Litearture Review . . . 85
5.3 Methodology . . . 87
5.3.1 Experimental Setup . . . 87
5.3.2 Numerical Models . . . 87
5.4 Results . . . 93
5.4.1 Stage 1: Turbulence Model Sensitivity . . . 93
5.4.2 Stage 2: Vertical Mesh Configuration Sensitivity . . . 96
5.4.3 Stage 3: Sediment Transport Sensitivity . . . 101
5.5 Discussion . . . 107
5.5.1 Hydrodynamic Response . . . 107
5.5.2 Scour Evolution . . . 108
5.6 Conclusions . . . 109

6 Conclusions and Recommendations for Future Work . . . 111
6.1 Conclusions . . . 111
6.2 Recommendations for Future Work . . . 112

Bibliography **114**

List of Figures

1.1 Examples of local scour around structures after the 2018 Indonesian Tsunami (Krautwald et al., 2021). 1

2.1 Extensive scour (up to 2.25 m) around a structure in Dichato after the 2010 Chile earthquake (Olsen et al., 2012) 9
2.2 Examples of the observed local scour around the structures in Palu Bay (Krautwald et al., 2021) (Permission obtained) 10
2.3 Horseshoe vortices and local scour around a bridge pier (Devi and Kumar, 2022) (Permission obtained) 12
2.4 Schematics of different failure modes (Adapted from (Lim et al., 2015)) 12
2.5 Experimental test setup of (Imamura et al., 2008) (Permission obtained) 20
2.6 The vertical release generation technique for simulating tsunami bores in laboratory settings (Wüthrich et al., 2018) (Permission obtained) 22
2.7 The scour pattern at the front and side faces of the square column (a, c, and e) and the rectangular column (b, d, and f). The green line shows the initial position of the sediment (McGovern et al., 2019) (Permission obtained) 26
2.8 The structural arrangement used by Elliott and Baker (1985) 31
2.9 Flowchart of the traditional models based on the Exner equation 35
2.10 Flowchart of the multiphase models (Eulerian) 37
2.11 Flowchart of the Lagrangian models 37

3.1 (a) Side view and (b) top view of the experimental setup (units in meters, not at scale) 41
3.2 Relationship between the Froude number and the impoundment depth normalized by the width of the structure for all tests 45
3.3 Snapshots of gate opening at t=0 s (left) and t=0.3253 s (right) for the test SC-H1 47
3.4 Non-dimensional gate opening time against impoundment depths 47
3.5 Comparison of the longitudinal non-dimensional water surface profile with analytical solution proposed by Ritter (1892) at (a) US1 and (b) US2 49
3.6 Temporal evolution of the non-dimensional bore height at the location of different ultrasonic sensors for the test SC-H1 50
3.7 Comparison of the bore front velocity against the equation proposed by Chanson (2006) for the rough bed condition. The circles are the points associated with the experimental results and crosses are the calculated nondimensional bore velocity based on Equation 3.6 for each individual test 50
3.8 Comparison of the experimental bore front velocity against available equations in the literature 51
3.9 Snapshots of the bore front movement during the test SC-H1 52
3.10 Calculation of the bore front velocity based on the bore arrival at different ultrasonic sensors for the tests SC-H1 52

3.11 Final bathymetry of the sediment section for the scenarios with short wall with the three impoundment depths (0.5, 0.6, and 0.7 m) 54
3.12 Snapshots from video footage captured from inside the structure for the case of the long wall illustrating the progression of scouring around the structure by bores generated by an impoundment depth of h_0=0.7 m 55
3.13 Timeseries of the water surface elevation at US3 (first row), scour depth at the upstream corner (middle row), and scour depth at the front face (last row) for the square column (first column), the short wall (middle column), and the long wall (last column). Red, green, and blue lines correspond to the 0.7 m, 0.6 m, and 0.5 m impoundment depths, respectively. 56
3.14 Correlation between the non-dimensional maximum scour depth at the upstream corners and the non-dimensional impoundment depth for all tests. 57
3.15 Timeseries of scour depth at the upstream corner (first row) and at the center of the front face (second row) for h_0=0.7 m (first column), h_0=0.6 m (middle column), and h_0=0.5 m (last column). Red, green, and blue lines correspond to the square column, short wall, and long wall, respectively. 58
3.16 Non-dimensional final scour depth against the non-dimensional width of structure at the top: upstream corner and bottom: front face. The dashed line is the fitted line to the data and the gray zone demonstrates the range of all experimental data. 59
3.17 Comparison of nondimensional scour depth versus nondimensional structural width between the results by April-LeQuéré (2022) and predictions from Equation (3.12) applied to his test configurations 60
3.18 Variation of bed profile with time in front and side faces of the short wall for h_0=0.7 m 61
3.19 Variation of bed profile with time in front and side faces of the long wall for h_0=0.7 m 62
3.20 Final scour profile of the sediment bed around different structures and for bores generated by the three impoundment depths h_0=0.7 m (top), h_0=0.6 m (middle), and h_0=0.5 m (bottom) 63
3.21 Scour depth normalized to the width of structure against Froude number together with the prescribed envelope by ASCE 7-22 (2022) for calculating the extent of the scour depth. Filled markers are associated with the maximum scour depth and hollow markers are for the final scour depth 64

4.1 Side view schematic of the flume (units in meter, not at scale) 69
4.2 Plan view schematic of the flume (units in meter, not at scale) 69
4.3 Different stages of the gate-opening in dam-break problem 70
4.4 Non-dimensional gate-opening time against the impoundment depth 71
4.5 Effect of noise filtering applied on the raw collected data for the SW-H1-A1 test 72
4.6 Snapshot of the video footage from GoPro1 camera showing the formation of horseshoe vortices in front of the wall 72
4.7 Comparison between the non-dimensional bore depth and the analytical solution proposed by Chanson (2006) 73
4.8 Comparison between the non-dimensional bore velocity and the analytical solution proposed by Chanson (2006) 74
4.9 Snapshots of the video footage by the wire micro-camera installed within the wall showing the progression of the scour depth at the front and side faces . . . 75

4.10 Time series of water surface elevation at the location of US3 (solid line), scour depth at the center of the front face (gray dashed line), and scour depth at the upstream corner (dotted line) of the wall together with the time of maximum scour depth (black dashed line at 24.7 s associated with 10 cm scour depth) for the SW-H3-A1 test 76
4.11 Maximum scour depth against impoundment depth categorized by the angle between the flow direction and the wall 77
4.12 Maximum scour depth against impoundment depth categorized by the wall width 78
4.13 Maximum scour depth against wall width categorized by the angle between the flow direction and the wall 79
4.14 Final bathymetry profile of the sediment section obtained from LiDAR scans for all the tests with the short wall 80
4.15 Comparison of the results obtained in this study with the envelope prescribed by the ASCE-7-22 (2022) standard 81

5.1 (a) Top view and (b) side view schematics of the flume (units in meters, not at scale) 87
5.2 Snapshots of the sediment section (a) before and (b) after the test 88
5.3 Horizontal mesh used in (a) MIKE3 HD/ST and (b) FLOW-3D simulations . . 89
5.4 Workflow of the three-stage numerical investigation 89
5.5 Vertical mesh configurations used in MIKE3 HD/ST 90
5.6 Vertical mesh resolutions tested in FLOW-3D 91
5.7 Comparison of experimental measurements with numerical simulations for FLOW-3D (left column) and MIKE3 HD/ST (right column) across the three turbulence models, where the rows respectively present the free-surface elevation at US1, velocity at the ADV location, free-surface elevation at US2, scour depth at the centre of the front face, and scour depth at the upstream corner. 94
5.8 Normalized statistical metrics for the FLOW-3D simulations for all parameters . 96
5.9 Model scores at each location obtained by averaging all normalized statistical metrics for each model and location 97
5.10 Final score of each turbulence model in FLOW-3D simulations 97
5.11 Final score of each turbulence model in MIKE3 HD/ST simulations 98
5.12 Comparison of the hydrodynamic responses for different vertical mesh configurations in FLOW-3D (left column) and MIKE3 HD/ST (right column) 99
5.13 Comparison of the local scour depth predictions for different vertical mesh configurations in FLOW-3D (left column) and MIKE3 HD/ST (right column) . 100
5.14 Final score S_m calculated for different layer thickness scenarios tested in MIKE3 HD/ST 102
5.15 Timeseries of the bed shear stress for the three tested vertical mesh configurations in MIKE3 HD/ST 102
5.16 Final score S_m calculated for different near bed vertical resolutions tested in FLOW-3D 103
5.17 Comparison of the hydrodynamic responses for different sediment discharge equations in FLOW-3D (left column) and MIKE3 HD/ST (right column) 104
5.18 Comparison of the local scour depth predictions for different sediment discharge equations in FLOW-3D (left column) and MIKE3 HD/ST (right column) 105
5.19 Final score S_m calculated for different sediment discharge equations tested in FLOW-3D 107

5.20 Final score S_m calculated for different sediment discharge equations tested in MIKE3 HD/ST 108

List of Tables

2.1 Summary of studies using solitary waves as a representation of tsunamis. 19
2.2 Summary of studies on the effects of structural shape on local scour 25
2.3 Summary of the findings of studies on scour around a single column 30
2.4 Summary of numerical models used for simulating scour around structures . . . 36

3.1 Configurations of tests conducted in the current study 42
3.2 Summary of the results 66

4.1 Configurations of tests 70
4.2 Summary of the maximum scour depth with the associated time for all tests . . 77

5.1 Horizontal element sizes used in the studied numerical models 88
5.2 Abbreviations used for each sediment discharge equation used in the tests nomenclature 91
5.3 Statistical indicators for the simulations against the experimental hydrodynamics measurements 95
5.4 Statistical indicators for the simulations against the experimental sediment transport measurements 95

List of Acronyms

ADV	Acoustic Doppler Velocimeter
ASCE	American Society of Civil Engineers
CCH	City and County of Honolulu
CFD	Computational Fluid Dynamic
DHI	Danish Hydraulic Institute
DTM	Dyanmic Two-parameter Mixed
FAVOR	Fractional Area/Volume Obstacle Representation
FEMA	Federal Emergency Management Agency
FEM	Finite Element Method
HD	Hydrodynamic
LES	Large Eddy Simulation
LiDAR	Light Detection and Ranging
LW	Long Wall
MARS	Multi-interface Advection and Reconstruction Solver
MCDA	Multi-Criteria Decision Analysis
RANS	Reynolds-Averaged Navier-Stokes
RMSE	Root Mean Square Error
SAS	Scale-Adaptive Simulation
SC	Square Column
SMAC	Simplified Marker and Cell
SMBTR	Structural Design Method of Buildings for Tsunami Resistance
SOS	Second-Order Sections
SST	Shear Stress Transport
ST	Sand Transport
SW	Short Wall
TLS	Terrestrial Lase Scanning
US	Ultrasonic Sensor
UVP	Ultrasonic Velocity Profiler
VOF	Volume of Fluid

List of Symbols

a	Wave amplitude (m)
a_1, a_2	Denominator filter coefficients (–)
B	Flume width (m)
B_p	Projected width of the wall (m)
b	Width of the column (m)
b_0, b_1, b_2	Numerator filter coefficients (–)
c	Wave celerity ($\mathrm{m\,s^{-1}}$)
d	Total water depth (m)
d_0	Impoundment depth (m)
d_{50}	Median grain size (m)
d_s	Scour depth (m)
$d_{s,\mathrm{corner}}$	Scour depth at the upstream corner (m)
$d_{s,\mathrm{front\ face}}$	Scour depth at the center of the front face (m)
$d_{s,\mathrm{max}}$	Maximum scour depth (m)
$d_{s,\mathrm{res}}$	Residual (final) scour depth (m)
D	Column or pile diameter (m)
f	Bed roughness coefficient (–)
f_c	Cutoff frequency (Hz)
f_s	Sampling frequency (Hz)
F_b	Froude number of the incoming bore (–)
F_o	Froude number of the overtopping flow (–)
Fr	Froude number (–)
$G(i, j)$	Gaussian kernel (–)
g	Gravitational acceleration ($\mathrm{m\,s^{-2}}$)
h	Still water depth (m)
h_0	Impoundment depth (m)
h_u	Upstream impoundment depth (m)
k	Turbulent kinetic energy ($\mathrm{m^2\,s^{-2}}$)
k	Kernel radius (grid cells or pixels, –)
L	Wave length (m)
Mw	Moment magnitude of an earthquake (–)
Re	Reynolds number (–)
S	Spacing between columns (m)
S_{max}	Maximum scour depth around a column (m)
$s_{m,p,c}$	Raw metric value for model m, parameter p, criterion c (–)
S_m	Final composite score for model m (–)
T	Wave period (s)
t	Time (s)

t_0	Gate opening time (s)
U	Bore front velocity ($\mathrm{m\,s^{-1}}$)
U_m	Maximum free surface velocity ($\mathrm{m\,s^{-1}}$)
u, v, w	Velocity components ($\mathrm{m\,s^{-1}}$)
u_*	Shear velocity ($\mathrm{m\,s^{-1}}$)
w	Structure width (m)
w_p	Weight of parameter p (–)
x	Distance downstream of the gate (m)
x_s	Bore front location (m)
$x[n]$	Input signal at time step n (–)
$y[n]$	Output (filtered) signal at time step n (–)
Z	Free surface elevation (m)
$Z(x, y)$	Raw bed elevation at (x, y) (m)
$Z_{\mathrm{filtered}}(x, y)$	Filtered bed elevation at (x, y) (m)
$\tilde{s}_{m,p}$	Aggregated score per parameter (–)
$\tilde{s}_{m,p,c}$	Normalized metric value (–)
α	Empirical coefficient in $U = \alpha\sqrt{g h_0}$ (–)
δ	Boundary layer thickness (m)
Δx	Horizontal grid spacing (m)
Δz	Vertical grid spacing (m)
ε	Turbulent dissipation rate ($\mathrm{m^2\,s^{-3}}$)
Φ	Dimensionless sediment transport rate (–)
ρ	Pearson correlation coefficient (–)
σ	Standard deviation (same unit as the variable)
σ	Sigma-coordinate for vertical mesh (–)
θ	Shields parameter (–)
θ_c	Critical Shields parameter (–)
ω	Specific dissipation rate ($\mathrm{s^{-1}}$)

Chapter 1. Introduction

1.1 Research Context

Tsunamis are large oceanic waves primarily generated by underwater earthquakes, landslides, or volcanic eruptions. The interaction of these waves with coastal areas can cause catastrophic damage to both human lives and infrastructure. Post-event field surveys following recent major tsunamis, such as the 2004 Indian Ocean Tsunami, the 2010 Chile Tsunami, the 2011 Tohoku Tsunami, and the 2018 Indonesian Tsunami, have consistently identified local scour around structures as one of the principal mechanisms contributing to structural failure (Borrero, 2005; Fritz and Borrero, 2006; Rossetto et al., 2007; Mikami et al., 2012; Chock et al., 2013; Palermo et al., 2013; Lim et al., 2015; Krautwald et al., 2021). Figure 1.1 presents examples of building failures resulting from local scour.

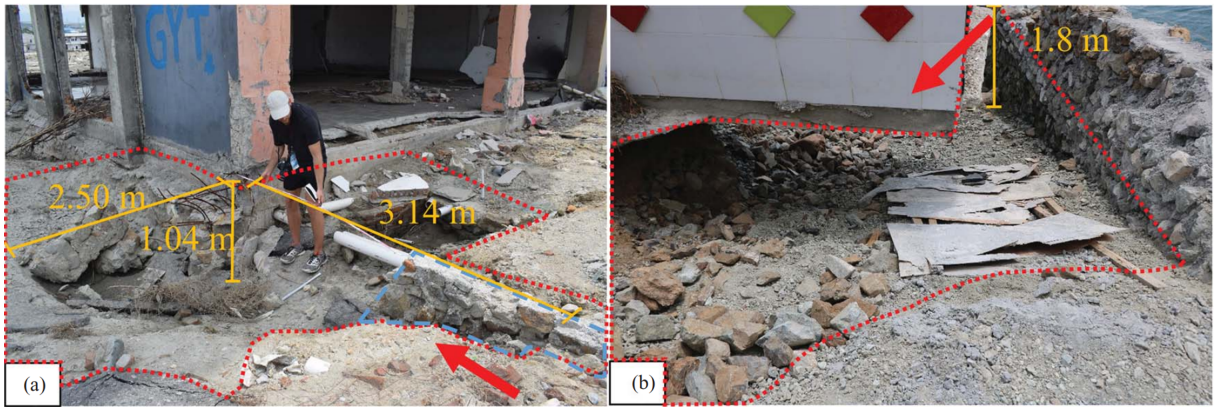

Figure 1.1: Examples of local scour around structures after the 2018 Indonesian Tsunami (Krautwald et al., 2021).

Despite the significance of this phenomenon, it has generally been overlooked in most existing design guidelines and standards. Among the available guidelines, only a few include specific provisions related to tsunami-induced effects. The Structural Design Method of Buildings for Tsunami Resistance (SMBTR) developed by Okada et al. (2005) in Japan represents one of the earliest attempts to provide guidance for designing buildings subjected to tsunami loads. However, this document lacks any consideration of local scour and focuses exclusively on the impact forces exerted by tsunami inundation.

Chapter 16 of the City and County of Honolulu Building Code (CCH, 2013) introduces limited consideration of factors such as sediment type, proximity to the shoreline, and inundation depth in the estimation of local scour depth. The Coastal Construction Manual (FEMA-P-55, 2011) and Guidelines for Design of Structures for Vertical Evacuation from Tsunamis (FEMA-P-646, 2019), both published by the Federal Emergency Management Agency (FEMA), also address tsunami-related design considerations. FEMA-P-55 (2011) assumes that tsunami-induced local scour can be estimated in a manner similar to that caused by typical storm surges, accounting only for the influence of pier diameter on scour depth. In contrast, while FEMA-P-646 (2019) provides general guidance for the design of tsunami evacuation structures, it does not include detailed methodologies for predicting local scour.

The only international standard that explicitly addresses the effects of tsunami-induced local scour on foundation design is ASCE-7-22 (2022). Chapter 6 of this standard introduces systematic

provisions for estimating scour depth based on parameters such as Froude number, sediment type (sand and gravel), and structural shape (square and circular). However, these provisions are primarily derived from studies conducted on column-type structures and therefore do not account for the scour mechanisms that develop around wall-type structures, which are more common in coastal infrastructure such as seawalls, building facades, and retaining structures. Furthermore, important parameters such as structural width and orientation relative to the incoming flow are not explicitly addressed. This limitation highlights a significant knowledge gap in understanding tsunami-induced scour processes around walls.

These gaps underline the need for a more comprehensive understanding of tsunami-induced local scour around wall-type structures. In particular, the absence of dedicated studies on wall geometries has limited the ability to develop reliable predictive formulations applicable to real coastal settings. A systematic investigation into how tsunami-like flows interact with wall-type structures, and how such interactions influence local scour characteristics, is therefore crucial to advancing current design knowledge and improving the resilience of coastal infrastructure.

1.2 Research Questions

Although local scour induced by tsunami inundation has been investigated in previous studies, the majority of existing research has predominantly focused on column structures, such as piles and bridge piers. In contrast, wall structures, which are more representative of coastal infrastructure such as building facades, have received considerably less attention. As a result, the influence of tsunami-like bores on local scour around such structures, as well as the role of structure geometry and orientation, remains inadequately understood. To address these gaps, this thesis is guided by the following research questions:

- How do tsunami-like dam-break bores influence the initiation, development, and maximum depth of local scour around coastal structures?
- What is the effect of bore characteristics, represented by the generating impoundment depth, on the magnitude and spatial distribution of local scour around walls?
- How does wall width influence local scour depth and scour hole geometry under tsunami-like bore conditions?
- How does the orientation of a wall relative to the incoming bore direction affect local scour patterns and the location of maximum scour depth?
- How does the temporal evolution of local scour around wall models vary under different bore and geometric configurations, and what governing mechanisms can be identified?
- To what extent can numerical hydrodynamic and sediment transport models reproduce experimentally observed scour processes around coastal structures subjected to tsunami-like bores?

These research questions define the objective and scope of the experimental program and numerical investigations presented in this thesis and provide a coherent framework for the interpretation of results and the development of conclusions relevant to tsunami-induced scour around coastal infrastructure.

1.3 Objectives

In light of the identified gaps in existing design standards and the limited understanding of tsunami-induced scour around wall-type structures, the primary objective of this study was to investigate the mechanisms of tsunami-induced local scour around wall-type coastal structures through a series of controlled laboratory experiments. The study focused on quantifying the influence of key parameters, namely the wall width, orientation relative to the flow direction, and impoundment depth, on the development and progression of local scour caused by unsteady tsunami-like dam-break bores. To achieve this, an extensive experimental program was conducted in the Large Dam-Break Flume in the Water Resources Laboratory of the University of Ottawa, Canada, where measurements of water surface elevation, flow velocity, and scour depth evolution were systematically recorded at multiple locations along the flume. High-speed cameras and other imaging instruments were also utilized to capture detailed video footage of the bore propagation and subsequent inundation process, providing valuable insights into the temporal evolution of flow and sediment interactions. The findings from this experimental campaign were intended to advance the understanding of tsunami-induced local scour and to contribute to the refinement of the scour provisions in future revisions of ASCE-7-22 (2022) standard.

A secondary objective of this research was to evaluate the ability of advanced numerical models to replicate the observed scour processes around wall-type structures under unsteady flow conditions. Considering the high cost and challenges associated with large-scale physical experiments, numerical modeling offers a complementary and scalable approach for studying tsunami-induced scour phenomena. In this context, two widely used hydrodynamic and sediment transport models, MIKE3 HD/ST and FLOW-3D, were employed and systematically assessed for their capability to reproduce the experimental observations. The comparison between these models provided valuable insight into their respective strengths and limitations in capturing complex unsteady flow–sediment–structure interactions. This evaluation ultimately supports the development of more reliable and computationally efficient methods for enhancing future design guidelines without relying exclusively on costly laboratory testing.

1.4 Scope and Limitations of the Study

The primary objective of this study was to investigate the mechanisms of tsunami-induced local scour around wall-type coastal structures and to evaluate the effects of wall width, orientation, and impoundment depth under unsteady tsunami-like dam-break conditions. Due to limitations in time and laboratory capacity, the scope of this study was defined as follows:

- The experiments were conducted at a 1:25 geometric scale.
- The study focused on a limited number of scenarios, specifically, three wall widths, three wall orientations, and three impoundment depths, to systematically examine the influence of these parameters on tsunami-induced local scour.
- All experiments were performed under dry-bed condition and the influence of wet-bed condition was not investigated.
- The effects of sediment characteristics were not considered. Moreover, tests were conducted over an idealized sediment bed, and the influence of complex topographic features was not included in the analysis.

- The tests were carried out over a flat-bed configuration, and the effects of bed slope and subsequent drawdown phase of tsunami inundation were not examined.

1.5 Novelty

Despite the extensive body of research on tsunami-induced local scour around column-type structures, the investigation of scour around walls has remained largely unexplored. Previous studies have primarily focused on column or pile-supported structures, overlooking the distinctive flow and sediment interaction patterns that develop around walls, which are commonly encountered in coastal environments such as building facades and retaining structures. No previous study has systematically investigated the effects of wall-specific parameters, such as wall width and orientation relative to the flow direction, on the development of local scour induced by unsteady tsunami-like dam-break bores. Therefore, this research represents the first comprehensive experimental investigation that quantifies the influence of these parameters on the depth and spatial distribution of local scour around wall-type structures.

In addition to its experimental contributions, this study introduces a significant advancement in the numerical modeling of tsunami-induced local scour. It represents the first effort to assess the performance of sediment transport models in simulating local scour around wall-type structures. Furthermore, the study presents a novel application of the MIKE3 HD/ST model, a model originally developed for large-scale coastal and estuarine simulations, to reproduce local scour processes under highly unsteady flow conditions. This evaluation provides valuable insight into the model's capabilities and limitations in representing localized sediment transport phenomena and establishes a foundation for extending its use in future tsunami-related scour studies.

1.6 Publications

1.6.1 Journal Publications

- Jazaeri, Seyed Abbas, Nistor, Ioan, Mohammadian, Abdolmajid, and Liu, Xin (2024). *A critical review on the tsunami-induced scour around structures.* Coastal Engineering Journal, Taylor and Francis, 1-28. https://doi.org/10.1080/21664250.2024.2380158

- Jazaeri, Seyed Abbas, Nistor, Ioan, Mohammadian, Abdolmajid, and Liu, Xin (2025). *Experimental Investigation of Structural Width Effects on Bore-Induced Scour Depth Around Walls.* Journal of Waterways, Ports, Ocean, and Coastal Engineering, ASCE, https://doi.org/10.1061/JWPED5/WWENG-2364, Accepted, in press

- Jazaeri, Seyed Abbas, Nistor, Ioan, Mohammadian, Abdolmajid, and Liu, Xin, *Experimental Investigation of Tsunami-Induced Local Scour Around Walls: Effects of Bore Depth and Structure's Geometry.* Coastal Engineering, Elsevier, Under review

- Jazaeri, Seyed Abbas, Nistor, Ioan, Mohammadian, Abdolmajid, and Liu, Xin, *Numerical Simulation of Local Scour Around Walls Under Unsteady Dam-Break Bores: Benchmarking MIKE3 HD/ST and FLOW-3D with MCDA.* Journal of Waterways, Ports, Ocean, and Coastal Engineering, ASCE, Under review

1.6.2 Conference Publications

- Jazaeri, Seyed Abbas, Nistor, Ioan, Mohammadian, Abdolmajid, and Liu, Xin (2025). *Experimental Study of Dam-Break Induced Local Scour Around Walls.* 41st IAHR World Congress, Singapore.
- Jazaeri, Seyed Abbas, Nistor, Ioan, Mohammadian, Abdolmajid, and Liu, Xin (2025). *Experimental Investigation of Tsunami-Induced Local Scour Around Walls.* 6th IAHR Young Professional Congress, Online.
- Jazaeri, Seyed Abbas, Nistor, Ioan, Mohammadian, Abdolmajid, and Liu, Xin. *Experimental and Numerical Modelling of Tsunami-Induced Local Scour around Walls.* Accepted at the 39th International Conference on Coastal Engineering, Galveston, Texas.

1.7 Outline of the Thesis

To address the objectives provided in Section 1.2, this thesis is structured as follows:

- **Section 1 - Introduction:** This section provides the overall context and motivation for the research. It introduces the background of tsunami-induced local scour, identifies the research gaps, defines the objectives and scope of the study, highlights its novelty, and summarizes related publications.
- **Section 2 - A critical review on the tsunami-induced scour around structures:** This section presents a comprehensive critical review of the existing literature on local scour around structures. It begins with an introduction to local scour phenomena, including post-event field observations, a review of existing design standards and guidelines, and an explanation of key preliminary concepts such as different types of scour, numerical approaches for sediment transport, and scaling considerations in experimental studies. The section then reviews the state of the art on tsunami-induced local scour around structures, covering laboratory tsunami generation methods, the effects of column geometry (cylindrical and square), structural arrangement influences, and numerical modeling of scour around columns. It concludes by emphasizing existing research gaps and identifying directions for future investigation.
- **Section 3 - Experimental Investigation of Structural Width Effects on Bore-Induced Scour Depth Around Walls:** This section presents an analysis of the effects of wall width and impoundment depth on local scour depth for walls oriented perpendicular to the flow direction. It begins with a hydrodynamic analysis of the experiments to verify data reliability and proceeds to examine the spatial and temporal evolution of scour. Two non-dimensional equations are proposed for estimating the local scour depth at both the center of the front face and the upstream corner of the wall, based on wall width and impoundment depth. The section concludes by comparing the experimental results with the ASCE-7-22 (2022) envelope for local scour prediction, highlighting the differences arising from the inclusion of wall-type structures.
- **Section 4 - Experimental Investigation of Tsunami-Induced Local Scour Around Walls: Effects of Impoundment Depth, Structural Width, and Structural Orientation:** This section investigates the combined influence of wall width, impoundment depth, and wall orientation relative to the flow direction on the local scour process. It begins with

a hydrodynamic assessment of the tests, followed by a detailed parametric analysis to identify the dominant parameters influencing the maximum scour depth. The section concludes with a comparison of the experimental findings against the ASCE-7-22 (2022) scour envelope, providing insight into the model's applicability to wall-type structures with different widths and orientations relative to the flow direction.

- **Section 5 - Numerical Simulation of Dam Break Induced Local Scour around Structures: A Comparison between MIKE3 HD/ST and FLOW-3D:** This section presents the numerical modeling component of the study, focusing on reproducing tsunami-induced scour around walls using MIKE3 HD/ST and FLOW-3D. The performance of both models is assessed through comparison with experimental results. The section presents a sensitivity analysis of model parameters including turbulence closure schemes, vertical mesh configuration, and sediment transport formulations. A statistical comparison using a multi-criteria decision analysis (MCDA) technique is conducted to evaluate model accuracy. Finally, the section discusses the detailed results of the best-performing simulation in each model and compares their respective strengths and limitations.

- **Section 6 - Conclusions and Recommendations for Future Work:** The final section synthesizes the key findings of the research and summarizes the major conclusions drawn from both the experimental and numerical investigations. It also outlines the main contributions of the study to the field of tsunami-induced local scour and provides recommendations for future work, including potential improvements to experimental methodologies, model formulations, and design standards.

Chapter 2. A Critical Review on the Tsunami-Induced Scour around Structures*

2.1 Introduction

Tsunamis are extreme waves generated by mostly earthquakes and landslides. Since historic times, tsunamis have caused huge casualties and damage to nearshore infrastructure. The 2004 Indian Ocean Tsunami, the 2010 Chile Tsunami, and the 2011 Tohoku Tsunami stand out as some of the most devastating tsunamis in recent history. Extensive post-event forensic field surveys have consistently highlighted local scour around structures as a prevalent mode of failure (Fritz and Borrero, 2006; Palermo et al., 2013; Sato and Okuma, 2014). Despite this, there are noticeable gaps in current design guidelines regarding the enhancement of building resilience to tsunami-induced local scour, underlining the critical need for further research in this area. Among the existing design guidelines, ASCE-7-22 (2022) Chapter 6 and its commentary offer comprehensive design criteria that take into account tsunami-related parameters such as inundation depth, run-up, and local scour. Nevertheless, the recommendations within these guidelines are predicated on a relatively narrow scope of research, leaving numerous factors unaddressed in the design criteria. This deficiency in the guidelines, coupled with the imperative for tsunami-resistant infrastructure, has catalyzed an expansion of research efforts in this domain.

Research on tsunamis encompasses both experimental and numerical studies. A pivotal consideration in experimental investigations is the choice of tsunami generation technique within laboratory environments. The solitary wave (Kato et al., 2001; Larsen et al., 2018; Xu and Huang, 2022) and dam break (Arnason et al., 2009; Imamura et al., 2008; Mehrzad et al., 2022) methods are the two predominant techniques extensively employed by researchers in this field. Moreover, while numerous studies have examined the impact of structural geometric characteristics (Dissanayaka and Tanaka, 2023; Shafiei et al., 2015; Triatmadja et al., 2011) and the configuration of structures in groups (April-LeQuéré et al., 2021) on local scour depth, notable research gaps remain in these areas. Additionally, numerical models are increasingly recognized as a viable alternative to the often-costly experimental tests for studying tsunami-induced local scour, garnering greater focus within the research community. The primary aim of this critical study is to undertake an exhaustive review of existing literature in this domain, identifying existing gaps and articulating research needs that will guide future investigations.

To achieve the goals of this review study, Section 1 serves as an introduction, providing an overview of notable post-tsunami field surveys, existing tsunami design guidelines, and foundational insights into tsunamis and the scouring mechanisms they trigger. Section 2 offers a detailed literature review on cutting-edge research concerning tsunami-induced local scour, covering various tsunami generation methods utilized in laboratory settings, the influence of structural geometry on local scour, the impact of structural arrangements on scouring process, and the current numerical models addressing this phenomenon. Section 3 aims to identify the prevailing gaps within this research area, proposing potential future research directions. Finally, Section 4 concludes the paper by underscoring the critical aspects that warrant additional exploration to enhance understanding and mitigation strategies regarding tsunami-induced scour

*Jazaeri, Seyed Abbas, Nistor, Ioan, Mohammadian, Abdolmajid, and Liu, Xin (2024). *A critical review on the tsunami-induced scour around structures.* Coastal Engineering Journal, Taylor & Francis, 1–28. https://doi.org/10.1080/21664250.2024.2380158

impacts.

2.1.1 Post Tsunami Field Surveys

The main source of information regarding the damage caused by tsunamis has been post-event forensic engineering field surveys usually conducted early in the aftermath of such events.

One of the most significant tsunamis in recent history is the 2004 Indian Ocean Tsunami which occurred on December 26, 2004. This event was triggered by an earthquake of moment magnitude Mw 9.0 in a region located 250 km southwest of the northern tip of Sumatra Island, Indonesia. Aerial photographs and post-tsunami field surveys confirmed that this event had a profound impact on many Asian countries bordering the Indian Ocean, including Indonesia, India, Thailand, and Sri Lanka. Remarkably, the waves of this tsunami even reached West African countries, namely Somalia, Tanzania, and Madagascar, despite being more than $5,000$ km away from the epicenter of the earthquake. Fritz and Borrero (2006) conducted a comprehensive field survey of coastal areas in these African nations with a particular focus on Somalia. In Bandarbeyla, situated in Somalia's Bari region, nearshore houses collapsed because of local scouring at building corners. Another surveyed location within Somalia's Bari region was Xaafuun Town, where the wave run-up reached a height of 7.5 m. The tsunami inundation resulted in the complete destruction of 812 houses, while 400 houses were damaged. Observations indicate that the primary cause of destruction of these houses was local scouring at their corners.

The area most severely affected by the 2004 Indian Ocean Tsunami was the Island of Sumatra in Indonesia, which is situated in close proximity to the epicenter of the earthquake. The colossal tsunami waves reached the shoreline of this region in approximately $15 - 20$ minutes, leaving many residents with insufficient evacuation time, especially given the lack of a tsunami warning system at the time. Consequently, this event resulted in a tragic toll of $128,645$ fatalities, $37,063$ individuals reported as missing, and $532,898$ displaced people (Borrero, 2005). Observations by Jaffe et al. (2006) and Saatcioglu et al. (2006) revealed that all the structures within this area were first affected by the very strong earthquake and subsequently obliterated by tsunami inundation, and significant evidence of scour was observed in the vicinity of numerous buildings.

Olsen et al. (2012) conducted a field survey following the 2010 Chile earthquake using the Terrestrial Laser Scanning (TLS) technique to determine the changes in nearshore topography due to the effects of the earthquake and the subsequent tsunami. They captured more than one billion data points from different locations along the Chilean coastline. In the town of Dichato, they identified approximately $1,500$ buildings that were completely destroyed and postulated that most of these buildings failed because of extensive scouring around their foundations. Figure 2.1 is a scanned image by the TLS system of a structure that did not collapse completely but which experienced a significant scour around its foundation (up to 2.25 m and about 300 m^3). Palermo et al. (2013) also documented that the majority of engineered buildings along the Chilean coastline withstood the forces induced by the tsunami and only suffered minor structural damages. In contrast, most non-engineered small houses were destroyed. Furthermore, certain infrastructure failed because of the scour around their foundations. For instance, the Echeverria roadway in Constitución experienced failure because of the embankment being washed away.

The 2011 Tohoku Tsunami in Japan was one of the turning points in the field of tsunami research, especially with respect to understanding and quantifying the local scour phenomena induced by tsunamis. This tsunami occurred as a result of an exceptionally strong earthquake of magnitude Mw 9.0 at 14:46 local time on March 11, 2011, on the east coast of Japan, and the waves were even observed on the west coast of the US (Chock et al., 2013). Different post-event field surveys were conducted in areas affected by the tsunami. Mikami et al. (2012) conducted

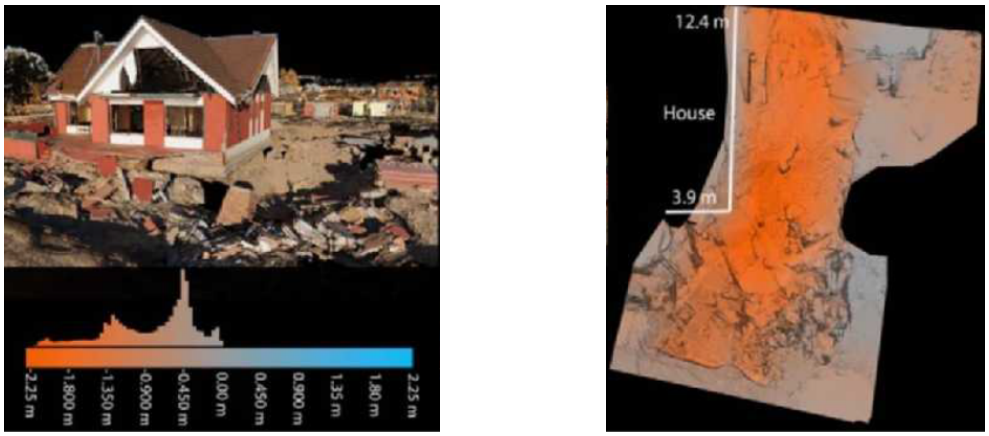

(a) Photo-mapped 3D scan (b) Deformation map

Figure 2.1: Extensive scour (up to 2.25 m) around a structure in Dichato after the 2010 Chile earthquake (Olsen et al., 2012)

post-disaster surveys in Miyagi and Fukushima to record the extent of the tsunami wave impact along the shoreline and analyzed the characteristics of damage to the infrastructure in these areas. In the town of Minamisanriku, they observed that most low-level buildings were destroyed because of the tsunami impact forces and local scour around the foundation. A significant observation of this study is that a sheltering building, which was constructed after the 1960 Chile Tsunami survived, although some scour around the foundation was observed. The design of this building was based on the Structural Design Method of Buildings for Tsunami Resistance (SMBTR) guideline for tsunami evacuation buildings by Okada et al. (2005) and published by the Building Center of Japan. Additionally, in Shizugawa, another evacuation structure was found to withstand the tsunami attack, experiencing only local scour around its sidewalls and corners. These observations revealed the importance of constructing nearshore structures according to guidelines specifically developed to account for tsunami waves and associated inundation. Sato and Okuma (2014) extensively examined the destruction of coastal structures in Fukushima Prefecture. They postulated that the formation of scour holes around the foundations of seawalls, especially on the landward side, resulted in their failure.

On September 28, 2018, an earthquake of moderate magnitude (Mw 7.5) struck near Palu Bay, Indonesia, drawing significant attention from the international coastal engineering community due to the unexpected severity of the resultant tsunamis given the earthquake's magnitude (Aránguiz et al., 2020). Researchers from Japan, Canada, and Germany conducted thorough post-disaster fieldwork to explore the mechanisms behind the destructive impact of tsunami inundation on structures (Stolle et al., 2020). Their observations revealed substantial scour holes adjacent to residential and commercial buildings, with depths reaching up to 1.5 m, extending 3.2 m perpendicular to, and 2.5 m parallel to the shoreline. Figure 2.2 depicts the extensive local scour around structural columns (Krautwald et al., 2021).

These findings suggest that, in addition to the structural damage from tsunami forces, local scour at the foundations of buildings is a critical factor in structural vulnerability to severe damage or collapse. Presently, among the few standards and guidelines that incorporate tsunami considerations into building design, only ASCE-7-22 (2022) addresses the specifics of the local scour effects around structures. Additional design guidelines offering recommendations regarding the maximum depth of tsunami-induced scour are elaborated upon in the following section.

(a) Scour around columns in Watusampu

(b) Scour at southern corner of Shops

Figure 2.2: Examples of the observed local scour around the structures in Palu Bay (Krautwald et al., 2021) (Permission obtained)

2.1.2 Tsunami Design Guidelines and Standards

Very few design guidelines have considered the effects of tsunami waves and associated coastal inundation on infrastructure. In this section, these guidelines and standards are briefly described.

SMBTR, which is a pioneering guideline for addressing tsunami loads on structures, was published by the Building Center of Japan (Okada et al., 2005). This document primarily concentrates on analyzing the impact of pressure on structures, especially evacuation buildings, during tsunami inundation. It offers a range of formulas to compute the tsunami load on structures based on the hydrostatic pressure distribution at a building's location. Additionally, the SMBTR contrasts the loads generated by tsunamis with those from seismic events, proposing various load combinations that are appropriate for structures made of reinforced concrete, steel frames, or wood. The document also includes recommendations for designing pressure-receiving surfaces, such as walls and windows. However, there are no provisions concerning the effect of scour on structural design.

Chapter 16 of the City and County of Honolulu Building Code (CCH, 2013) addresses the impact of flood forces on buildings by incorporating regulations that account for tsunami-related forces. It specifies that the scour depth depends on variables such as sediment type (sand, silt, or clay), the structure's proximity to the shoreline, and the inundation depth at the building's location. Consequently, this code proposes specific foundation-depth restrictions based on these parameters. Nonetheless, scholarly research, as discussed later in this paper, indicates that the scouring mechanism around structures is influenced by a broader array of parameters than those outlined in this code.

The Federal Emergency Management Agency (FEMA) has developed two pertinent design guidelines for coastal construction: FEMA-P-55 (2011), which concentrates on the impacts of wind and waves and sets forth design standards for buildings in coastal zones, and FEMA-P-646 (2019), known as the "Coastal Construction Manual and Guidelines for Design of Structures for Vertical Evacuation from Tsunamis". Despite the considerable differences in the wavelength and period between tsunami waves and typical tropical storm surges, FEMA-P-55 (2011) suggests that analogous design methodologies may be applied to both scenarios. The estimated maximum scour depth around an isolated circular column, directly exposed to the flood direction, is postulated to be double the column diameter ($S_{max} = 2D$), whereas for a group of columns or foundation piles, the maximum scour depth is predicted to be three times that of a single column ($S_{max} = 6D$). These coefficients were derived from the existing literature at the time, notably in the research by Sumer et al. (2001). However, while FEMA-P-646 (2019) is dedicated to tsunami-specific measures, it offers only general recommendations and lacks detailed structural design guidelines related to local scour for tsunami-resistant construction.

Chapter 6 and its commentary of the ASCE-7-22 (2022) is the most thorough prescriptive guide for assessing tsunami-induced loads and their effects on structures. This standard diverges from previous guidelines by offering a systematic approach for determining the maximum tsunami inundation depth, run-up, and flow velocity based on site-specific factors and historical data. The standard sets forth foundation design criteria that cover local and plunging scours, considering various parameters for calculating the design scour depth, such as the Froude number, sediment characteristics, and structural shape. Despite its breadth, this standard is based on a limited selection of field and experimental research, which may restrict its applicability in certain scenarios. Moreover, it does not account for several factors, including the orientation of structures relative to the flow direction, mutual influence of neighboring structures on scour, and proportion of the structure's width to its length, due to the current paucity of research in these areas.

2.1.3 Tsunami Inundation

One of the tsunami characteristics that has been widely used by coastal scientists to study the effects of this phenomenon on coastal zones is the inundation height (Kihara et al., 2021; Li et al., 2022; McGovern et al., 2023; Yoshii et al., 2018). The inundation height is defined as the height of the tsunami surge or tsunami bore above the local sea level (Mori et al., 2011). The inundation height depends on the topography of the coastal area and can vary widely for a unique tsunami. According to the field surveys by Tsuji et al. (2006) the maximum inundation height observed during the 2004 Indian Ocean Tsunami was 19.6 m at Ban Thung Dap of Phra Thong Island. In the case of the 2011 Tohoku Tsunami in Japan, Mori et al. (2011) reported inundation height up to 30 m in certain regions along the Tohoku coastline. Such a large coastal inundation can cause catastrophic damage to coastal buildings and lead to the loss of human lives. The cost of the damage caused by the 2011 Tohoku Tsunami was estimated at approximately $360 billion (Lebreton and Borrero, 2013). The total number of confirmed dead or lost people for the Indian Ocean and Tohoku tsunamis were $230,000$ and $19,000$, respectively (Kawachi et al., 2020; Synolakis et al., 2005). Therefore, it is essential to adequately understand the characteristics of tsunami inundation and its effects on the coastal infrastructure and communities.

2.1.4 Scour-Induced Failure Modes of Structures due to Tsunami Inundation

Lim et al. (2015) conducted a comprehensive examination of structural failures following the 2004 Indian Ocean and 2011 Tohoku tsunamis through post-event field surveys, identifying local scour, structural overturning, and sliding as the predominant failure modes. In the context of tsunamis, local scour is defined as the movement of sediment surrounding a structure in response to a tsunami inundation. As the flow strikes the structure, it generates horseshoe and lateral vortices, leading to sediment movement (Figure 2.3). Nakamura et al. (2008) observed significant erosion with dimensions of 5.5 m in width and 1.5 m in depth at Kalapakkom, India, after the 2004 Indian Ocean Tsunami, which contributed to the structural failure. Hence, the investigation of tsunami-induced local scour has attracted global research interest (Amini et al., 2012; Qi et al., 2012; Mitobe et al., 2014; Zhang et al., 2020). Nonetheless, the complexity of modeling tsunami inundation in laboratory settings poses significant challenges.

Overturning transpires when the momentum induced by the inundation depth on one side of a structure surpasses its designed resistance (Figure 2.4-a). Moreover, the disparity in hydrostatic pressure on opposite sides of a structure, caused by frontal run-up and back drawdown, augments

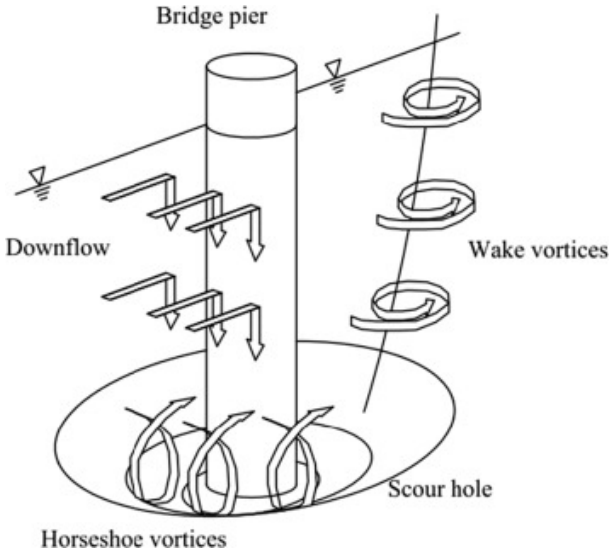

Figure 2.3: Horseshoe vortices and local scour around a bridge pier (Devi and Kumar, 2022) (Permission obtained)

the likelihood of sliding failure (Figure 2.4-b). According to Lim et al. (2015) and Jayaratne et al. (2016), such failure modes were predominantly observed in coastal dikes and seawalls following the 2011 Tohoku Tsunami, highlighting deficiencies in existing design standards for coastal structures to withstand tsunami forces. To support such deficiencies, several studies (Al-Faesly et al., 2012; Harish et al., 2022; Nistor et al., 2009; Nouri et al., 2010) have investigated the forces exerted on structures under various tsunami inundation parameters.

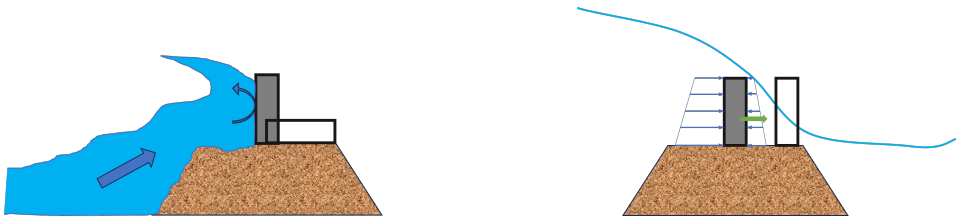

(a) Overturning (b) Sliding

Figure 2.4: Schematics of different failure modes (Adapted from (Lim et al., 2015))

2.1.5 Different Types of Scouring Induced by Tsunami Inundation

Field surveys conducted after the 2004 Indian Ocean and 2011 Tohoku tsunamis have revealed different scour types. This review already expended on local scour mechanisms in Section 2.1.4. Another type, typically observed around seawalls and dikes, is overtopping scour, which arises when tsunami inundation overflows coastal structures, leading to the formation of plunge pools on their landward sides because of substantial downward energy (Kato et al., 2012; Zhang et al., 2017). Maqtan et al. (2018) conducted an experimental investigation into the effects of various parameters on tsunami-induced scour behind vertical seawalls. These parameters included the relative freeboard, defined as the ratio of freeboard to seawall height, as well as the Froude number of the incoming tsunami bore (F_b) and that of the overtopping flow (F_o). The study's findings revealed that F_b exhibits the strongest correlation with the scour depth caused by the tsunami behind the seawall, achieving a correlation factor of 0.992.

Furthermore, Tonkin et al. (2013) delineated channelized and general scour as a consequence of tsunami inundation. The constriction of the flow path in urban layouts can accelerate tsunami bores, which amplifies shear stresses and leads to channelized scour. General scour also refers to the widespread erosion of sediment caused by the high velocity and shear stress of water flowing over the soil in open areas.

2.1.6 Numerical and Experimental Modeling of Tsunami-Induced Scour

The study of tsunami-induced scour around structures encompasses both experimental and numerical modeling approaches. Experimental modeling, despite its limitations, is crucial for addressing the complexities of sediment transport, an area fraught with uncertainties (Roulund et al., 2005). Although laboratory experiments can elucidate certain details that are not readily apparent in numerical simulations, they are often expensive and challenging, especially considering scale effects. Conversely, numerical modeling offers a more expedient and cost-effective alternative, albeit with more simplified assumptions. Moreover, the applicability of sediment discharge equations, which are commonly devised for specific conditions, may not extend to all scenarios (Díaz et al., 2008).

2.1.7 Scaling and Similarity in Tsunami Scour Studies

In experimental studies on tsunami-induced local scour around structures, three primary length characteristics are considered critical: the flow depth, the size of the structure, and the median grain size of the sediment (D_{50}). Among the similarity laws applied, Froude scaling is most frequently utilized due to its relevance in modeling fluid flow dynamics. However, when the focus extends to sediment transport, the straightforward application of Froude scaling to sediment size becomes problematic. This issue arises because very fine sediments, those smaller than 0.1 mm, exhibit cohesive behavior, markedly different from the non-cohesive properties of sand and gravel (Ettema et al., 1998).

To address this issue, researchers frequently utilize the non-dimensional shear stress, or Shields parameter, as a scaling criterion. This approach ensures that both the model and prototype exhibit comparable behaviors under similar conditions. Nonetheless, this approach of distorted scaling may lead to inaccuracies in the modeled scour depth, as highlighted by Lee and Sturm (2009).

Moreover, Melville and Chiew (1999) suggest that the influence of sediment particle size on local scour depth becomes negligible when the ratio of the characteristic length of the structure to the D_{50} of the sediment particles exceeds 50. When the sediment coarseness D/D_{50} is less than 50, the sediment is considered relatively coarse in comparison to the structure. In this scenario, the reduced intensity of horseshoe vortices, along with energy dissipation within the sediment pores, can influence the depth of scour. Conversely, when sediment coarseness exceeds 50, the scour depth is independent of sediment coarseness, and the effects of the two aforementioned factors become negligible. Therefore, it is advisable to maintain this ratio along with adherence to the similarity dictated by the Shields parameter. This dual adherence helps in achieving a more reliable replication of natural scour processes in scaled models.

2.1.8 Objectives

Numerous researchers have examined the phenomena of tsunamis and their associated sediment transport. Takahashi et al. (2001) critically evaluated the applicability of existing sediment

transport formulas to tsunamis, analyzing data from the 1960 Chilean Tsunami. They highlighted that most traditional empirical formulas, designed for low shear stresses, are inadequate for the substantial forces exerted by tsunamis. Additionally, these formulas often assume that the suspended load concentration profile is in an equilibrium state, which is not applicable to tsunami conditions. In response, they conducted experimental tests that mimicked tsunami waves and introduced a new formula for sedimentation during such events. This model was validated using data from the 1960 Chilean Tsunami.

Kihara et al. (2012) developed a 3D numerical model to explore the tsunami-induced sediment deposition processes around a harbor, incorporating the innovative aspect of secondary flows in sedimentation. This consideration is crucial for tsunami-induced sediment transport, as tsunami waves typically have longer wavelengths and periods compared to the usual storm waves encountered in coastal regions. Furthermore, the inundated areas experience topographical changes over extended durations. The researchers validated their model's results against the experimental findings from Fujii et al. (2009), which focused on an idealized harbor and the sediment transport processes surrounding it. This validation underscores the model's effectiveness in capturing the complex dynamics of tsunami-induced sediment transport influenced by secondary flows.

One of the significant challenges in the numerical simulation of real-world tsunamis is the scarcity of observed data, which complicates model calibration and validation. However, the 2011 Tohoku Tsunami at Sendai Plain presented a unique case with an abundance of high-resolution measurements taken before and after the tsunami. This extensive dataset allowed researchers to refine their models with a higher degree of accuracy. Sugawara et al. (2014) leveraged this data to examine the tsunami-induced sediment transport phenomena in both offshore and onshore areas. They emphasized the importance of using coupled hydrodynamic and sediment transport numerical models to accurately assess the volume of sediment deposits resulting from tsunamis. This approach ensures a more comprehensive understanding of the sediment dynamics influenced by such catastrophic events.

Following the 2011 Tohoku Tsunami, Yamashita et al. (2016) utilized the model proposed by Takahashi et al. (2001) to analyze sediment transport processes in Hirota Bay. Their research covered a large area, demonstrating applicability of the model to large-scale simulations. The model proved capable of accurately predicting the spatial distribution and the quantity of sedimentation and erosion, with most erosion occurring due to the powerful initial wave and its return flow. An intriguing outcome of this study was the observation that numerical models not integrated with sediment transport models tend to predict slower run-ups, rendering their results less reliable for subsequent sediment transport analyses.

In light of the escalating environmental challenges and the growing risk associated with tsunamis, it is imperative to gain a deeper understanding of various aspects of this phenomenon to enhance the resilience of nearshore structures. The primary goal of this critical study is to conduct a comprehensive review of the current state of the art only in the context of tsunami-induced local scour around structures. It should be noted that the scour behind seawalls is beyond the scope of this study. Through this review, the main objective was to identify existing research gaps and underscore the forthcoming requirements and priorities within this field of study.

2.2 State of the art in Tsunami-Induced Scour around Structures

The phenomenon of flow-induced scour around structures has been a subject of analysis for many years, with much of the earlier research focusing on current-induced local scour in rivers and wave-induced scour around coastal structures. Sumer et al. (2001) provided a comprehensive summary of the results from a three-year research program carried out by various institutions within the European Union. This program encompassed both numerical and experimental investigations of scour around vertical piles and breakwaters. Additionally, their research extended to studying the effects of pore pressure on scour processes around structures and on general sediment transport phenomena. This extensive collaboration highlighted key insights into the mechanics of scour and sediment dynamics, contributing significantly to the understanding of these complex interactions.

Kiraga and Popek (2020) investigated the effects of two different check gates on the scour occurring both downstream and upstream of the structure. Their study was twofold: it involved a series of laboratory tests designed to simulate river flow, alongside a numerical analysis aimed at assessing the performance of various existing formulas for estimating local scour depth around structures. Based on the insights gained from their experimental data, the authors proposed an optimized version of the equation originally developed by Straub (1934). This refined equation better aligns with the observed behaviors and outcomes from their experiments, offering a more accurate tool for predicting scour depths in similar hydraulic environments.

Yu et al. (2022) explored the local scour depth induced by waves, currents, and the combined effects of wave-current conditions around a permeable breakwater. Their findings revealed that both the depth and the area of the scour hole increased with the height and period of waves under wave conditions, and with water depth and flow velocity under current conditions. Furthermore, the study highlighted that the combined wave-current conditions not only resulted in a deeper scour hole but also extended the time required to reach the equilibrium scour depth. This comprehensive analysis underscores the complex interactions between hydrodynamic forces and their cumulative impact on scouring processes around marine structures.

Much of the research development in the field of local scour around structures, as highlighted in previous discussions, has primarily focused on steady flow conditions. Consequently, the equations and relationships proposed in these studies are not directly applicable to the unique dynamics of tsunami-induced local scour around structures. This distinction is critical, as tsunamis present transient, high-energy flow conditions that differ significantly from the steady-state scenarios typically modeled in scour research. The rest of this section offers a detailed review of the state-of-the-art in the literature by addressing different aspects of tsunamis and the resultant local scour around structures. Initially, the section appraises the various methodologies employed to simulate tsunamis effects in laboratory settings. Subsequently, the discourse examines how structural geometry influences the local scour caused by tsunamis. The review then proceeds to evaluate research concerning local scour surrounding a group of structures. This section culminates in highlighting recent advancements in the numerical modeling of tsunami-induced local scour around structures.

2.2.1 Tsunami Generation Methods in Laboratory

Accurate replication of tsunami bores within a laboratory context is essential for examining the dynamics of tsunami inundation and the scour it induces. This section concisely outlines the salient features of tsunamis, and then proceeds with an in-depth literature review of the

two prevalent techniques employed to simulate tsunami inundation in a controlled experimental environment.

Overview of Tsunami Modelling Parameters

Understanding the parameters of tsunamis is imperative before initiating laboratory experiments. Presented herein is a compilation of the most significant tsunami parameters.

- **Source of generation**: The distance between the origin of a tsunami and the shoreline influences its behavior upon arrival. FEMA-P-646 (2019) classified tsunamis into three categories based on their travel time: (1) far-source tsunamis, taking over three hours to reach the shore; (2) mid-source tsunamis, with one to three hours of travel; and (3) near-source tsunamis, arriving under an hour at the shoreline. Consequently, the categorization of a single tsunami can vary across geographic locations.

- **Energy**: The vast amount of energy transported by tsunamis to the shoreline is a critical aspect of their nature, profoundly influencing their potential for destruction upon impact (Rahman et al., 2021).

- **Amplitude**: Tsunamis are characterized by relatively low amplitudes in deep-ocean waters. However, as they approach coastal areas where the depth decreases, the wave amplitude significantly increases, potentially rising to tens of meters (Sun et al., 2019).

- **Wavelength and period**: Tsunami waves possess exceptionally long wavelengths, with periods extending from minutes to hours, contrasting sharply with shorter periods of ordinary wind-generated ocean waves (Tanioka et al., 2022). This distinction necessitates laboratories to employ specific methods to accurately simulate tsunami waves.

- **Run-up and inundation depth**: Run-up is the vertical height above sea level reached by a tsunami, as it inundates inland areas. In contrast, inundation depth is the depth of water above normal sea level at specific locations as the tsunami moves inland. Both metrics are crucial for understanding tsunamis and their associated scour effects on structures (Borrero et al., 2023).

- **Bore front velocity**: This is the speed at which the leading edge of a broken tsunami wave advances inland from the coastline. This parameter is integral to the analysis of scour induced by tsunamis around structural foundations and necessitates precise replication in experimental modeling (Chuang et al., 2020).

Understanding tsunami characteristics is essential for selecting suitable laboratory simulation techniques. Tsunami waves and bores can be replicated using various methods; for instance, Tadepalli and Synolakis (1994) employed N-waves, Synolakis et al. (1988) used Cnoidal waves, Nouri et al. (2010) employed dam-break waves, while Goseberg et al. (2013) adopted pump-driven long waves. Subsequently, this paper will detail two prevalent laboratory methods favored by researchers and will discuss their merits and limitations.

Solitary Waves and their Application in Scour Studies

Tsunamis are recognized for their long wavelengths and periods and can traverse the deep ocean rapidly and with negligible energy dissipation. Upon encountering the reduced depths of nearshore coastal regions, these waves experience alterations with a reduction in wavelength

and velocity as well as wave breaking and/or surging, particularly in areas with sharp seabed inclines (Tanioka et al., 2022). The similarity of these characteristics to solitary wave theory has led to the widespread use of piston-type wavemakers in laboratories for the generation of solitary waves as tsunami wave proxies. This section reviews the empirical studies that have adopted solitary waves to represent tsunamis.

Kato et al. (2001) conducted experimental studies on scour depth progression around structures during tsunami inundation using solitary waves to mimic tsunami conditions. These waves were produced by a piston-type wavemaker capable of creating solitary waves with wavelengths of 2.4 m. Their experiments consisted of three still water depths: $h = 2.45 \pm 0.2$ m, and wave amplitudes ranging from $a = 0.11$ m to 0.34 m. This resulted in water depths d extending from 1.91 m to 2.99 m. Wave celerity, c, is a function of the water depth, d, and can be calculated as follows:

$$c = \sqrt{gd} \tag{2.1}$$

According to this equation, the celerity of the waves in Kato et al. (2001) was estimated to be between 4.33 m/s and 5.42 m/s. Although their study lacked information on the test scale, a subsequent study by Tonkin et al. (2003), using the same facilities and similar wave parameters, noted having considered a 1 : 10 scale. Assuming a correspondence between the two studies, wave amplitudes in these tests potentially represented real-world tsunami amplitudes ranging from 1.1 m to 3.4 m, aligning with observed tsunami data (Rossetto et al., 2007; Tanioka et al., 2022; Tsuji et al., 2006). However, when applying Froude scaling, the real-scale (prototype) periods of the generated waves in these experiments were between 4.43 s and 5.54 s, significantly shorter than typical tsunami wave periods.

Nakamura et al. (2008) conducted experimental analyses to investigate the scour patterns induced by tsunamis around a square structure by employing a piston wavemaker for wave generation. The Froude scaling ratio in the tests was 1 : 20. They produced solitary waves with a 6 s period and isolated long waves with a 14 s period. The solitary waves exhibited velocities between 0.88 m/s and 2.29 m/s, and wavelengths from 5.28 m to 13.74 m. Isolated long waves celerity varied from 1.94 m/s to 2.26 m/s, with wavelengths of 27.16 m to 31.64 m. In prototype scale, the solitary waves achieved celerity similar to that of typical tsunamis but with shorter periods compared to typical real-world tsunamis, which often span several minutes ($c = 10.24$ m/s and $T = 26.83$ s), while the isolated long waves exhibited wavelengths and periods more aligned with actual tsunami events ($L = 633$ m and $T = 62.61$ s).

Chen et al. (2013) conducted experimental tests to investigate tsunami-induced scour around coastal roadways, employing a piston-type wavemaker to generate solitary waves with an average period of 2.4 s. Referencing the work of Tregnaghi et al. (2009), the authors noted that typical tsunami wave periods are approximately 20 min. This information suggests a time scale (model to prototype wave period) of approximately 1 : 500 for their study. Moreover, they observed that the equilibrium scour depth in their experiments was achieved within 63 s to 132 s. Using the 1 : 500 time scale, this corresponds to a prototype scale duration of 9 to 18 hours to reach equilibrium scour depth around coastal roadways, which is implausibly long. Additionally, the application of such a small-scale model to study flow-induced scour presents significant challenges and may compromise the accuracy of the results.

Larsen et al. (2018) explored tsunami-induced erosion around monopile foundations through experimental tests. They generated tsunami waves using a programmable pump capable of producing a solitary-like wave with controllable flow velocity. Despite the wave's resemblance to solitary waves, the authors noted its adjustable velocity and period as a means to address the discrepancy between the shorter periods of solitary waves and actual tsunami waves. Roulund

et al. (2005) indicated that for flows with a Froude number below 0.2, the scour depth is mainly governed by the boundary layer with minimal impact from the near-surface flow. Building on this, Larsen et al. (2018) argued that the kinematic and geometric similarity between the model and real-world cases can be achieved using non-dimensional parameters $U_m^2/(gD)$ and δ/D, where U_m is the maximum free stream velocity, δ represents the boundary layer thickness, and D is the pile diameter. In these experiments, the scaled prototype periods ranged from 592 to 2416 s, aligned with the typical tsunami wave periods. However, studies by Fritz et al. (2006) and Iwai and Goto (2021) on the 2004 Indian Ocean and 2011 Tohoku tsunamis revealed that the actual Froude numbers, based on video analysis during these events, ranged from 0.61 to 1.04 and 0.7 to 2.0, respectively. This suggests that assuming a Froude number around 0.2, as in Larsen et al. (2018) may not accurately represent real-world tsunami conditions, except for some limited periods of the inundation such as when it reaches the maximum spatial flood extent.

Xu and Huang (2022) investigated the scour effects of tsunamis on pile breakwaters, noting the challenges of using a single solitary wave for laboratory simulations, owing to scaling limitations. They referenced the study by Xu et al. (2019), which demonstrated that an equivalent wave period can be calculated for a series of consecutive solitary waves, resulting in a longer period than that of an individual solitary wave. According to Xu and Huang (2022), this approach more effectively captures the essential characteristics of tsunami waves in the context of scouring around pile breakwaters. Although the wave period in these tests was approximately 0.4 s, the scale factor was not provided for the experiments, making it difficult to fully assess the validity of this approach. Table 2.1 summarizes the studies presented in this section.

Dam-Break Waves and their Application in Scour Studies

Numerous studies have examined solitary waves as a proxy for real tsunami waves; however, the discrepancy in wave periods between the two remains a critical issue for researchers. Chanson (2006) examined videos from the 2004 Indian Ocean Tsunami in Banda Aceh, Indonesia, which revealed similarity between the dynamics of the tsunami bore and the dam-break waves. The genesis of dam-break wave analysis dates back to Ritter (1892), who formulated an analytical solution for a theoretical dam-break scenario over an idealized, frictionless, horizontal, and dry bed. Subsequently, Chanson (2006) advanced this field by introducing two distinct sets of equations applicable to dam-break wave propagation over either frictionless (idealized) or rough beds. Each of these sets comprises three equations that delineate the velocity of the bore front, its spatial positioning, and the bore profile. According to Chanson (2006), the governing equations, specifically regarding the rough-floor scenario, are in good agreement with real tsunami-bore hydrodynamics. The equations are as follows:

$$\frac{8}{3}\frac{1}{f}\frac{\left(1-0.5\frac{U}{\sqrt{gd_0}}\right)^3}{\frac{U^2}{gd_0}} = \sqrt{\frac{g}{d_0}}t \tag{2.2}$$

$$\frac{x_s}{d_0} = \left(1.5\frac{U}{\sqrt{gd_0}}-1\right)\sqrt{\frac{g}{d_0}}t + \frac{4}{f\frac{U^2}{gd_0}}\left(1-0.5\frac{U}{\sqrt{gd_0}}\right)^4 \tag{2.3}$$

where f is the bed roughness, d_0 is the initial water depth behind the dam, U is the bore front velocity, x_s is the bore front location, and g is the gravitational acceleration. The bore profile equation (Equation 11 in Chanson (2006)) is not presented herein because of space limitations.

Imamura et al. (2008) utilized a dam-break bore to investigate the effects of tsunami bores on the displacement of a cubic box, serving as a surrogate for large boulders. The experimental

Table 2.1: Summary of studies using solitary waves as a representation of tsunamis.

Reference	Location	Flume Dimensions			Wave Type	Wave Characteristics (Prototype Scale)			Notes
		Length [m]	Width [m]	Depth [m]		Celerity [m/s]	Wavelength [m]	Wave Period [s]	
Kato et al. (2001) Tonkin et al. (2003)	Public Works Research Institute, Tsukuba, Japan	135.0	2.0	5.0	Solitary Wave	[13.69 – 17.14]	Up to 24.0	[4.43 – 5.54]	-
Nakamura et al. (2008)	Department of Civil Engineering at Nagoya University, Japan	30.0	0.7	0.9	Solitary wave	[3.93 – 10.24]	[105.6 – 274.8]	26.83	-
					Isoloated long wave	[8.68 – 10.11]	[543.2 – 632.8]	62.61	-
Chen et al. (2013)	Changsha University of Science and Technology, China	40.0	0.5	0.8	Solitary wave	NA	NA	NA	Scout around coastal roadways
Larsen et al. (2018)	Technical University of Denmark, Denmark	35.0	2.0	0.5	Solitary-like wave	NA	NA	[592.0 – 2416.0]	Froude number is less than typical real-world tsunamis
Xu and Huang (2022)	Provincial Key Laboratory, Water-Sediment Science and Water Disaster Prevention of Humans, China	40.0	0.5	0.8	Consecutive solitary waves	NA	NA	NA	Scale factor is not mentioned

setup is depicted in Figure 2.5, which illustrates a flume equipped with two vertical gates. Upon attaining its peak run-up height and initiating the drawdown phase, the drainage gate was opened to facilitate dewatering of the backwash flow. To align the experimental model with actual tsunami phenomena, Imamura et al. (2008) calculated the Froude, Reynolds, and Shields numbers for experimental tests and juxtaposed them with those from various historical tsunamis. Notably, they observed that the Shields numbers for the 1771 Meiwa and 1960 Chile tsunamis, as inferred from aerial photography of the Japanese coastline, ranged from 5 to 10. Specifically, for the 1771 Meiwa Tsunami, the Froude number was below 1.0, whereas the Reynolds number was approximately 10^7. The corresponding dimensionless numbers derived from the experimental tests were within similar ranges: 4 to 10 for the Shields number, under 1.3 for the Froude number, and around 10^4 for the Reynolds number. This demonstrates a considerable correlation with the hydrodynamics of actual tsunamis.

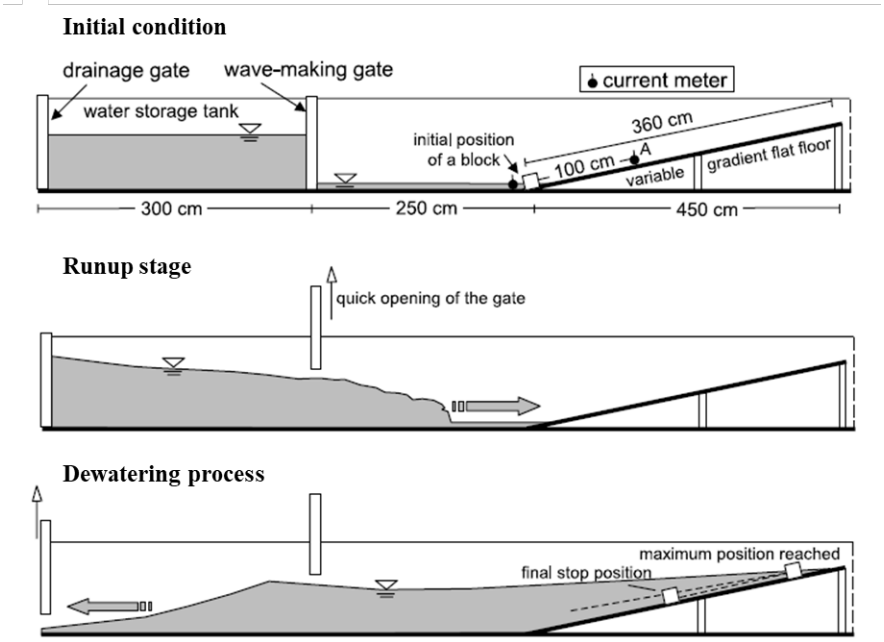

Figure 2.5: Experimental test setup of (Imamura et al., 2008) (Permission obtained)

Leal et al. (2009) conducted a sequence of laboratory experiments to investigate the influence of movable beds on the propagation of dam-break bores. This was achieved by initiating a dam-break bore through the operation of a vertical lift gate. The experimental setup included a movable bed that extended throughout the flume, including the area upstream of the gate. Their study focused on two types of bed materials, sand and pumice, while also including tests on a solid bed. The primary objective was to assess the impact of the movable bed on the hydrodynamic characteristics of bore propagation without delving into the scouring process. However, the reliability of the findings was compromised by the limitations of the measurement instruments. For instance, water level measurements were derived from pressure transducers based on the assumption of a hydrostatic pressure distribution. This assumption is problematic given the unsteady nature of dam-break flows, which are characterized by significant non-hydrostatic pressures. Consequently, the results of the study should be interpreted with caution because of measurement inaccuracies.

Arnason et al. (2009) examined the reciprocal effects of tsunami bores and structures under wet-bed conditions. Their experimental setup involved a constant still water depth of 20 mm downstream of the gate, whereas the impoundment depth upstream varied from 100 to 300 mm

across different tests. The authors noted the gate opening time to be 0.2 s. Referencing the work of Lauber and Hager (1998), it was highlighted that for an ideal dam-break bore, the non-dimensional gate opening time should be less than $\sqrt{2}$. This non-dimensional time is calculated using the formula $t\sqrt{g/h_0}$, where t is the opening time and h_0 is the impoundment depth. In the study of Arnason et al. (2009), this value ranged from 1.14 (for an impoundment depth of 300 mm) to 1.98 (for 100 mm), indicating that, in some instances, the experiments exceeded the recommended threshold. Furthermore, Arnason et al. (2009) acknowledged discrepancies between the observed bore-front velocity and its location as well as the findings reported by Chanson (2006). However, the study did not address the issue of gate opening time. This omission suggests a potential area of weakness in their methodology or analysis, as the gate opening time directly influences the characteristics of the generated bore and, consequently, the experimental outcomes.

One year later, an extensive investigation of the forces exerted by tsunami waves on structures was undertaken by Nouri et al. (2010). This study encompasses a range of parameters, including the forces impacting cylindrical and square structures, vertical distribution of pressure, dynamic response of cylindrical structures to the tsunami bore, influence of flow constriction on its hydrodynamics, and impact of debris on the structures. The experimental setup included a flume equipped with a swing gate, characterized by an opening duration of approximately 0.25 s. Nouri et al. (2010) noted that the impoundment depths employed in the study ranged from 0.5 m to 1 m. Furthermore, the gate's non-dimensional opening time spanned from 0.78 to 1.11, aligning with the acceptable range established by Lauber and Hager (1998). A significant finding arose from comparing the outcomes of the current study with those of Arnason et al. (2009). It was observed that the inconsistencies previously noted in the results of Arnason et al. (2009) were no longer apparent, underscoring the significance of adhering to the critical opening time criterion to enhance the reliability of the results.

Al-Faesly et al. (2012) conducted a detailed investigation of the hydrodynamic forces exerted on structures by the tsunami bores. Their study incorporated an assessment of three significant historical tsunamis: the 2004 Indian Ocean, the 2010 Chile, and the 2011 Tohoku events. Drawing on the work of Chanson (2006), they utilized dam-break bores to simulate tsunami bores. The experimental setup included a flume equipped with a swing gate, with the gate-opening time adhering to the criteria established by Lauber and Hager (1998). The key measured parameters included bore velocity and flow depth, as well as the forces applied to the structures. Additionally, this research delved into the impact of employing mitigation walls positioned in front of structures, aiming to assess their effectiveness in diminishing the forces exerted on the structures.

Lavictoire et al. (2014) executed a series of experimental tests to explore bore-induced local scour around a circular structure, utilizing a similar experimental setup as Al-Faesly et al. (2012). This consistency in experimental design allows for the potential integration of scour data with the forces exerted on structures by tsunamis in future analyses. The experiments employed a composite steel and wood swinging gate to generate dam-break bores, with the non-dimensional opening time of the gate meeting the criteria set forth by Lauber and Hager (1998) for generating ideal bores. The study primarily focused on examining the influence of sediment particle size and impoundment depth on the scour depth around such structures.

Wüthrich et al. (2018) introduced an innovative technique for simulating tsunami bores in laboratory settings. This method, termed the "vertical release generation technique", entails the use of two vertically aligned reservoirs, with the lower reservoir being fully filled with water. These reservoirs were connected using a series of three vertical pipes, and the lower reservoir was linked to the upstream section of the flume through an inlet. At the start of the test, operators opened the pipe valves, initiating a flow of water into the flume, driven by the differential water heads between the two reservoirs, as depicted in Figure 2.6. This technique was shown to produce

a surge that closely resembled the classic dam-break scenario in terms of bore front velocity and flow depth. This study explored the behavior of tsunami bores under both wet- and dry-bed conditions and concluded that a wet-bed state diminishes the significant variability in the Froude number throughout the experiments. The researchers employed an Ultrasonic Velocity Profiler (UVP) to measure the velocity profile across the water column. While the study did not delve into the impact of valve opening time on bore development, it is noted that valve operation, being significantly faster than the opening of large swings or vertical gates, potentially facilitates the generation of an ideal dam-break bore. However, further discussion and analysis are required to accurately compare the outcomes of this technique with real-world tsunami behaviors.

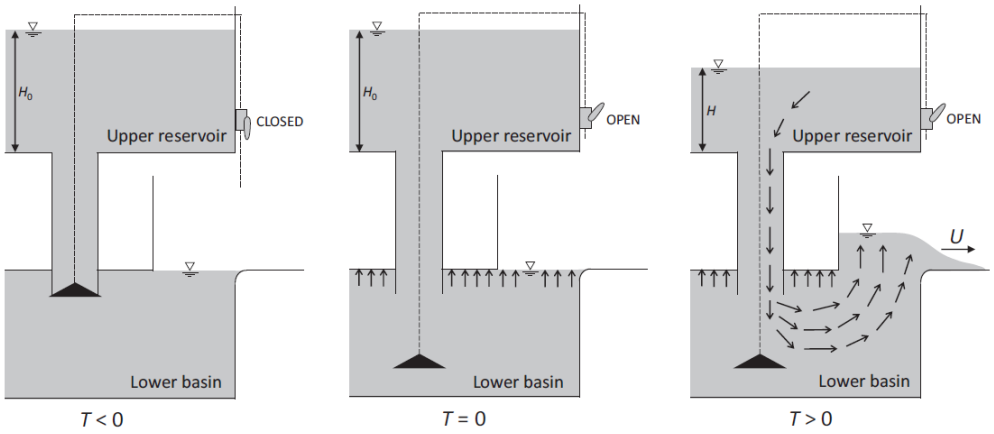

Figure 2.6: The vertical release generation technique for simulating tsunami bores in laboratory settings (Wüthrich et al., 2018) (Permission obtained)

Mehrzad et al. (2022) carried out a series of experimental tests using the University of Ottawa's Dam-break Flume to investigate the impact of impoundment depth on the scour around a square structure. Drawing on the prior study by Stolle et al. (2019), which also utilized the same flume, Mehrzad et al. stated that the non-dimensional opening time of the gate (T_0) is dependent on the impoundment depth (h_u) as follows:

$$T_0 = 1.47 - 1.19h_u \tag{2.4}$$

According to this equation, the non-dimensional opening time of the swing gate in their experiments, with the impoundment depths of 0.2 ± 0.05 m, ranged from 1.17 to 1.29, aligning with the criteria set by Lauber and Hager (1998) for an ideal dam-break model. The study adopted a $1 : 40$ length scale based on Froude similarity, while acknowledging the impossibility of scaling the sediment particle diameter using the same length scale. Consequently, the selection of parameters was guided by the need to maintain similarity in the non-dimensional shear stress (Shields parameter) between the model and the prototype.

Evaluation of Tsunami Generation Methods

In laboratory simulations of tsunamis, both solitary waves and dam-break problems have distinct advantages and limitations. Solitary waves, characterized by a single, large-amplitude wave, provide a rather simplistic model that facilitates the study of nonlinear and long-distance propagation characteristics of tsunamis (Synolakis and Bernard, 2006). However, the solitary wave model not only oversimplifies the complex, multi-wave nature of tsunamis, but also typically features shorter wave periods compared to real-world tsunamis, thus failing to accurately represent

their generation, evolution, and interaction with coastal topography (Madsen et al., 2008). In contrast, dam-break waves are useful for studying the immediate impacts of tsunamis, including inundation and local scouring Liu et al. (2008). However, they fall short in depicting the long-distance propagation and gradual evolution of wave characteristics observed in real tsunamis. Although both methods offer valuable insights, their limitations suggest the need for careful selection based on the specific tsunami behaviors under investigation.

2.2.2 Effects of Structure's Geometry on Local Scour

The primary aim of research into tsunami-induced scour around structures is to elucidate the underlying erosion mechanisms, thereby enhancing the guidelines for structural design. Among the various factors that influence scour, the geometric properties of the structure are particularly significant. Considering structures of sufficient height to preclude the overtopping phenomena, two key geometric attributes warrant attention: the shape of the structure (e.g., square, circular) and its dimensions (length and width). This section presents an exhaustive review of the existing literature that focuses on the impact of these specific parameters on the depth of scour induced by tsunamis.

Shape of Structure

Triatmadja et al. (2011) explored the influence of the column shape on local scour by utilizing a dam-break wave to generate tsunami-like bores. The gate's opening time was set at 0.4 s, aligned with the criteria mentioned in Lauber and Hager (1998) for an ideal dam-break bore. The experimental setup featured a flume with a 2 m horizontal sediment pit immediately following the gate and a 7 m sediment section with a slope of $1/100$. Based on the Froude similarity, the experiments were scaled down to a $1 : 100$ ratio. The median sediment grain size was 0.3 mm and the circular column used in the tests had a diameter of 0.033 m, while the square column dimension was 0.045 m. These structures are positioned on a sloped sediment section. The findings revealed that the maximum scour depth around the square column was marginally greater than that measured around the cylindrical structure. However, several concerns can be raised regarding this study's methodology. First, the experiments were conducted on an extremely small scale, potentially leading to significant scaling effects. Second, when using the dam-break method, it is typically recommended that a non-erodible section should be considered immediately after the gate to ensure a fully developed flow. In studies such as this and of Leal et al. (2009), the general scour occurring downstream of the gate can influence the hydrodynamic conditions of the flow. This aspect of the methodology may have affected the results, suggesting the need for further investigation to corroborate these findings.

Shafiei et al. (2015) explored the influence of structural geometry on scour caused by tsunamis around different structures. The experimental setup consisted of a flume connected to a large reservoir by means of an automatic vertical gate. A sand bed with a median grain size of 0.85 mm was placed 10 m downstream of the gate to facilitate fully developed flow conditions. The study examined three distinct structural shapes: circular, square, and diamond, which is essentially a square column rotated by 45°. The size of these structures, measured as the width of the square and diamond shapes and diameter of the cylinder, was uniform at 0.3 m. The results indicated that the maximum scour depth observed for the square structure was approximately 25% greater than that of the diamond-shaped structure, while the circular structure exhibited the lowest scour depth. The study also noted that for all tested geometries, the maximum scour depth consistently occurred at the corners of the columns.

Jayaratne et al. (2018) and Jordan et al. (2019) conducted comparative laboratory investigations to evaluate the scouring at the upstream face of square and circular structures. It is imperative to note that in these experiments, the width of the structures was commensurate with that of the flume, preventing the passage of tsunami bores along the structures. In their study, Jayaratne et al. (2018) employed a square column situated within a sediment section of a flume and generated dam-break bores using a manually operated gate. This study revealed that the maximum scour depth is located at the upstream centerline of the structure. This finding diverges from prior and subsequent research works, which typically identify the corners of structures as the locations of the maximal scour depth. Such divergence in results could be attributed to the restricted lateral flow in the setup of Jayaratne et al. (2018), leading to an intensified flow concentration at the centerline. Concurrently, Jordan et al. (2019) replicated the experimental setup with a circular structure. Their findings indicated that the maximum scour depth occurred at the sides of the structure, which was likely due to the circular column's ability to redirect flow. These authors inferred that under these specific conditions, the maximum scour depth for square structures is less than that for circular structures. This conclusion contrasts the findings of Triatmadja et al. (2011) and Shafiei et al. (2015).

Dissanayaka and Tanaka (2023) conducted a detailed investigation into the impact of flow regimes, as well as the shape and size of structures, on tsunami-induced local scour surrounding a single emergent piloti-type column. Their experimental setup involved a flume measuring 0.5 m in width, with the maximum width of the column being 0.067 m, thereby mitigating any potential blockage effects from the flume's side walls. The flow in these experiments was initiated using a pump connected to the base of the flume. Both the subcritical and supercritical flow regimes were analyzed in this study. Their findings revealed that the maximum scour depth surrounding a square column exceeded that around a circular column of comparable dimensions. To facilitate practical applications, Dissanayaka and Tanaka (2023) proposed empirical equations for estimating the scour depth under various flow regimes and bed slopes based on several non-dimensional parameters. These formulas comprise separate sub-equations for circular and square columns. A critical aspect to consider in the interpretation of these findings is the diminutive scale of their tests. The small scale of the experimental setup raises concerns regarding the potential magnification of scaling issues, which could affect the generalization of the results to real-world scenarios.

The formation of horseshoe vortices, which is a critical factor in local scour phenomena, exhibits distinct behavior in front of square and circular columns of identical dimensions. The inherent curved geometry of a circular column facilitates the lateral dispersion of these vortices to the side faces rather than their accumulation at the centerline of the front face, as is more common with square columns. This physical mechanism leads to the expectation of deeper scour hole formation in front of square columns. Within the scope of the studies outlined in this section, as summarized in Table 2.2, the research conducted by Shafiei et al. (2015) stands out for its reliability and consistency with the theoretical expectations regarding the impact of structural shape on local scour depth. The inherent complexities and uncertainties associated with sediment transport phenomena underscore the importance of employing consistent experimental setups when the objective is to isolate and assess the impact of specific variables such as structural geometry. This highlights the difficulty of directly comparing the outcomes across different studies. Furthermore, it is important to note that many investigations in this field have been conducted at considerably small scales. This limitation not only affects the direct applicability of the results, but also presents an opportunity for future research. Further exploration, particularly on a larger scale, could provide more comprehensive insights into the effects of the structural shape on local scour patterns, thereby enhancing the applicability of these studies to real-world

scenarios.

Table 2.2: Summary of studies on the effects of structural shape on local scour

Reference	D_{50} [mm]	Shape	Order of the maximum scour depth around each structural shape	Notes
Triatmadja et al. (2011)	0.30	Circular Square	Square > Circular	-
Shafiei et al. (2015)	0.85	Circular Square Diamond	Square > Circular > Diamond	-
Jayaratne et al. (2018) Jordan et al. (2019)	0.22	Circular Square	Circular > Square	Width of the column was equal to the flume's width
Dissanayaka and Tanaka (2023)	0.90	Circular Square	Square > Circular	-

Size of Structure

The dimensions of a structure represent another geometric characteristic that influences the tsunami-induced scour. Nakamura et al. (2008) examined the impact of various parameters, including the incident wave height, wave period, sediment particle size, and structure width, on scour patterns around a square structure. This study specifically compared square structures with widths of 0.1 m and 0.14 m. The findings revealed that variations in the width of the structure influenced both the maximum scour depth and the pattern of the scour hole. An increase in the structural width resulted in a shift in the maximum scour depth location, moving from the corners of the structure to its upstream face centerline. Furthermore, the research demonstrated an increment in the maximum scour depth from 14 cm for a width of 0.1 m to 16 cm for a width of 0.14 m. This change is attributed to the intensified concentration of horseshoe vortices at the frontal face of the structure with an increase in column width. However, it is important to note, as highlighted in Section 2.2.1, that the wave period used in this study to simulate tsunami waves was shorter than that of actual tsunamis. Consequently, the applicability of these results to real-world tsunami scenarios is limited.

The experimental study conducted by McGovern et al. (2019) focused on analyzing the impact of structural dimensions on local scour patterns around structures subjected to tsunami inundation. The research utilized a square column with dimensions of 0.2×0.2 m and a rectangular structure measuring 0.4×0.2 m, with the longer side aligned perpendicular to the flow direction. The generated tsunami wave had a period of 147 s, and the scale of the experiments was set at $1:50$. This scaling implies that the equivalent real-world tsunami wave period would be approximately 17.3 minutes (1038 s). To monitor scour development, cameras were installed inside the columns. The observed data, as illustrated in Figure 2.7, indicate a greater scour depth at the corners than at the centerline. This observation led to the conclusion that lateral vortices were primarily responsible for the scour around the structures, whereas horseshoe vortices had a minimal impact on scour formation. These lateral vortices originated at the corners and moved toward the centerline. However, in the case of the rectangular column, the intensity was not strong enough to

affect the centerline, resulting in a zone near the centerline where no scouring was observed (as shown in Figure 2.7-f). Moreover, the findings of this study indicated that the maximum scour depth for the rectangular column exceeded that of the square column. This difference highlights the influence of structural shape on the scouring process.

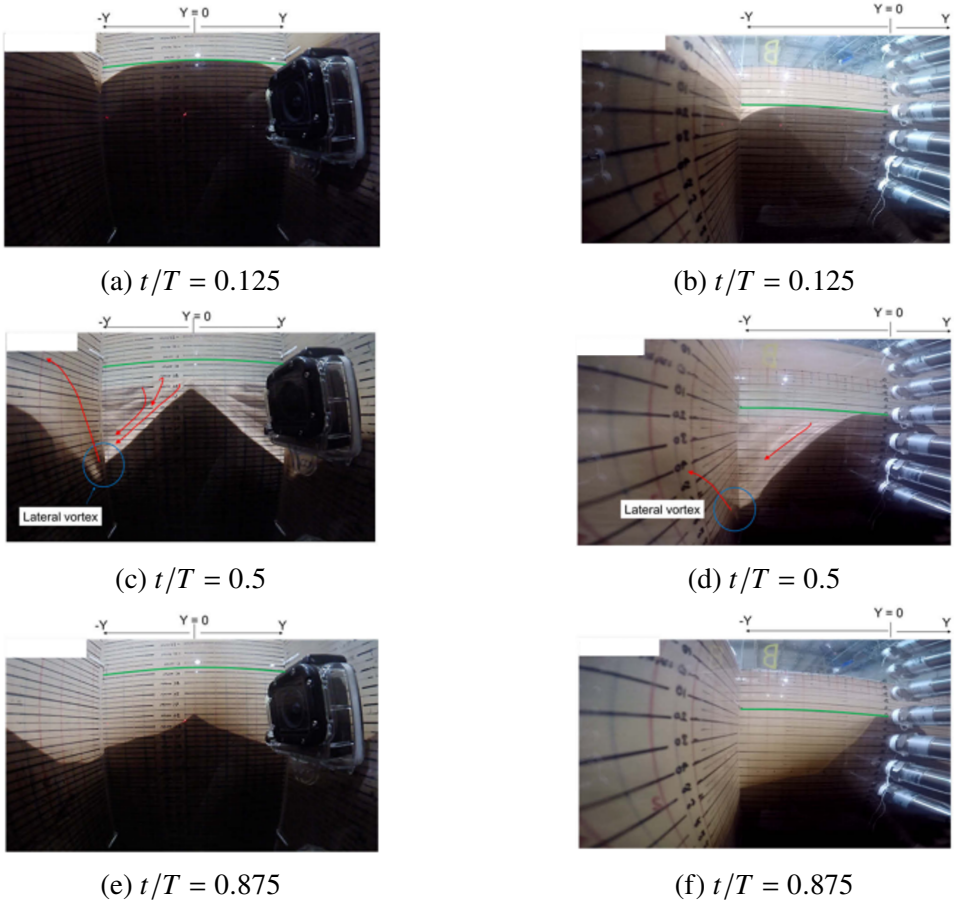

(a) $t/T = 0.125$ (b) $t/T = 0.125$

(c) $t/T = 0.5$ (d) $t/T = 0.5$

(e) $t/T = 0.875$ (f) $t/T = 0.875$

Figure 2.7: The scour pattern at the front and side faces of the square column (a, c, and e) and the rectangular column (b, d, and f). The green line shows the initial position of the sediment (McGovern et al., 2019) (Permission obtained)

April-LeQuéré et al. (2020) conducted a study using Flow3D software to explore the impact of the lateral spacing between multiple columns on tsunami-induced scour around structures. The numerical model employed in their study was calibrated against the maximum scour depth found in the experimental tests of Mehrzad et al. (2016) pertaining to a single-column setup. One of the scenarios in their study involved two adjoining columns that resembled a structure with doubled width. In this configuration, they observed a 48% increase in the maximum scour depth attributed to the increased effective width of the structure, which intensified the concentration of horseshoe vortices at the front of the column. The research highlighted discrepancies between the numerical and physical models. In the numerical model for a single column, the maximum scour depth was located at the corners of the structure. In contrast, the physical model of Mehrzad et al. (2016) showed that the maximum scour depth occurred at the centerline. However, for the wider column scenario, both the numerical and experimental models consistently exhibited the maximum scour depth at the corners. The study also revealed differences in the scour hole patterns downstream of the structures. In the single-column case, the scour hole extended to the downstream face and was influenced by the circular motion of the lateral vortices. Conversely,

when the width of the column was doubled, the centerline of the downstream face was shielded from these lateral vortices. These findings underscore the importance of further investigation into the effects of structural sheltering on tsunami-induced scour.

The findings presented in this section indicate that the maximum scour depth generally increases with the width of the structure. However, there was notable divergence in the observed scour patterns across these studies. Nakamura et al. (2008) observed that for smaller structures, the maximum scour depth typically occurred at the corners, whereas for wider columns, it shifted to the centerline. Conversely, McGovern et al. (2019) found that the maximum scour depth consistently occurred at the corners for both small and large structures. Furthermore, April-LeQuéré et al. (2020) noted in their numerical model that the maximum scour depth was located at the corners for structures of varying sizes. The disparities in these results could be attributed to the different methodologies employed to simulate tsunami inundation across these studies. Such inconsistencies underscore the need for further research in this area, particularly because of the limited information available for validation of these models. This gap in understanding highlights the importance of continued investigation of the dynamics of tsunami-induced scour around structures of varying dimensions to develop a more comprehensive understanding of these phenomena.

2.2.3 Effect of Structures' Arrangement on Local Scour Pattern

Single Structure

Various investigations have been conducted to explore local scouring phenomena around a single column. This area of research, detailed in previous sections of this paper, includes works such as those by April-LeQuéré et al. (2020), Dissanayaka and Tanaka (2023) ,Jayaratne et al. (2018) ,Jordan et al. (2019), Larsen et al. (2018), McGovern et al. (2019), Nakamura et al. (2008), and Triatmadja et al. (2011). This section presents additional scholarly contributions pertaining to the study of local scours around individual structures.

Kato et al. (2001) conducted a detailed study on tsunami-induced erosion around a circular column utilizing solitary waves as a proxy for tsunamis, as detailed in Section 2.2.1. In this study, the erosion and sediment deposition processes were recorded using a trio of cameras positioned inside a cylinder with a diameter of 50 cm. These cameras were oriented to capture views offshore, along the shore, and onshore. The column was situated on a slope with a $1/20$ gradient, and the investigation encompassed three distinct still-water depths. These depths were chosen to simulate various scenarios including the structure being located offshore, at the shoreline, and inshore. A key observation of this study was the disparity in scour depths at different locations around the column. The analysis of the video data revealed that the maximum scour depth on the offshore side was significantly greater (up to five times) than the final equilibrium scour depth. However, an intriguing aspect of their findings was that, despite the offshore side experiencing a larger maximum scour depth, its final equilibrium scour depth was less than that observed on the inshore side. This aspect of the study highlights the complex dynamics of sediment erosion and deposition in coastal environments, particularly under the influence of tsunami-like conditions.

Tonkin et al. (2003) conducted a study on scour around a cylindrical structure during tsunami inundation, building on the experimental setup used by Kato et al. (2001). However, Tonkin et al. (2003) expanded the scope of their research to include both sand and gravel beds. Tonkin et al. (2003) found that the deepest equilibrium scour depth occurred at the back face of the column in the sand bed, whereas for the gravel bed, it was at the front face. This study critically evaluated the conventional understanding of the impact of shear stress (as characterized by the Shields parameter) on the scouring process around structures. For gravel beds, initial increases in the

bed level at the back face were observed, with the maximum scouring rate and Shields parameter occurring simultaneously. During the wave drawdown stage, the scouring rate decreased, and minor sediment deposition occurred at the back face. This observation aligns with theories that attribute scouring predominantly to the bed shear stress. Conversely, for the sand beds, the maximum scouring rate was recorded during the drawdown stage. This finding is significant because it implies that the scouring rate increased when the flow velocity, and correspondingly, the Shields parameter, decreased, challenging the classical approach. Furthermore, the equilibrium scour depth at the front face for the gravel bed exceeded that of the sand bed, which contradicts the expectations based on the Shields parameter. However, the final scour depth at the back face for the sand bed was greater than that at the gravel bed. The authors proposed that pore water pressure is a critical parameter that is overlooked in the classical approach. At the drawdown stage, the rapid reduction in effective stresses and high pore water pressure in the sand led to an accelerated scour rate. In contrast, the larger porosity of the gravel meant that the excess pore water pressure did not significantly influence the scour rate. This unique finding presented by Tonkin et al. (2003), which was not observed in previous studies, highlights a potential subject for further investigation in this field.

Lavictoire et al. (2014) investigated the tsunami-induced local scouring process around a circular column using two distinct sediment types: sand and gravel. This approach differs from that of Tonkin et al. (2003), as tsunami bores were generated through the sudden opening of a rapidly-opening swing gate. The study revealed that the deepest equilibrium scour depth was consistently observed at the front side of the column for both sediment types, a finding that diverges from that of Tonkin et al. (2003). Notably, Lavictoire et al. (2014) observed that the final scour depth at the front face in sand exceeded that observed when using gravel, which differed from the observations of Tonkin et al. (2003). This variation underscores the importance of selecting suitable tsunami generation methods for laboratory experiments. Additionally, Lavictoire et al. (2014) examined the scour induced by secondary bores, a scenario in which the reservoir was refilled and water flowed over a pre-existing eroded bed without leveling the original scour hole. This leads to sediment movement into the scour hole and a consequent reduction in the maximum scour depth. Nonetheless, the presence of a scour hole around the structure was still evident.

Shafiei et al. (2015) conducted a detailed investigation of the tsunami-induced scouring around a single column. The specifics of this study and its findings regarding the impact of the structural geometry on the scour depth are detailed in Section 2.2.2. A key focus of their study was the influence of the structure embedment depth on scour depth. Their findings revealed that structures with greater embedment exhibit larger scour holes. The embedment depth was found to significantly affect the maximum scour depth up to a certain threshold, beyond which the scour depth stabilized.

Mehrzad et al. (2022) conducted a series of experimental tests to explore tsunami-induced scour around a square structure by adopting a dam-break methodology. A video camera was positioned inside the structure to monitor the erosion process. Mehrzad et al. (2022) observed, similar to the findings of Kato et al. (2001) and Tonkin et al. (2003), that the maximum scour depth exceeded the equilibrium scour depth, which was attributed to run-up and drawdown processes. The study also revealed that the scour depths at the corners of the square structure were marginally greater than those along the centerline of the front face, and both were deeper than those on the side faces.

Rajaie et al. (2023b) explored the tsunami-induced local scour around a square column situated on both horizontal and sloped wet beds. To simulate tsunami conditions, the researchers employed dam-break bores and varied the still-to-impoundment depth ratios to examine the

impact of both subcritical and supercritical flows on the scouring processes. They observed that the deepest scour holes consistently formed at the corners of the structure, independent of the bed slope or flow regime. Additionally, it was noted that the scour depth at the sides of the structure exceeded that at the front face. A particularly intriguing aspect of the study was the use of cameras installed inside the structure to visually document the erosion process. The findings revealed that the erosion rate on the side faces was greater than that on the front face when the bed was horizontal. Conversely, on sloped beds, the erosion rates at the side and front faces were nearly identical. Furthermore, the maximum scour depth observed around the structure on a horizontal bed was found to be almost twice as large as that on a sloped bed, highlighting the significant influence of bed orientation on the dynamics of scouring.

Table 2.3 provides a comparative summary of various studies on the scour depth in tsunami simulations. Notably, the location of the maximum scour depth for sand in the studies by Kato et al. (2001) and Tonkin et al. (2003) diverges from that in other studies, highlighting the significant influence of tsunami generation methods on sediment transport results. The variation in the maximum scour depth locations in other studies can be attributed to the differences in impoundment depths. For instance, Lavictoire et al. (2014) noted the maximum scour depth at the sides of the column for larger impoundment depths while recording a more uniform scour depth across both the front and side faces at lower impoundment depths. In addition, the geometry of the structure plays a crucial role in determining the location of the maximum scour depth. Lavictoire et al. (2014) and Shafiei et al. (2015) observed the maximum scour depth at the side face of a circular column. In contrast, Shafiei et al. (2015) and Mehrzad et al. (2022) found the maximum scour depth at the corners of a square column, indicating how the structural shape influences scour patterns.

Scour around Multiple Structures

The existing body of research is primarily focused on scour phenomena induced by steady and unsteady flows around individual structures, with limited investigation of scour around a group of structures. This section critically evaluates the findings of the few studies that have been conducted in this area.

Elliott and Baker (1985) conducted research on the scour around multiple structures under steady-state flow conditions. Their experimental setup involved rectangular columns within a 2 m sediment section containing uniform sand (D_{50} = 0.5 mm). The columns were 150 mm long and 46 mm wide (Figure 2.8). The number of columns was varied from one to five. Their findings indicated an increase in scour depth with closer proximity to the structures, while also identifying a threshold ($S/b > 7$) beyond which the mutual influence of structures on scour depth becomes minimal.

In a later study, Beg (2010) explored the impact of lateral spacing on scour around groups of circular bridge piers under steady-flow conditions. The non-dimensional lateral spacing S/D (D representing the pier diameter) was varied from one to eight. The findings indicated that at a spacing-to-diameter ratio (S/D) of eight, the maximum scour depth resembled that of a single column, albeit with a longer scour hole downstream. This led to the recommendation that to mitigate more extensive and deeper scour holes, the non-dimensional lateral spacing should exceed eight. This research, similar to Elliott and Baker (1985), is limited in its application to tsunami-induced scour because of its focus on steady flows.

After the catastrophic 2011 Tohoku Tsunami in Japan, which had repercussions in certain US coastal areas, the California Geological Survey collaborated with various agencies and academic institutions to conduct an exhaustive field survey. Their research, particularly in Crescent City

Table 2.3: Summary of the findings of studies on scour around a single column

Reference	Tsunami generation technique	D_{50} [mm]	Shape	Location of maximum scour depth	Notes
Kato et al. (2001)	Solitary wave	0.35 (Sand)	Circular	Side and back faces	For the small wave height to still water depth ratio, the scour depth at all faces was the same
Tonkin et al. (2003)	Solitary wave	0.35 (Sand)	Circular	Back face	Pore water pressure effect on the scour mechanism discussed
		3.50 (Gravel)		Front face	
Lavictoire et al. (2014)	Dam-break	1.00 (Sand)	Circular	Side face	For lower impoundment depths, the scour depth was uniform at the front and side faces
		10.00 (Gravel)		Side face	
Shafiei et al. (2015)	Dam-break	0.85 (Sand)	Circular	Side face	The front and side faces had the same erosion, and it was less than the corners
			Square	Corner	
			Diamond	Side face	
Mehrzad et al. (2022)	Dam-break	1.00 (Sand)	Square	Corner	The scour depth at the side faces was much less than the front and corners
Rajaie et al. (2023b)	Dam-break	0.50 (Sand)	Sqaure	Corner	The scour depth at the side face was larger than the front face

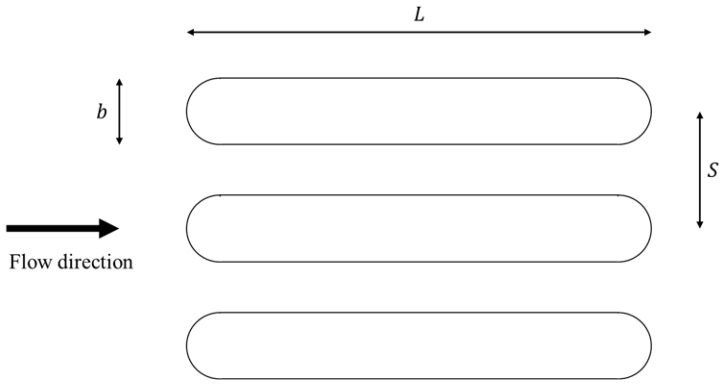

Figure 2.8: The structural arrangement used by Elliott and Baker (1985)

and Santa Cruz Harbors, identified that the constriction of the tsunami bore path between adjacent buildings intensified the scour depth (Wilson et al., 2012).

More recently, April-LeQuéré et al. (2021) employed Flow3D for the numerical analysis of tsunami-induced scour around a group of structures, considering lateral spacings (S/b) ranging from 0 to three. Their results indicated that for S/b ratios of two and three, the scour pattern closely mirrored that of a single column, with the exception of a longer downstream scour hole. Notably, the lateral spacing threshold impacting the scour pattern in this study was lower than the previously reported thresholds ($S/b = 7$ in Elliott and Baker (1985) and $S/D = 8$ in Beg (2010)).

In summary, the impacts of lateral spacing on scour depths caused by steady flows and tsunami bores differed significantly. The hydrodynamic characteristics of the flow are pivotal in determining the scour patterns around structures. Therefore, the existing design guidelines based on steady flows may not be adequate for tsunami-resistant structures. All studies have consistently shown that the presence of adjacent structures leads to longer scour holes, posing potential risks to the foundations of downstream structures. This necessitates the incorporation of adequate spacing in the design guidelines, particularly in tsunami-prone areas.

2.2.4 Numerical Modeling of Tsunami-Induced Scour

Experimental modeling offers important insights into the scouring process around structures during tsunami inundation. However, its practical applications have several limitations. First, the requisite facilities for such experimental modeling are not available in all laboratories. In addition, many existing flumes are not appropriate for experiments that require a large scaling factor. Second, experiments associated with scouring tend to be sometimes costly because of the high expense of recovering sediments carried away by the flow. Conversely, advancements in numerical schemes and computational technologies, combined with their greater accessibility and cost-effectiveness, position numerical models as a viable alternative to laboratory tests.

In the realm of numerical simulations for scour around structures, two predominant methodologies are commonly employed. The initial method involves solving a hydrodynamic model for the water phase and utilizing the Exner equation, employing shear stress estimates derived from flow velocities, to simulate bed-level evolution. Conversely, the second method considers the erodible section as a non-Newtonian fluid with high viscosity and solves Navier-Stokes equations for both phases concurrently as a multiphase flow. In this case, the interface of water and sediment phases represents the bed level at each time step. This section provides a review of the various studies that have implemented these methods.

Nakamura et al. (2008) initially resolved the Navier-Stokes equations using the Volume of

Fluid (VOF) method, incorporating Large Eddy Simulation (LES) and Dynamic Two-parameter Mixed (DTM) models for the representation of turbulent vortices at both grid and sub-grid scales. The implementation of the VOF method involved the use of the Simplified Marker and Cell (SMAC) scheme for addressing the pressure boundary conditions on the free surface, along with the employment of the Multi-interface Advection and Reconstruction Solver (MARS) to facilitate the formation of a continuous interface. For the sediment transport model, Nakamura et al. (2008) expanded the two-dimensional Finite Element Method (FEM), originally proposed by Hur et al. (2007), to model the wave-induced displacement of sand. This approach involves the computation of suspended sediment particles using a Lagrangian framework, a method noted for its computational intensity. Furthermore, the evolution of the sand bed in their model was simulated by considering the pore water pressure exerted on sediment particles. By comparing their numerical results with experimental data concerning scour around a square column, the authors identified certain limitations in their numerical method for simulating tsunami-induced scour. A key deficiency was the oversight of the impact of turbulent vortices and shear stress on erosion. Instead, small-scale strains were considered the primary cause of scouring, which is a significant drawback of their approach.

Stahlmann (2013) conducted both experimental and numerical studies on the scouring mechanism around tripod foundations of offshore wind turbines. The research employed the OpenFOAM source code as the hydrodynamic solver and incorporated a nonequilibrium sediment transport model that accounted for both the bedload and suspended load. The turbulence within the model was addressed using the k–ω Shear Stress Transport (SST) model. Additionally, the bed load discharge formula proposed by Engelund and Fredsøe (1976) was integrated into the Exner equation. The model also includes the solution of the advection-diffusion equation for the suspended load concentration. The experimental setup included a wavemaker at the upstream end of the flume, which generated a sequence of approximately 4000 short waves, emulating typical open ocean conditions. A comparison between the experimental and numerical results revealed that although the local scour pattern around the front leg of the tripod was similar, the numerical model underestimated the equilibrium scour depth. However, the model demonstrated that the scour depth reached an equilibrium state relatively early in the simulation process after approximately 250 out of the total 4000. This finding aligns with the results obtained using a physical model.

Larsen et al. (2017, 2018) conducted both numerical and experimental investigations to examine the scouring effects induced by tsunamis around monopile foundations. In these studies, an advanced computational model called sediMorph, originally developed by Jacobsen (2011) and implemented in the OpenFOAM framework, was utilized. This model addresses the three-dimensional Reynolds-Averaged Navier-Stokes (RANS) equations, integrating the k–ω turbulence model and encompassing both bedload and suspended-load sediment transport mechanisms. Although the model demonstrated a high degree of accuracy in simulating the evolution of scour depth, notable overestimations were observed during the initial stages. The model demonstrated a high degree of accuracy in simulating the temporal progression of scour depth. However, it was noted that there were instances of overestimation in the initial stages of the scour depth evolution. The researchers attributed this discrepancy to the potential non-ideal flattening of the bed post-experimentation, which might have led to inconsistencies between the initial conditions of the numerical simulations and the experimental setup.

April-LeQuéré et al. (2020) conducted a detailed study focusing on the numerical modeling of tsunami-induced scour around a square column. A comparative analysis was conducted between the open-source Delft3D model and the commercially available Flow-3D software in conjunction with an evaluation of the Van Rijn and Nielsen sediment discharge equations. Delft3D, which

solves shallow water equations and considers hydrostatic pressure for cases in conjunction with its morphodynamic module, was juxtaposed against Flow-3D. Flow-3D, which is used to solve fully 3D Navier-Stokes equations, incorporates hydrodynamic pressure and is more effective in capturing vortices around structures. The sediment transport models in both systems were calibrated using the maximum scour depth measurements from Mehrzad et al. (2016). April-LeQuéré et al. (2020) noted that while both numerical models successfully replicated the scour hole development downstream of the column, Flow-3D yielded superior results on the upstream face. The researchers observed that Delft3D's hydrostatic assumption led to a lack of detection of horseshoe vortices at the front face of the column, thereby impacting the accuracy of its scour predictions. Another significant limitation of Delft3D is its disregard for slope stability criteria in the sediment transport module. In Delft3D simulations, the maximum scour depth occurred at the upstream corners of the structure, whereas Flow-3D indicated the maximum scour depth at the centerline of the upstream face, aligning more closely with experimental observations. Furthermore, it was concluded that the Nielsen sediment discharge equation implemented in Flow-3D demonstrated superior performance in simulating tsunami-induced scour around structures.

To investigate scour phenomena around structures induced by unsteady flows, Nagel et al. (2020) employed the sedFoam solver, which was initially developed by Chauchat et al. (2017). This solver is an extension of the OpenFOAM framework and represents a 3D Eulerian-Eulerian model. Unlike conventional sediment transport models that employ the Exner equation to track bed evolution, this model considers the erodible phase as a non-Newtonian fluid. It modifies and solves the Navier-Stokes equations for both the fluid and sediment phases, incorporating specific terms in the momentum equation to account for phase interactions. The study juxtaposed the outcomes from the classical k–ε turbulence model with those from a reformulated k–ω equation tailored for multiphase challenges. It also incorporates bed slope stability considerations. Initially, the accuracy of the model was validated against a sediment transport scenario without obstruction. Subsequently, it was applied to a 3D simulation of the scour around a cylindrical column. While not specifically modeling tsunami conditions, these scenarios involved fully unsteady flows. A comparison of the maximum scour depths at the front face of the column revealed that for the initial 300 s of simulation, both the modified k–ω and k–ε methods were closely aligned with the empirical data from Roulund et al. (2005). However, as the simulation progressed, the modified k–ω method yielded underestimated results, whereas the k–ε method yielded overestimations. Both turbulence models consistently underestimated the scour depths at the back face of the column. Notably, the k–ε model failed to accurately simulate turbulent vortices at the backside of the column. Two principal conclusions emerged from this research: first, the necessity of incorporating slope stability in scour analysis around structures owing to its significant influence on sediment transport, and second, the imperative need for refined turbulence models within multiphase frameworks to effectively capture the complex dynamics of turbulent flows around structures.

Zhang et al. (2020) devised a second-order finite volume model by integrating a projection method on an unstructured mesh. This model incorporates a sigma-coordinate at the fluid-sediment interface, enabling it to track abrupt bed elevation changes. A critical component of their approach was the integration of the Large Eddy Simulation (LES) turbulence model, specifically tailored to capture the complex dynamics of horseshoe vortices occurring in front of cylindrical structures. The focus of this model is predominantly on bedload transport. To this end, the bedload transport equation formulated by Engelund and Fredsøe (1976) was incorporated in their study. In addition, the authors incorporated a sand slide model. This model ensures that the bed slope between the adjacent cells does not exceed the angle of repose of the bed material. The

model achieves this by adjusting the bed elevation in each cell after every time step, aligning it with the angle of repose, and adhering to mass conservation principles. The spatial discretization of the model is characterized by small prism control volumes with triangular cross sections in the horizontal plane and uniform depths in the vertical plane. By comparing their model outputs with experimental data from Roulund et al. (2005), the authors demonstrated the effectiveness of the model. Notably, it successfully captured both horseshoe vortices and dynamic bed evolution, which are crucial elements in understanding sediment transport and scour phenomena. While the test case in this study does not directly represent tsunami conditions, it involves critical elements such as unsteady flow and horseshoe vortices, which are pertinent to tsunami-induced scour around structures. This demonstrates the potential applicability and effectiveness of the model in simulating scour phenomena induced by tsunamis.

Song et al. (2022) developed a three-dimensional model employing the immersed boundary method to simulate scour phenomena caused by unsteady flows. This study utilized the pisoFOAM solver within the OpenFOAM framework for hydrodynamic modeling. The k–ω SST-SAS turbulence closure equation was employed to capture flow vortices. The model calculates the shear velocity using the law of the wall and incorporates specific treatments to mitigate oscillations in the shear stress. Sediment discharge was computed following Engelund and Fredsøe (1976), and bed level evolution was captured using the Exner equation. Notably, the suspended sediment load was not considered in this model. The authors validated their hydrodynamic and morphodynamic models using the experimental data from Roulund et al. (2005). Their numerical results indicated that the maximum scour depth typically occurred on either side of a circular column. Notably, they observed that the particle movement within the scour hole continued even after reaching an equilibrium stage at the bed level, constrained by slope stability considerations. However, the model underestimated the maximum scour depths at the upstream and downstream faces of the column. This discrepancy was attributed to two primary factors: the inability of the k–ω SST-SAS turbulence model to accurately capture horseshoe vortices in shallow bed layers and the omission of the suspended sediment load from the study. Despite achieving superior results compared with prior numerical models, the methodology presented by Song et al. (2022) requires significant computational resources.

Li et al. (2023) conducted an in-depth study using Flow-3D to analyze the effects of solitary waves on scour around structures. Their approach integrated the Van Rijn formula for bedload discharge and the k–ω model for turbulence closure in the RANS equations. Flow-3D accounts for both the bedload and suspended sediment loads. The temporal dynamics of the suspended load were modeled using an advection-diffusion equation for sediment concentration, whereas bed-level changes were governed by the Exner equation, as outlined by Flow Science (2019). The research team initially validated their hydrodynamic models, noting a minor discrepancy between the numerical results and the actual measurements of the velocity profiles and water levels. The authors speculated that the inaccuracies in the velocity profiles could be attributed to two primary factors. First, the complex nature of wave transformation, breaking, and shoaling presents significant challenges to the accuracy of numerical modeling. Second, the velocities recorded in the experiments were measured using a Nortek HR Aquadopp, which is subject to measurement error. Additionally, the observed discrepancies in the water level measurements were potentially caused by the generation of non-ideal solitary waves during the experimental procedures. Their findings revealed that the maximum scour depth typically occurs at the front corners of the structures. Furthermore, researchers simulated the same scenarios using a rigid bed. These simulations aimed to compare the wave forces exerted on the structures under different bed compositions. The results indicated that the wave forces in the scenarios with erodible beds were significantly higher than those in the rigid bed cases. These findings led to the conclusion

that wave forces in cases with erodible beds should be considered in structural design to mitigate the impacts of wave forces.

Table 2.4 provides a comparative analysis of various studies, highlighting the differences in the numerical models employed to simulate sediment transport. A critical limitation identified in traditional models based on the Exner equation is their reliance on empirically derived sediment-discharge equations. These equations are specifically tailored to certain sediment materials, specific sediment sizes, and a range of Reynolds numbers, and their applicability to scenarios beyond these parameters is limited. Furthermore, these equations are based on the assumption of steady flow, a condition that does not accurately reflect scenarios such as tsunami bores. Despite this limitation, traditional methods offer significant advantages in terms of their computational efficiency. This efficiency renders them particularly practical for addressing real-world, large-scale problems. In contrast, more recent approaches to sediment transport modeling, such as Lagrangian-Eulerian solvers, have been observed to provide greater accuracy compared to traditional methods. However, these advanced methods encounter several challenges. First, they are associated with higher computational costs due to increased model complexity. Second, there is a notable deficiency in the appropriate turbulence models tailored for these advanced methods. Figure 2.9 to Figure 2.11 provide detailed flowcharts for all the reviewed models, offering a visual representation of their methodologies.

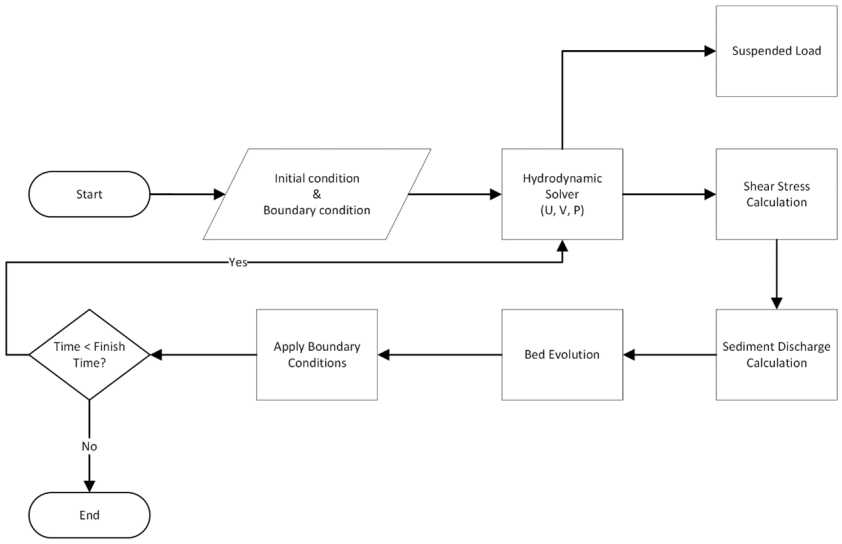

Figure 2.9: Flowchart of the traditional models based on the Exner equation

2.3 Research Needs and Future Possible Directions

This study aimed to perform an exhaustive review of the existing research on tsunami-induced scour around structures, identify gaps, and suggest areas for future investigation. This review encompasses both experimental and numerical methods to better understand this complex physical phenomenon.

Wave generation is a critical aspect of tsunami research. The traditional use of solitary waves as tsunami wave surrogates is questioned given their significantly smaller wave period and wavelength at model scale, when compared to real tsunamis, as highlighted by Madsen et al. (2008). Although dam-break methods, following Chanson (2006), have been used, their relatively high cost due to the need for fast gate opening mechanisms makes them prohibitive for many

Table 2.4: Summary of numerical models used for simulating scour around structures

Reference	Suspended load	Free surface	Hydrodynamic	Mesh type	Bed evolution	Equilibrium / Nonequlibrium	Turbulence	Bedload discharge equation	Sand slide
Nakamura et al. (2008)	Yes	VOF	3D Navier-Stokes	Structured	Lagrangian	Equilibrium	LES/DTM	NA	No
Stahlmann (2013)	Yes	VOF	3D Navier-Stokes	Structured	Exner	Nonequilibrium	k-ω SST	Engelund and Fredsøe	Yes
Larsen et al. (2017, 2018)	Yes	NA	3D Navier-Stokes	Structured	Exner	Nonequilibrium	k-ω	Engelund and Fredsøe	Yes
April-LeQuéré et al. (2020)	Yes	VOF	3D Navier-Stokes	Structured	Exner	Nonequilibrium	LES	Nielsen / VanRijn	Yes
	Yes	NA	Shallow water equations	Structured	Exner	Equilibrium	k-ε	VanRijn	No
Nagel et al. (2020)	Yes	NA	3D Navier-Stokes	Structured	Multiphase (Eulerian)	Equilibrium	Reformulated k-ω	NA	Yes
Zhang et al. (2020)	No	σ-coordinate	3D Navier-Stokes	Unstructured	Exner	Equilibrium	LES	Engelund and Fredsøe	Yes
Song et al. (2022)	No	VOF	3D Navier-Stokes	Unstructured	Exner	Equilibrium	k-ω SST-SAS	Engelund and Fredsøe	No
Li et al. (2023)	Yes	VOF	3D Navier-Stokes	Structured	Exner	Nonequlibrium	k-ω	VanRijn	Yes

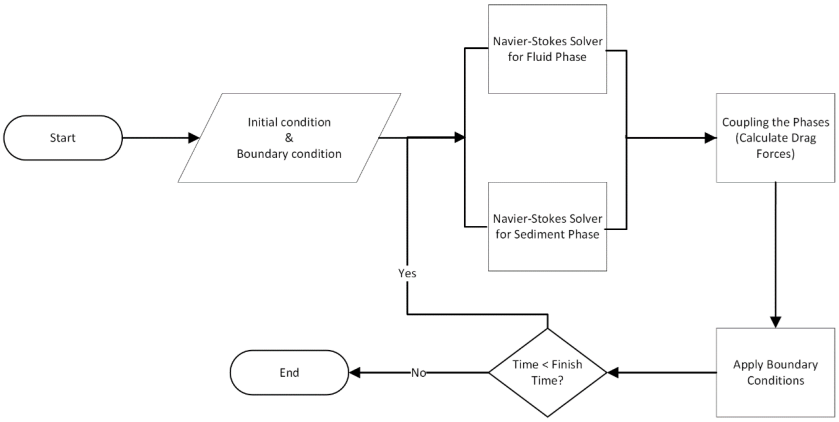

Figure 2.10: Flowchart of the multiphase models (Eulerian)

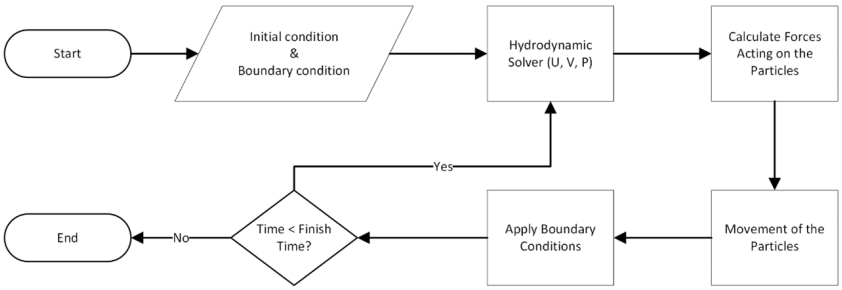

Figure 2.11: Flowchart of the Lagrangian models

laboratories. The study also noted a lack of detailed descriptions of alternative methods used for generating tsunami waves, suggesting that future research should delve into the specifics of these methods and propose new techniques for simulating tsunami inundation in labs.

Scaling effects pose a major challenge in laboratory tests, particularly tsunami-related experiments employing sediments. To accurately replicate turbulent flows and the effects on scouring around structures, scaling based on the Reynolds number is necessary, as opposed to the commonly used Froude number. In addition, due to the differing behaviors of cohesive and non-cohesive soils, sediment particle size scaling becomes problematic. Therefore, conducting tests with larger length scales is recommended to minimize scaling issues.

This study identifies a gap in the understanding of the impact of the angle between the flow direction and structure on scouring mechanisms. Only Shafiei et al. (2015) explored the effect of a 45° angle between the flow and the structure, indicating that this angle influences the maximum scour depth. Further research in this area could enhance the design guidelines for structures in tsunami-prone areas.

The concept of sheltering and arrangement of structures, as examined by April-LeQuéré et al. (2021), is another area that requires further investigation. While some studies have examined scour around groups of structures or bridge piers, scour around individual elements within these groups under unsteady, highly turbulent flow conditions has been largely overlooked. Although challenging owing to the size of the required facilities, this topic is more relevant for real-world scenarios and warrants further investigation.

This study points out discrepancies in the literature regarding how a structure's size affects local scour patterns. In addition to the fact that most of the current findings are based on steady flow assumptions, which do not accurately represent tsunami inundation, more detailed studies are required to understand the influence of the structural dimensions on tsunami-induced scour

mechanisms.

In the realm of numerical modeling, there are several avenues for improvement. Current methods often solve hydrodynamic and sediment transport models separately. Two-way coupled models that consider the interaction between fluid and sediment dynamically should be able to provide more accurate results. Despite the high computational cost of advanced models, advancements in computer technology are making these methods more feasible for simulating real-world phenomena such as scour induced by tsunami inundation. Finally, this study emphasizes the need to incorporate more efficient and accurate turbulence models, as vortices play a crucial role in scouring around structures. The current models may not effectively capture small-scale vortices. As suggested by Nagel et al. (2020), although multiphase approaches are promising and computationally efficient, they require the development of new turbulence models to improve their accuracy and reliability.

2.4 Conclusion

In the aftermath of the 2004 Indian Ocean and 2011 Tohoku tsunamis, post-tsunami forensic engineering field surveys have highlighted local scour around structures as the predominant cause of building failures. Despite the inclusion of this phenomenon in design codes for shoreline construction, its various aspects warrant further investigation. Some of the key aspects which the authors deem as requiring investigation are as follows.

1. In the context of tsunami-induced scour around structures, sediment particle size and the vortices are critical elements. These cannot be effectively scaled using Froude scaling principles, underscoring the importance of large-scale laboratory experiments to minimize scaling discrepancies.

2. The influence of individual structures on scour patterns around adjacent structures is substantial; however, this factor has been overlooked in existing studies. Future research should prioritize this area to enhance understanding and inform construction practices.

3. The orientation of a structure relative to the flow direction and its geometry has a substantial impact on the scour hole patterns and maximum scour depth. Research in this domain, which more accurately reflects real-world conditions, is essential for developing comprehensive design guidelines and standards.

4. High-resolution meshing is essential, particularly in the vicinity of structures, to accurately capture the intricacies of vortices in numerical models. This approach is vital for a more realistic representation of tsunami-induced local scours near buildings. There is also a need for more representative, physically-based turbulence models which should lead to an improve in the numerical model results.

Chapter 3. Experimental Investigation of Structural Width Effects on Bore-Induced Scour Depth Around Walls*

3.1 Introduction

Tsunamis are extreme waves that impact shorelines. Most often the large ones are triggered by relatively rare events such as submarine earthquakes, landslides, or volcanic eruptions. These massive waves can cause catastrophic damage to coastal communities and nearshore infrastructure.

Post-tsunami field surveys play a crucial role in evaluating the extent of damage caused by tsunami inundation. Comprehensive analyses of these surveys, as discussed in studies by Ghobarah et al. (2006), Fritz et al. (2006), Mikami et al. (2012), Olsen et al. (2012), and Stolle et al. (2020), have consistently identified local scour around infrastructure foundations as a main cause of failure for coastal structures. In particular, field investigations following the 2004 Indian Ocean and the 2011 Tohoku tsunamis provided valuable insights into the dynamics of tsunami-induced scour around these structures (Ghobarah et al., 2006; Jaffe et al., 2006; Palermo et al., 2013; Sato and Okuma, 2014). These studies emphasized the importance of incorporating local scour considerations into design codes for shoreline buildings, recognizing it as a critical factor influencing the vulnerability of these structures to severe damage or collapse.

Current design guidelines often overlook or improperly estimate the impact of tsunami waves and associated coastal inundation on infrastructure. The Structural Design Method of Buildings for Tsunami Resistance (SMBTR) by Okada et al. (2005) is one of the earliest guidelines to address forces exerted by tsunamis on buildings, proposing various load combinations specifically for the design of evacuation structures. However, it lacks provisions for tsunami-induced local scour. The City and County of Honolulu Building Code (CCH, 2013), in Chapter 16, accounts for limited factors such as sediment type, proximity to the shoreline, and inundation depth when determining local scour depth, providing basic design restrictions.

The Federal Emergency Management Agency (FEMA) has issued FEMA-P-55 (2011) and FEMA-P-646 (2019), which provide guidelines relevant to coastal structures and the assessment of wave impacts on them. FEMA-P-55 (2011) suggests that although tsunami inundation characteristics differ from those of typical tropical storm surges, similar principles might be applied to estimate local scour depth, recommending that the maximum scour depth around a circular column be considered as twice its diameter. In contrast, FEMA-P-646 (2019) addresses the design of tsunami evacuation buildings but lacks detailed structural design guidelines for local scour depth. ASCE-7-22 (2022), in Chapter 6, offers the most comprehensive provisions on tsunami-induced local scour, accounting for parameters such as flow Froude number, sediment characteristics (sand and gravel), and structural shape (square and circular) and its dimensions. However, it does not cover additional potential factors that could affect maximum scour depth such as the width of structure as well as its orientation with respect to the flow direction.

Several experimental tests have been conducted in laboratory settings to investigate the effects of those overlooked parameters. A critical initial step in these studies is the selection of an

*Jazaeri, Seyed Abbas, Nistor, Ioan, Mohammadian, Abdolmajid, and Liu, Xin (2025). *Experimental Investigation of Structural Width Effects on Bore-Induced Scour Depth Around Walls.* Journal of Waterways, Ports, Ocean, and Coastal Engineering, ASCE, https://doi.org/10.1061/JWPED5/WWENG-2364, Accepted, in press.

appropriate method to simulate real-world tsunami inundations. Researchers have used various methods such as solitary waves (Kato et al., 2001; Tonkin et al., 2003; Nakamura et al., 2008; Chen et al., 2013; Larsen et al., 2018; Xu and Huang, 2022) and dam-break bores (Imamura et al., 2008; Arnason et al., 2009; Leal et al., 2009; Nouri et al., 2010; Al-Faesly et al., 2012; April-LeQuéré et al., 2021) for this purpose. While solitary waves are widely used, their shorter wave periods and wavelengths compared to real tsunami waves raise concerns regarding their applicability to real-world scenarios (Madsen et al., 2008). In contrast, Chanson (2006) compared the hydrodynamics of dam-break bores with video footage from the 2004 Indian Ocean Tsunami, and concluded that dam-break bores provide an accurate representation of tsunami inundation. Jazaeri et al. (2024) conducted a comprehensive comparison of studies employing either solitary waves or dam-break bores as proxies for tsunami inundation.

The literature on tsunami-induced scour around structures is extensive. Kato et al. (2001) and Tonkin et al. (2003) examined the impact of sediment grain size on scour around circular columns using solitary waves in a laboratory setting, highlighting the significant role of the pore water pressure in the scouring process. While previous studies, such as Rajaie et al. (2023a), Hu et al. (2025) and Hu and Li (2025), have identified pore water pressure as a key parameter influencing local scour around structures, this parameter was not examined in the present study. Lavictoire et al. (2014) explored the effect of scour due to tsunami bores around structures for a wider range of sediment (sand and gravel) using dam-break waves. Shafiei et al. (2015) investigated the influence of the structural shape (circular, square, and diamond) on scour depth, while Mehrzad et al. (2022) employed dam-break generation techniques to study the scour depth and pore water pressure variation around square columns of different size under both dry- and wet-bed conditions.

The flow field around walls differs significantly from that around a square column, particularly in the development and interaction of horseshoe and lateral vortices. In the case of a square column, flow separation at the upstream face leads to the formation of a horseshoe vortex system and lateral vortices, which are the primary drivers of local scour at the base (Islam et al., 2012). In contrast, walls exhibit more complex vortex dynamics. The elongated face increases the surface area for boundary layer development, enhancing the strength and persistence of lateral vortices, while often weakening or distorting the horseshoe vortex due to delayed separation and altered stagnation zones (Liu et al., 2025). This weakening process can result in shallower scour depths at the corners of the walls.

To the best of the authors' knowledge, no research to date has investigated local scour depth around rectangular walls as existing studies have focused exclusively on columns. Therefore, this study aims to advance understanding of the effect of wall width on tsunami-induced local scour depth by conducting experimental tests in the Large Dam-Break Flume at the Water Resources Laboratory of the University of Ottawa, Canada.

The remainder of this paper is organized as follows. Section 3.2 outlines the methodology used in this study, detailing the flume setup, instrumentation for data collection, test procedure, and scaling effects. Section 3.3 presents observations from the tests, examining the hydrodynamic characteristics of the dam-break bores and comparing them with available analytical solutions. Additionally, this section discusses the influence of both the inundation depth and the wall width on the local scour depth. Section 3.4 discusses the limitations of this study and finally, Section 3.5 provides a conclusion of the results, highlighting findings relevant to improving current tsunami design guidelines.

3.2 Methodology

This section outlines the methodology employed in this study. It begins with an explanation of the flume setup and details of the test matrix employed. Subsequently, the instruments used to capture various flow and scour parameters at different locations along the flume are described. The procedure followed to conduct the tests is then presented, and, finally, considerations related to the scaling of the tests are discussed.

3.2.1 Experimental Setup and Test Matrix

All experimental tests presented in this study were conducted in the Large Dam-Break Flume at the Water Resources Laboratory, University of Ottawa, Canada. The flume measures 30.3 m in length, 1.5 m in width, and 1.5 m in depth. It includes a 16 m reservoir located at its upstream end equipped with a rapidly opening swing gate. Downstream of the gate, a 3.3 m approach slope with a 1:11 gradient elevates the flume bed by 0.3 m to accommodate the sediment bed section. Following the slope, there is the 4.2 m long false floor (False Floor 1) leading into the sediment section. Schematic of the flume is shown in Figures 3.1.

The sediment bed section itself spans 4.1 m and includes two parts: a 0.2 m gabion filled with fine gravel (median grain size of 30 mm), followed by a 3.9 m section of sand with a median grain size (D_{50}) of 0.11 mm. The gabion section ensures a smooth transition between the fixed and erodible beds to prevent excessive erosion at the start of the sand bed section. Finally, the 2.2 m false floor (False Floor 2) follows the sediment section, ending in a drain, designed to prevent backflow.

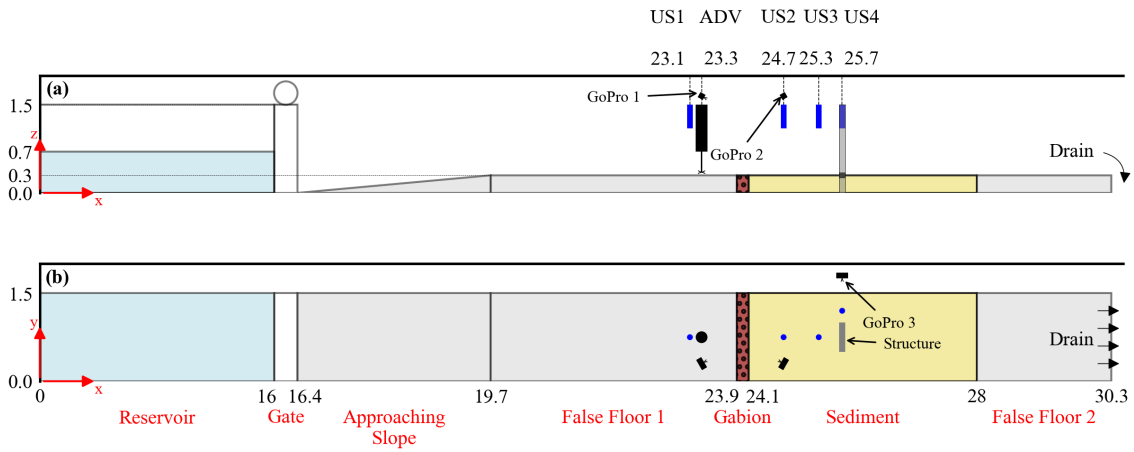

Figure 3.1: (a) Side view and (b) top view of the experimental setup (units in meters, not at scale)

To investigate the effects of structure width on tsunami-induced local scour depth over a dry-bed condition downstream of the gate, nine tests were conducted with varying structure widths and impoundment depths. The model structures employed in these tests included a square column (0.1×0.1 m), a short wall (0.3×0.1 m), and a long wall (0.5×0.1 m). The width of the long wall was set to 0.5 m to comply with criterion established by Melville and Chiew (1999), which recommends a blockage ratio of the flume (ratio of structure width, w, to flume width, B) of less than 33% to avoid the influence of the flume walls on the scour depth. The impoundment depths used in this study were 0.7 m, 0.6 m, and 0.5 m, denoted respectively as H1, H2, and H3. A summary of the conducted tests is presented in the test matrix in Table 3.1. The test nomenclature consists of two components. The first specifies the structure type, with SC representing sqaure

column, SW representing short wall, and LW representing long wall. The second component indicates the impoundment depth, with H1, H2, and H3 corresponding to 0.7 m, 0.6 m, and 0.5 m, respectively.

Table 3.1: Configurations of tests conducted in the current study

Test name	Structure width (m)	Impoundment depth (m)	Mean Froude Number
SC-H1	0.1	0.7	0.96
SC-H2	0.1	0.6	0.90
SC-H3	0.1	0.5	0.29
SW-H1	0.3	0.7	0.70
SW-H2	0.3	0.6	0.65
SW-H3	0.3	0.5	0.18
LW-H1	0.5	0.7	0.62
LW-H2	0.5	0.6	0.59
LW-H3	0.5	0.5	0.43

3.2.2 Instrumentation

This experimental test program utilized a set of instruments to capture key flow and sediment transport characteristics along the flume, which are essential for analyzing the scouring mechanism and its spatio-temporal development. The instrumental setup included the following items:

Four ultrasonic sensors (Massa Products Corporation, 2023), named as US1 to US4, with a measuring spatial accuracy of 1 mm and a measuring range from 0.1 m to 1.0 m, were installed along the flume to record the time-history of water surface elevation. These sensors serve multiple purposes as follows. First, the collected data were used to validate the generation of an ideal dam-break bore by comparing the recorded data with the analytical solution proposed by Chanson (2006) for the dam-break problem. Secondly, they were used to calculate the flow Froude number, in conjunction with data from the Acoustic Doppler Velocimeter (ADV). Three of these sensors were also positioned around the structure on the sediment bed section to measure the time-history of the water surface elevation in the vicinity of the scour hole.

A Nortek Vectrino ADV (Nortek AS, 2018) with a measuring accuracy of 1 mm/s, was positioned upstream of the gabion section to measure flow velocity at 2 mm above the flume bed before the water reaches the erodible section. Due to the unreliability of ADV data in highly turbulent flows, the ADV was not placed in the close vicinity of the structure, where vortices and turbulence persisted for most of the test duration.

The USs and the ADV were connected to an HBK MX1601B data acquisition system (Hottinger Brüel & Kjær GmbH, 2025), which ensures precise and synchronized data collection. This system operated at a sampling rate of 300 Hz and converted analog signals from all instruments into digital format. It offers 16 individually configurable channels for versatile data acquisition.

Three GoPro HERO 7 cameras (GoPro, Inc., 2018) were purposefully positioned along the flume. The first camera, located in the vicinity of the structure, was looking downstream, and was used to visually observe the formation of horseshoe and lateral vortices in front of the structure. The second camera aimed to capture images of the upstream side of the flume and, in combination with the bed grid drawn on the first section of the false floor, its recordings were

used to measure the velocity of the advancing bore front. The third GoPro camera was placed immediately outside the flume, looking through the side glass wall, and was used to monitor and measure the amount of general surface scour occurring farther away from the structure. In addition, two Depstech DS300 wire video-cameras (Depstech, 2021), were installed inside the structure to observe the time-history of the scour of the sediment bed, enabling video observation of its development along all its interior side.

A Leica ScanStation P50 (Leica Geosystems AG, 2019) Terrestrial Laser Scanning (TLS) system with ±1.2 mm measuring accuracy was employed at the end of each experimental test to scan in detail the bathymetry of the sediment section, providing in-depth topographical data of the final scoured areas.

3.2.3 Test Procedure

In all tests conducted in this study, the gate remained closed while the reservoir was filled with water to the specified depth corresponding to each test. Prior to starting each test, the sediment bed was filled and leveled using dry sediment, sand with D_{50} = 0.11 mm. Subsequently, all instruments were connected to the data acquisition system, and the GoPro and wire cameras were positioned in their designated locations.

The gate was operated via an automatic control panel equipped with a switch and was then rapidly opened. To ensure proper synchronization of the data acquisition, both data and video recordings commenced precisely when the gate-opening switch was engaged. Upon the rapid gate opening, the impounded water was released, generating the dam-break bore. When the flow reached the structure, horseshoe vortices and associated turbulence formed, initiating the local scouring process.

To quantify the scour depth evolution over time, all frames from the wire camera recordings (captured at 20 frames per second) were sequentially examined and undisturbed bed elevation was precisely localized. Scour depths at target locations were manually logged using the reference grid lines drawn on the structure, which had a resolution of 0.25 cm.

The data were recorded for a duration of 60 seconds, beyond which no further significant scouring was observed. Five hours after each test, once the flume had been completely drained, the TLS system was employed to capture the final scour geometry around the structure installed in the sediment section.

3.2.4 Scaling Considerations

In hydraulic engineering, scaling is a fundamental concept, particularly when investigating complex phenomena such as induced scour around structures. Two primary scaling approaches are commonly employed: Reynolds scaling and Froude scaling. Reynolds scaling is based on the Reynolds number, which is a dimensionless parameter that expresses the ratio of inertial forces to viscous forces. However, in the context of tsunami-induced scour and sediment transport, Reynolds scaling presents certain limitations, as it often requires models of impractically large sizes or the use of fluids with high viscosities to achieve similarity, making it less practical to simulate large-scale phenomena such as tsunamis. As a result, the authors acknowledge that scaled laboratory models typically operate at lower Reynolds numbers than their full-scale counterparts (Lozano-Durán et al., 2020), leading to a Reynolds inconsistency that can suppress turbulence intensity and potentially underpredict the effects of turbulence-driven sediment transport.

In experimental studies investigating tsunami-induced local scour around structures, Froude scaling has been commonly used due to its relevance in modeling fluid flow dynamics (Qi et al.,

2012; Robertson et al., 2013; Larsen et al., 2017; Wüthrich et al., 2018; Mehrzad et al., 2022; April-LeQuéré et al., 2021; Rajaie et al., 2023b). The Froude number represents the ratio of inertial forces to gravitational forces and is particularly effective in replicating wave motion and fluid behavior governed by gravity, both of which are critical to understanding scour mechanisms. Based on observations from the 2004 Indian Ocean and 2011 Tohoku tsunamis, the Froude number during real tsunami inundation was shown to typically range between 0.7 and 2.0 (Fritz et al., 2006; Iwai and Goto, 2021). Consequently, it is essential to maintain the average Froude number within this range during the tests in order to ensure similarity with real-world tsunami inundation conditions.

In addition, in experimental studies of tsunami-induced local scour around structures, three primary length characteristics are considered critical: the flow depth, the structure size, and the sediment D_{50}. Froude scaling can be applied effectively to the flow depth and the structure size. However, when considering sediment transport, directly applying Froude scaling to sediment size becomes problematic. This issue arises because of very fine sediments, those smaller than 0.1 mm, which may exhibit cohesive behavior, something which is significantly different from the non-cohesive properties of sand and gravel (Ettema et al., 1998).

To address the challenge of scaling sediment size, researchers often use the non-dimensional shear stress, or the Shields parameter, as a scaling criterion. This approach ensures that both the model and the prototype exhibit comparable behaviors under similar flow conditions. However, the use of this distorted scaling can lead to inaccuracies in the modeled scour depth, as highlighted by Lee and Sturm (2009). This distortion alters the near-bed turbulence structure and the interaction between coherent flow structures and sediment particles, often enhancing local entrainment processes. As a result, equilibrium scour depths measured in laboratory models and subsequently upscaled to prototype dimensions using Froude scaling tend to represent conservative estimates. While the Shields parameter is a useful criterion for assessing the threshold of sediment motion in small-scale experiments, it does not fully capture the dynamics of suspended load transport, especially under distorted scaling. In tsunami-induced scour, particularly at prototype scales, suspended sediment transport has been shown to dominate due to high shear velocities, unsteady bores, and transient seepage effects (Hu et al., 2025; Hu and Li, 2025). In contrast, small-scale Froude-based models often operate at lower Reynolds numbers and with coarser relative sediment size, leading to Rouse numbers significantly greater than unity. This implies that sediment transport in such experiments is predominantly bedload-driven, underrepresenting the contribution of suspension seen in full-scale events. Consequently, the present model may overestimate the importance of bed-scour processes while underpredicting the full extent of scour driven by turbulence and dynamic seepage effects. On the other hand, according to Melville and Chiew (1999), if the ratio between the characteristic length of the structure and the median sediment grain size exceeds 50, the influence of sediment grain size on local scour around the structure becomes negligible. In this study, the lowest ratio between the structure's width, for tests with the square column (w = 0.1 m), and the median sediment grain size (D_{50} = 0.11 mm) was 909 which met the criterion proposed by Melville and Chiew (1999). Therefore, these limitations should be carefully considered when generalizing the current findings to field-scale tsunami events.

The scour depth d_s produced by a dam-break bore around a fixed structure of width w in flow of the depth h, characteristic velocity of U, and gravity g may be written as $d_s = f(w, h, U, g)$ when fluid properties and sediment characteristics are fixed (constant D_{50} of 0.11 mm). Application of the Buckingham-PI theorem then yields the reduced dependence as follows:

$$\frac{d_s}{w} = C \times Fr^a \left(\frac{h}{w}\right)^b, Fr = \frac{U}{\sqrt{gh}} \tag{3.1}$$

The independence of the non-dimensional parameters was examined by calculating the correlation between the Froude number and the impoundment depth, normalized by the width of the structure. Figure 3.2 presents the results for all tests. As depicted in the figure, the correlation is 0.1874, indicating a weak relationship between these two parameters.

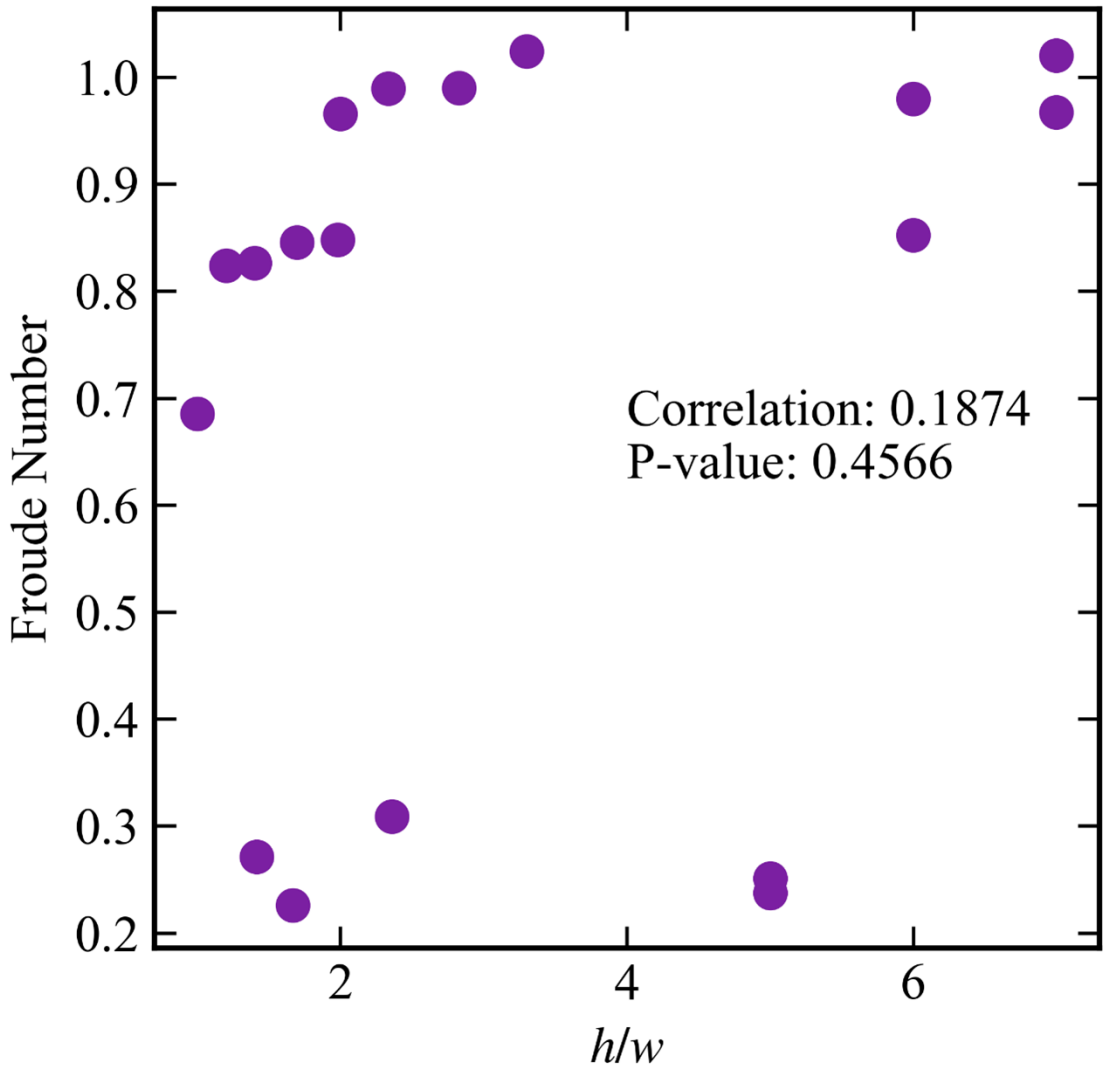

Figure 3.2: Relationship between the Froude number and the impoundment depth normalized by the width of the structure for all tests

Equivalently, for the alternative normalization used herein,

$$\frac{d_s}{h} = \tilde{C} \times Fr^a \left(\frac{w}{h}\right)^{b-1} \tag{3.2}$$

These relations are mathematically equivalent representations of the same Π-space model. Because viscosity and sediment properties are constant across tests and the flow is fully turbulent, Reynolds number and sediment dependent effects are absorbed into the factors C and $\tilde{C}$. Exposure

duration was also held approximately constant and was therefore not retained. It should be noted that over the tested parameter ranges, both Equations 3.1 and 3.2 are well represented by linear fits.

In this study, a 1:25 scale model was thus employed, utilizing Froude scaling. Given this length scale, the time scale, calculated as the square root of the length scale, was 1:5. Based on the conducted tests, the inundation time varies from approximately 2 minutes for an impoundment depth of 0.5 m to about 3.5 minutes for an impoundment depth of 0.7 m. Accordingly, the corresponding prototype impoundment depths range from 12.5 m to 17.5 m. Applying the time scale factor, the corresponding prototype-scale tsunami inundation time would range from 10 to 17.5 minutes, aligning with typical inundation durations observed in real case tsunamis (Mikami et al., 2012). This scale is selected to balance the need for detailed observation of sediment transport mechanisms with the practical constraints of laboratory testing.

3.3 Results

The first step, before conducting any detailed analysis, is to verify the validity of the measured data. To achieve this, the hydrodynamics of the dam-break problem are validated against analytical solutions available in the literature, as described below in Section 3.3.1.1. Once the data validity is confirmed, further analysis is pursued. Sections 3.3.2.2 and 3.3.3.3 examine the effects of impoundment depth and structure width on local scour depth around the structure, respectively.

3.3.1 Hydrodynamics

To validate the hydrodynamics of the dam-break bores generated in this study, several flow characteristics are compared against analytical solutions available in the literature.

Gate Opening Time

One of the initial tests to confirm the validity of the hydrodynamic conditions involves checking the gate opening time. According to Lauber and Hager (1998), to achieve ideal dam-break bores, the non-dimensional gate opening time must satisfy the following criterion:

$$t_0 \sqrt{\frac{g}{h_0}} < \sqrt{2} \tag{3.3}$$

In this equation, t_0 represents the actual gate opening time, h_0 is the impoundment depth, and g is the gravitational acceleration. To ensure that this criterion is respected, the gate opening time was calculated using snapshots taken with the GoPro2 camera, which was positioned to capture the field of view of the upstream end of the flume. Fig. 3.4 presents an example of these snapshots for the test SC-H1. It is important to note that the gate opening time refers to the moment when the gate was no longer in contact with the water in the reservoir, rather than the moment when the gate was fully open.

The average gate opening times for tests with similar impoundment depths are calculated using the snapshots and compared against the criteria established by Lauber and Hager (1998). As shown in Fig. 3.4, the non-dimensional gate opening times for all impoundment depths fall within the acceptable range for the formation of ideal dam-break bores.

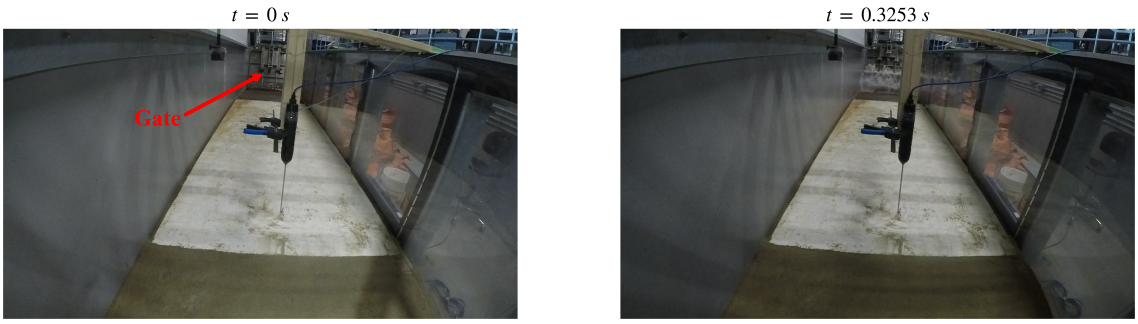

Figure 3.3: Snapshots of gate opening at t=0 s (left) and t=0.3253 s (right) for the test SC-H1

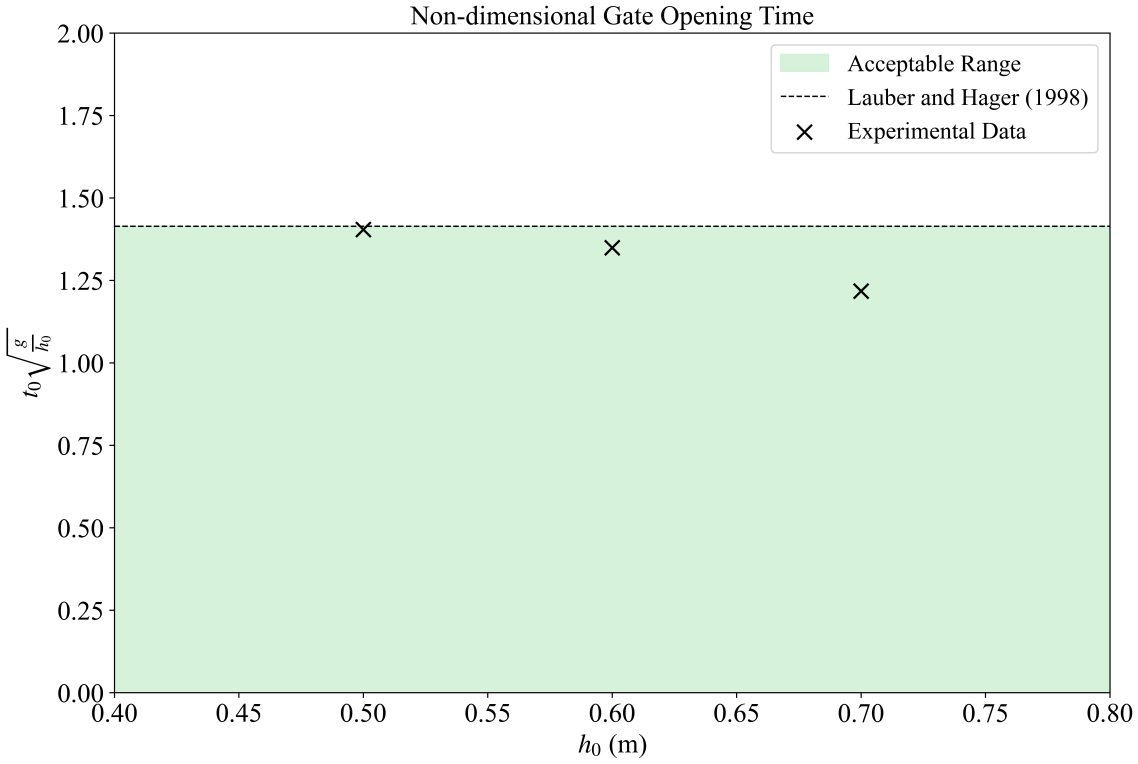

Figure 3.4: Non-dimensional gate opening time against impoundment depths

Bore Depth

The analysis of the governing equation for the dam-break problem dates back to Ritter (1892), who proposed a parabolic profile for dam-break bores over an idealized, frictionless, horizontal, and dry bed. This equation provides a relationship for the bore depth, h, as a function of time, t, at a given position downstream of the gate, x, and is expressed as follows:

$$\frac{h}{h_0} = \frac{1}{9}\left(2 - \frac{x}{t\sqrt{gh_0}}\right)^2 \tag{3.4}$$

This equation is used as a reference to validate the experimental bore depth measurements. Fig. 3.5 compares the measured non-dimensional longitudinal water surface profile against the theoretical solution by Ritter (1892). The result indicates good agreement between the experimental data and the theoretical solution at US1 and US2. The small discrepancy in Fig. 3.5 may be attributed to the presence of the erodible bed, which affects the hydrodynamics of the bores.

Fig. 3.6 illustrates the time series of the non-dimensional bore height at different ultrasonic sensors for the test SC-H1. It is important to note that the maximum depth recorded at the location of US3 (in front of the structure) is attributed to the turbulent flow generated when the bore impacts the structure. However, the decrease in bore height, which is attributed to the viscous and diffusive behavior of the flow over a rough bed, is clearly visible with the arrival of the secondary bores which are less energetic. This pattern can be seen after a non-dimensional time of approximately 200 in Fig. 3.6.

Bore Front Velocity

Chanson (2006) employed the method of characteristics and proposed two equations for calculating the dam-break bore front velocity, applicable to both ideal (frictionless) and non-ideal (rough) beds. He compared the rough bed equation with video footage from the 2004 Indian Ocean Tsunami and found that the results aligned well with the hydrodynamics of the tsunami-induced overland bores. According to his analysis, the bore front velocity, U, over a frictionless bed can be calculated as follows:

$$U = 2\sqrt{gh_0} \tag{3.5}$$

For a rough bed with a Darcy friction factor f, the bore front velocity is given by:

$$\frac{8}{3}\frac{1}{f}\frac{\left(1 - \frac{1}{2}\frac{U}{\sqrt{gh_0}}\right)^3}{\frac{U^2}{gh_0}} = t\sqrt{\frac{g}{h_0}} \tag{3.6}$$

The value of the Darcy friction factor can be estimated based on the equation proposed by Blasius (1913) for turbulent flows as follows:

$$f = 0.3164Re^{-0.25} \tag{3.7}$$

where Re is the Reynolds number. The Darcy friction factor for each individual test was calculated based on the data collected at the locations of US1 and the ADV. Using this approach, good agreement for bore front velocity is shown between the analytical solution proposed by Chanson (2006) and the experimental measurements, as illustrated in Fig. 3.7.

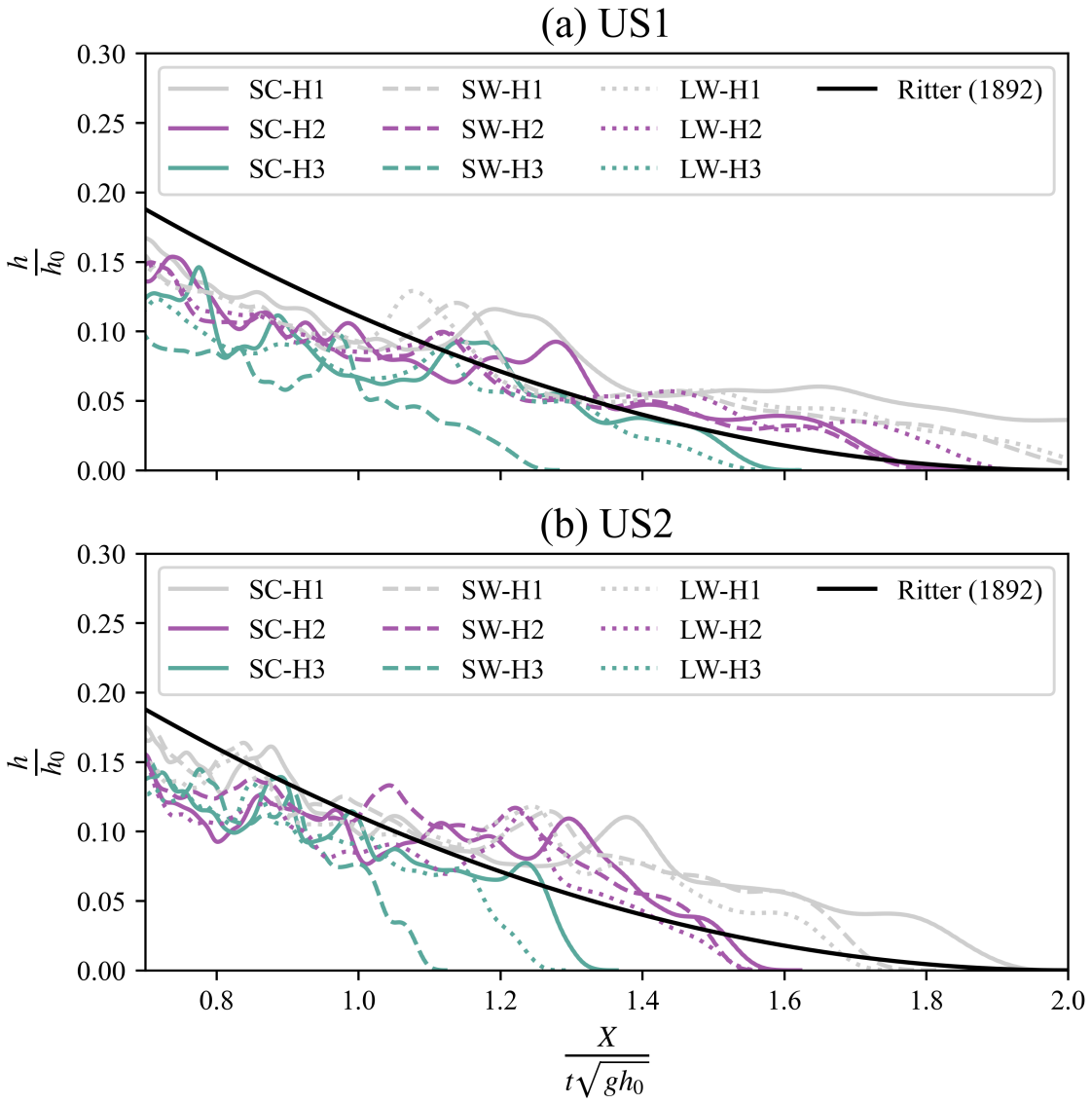

Figure 3.5: Comparison of the longitudinal non-dimensional water surface profile with analytical solution proposed by Ritter (1892) at (a) US1 and (b) US2

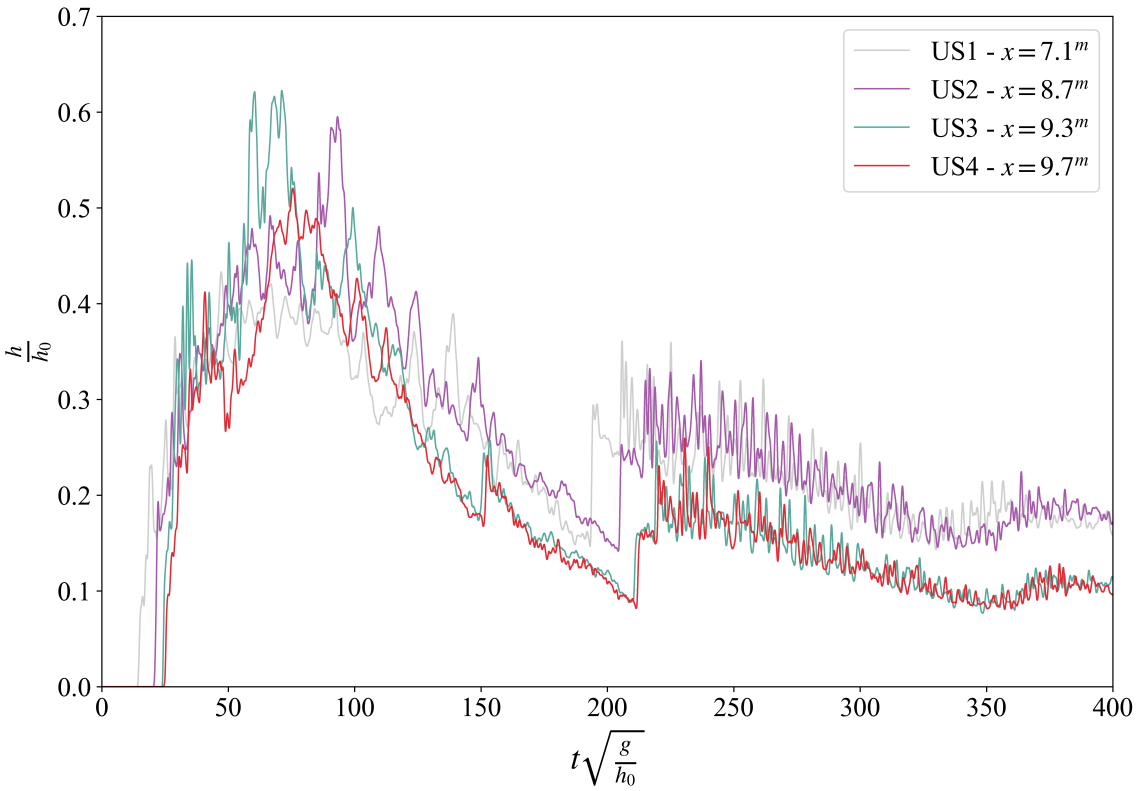

Figure 3.6: Temporal evolution of the non-dimensional bore height at the location of different ultrasonic sensors for the test SC-H1

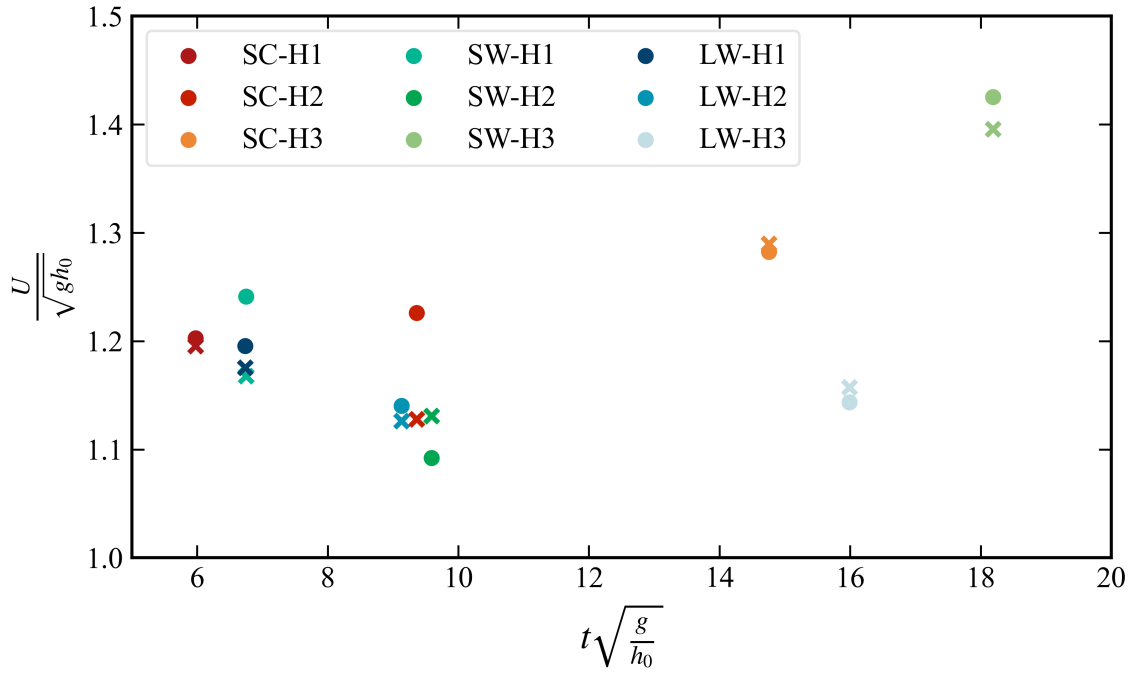

Figure 3.7: Comparison of the bore front velocity against the equation proposed by Chanson (2006) for the rough bed condition. The circles are the points associated with the experimental results and crosses are the calculated nondimensional bore velocity based on Equation 3.6 for each individual test

There are various formulations in the literature for calculating the bore front velocity of tsunamis (Bryant, 2001; Iizuka and Matsutomi, 2000; Kirkoz, 1983; Matsutomi and Okamoto, 2010; Murty, 1977). All these equations have a general form as follows:

$$U = \alpha\sqrt{g h_0} \tag{3.8}$$

The difference among these various formulae lies in the value of the coefficient α. Moreover, FEMA-P-55 (2011) and CCH (2013) design standards proposed two different equations for calculating tsunami inundation bore front velocity. FEMA-P-55 (2011) suggests that α should be equal to 2, while CCH (2013) recommends that the magnitude of the bore front velocity should match the magnitude of impoundment depth. Fig. 3.8 compares the available formulae from the literature with the experimental data obtained in this study. A curve, based on Equation 3.8, has been fitted to the measured bore front velocities, resulting in $\alpha = 0.85$, which falls between the provisions by CCH (2013) and FEMA-P-55 (2011).

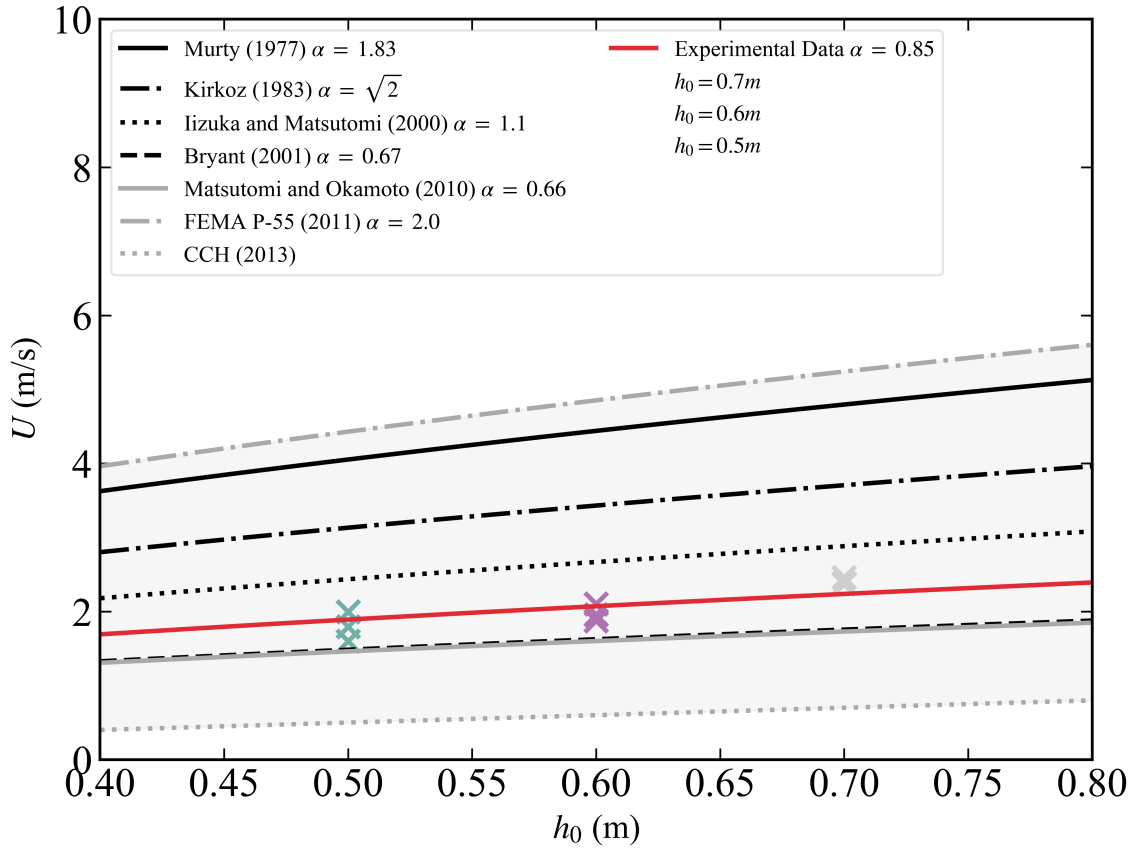

Figure 3.8: Comparison of the experimental bore front velocity against available equations in the literature

To further validate the accuracy of the collected data, the bore front velocity was calculated using images captured by GoPro2 and compared with the bore arrival times recorded at various ultrasonic sensor locations. As shown in the images in Fig. 3.9, which are taken during test SC-H1, the bore front travels two grid lines (40 cm distance) between t = 1.071 s and t = 1.232 s, resulting thus in a calculated bore front velocity of 2.48 m/s. Additionally, the bore front velocity determined from the bore arrival times at the different ultrasonic sensors was 2.49 m/s, as shown in Fig. 3.10. The close agreement between the two methods confirms the reliability of the collected data.

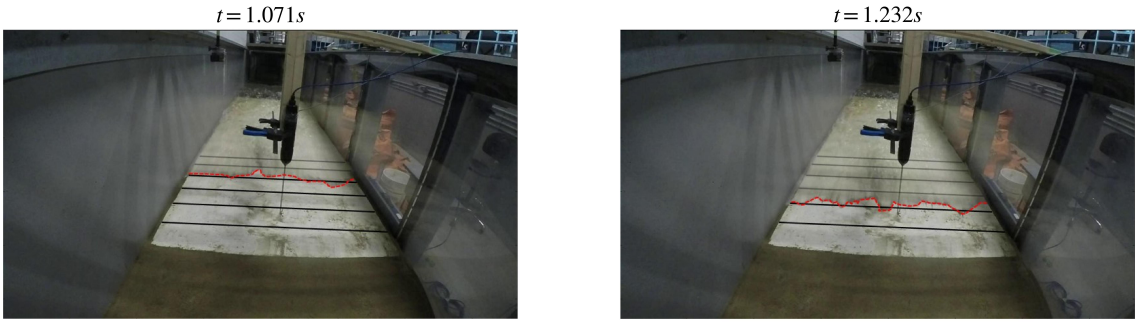

Figure 3.9: Snapshots of the bore front movement during the test SC-H1

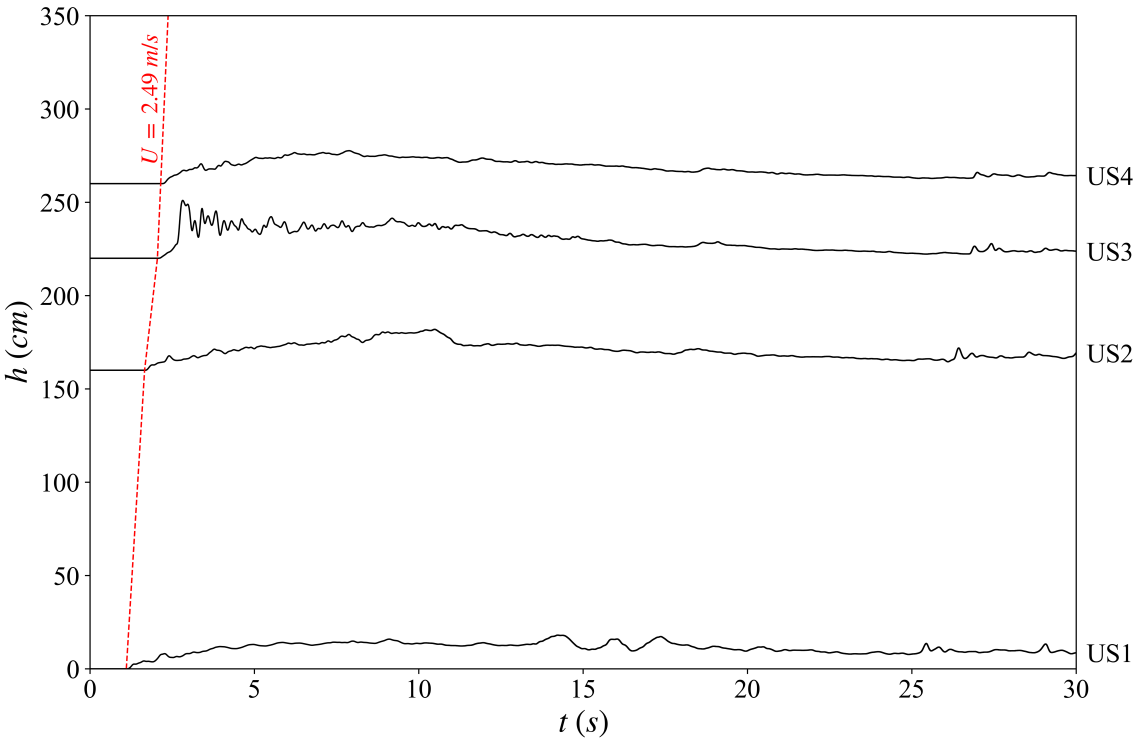

Figure 3.10: Calculation of the bore front velocity based on the bore arrival at different ultrasonic sensors for the tests SC-H1

3.3.2 Effect of the Impoundment Depth on the Scour Depth

One of the key findings of this study is that through increasing the initial impoundment depth, the subsequently generated bores led to a deeper scour hole around the structure. This relationship is evident in the bathymetry profiles obtained after each test using TLS. Fig. 3.11 presents the results for the SW-H1, SW-H2, and SW-H3 tests. It should be noted that the gray sections at the lateral boundaries are associated with the noise filtration technique applied to the bathymetry data. A multidimensional Gaussian filter was used to smooth the raw TLS data by averaging nearby points in a weighted manner as below:

$$Z_{\text{filtered}}(x, y) = \sum_{i=-k}^{k} \sum_{j=-k}^{k} G(i, j) \times Z(x - i, y - j) \tag{3.9}$$

where Z is the elevation of each point and $G(i, j)$ is the 2D Gaussian kernel defined as follows:

$$G(i, j) = \frac{1}{2\pi\sigma^2} \exp\left(-\frac{i^2 + j^2}{2\sigma^2}\right) \tag{3.10}$$

In Equation 3.10, σ is the standard deviation of the Gaussian kernel. The value of k in Equation 3.9 is set to 3σ beyond which the kernel value would be too small and does not affect the filtering process. In this study, a typical σ value of 5 was used (Virtanen et al., 2020).

For all tests in this study, the time series of the scour depth at both the front face and at the upstream corner of the structure were meticulously extracted from the video footage recorded by the camera located inside the structure, at the level of the initial sediment bed. Snapshots of these videos are presented in Fig. 3.12 for the LW-H1 test. These results, along with the time series of surface elevation at the location of US3, are shown in Fig. 3.13 and indicate a higher rate of erosion observed after the arrival of the bore at the structure for tests with greater impoundment depths for all structures. Furthermore, they indicate that the potential instability of the structure, associated with the maximum scour depth, is more likely to occur sooner for higher impoundment depths.

In Fig. 3.14, the non-dimensional forms of maximum scour depth at the upstream corner and impoundment depth are plotted to investigate their correlation. The results reveal a consistent pattern for the case of all structures, characterized by almost same slopes of the fitted lines but varying intercepts. This indicates that while the rate of change in scour depth with respect to impoundment depth is comparable among the cases with different structures, the absolute values of scour depth differ depending on the width of structure. The fitted lines for all cases delineate a plan area (the shaded zone shown in Fig. 3.14) that can serve as a predictive tool for estimating scour depth (d_s) based on impoundment depth. This surface provides some guidance for predicting scour depth under bores generated by different impoundment depths.

3.3.3 Effect of Width of Structure on Scour Depth

One of the key observations regarding the effect of structure width on the scour depth is that for walls, the maximum scour depth at the upstream corners was significantly greater than the maximum scour depth observed at the center of the front face. Moreover, this difference increased with an increase in the structure's width. This pattern is evident in the results obtained for bores generated by different impoundment depths, as shown in Fig. 3.15. These plots indicate that, for the square column, the scour depths at the center of the front face and upstream corners are nearly identical, while the maximum difference between the scour depth at these two locations occurs in the case of the long wall. It is also observed that the maximum scour depth is reached faster in

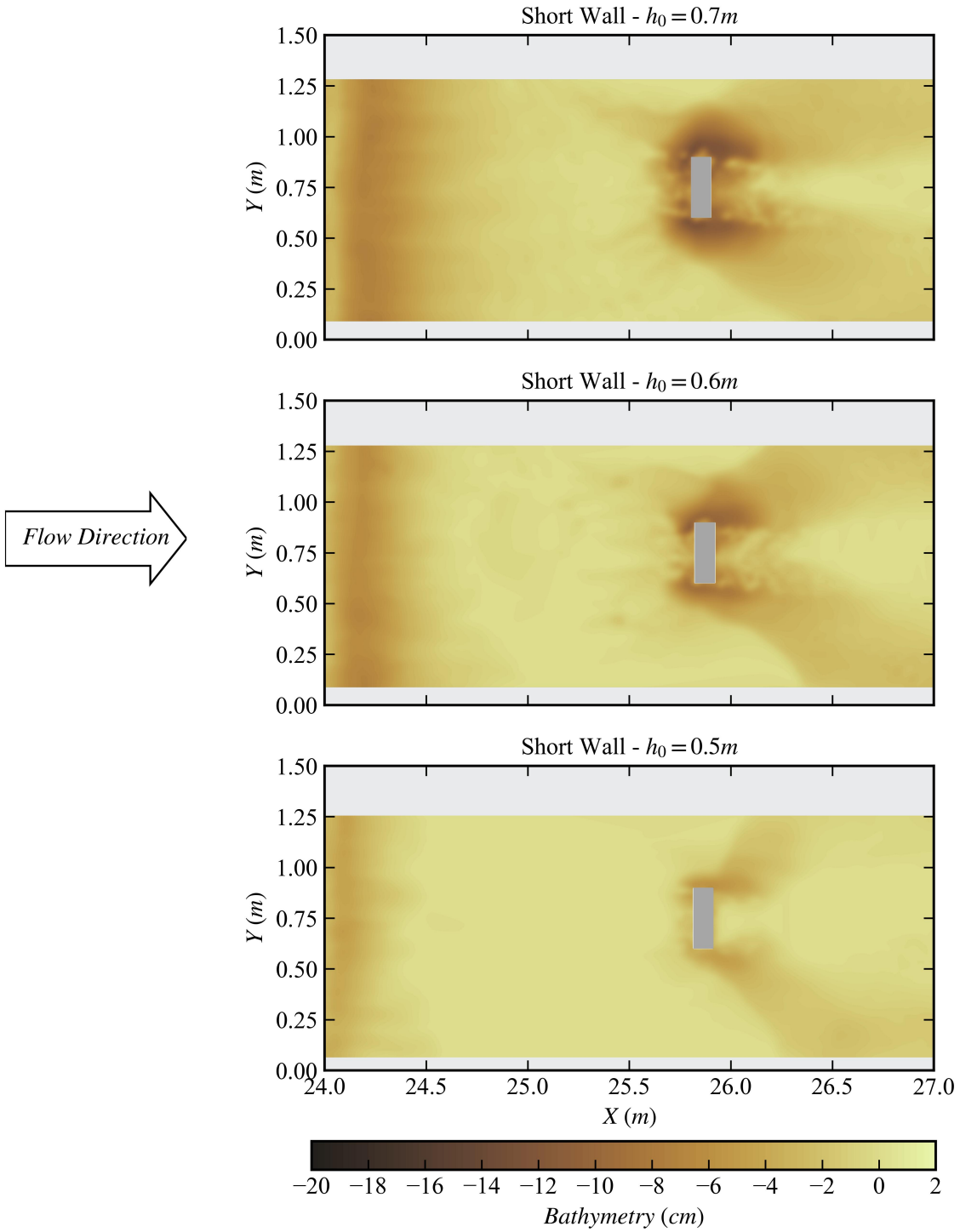

Figure 3.11: Final bathymetry of the sediment section for the scenarios with short wall with the three impoundment depths (0.5, 0.6, and 0.7 m)

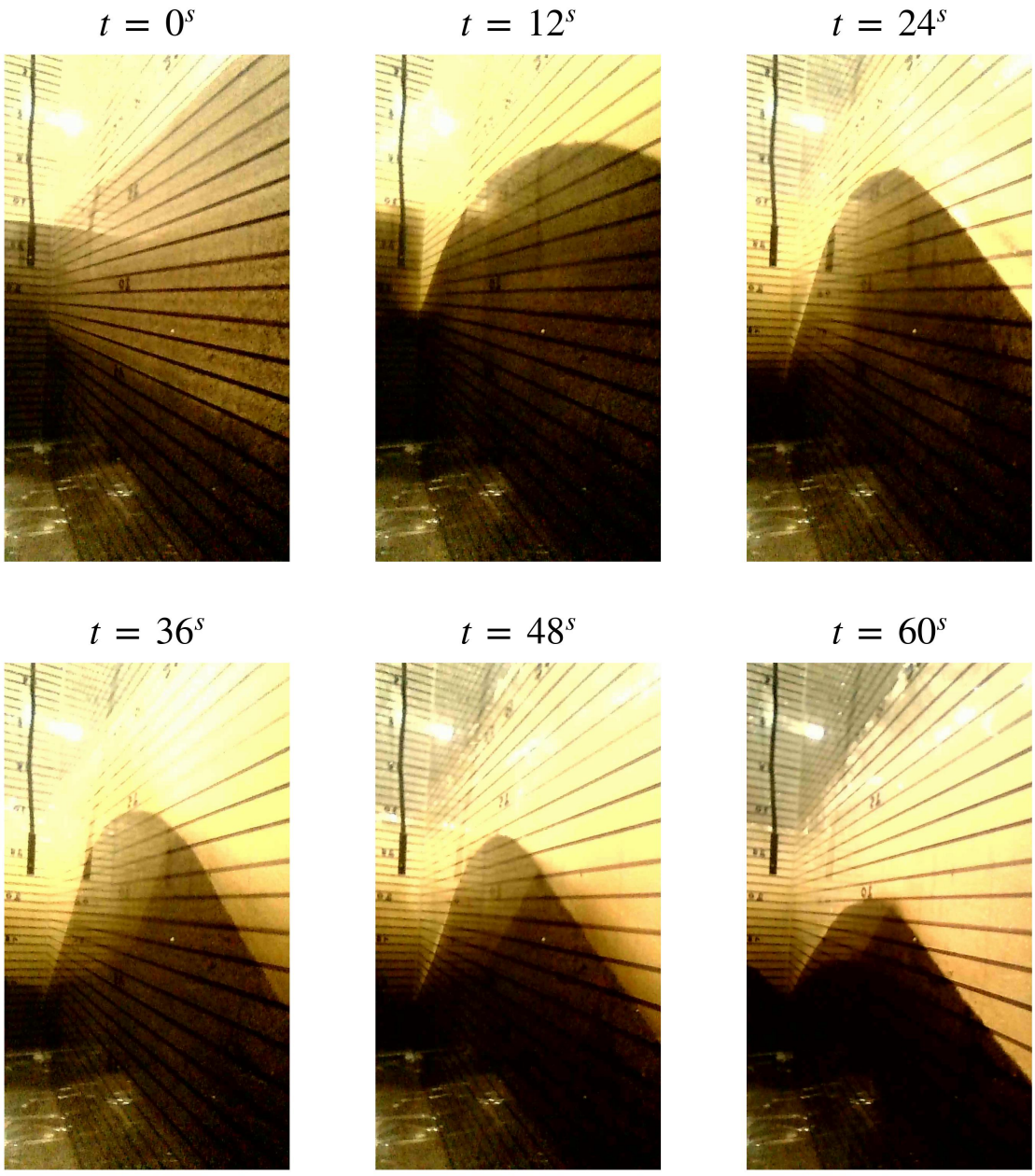

Figure 3.12: Snapshots from video footage captured from inside the structure for the case of the long wall illustrating the progression of scouring around the structure by bores generated by an impoundment depth of h_0=0.7 m

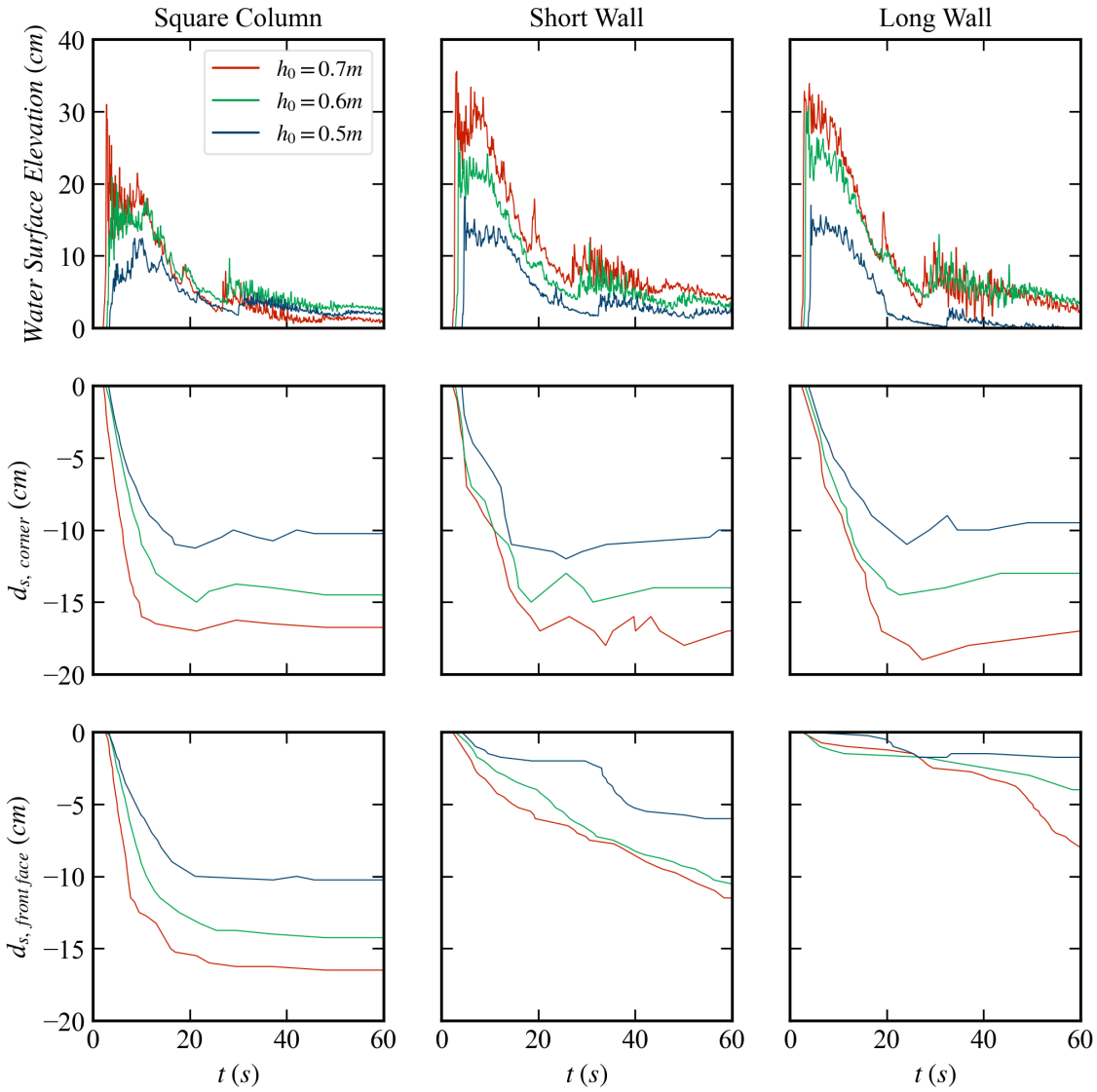

Figure 3.13: Timeseries of the water surface elevation at US3 (first row), scour depth at the upstream corner (middle row), and scour depth at the front face (last row) for the square column (first column), the short wall (middle column), and the long wall (last column). Red, green, and blue lines correspond to the 0.7 m, 0.6 m, and 0.5 m impoundment depths, respectively.

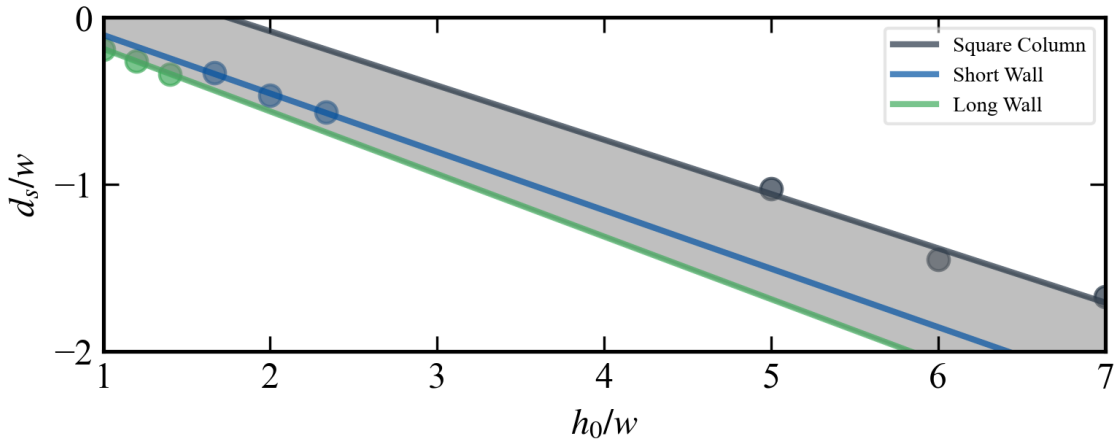

Figure 3.14: Correlation between the non-dimensional maximum scour depth at the upstream corners and the non-dimensional impoundment depth for all tests.

time for the square column compared to the short wall, and for the short wall compared to the long wall. This finding indicates that structures with narrower widths may be more at risk from earlier failure, as the critical moment, i.e. when the maximum scour depth is reached, occurs earlier than for longer structural elements.

Plotting the non-dimensional final scour depth (d_s/h_0) against the non-dimensional width of the structure (w/h_0) offers valuable insights into the variation of scour depth at both the front face and upstream corners of the structure. In Fig. 3.16, the top plot indicates some correlation between the final scour depth at the upstream corners and the width of the structure. Conversely, the bottom plot shows that the width of the wall plays a role in the scour depth magnitude at the front face of the structure, with narrower structures resulting in deeper scour depths at the center of the structure face. This finding suggests that design provisions for structural foundations at the front face, which is directly exposed to tsunami inundation, could be less stringent for wider structures. However, the final scour depth at the upstream corners appears to be less influenced by the width of the structure, emphasizing the need for consistent design considerations at these corners regardless of width. The dotted lines in Fig. 3.16 (Equations 3.11 and 3.12, respectively for scour depth at the upstream corner and center of the front face) represent the fitted lines to the data, and the gray zones illustrate the range of data parallel to these lines. Although the intercept of the fitted line for the front face is slightly deeper than that for the upstream corners, the final scour depth value for the lower end of the parameters in this study ($w/h_0 = 0.1/0.7 = 0.143$) is nearly the same for both locations, which aligns with the experimental observations.

$$d_{s,\text{corner}} = 0.03w - 0.24h_0 \tag{3.11}$$

$$d_{s,\text{front face}} = 0.23w - 0.27h_0 \tag{3.12}$$

The coefficient of determination (R^2) for Equation 3.11 is 0.23, indicating a weak linear correlation between the nondimensional width and scour depth at this location. This suggests that additional parameters or nonlinear interactions may influence the scour behavior at the upstream corner. In contrast, Equation 3.12 yields an R^2 of 0.97, demonstrating a strong linear relationship and indicating that the nondimensional width alone is a reliable predictor of scour depth at this location within the tested range. It should be noted that these empirical relationships are derived based on the specific test conditions of this study and are therefore valid only within the tested parameter bounds, namely structure widths between 0.1 m and 0.5 m and impoundment depths

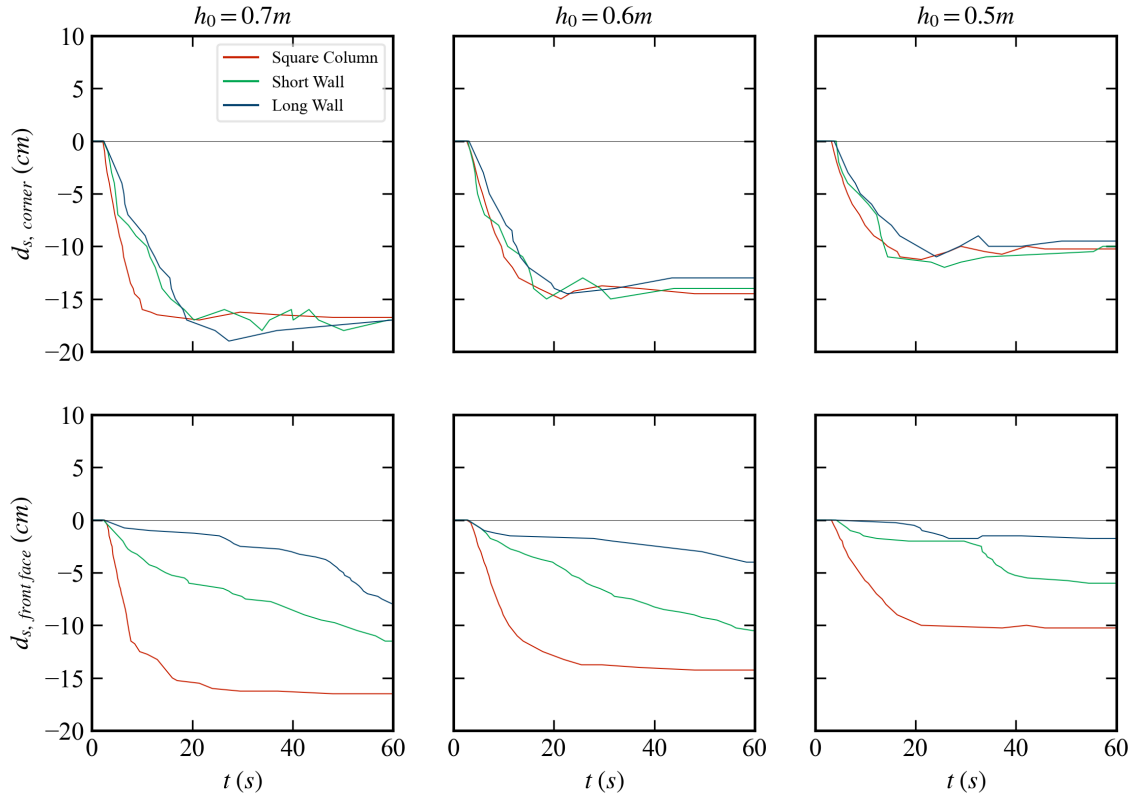

Figure 3.15: Timeseries of scour depth at the upstream corner (first row) and at the center of the front face (second row) for h_0=0.7 m (first column), h_0=0.6 m (middle column), and h_0=0.5 m (last column). Red, green, and blue lines correspond to the square column, short wall, and long wall, respectively.

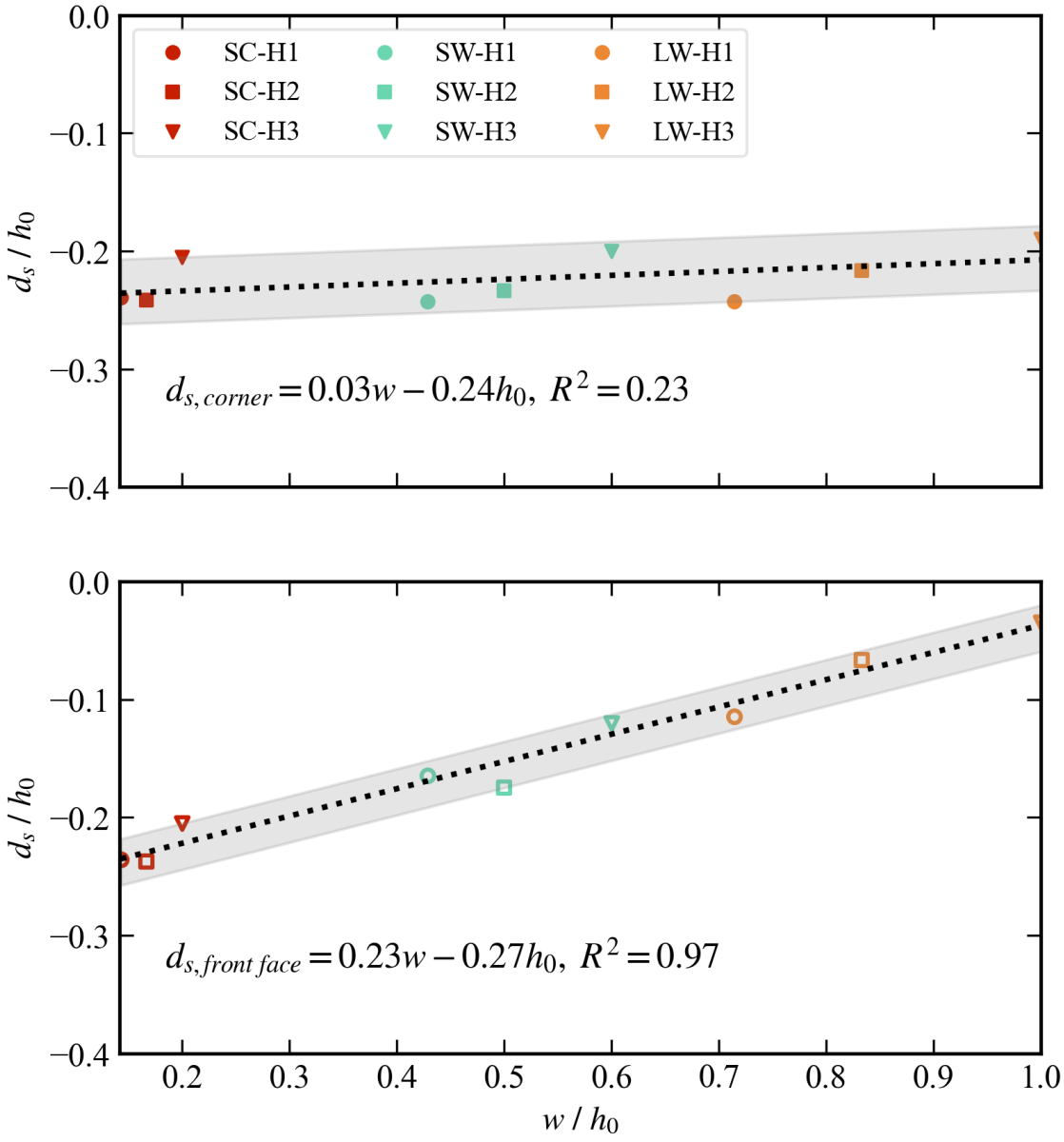

Figure 3.16: Non-dimensional final scour depth against the non-dimensional width of structure at the top: upstream corner and bottom: front face. The dashed line is the fitted line to the data and the gray zone demonstrates the range of all experimental data.

between 0.5 m and 0.7 m. Further caution is advised when applying these equations outside this range, particularly due to the presence of negative intercepts, which may lead to unreliable scour predictions. Moreover, given the inherent complexity and nonlinear nature of sediment transport and scour processes, the use of nonlinear or piecewise models may be necessary to accurately represent scour behavior beyond the parameter space investigated in this study.

To evaluate the consistency of the present results, scour depths measured in the square column tests were compared with those reported by April-LeQuéré (2022), whose experiments were conducted in the same flume facility. For this comparison, the predicted scour depths computed using the fitted equation from this study (Equation 3.12), applied to the test configurations reported by April-LeQuéré (2022), were compared with their experimental data (Fig. 3.17). While the general trends are comparable, slight discrepancies were observed between the predicted scour depths and the experimental values. One likely explanation for the discrepancy in the last test is that it was conducted with an impoundment depth of 0.45 m, which falls outside the validity range of the fitted equation (impoundment depths between 0.5 m and 0.7 m). Additionally, the consistent offset between the two datasets may be attributed to differences in the location of the structure relative to the dam-break gate, which affects the energy of the incoming flow and the strength of the generated vortices. As the exact position of the structure was not reported by April-LeQuéré (2022), a direct quantitative comparison was not feasible.

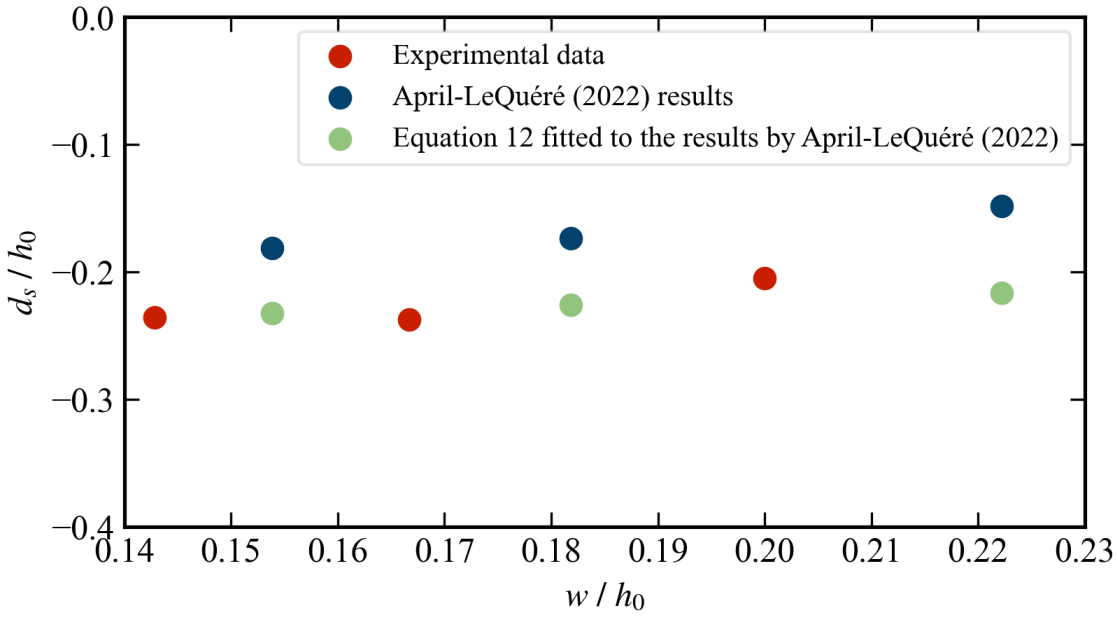

Figure 3.17: Comparison of nondimensional scour depth versus nondimensional structural width between the results by April-LeQuéré (2022) and predictions from Equation (3.12) applied to his test configurations

Figures 3.18 and 3.19 illustrate the time series of bed profiles around the short and long walls, respectively, for 0.7 m impoundment depth. These plots present results for only half the length of the front and side faces. According to these figures, the rate of erosion at the upstream corner, after the arrival of the bore front, is higher than that at the center of the front face. Additionally, after the arrival of secondary bores, a small amount of deposition is observed at the upstream corners, while the center of the front face continues to experience consistent scour throughout the tests. The rate of erosion at the center of the front face became more pronounced compared to the upstream corner and side face with the arrival of the secondary bores. For instance, in Fig.

3.18, the difference in bed profile between t=32.15 s and t=48.35 s at the front and side faces highlights this pattern. Similarly, in Fig. 3.19, the difference between t=40.45 s and t=59.5 s at the front and side faces further supports this observation.

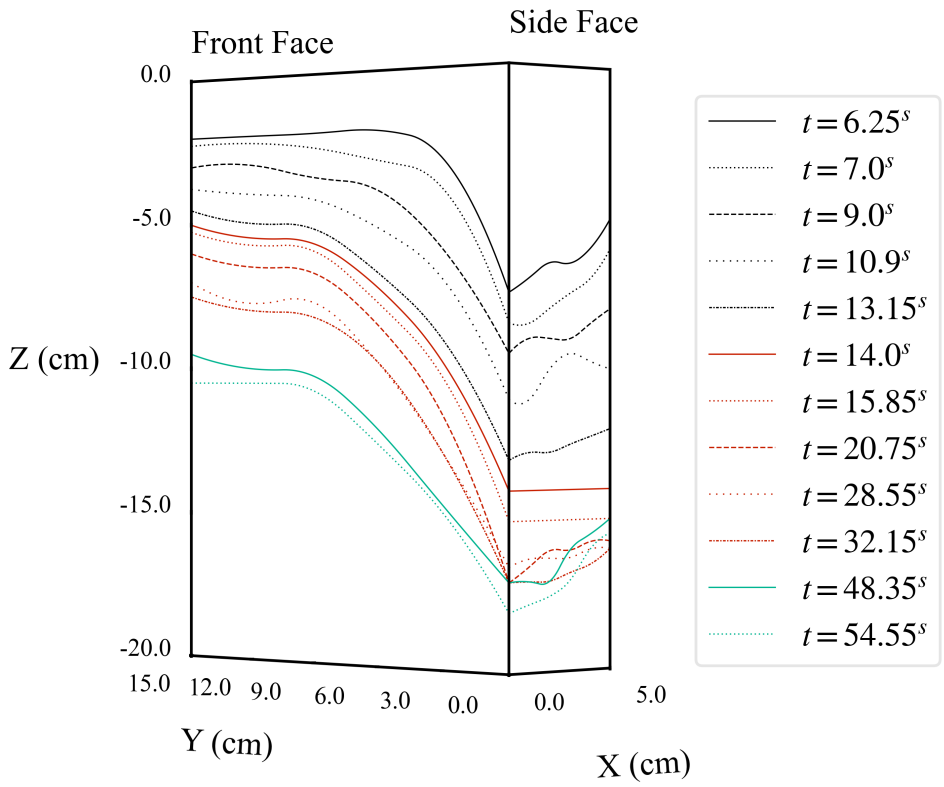

Figure 3.18: Variation of bed profile with time in front and side faces of the short wall for h_0=0.7 m

At the end of each test, the final sediment scour profile was measured using the TLS system. The plots shown in Fig. 3.20 align consistently with the finding that wider structures exhibit a greater difference between the scour depth at the center of the front face and the upstream corners. Additionally, these plots demonstrate that the location experiencing the maximum scour depth in all cases is the upstream corner of the structure, even for the lowest impoundment depth of 0.5 m.

Finally, the results of this study are compared with the prescribed envelope in ASCE-7-22 (2022) for calculating the vertical extent of scour depth, normalized to the structure's width, as a function of the Froude number. Fig. 3.21 illustrates this envelope alongside the results obtained in this study. The Froude number for each test is calculated as the mean value over time, from the beginning of the test until the moment when the maximum scour depth occurs. In this plot, filled points represent the maximum scour depth of each test, while empty points correspond to their final (residual) scour depths, which are slightly smaller in all cases due to backfilling by the secondary bores. One can observe that the scatter points for the square column lie outside the envelope prescribed by ASCE-7-22 (2022), whereas the results for the walls fall within the suggested range. This observation is significant, as the ASCE-7-22 (2022) envelope was developed based on results from previous studies involving exclusively columns rather than walls. This discrepancy may arise from the fact that the column used in the present

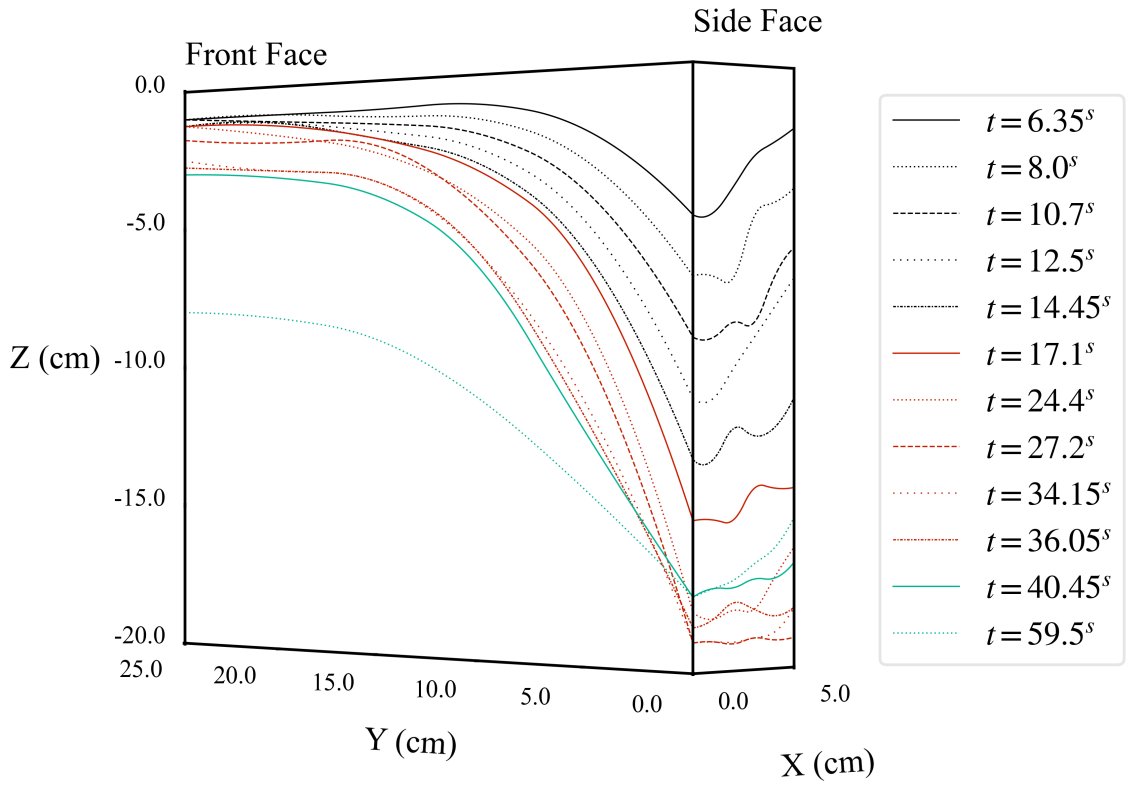

Figure 3.19: Variation of bed profile with time in front and side faces of the long wall for h_0=0.7 m

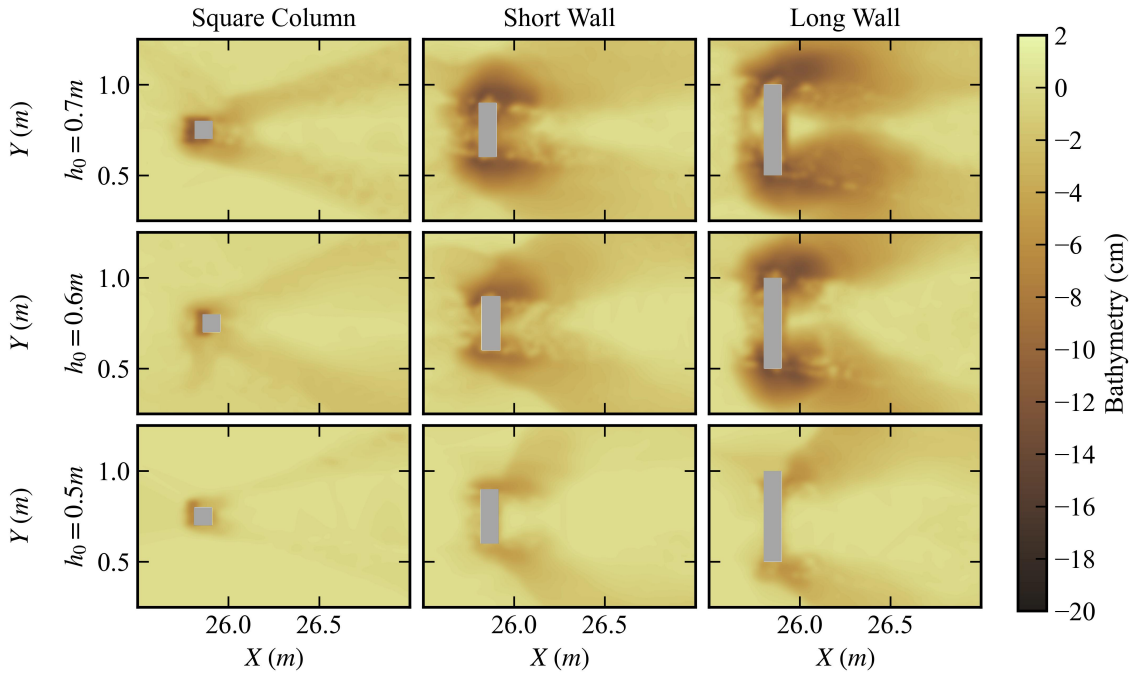

Figure 3.20: Final scour profile of the sediment bed around different structures and for bores generated by the three impoundment depths h_0=0.7 m (top), h_0=0.6 m (middle), and h_0=0.5 m (bottom)

experiments is significantly smaller in scale compared to those used in the studies underpinning the ASCE-7-22 (2022) envelope. Larger structural elements such as walls tend to restrict lateral flow, modify vortex structures, and increase flow acceleration at the corners, all of which can alter local scour patterns. Moreover, normalizing scour depth solely by the projected width of the structure may obscure the influence of other critical factors, such as structural shape, aspect ratio, or flow conditions, potentially limiting the generalizability of such envelope. These observations underscore the need for future revisions of design guidelines to consider a broader range of structural geometries, including walls and small-scale elements, which are increasingly common in coastal and urban infrastructure.

3.4 Discussion

There are several limitations associated with this study. First, scaling effects, inherent in experimental research, influence the results, particularly in tests involving sediment transport (as discussed in Section 3.2.4). Consequently, the findings of this study may be limited to the specific sediment characteristics examined in this study, particularly when the median grain size falls outside the acceptable range proposed by Melville and Chiew (1999).

Furthermore, the study investigated the influence of impoundment depth on local scour depth considering three impoundment levels which may be insufficient to fully characterize the relationship between bore characteristics and scour depth, particularly if this relationship exhibits non-linear behaviour.

The sediment section depth in the experimental setup was limited to 0.3 m, restricting the ability to test higher impoundment depths. Future work should address this constraint to extend the applicability of the findings. One potential solution is to develop a robust numerical model

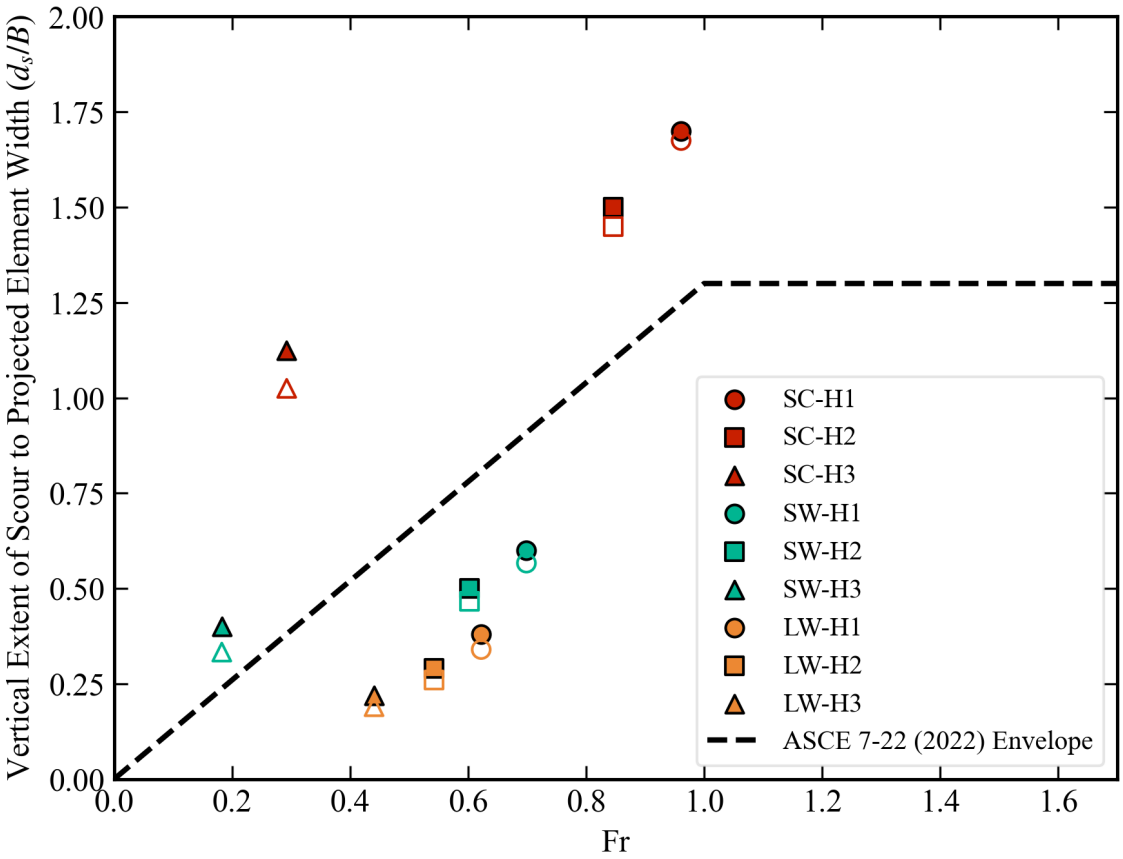

Figure 3.21: Scour depth normalized to the width of structure against Froude number together with the prescribed envelope by ASCE 7-22 (2022) for calculating the extent of the scour depth. Filled markers are associated with the maximum scour depth and hollow markers are for the final scour depth

calibrated and validated using the available experimental data that can then be used to explore a broader range of impoundment depths. It should be noted that extending such numerical models to prototype-scale scenarios requires careful consideration of computational efficiency and physical fidelity. Approaches such as those presented by Fuhrman et al. (2014) and Larsen et al. (2017) offer valuable strategies for achieving this balance through detailed modeling frameworks that remain computationally feasible.

Another limitation is the inundation duration. This investigation isolates the effects of the tsunami bore front on local scour, omitting the influence of subsequent inundation cycles typically present in real tsunami scenarios (Richmond et al., 2012; Masaya et al., 2020). Conducted over a horizontal sediment bed, the experiments generated scour exclusively from the incoming flow. Accordingly, erosion patterns at the downstream face may not capture the full scope of real-world processes. Prior studies have indicated that the drawdown phase over sloped beds can also generate considerable erosion on the landward side of structures (April-LeQuéré et al., 2022; Schendel et al., 2024; Hu et al., 2025; Hu and Li, 2025).

3.5 Conclusion

Based on the experimental investigation and analyses in the current study, the following conclusions can be drawn

- During bore inundation, structures with narrower widths reach the critical scour depth faster than wider ones.

- For all types of structures, the maximum scour depth consistently occurs at the upstream corners, regardless of the structure's width. In the case of the column, the scour depth at the upstream corners is comparable to that at the center of the front face. However, as the structure's width increases, scour depth at the corners becomes significantly deeper than that observed at the center of the front face. For instance, the nondimensional maximum scour depths (d_s/h_0) for the SC-H1 test (square column, 0.7 m impoundment depth) at the upstream corners and the center of the front face are respectively -0.239 and -0.236, while they are -0.242 and -0.114 for the case with the LW-H1 test (long wall with 0.7 m impoundment depth). Table 3.2 summarizes the results for all the tests. From an engineering standpoint, upstream corners should govern local scour checks, and increased width does not confer inherent safety. Within the tested range ($w/h_0 = 0.14 - 1.0$), front face scour diminishes with width, but corner scour remains approximately unchanged and typically controls embedment and local protections. These statements apply to rectilinear, vertical-faced structures on non-cohesive sand subjected to unsteady bores. Different geometries, cohesive soils, or armored beds may require reassessment of these findings.

- Observations reveal that upstream corners experience some deposition after the arrival of secondary bores, while the center of the front face undergoes continuous scouring. This indicates that post-tsunami field surveys may not capture the maximum scour depth at the upstream corners. Consequently, relying solely on field surveys for developing design guidelines may be insufficient, emphasizing the need for additional laboratory analyses.

- This study proposes equations for estimating scour depth at both the upstream corners and the center of the front face, based on structure width and impoundment depth. However, these equations are valid only within the parameter ranges investigated in this study, and their applicability beyond these ranges should be carefully evaluated.

Table 3.2: Summary of the results

Test name	Nondimensional width (w/h_0)	Nondimensional maximum scour depth at the upstream corner ($d_{s,corner}/h_0$)	Nondimensional maximum scour depth at the front face ($d_{s,frontface}/h_0$)
SC-H1	0.1429	-0.2393	-0.2357
SC-H2	0.1667	-0.2417	-0.2375
SC-H3	0.2	-0.205	-0.205
SW-H1	0.4286	-0.2429	-0.1643
SW-H2	0.5	-0.2333	-0.175
SW-H3	0.6	-0.2	-0.12
LW-H1	0.7143	-0.2429	-0.1143
LW-H2	0.8333	-0.2167	-0.0667
LW-H3	1.0	-0.19	-0.035

Chapter 4. Experimental Investigation of Tsunami-Induced Local Scour Around Walls: Effects of Bore Depth and Structure's Geometry*

4.1 Introduction

Tsunamis are massive waves typically generated by underwater events, such as earthquakes and landslides, which propagate towards shorelines. Upon reaching coastal regions, these waves can cause catastrophic damage to communities and their infrastructure. Notable tsunamis in recent history include the 2004 Indian Ocean, 2010 Chilean, 2011 Tohoku, and 2018 Indonesian tsunamis. Comprehensive post-event field surveys have been conducted following these tsunamis (Fritz et al., 2006; Ghobarah et al., 2006; Mikami et al., 2012; Olsen et al., 2012; Stolle et al., 2020) to quantify the damage caused by tsunami inundation and identify structural failure patterns. These surveys aimed to enhance the existing design guidelines for coastal structures subjected to tsunami impacts.

Many field surveys (Jaffe et al., 2006; Saatcioglu et al., 2006; Palermo et al., 2013; Sato and Okuma, 2014; Krautwald et al., 2021) have consistently identified local scour around buildings and walls as one of the most frequently observed failure mechanisms. Nevertheless, existing design guidelines addressing the impact of tsunamis on structural design offer limited provisions for scour-related considerations. When estimating local scour depth, the City and County of Honolulu Building Code (CCH, 2013) accounts only for the influence of sediment type, the structure's proximity to the shoreline, and inundation depth. Additionally, the Coastal Construction Manual (FEMA-P-55, 2011) and Guidelines for Design of Structures for Vertical Evacuation from Tsunami (FEMA-P-646, 2019), both developed by the Federal Emergency Management Agency, include limited provisions related to scour depth. Specifically, FEMA-P-55 (2011) considers only the diameter of the structure in determining the local scour depth, whereas FEMA-P-646 (2019) does not mandate detailed scour considerations and provides only general guidance. The most comprehensive and up-to-date existing standard is Chapter 6 of the ASCE-7-22 (2022), which contains a dedicated section on tsunami-induced local scour. However, several critical factors such as scour around walls and the effect of angle of attack on scour depth have not been addressed in this standard. Furthermore, the provisions of ASCE-7-22 (2022) rely on a limited number of studies, indicating that further research is necessary to enhance and refine these guidelines.

Most research conducted on local scour around structures has primarily focused on scour surrounding columns. Within this body of work, certain studies have specifically examined scour around circular columns (Kato et al., 2001; Tonkin et al., 2003; Lavictoire et al., 2014), while others have focused on scour around square columns (April-LeQuéré et al., 2022; Mehrzad et al., 2022; Rajaie et al., 2023b). Few studies have indirectly examined the influence of column rotation on scour depth. Khosronejad et al. (2012) explored the effects of structural geometry on local scour by conducting both experimental and numerical tests using circular, square, and

*Jazaeri, Seyed Abbas, Nistor, Ioan, Mohammadian, Abdolmajid, and Liu, Xin, *Experimental Investigation of Tsunami-Induced Local Scour Around Walls: Effects of Bore Depth and Structure's Geometry.* Coastal Engineering, Elsevier, under review.

diamond-shaped columns, the latter being a square column rotated 45 degrees. Their findings indicated that the maximum scour depths were greater for square and circular columns than for the diamond configuration, due to the more complex intense turbulent vortices responsible for scour formation. Similarly, Shafiei et al. (2015) compared the same three shapes and concluded that the square column exhibited the deepest scour, followed by circular and diamond-shaped columns. Bordbar et al. (2021) developed a numerical model to simulate local scour around square and diamond columns under steady current and live-bed conditions. Their results revealed that the formation of strong horseshoe vortices around the square column resulted in greater maximum and residual scour depths. Hurtado-Herrera et al. (2024) also employed numerical modeling to compare the scour depths between square and diamond-shaped structures in narrow channels under steady flow. Despite these extensive investigations into columns, literature addressing local scour around walls remains limited. Zarrati et al. (2004) investigated the use of collars to protect rectangular bridge piers from local scour under steady currents. More recently, Zhang et al. (2025) conducted an experimental study on local scour around a rectangular bridge pier in a flume and validated the results using numerical simulations performed using Flow-3D software (Flow Science, 2019).

To the best of authors' knowledge, the present study is the first to examine the effect of the angle between the flow direction and a wall on local scour depth under unsteady flow conditions. To this end, a series of experimental tests were conducted to investigate the influence of this parameter with the objective of enhancing the existing design guidelines.

The remainder of this paper is organized as follows. Section 4.2 describes the setup of the large dam-break flume at the Water Resources Laboratory, University of Ottawa, Canada, along with the test matrix and instrumentation used. Section 4.3 presents the results of the study, beginning with data preprocessing and validation of the dam-break hydrodynamics, followed by discussion of the temporal evolution of scour depth and a detailed parametric analysis of the factors affecting maximum and residual scour. This section also includes a comparison with the ASCE-7-22 (2022) standard. Finally, Section 4.4 synthesizes the key findings and discusses the limitations of the study, along with suggestions for future research directions.

4.2 Flume Setup and Test Matrix

To gain a better understanding of the mechanisms governing local scour around walls, a series of experimental tests were conducted in the Large Dam-Break Flume of the Water Resources Laboratory at the University of Ottawa, Canada. The flume features a 16 m long reservoir at its upstream end, separated from the rest of the flume by a piston-activated, rapidly opening swing gate. A key characteristic of this large dam-break gate is its ability to open in an extremely short time, ensuring the generation of an ideal dam-break bore, as per the criterion proposed by Lauber and Hager (1998). According to this criterion, the non-dimensional gate-opening time must be less than the square root of two, expressed mathematically as follows:

$$t_0\sqrt{\frac{g}{h_0}} < \sqrt{2} \tag{4.1}$$

where t_0 represents the actual gate-opening time, g is the gravitational acceleration, and h_0 denotes the impoundment depth in the reservoir. Immediately downstream of the gate, a 3.3 m long approaching slope was constructed to elevate the flume bed by 0.3 meters, allowing thus for the installation of the sediment section. This was followed by a 4.2 m long false floor section. A 0.2 m long gabion was placed downstream of the false floor to provide a smoother transition

between the solid bed (false floor) and the erodible bed (sand section), thereby preventing the formation of a large scour hole at the beginning of the sand section. Following the gabion lied a 3.9 m sediment section, within which the wall models were installed. Finally, at the downstream end of the flume, a second false floor, measuring 2.3 m in length led to a vertical-drop drain designed to prevent back-propagating flow and evacuate the flow into the underground reservoir. Side- and top-view schematics of the flume are presented in Figures 4.1 and 4.2, respectively.

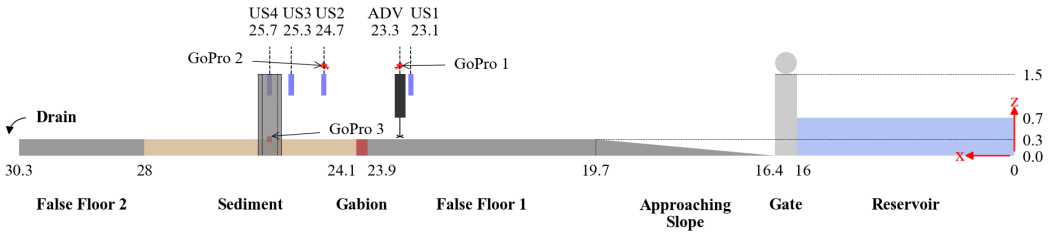

Figure 4.1: Side view schematic of the flume (units in meter, not at scale)

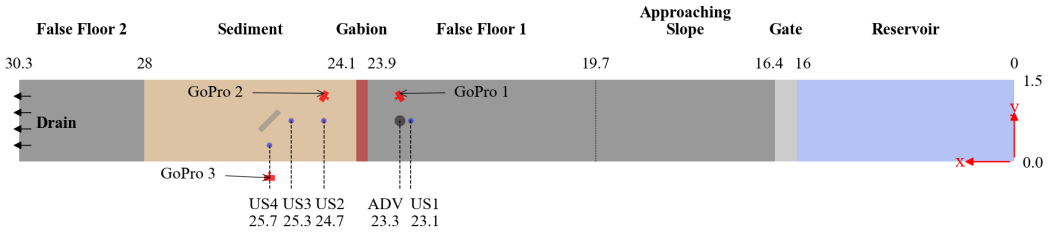

Figure 4.2: Plan view schematic of the flume (units in meter, not at scale)

Various instruments were employed to capture key parameters related to flow hydrodynamics and sediment transport. Four ultrasonic sensors (US) were positioned at locations indicated in Figure 4.1 to record the time-history of the water surface elevations at specific points along the flume. An Acoustic Doppler Velocimeter (ADV) was positioned at the end of the first false floor to measure the time-history of the flow velocity. It is important to note that the ADV was not placed closer to the test wall because of its limitations in accurately capturing the velocity in highly turbulent flow conditions generated by the roller formed at the upstream face of the wall. Three GoPro cameras were positioned inside and outside the flume. Two cameras recorded the upstream and downstream ends of the flume, while the third camera was mounted outside the flume to capture the wall through the transparent side wall of the flume. Furthermore, two miniature wire cameras were installed within the wall to monitor the temporal evolution of scour depth at both the front and side faces. Finally, a Terrestrial Laser Scanning (TLS) system was employed upon completion of each test to obtain high-resolution scans of the final bathymetry of the sand section. Data acquired from the TLS system were essential for interpreting the overall scour pattern around the wall.

To investigate the influence of the angle of attack on local scour depth, three orientations of the model walls were considered in this study: 0° (wall model perpendicular to the flow), 45° rotated wall, and 90° (wall model parallel to the flow). Additionally, to ensure the reliability of the results and broaden the applicability of the findings, three impoundment depths (0.5 m, 0.6 m, and 0.7 m) and two structural widths (0.3 m and 0.5 m) were examined. All walls had a uniform thickness of 0.1 m. A summary of all test configurations is provided in the test matrix shown in Table 4.1. The test nomenclature consists of three components: (1) the wall width (SW for short

wall, LW for long wall), (2) the impoundment depth (H1, H2, or H3), and (3) the angle between the wall and the flow direction (A1, A2, or A3).

Table 4.1: Configurations of tests

Structure type	Orientation angle with respect to flow direction	Impoundment depth H1
Short Wall (0.3m × 0.1m)	**A1=0°**	SW-H1-A1
	A2=45°	SW-H1-A2
	A3=90°	SW-H1-A3
Long Wall (0.5m × 0.1m)	**A1=0°**	LW-H1-A1
	A2=45°	LW-H1-A2
	A3=90°	LW-H1-A3

4.3 Results

4.3.1 Data Validation and Preprocessing

Before conducting analysis of the recorded data, it is essential to verify their quality. The initial validation step involved assessing the gate-opening time. To ensure the generation of ideal dam-break bores, the gate-opening time must satisfy the criterion proposed by Lauber and Hager (1998), as defined by Equation 4.1. It is important to note that the actual gate-opening time refers to the moment when the gate is no longer in contact with the water, rather than the total duration required for the gate to become fully open (Figure 4.3). For every experiment the opening time was extracted from frame-by-frame analysis of video snapshots captured by camera GoPro 2, which was oriented toward the upstream side of the gate. Subsequently, the average opening time for tests sharing an identical impoundment depth was calculated and presented in non-dimensional form as a function of impoundment depth (Figure 4.4). The curve shown in this figure corresponds to the left-hand side of Equation 4.1, derived using the mean gate-opening time across all 18 tests. This indicates that an impoundment depth of 0.5 m is close to the minimum value that allows ideal dam-break bore generation with existing laboratory facilities.

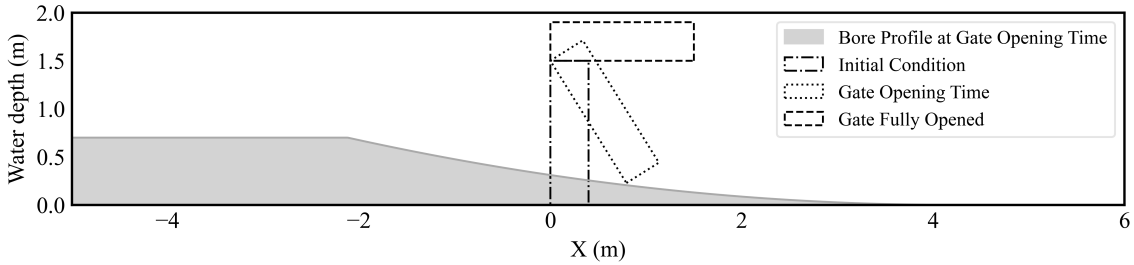

Figure 4.3: Different stages of the gate-opening in dam-break problem

To reduce high-frequency noise in the ultrasonic sensor and ADV records, a digital low-pass Butterworth filter was applied with a cutoff frequency of f_c = 5 Hz and a sampling rate of f_s = 300 Hz, which is consistent with the specifications of the data acquisition system. The filter was implemented as a cascade of second-order sections (SOS) to ensure computational efficiency and

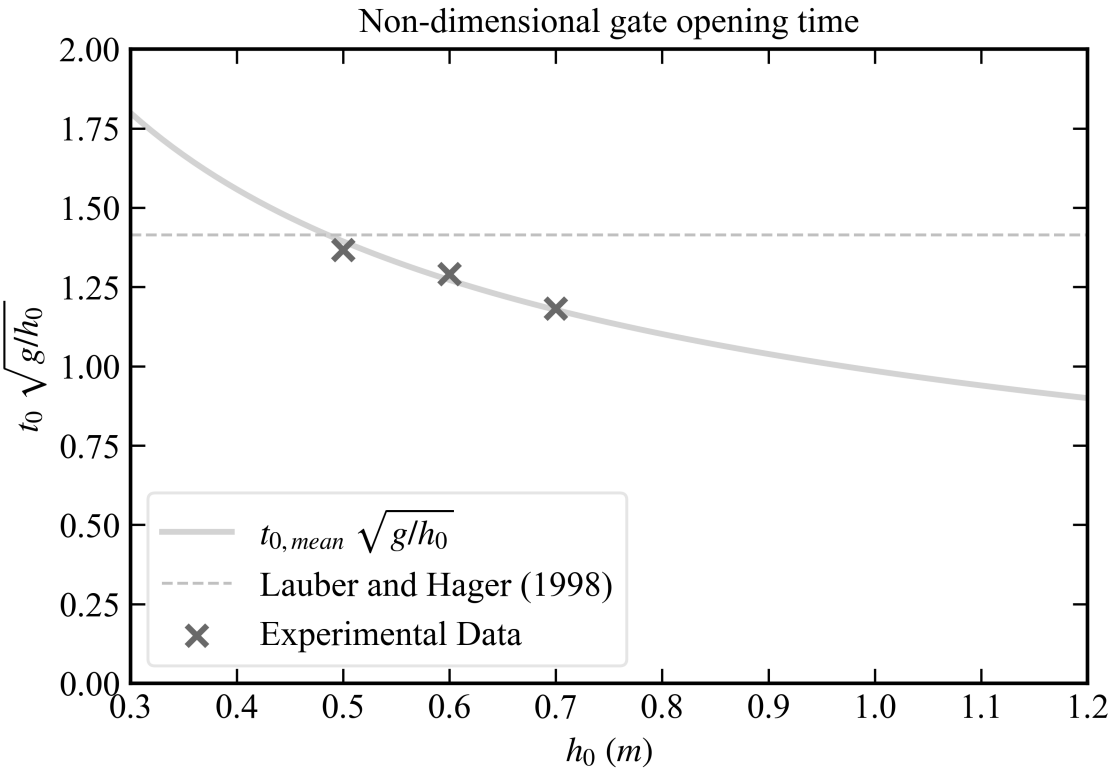

Figure 4.4: Non-dimensional gate-opening time against the impoundment depth

numerical stability (Virtanen et al., 2020). Each section followed the discrete-time difference equation.

$$y[n] = b_0x[n] + b_1x[n-1] + b_2x[n-2] - a_1y[n-1] - a_2y[n-2] \tag{4.2}$$

where $x[n]$ and $y[n]$ denote the input and output signal values at time step n, and b_0, b_1, b_2, a_1, and a_2 are the section-specific filter coefficients obtained through standard filter design procedures. Two such sections were applied in series to achieve a fourth-order response, effectively preserving physical signal components with periods longer than 0.20 s while attenuating higher-frequency noise (Butterworth, 1930).

Figure 4.5 presents the raw and filtered time-history of the water surface elevation data recorded by the four ultrasonic sensors. For US1, which was installed over the false floor and situated furthest upstream from the wall, the filtered and unfiltered signals closely align, indicating minimal presence of high-frequency noise. In contrast, US3, positioned directly upstream of the wall where the dam-break bore impacts the wall and generates highly turbulent flow, exhibited pronounced high-frequency fluctuations that were effectively attenuated by the filter. The formation of horseshoe vortices in front of the wall at the location of US3 is illustrated in Figure 4.6 Sensors US2 and US4, situated above the sediment section, exhibited intermediate behaviour.

4.3.2 Dam-Break Hydrodynamic Validation

Chanson (2006) derived an analytical solution to the dam-break problem by applying the method of characteristics to the governing equations. The analysis indicated that the instantaneous removal

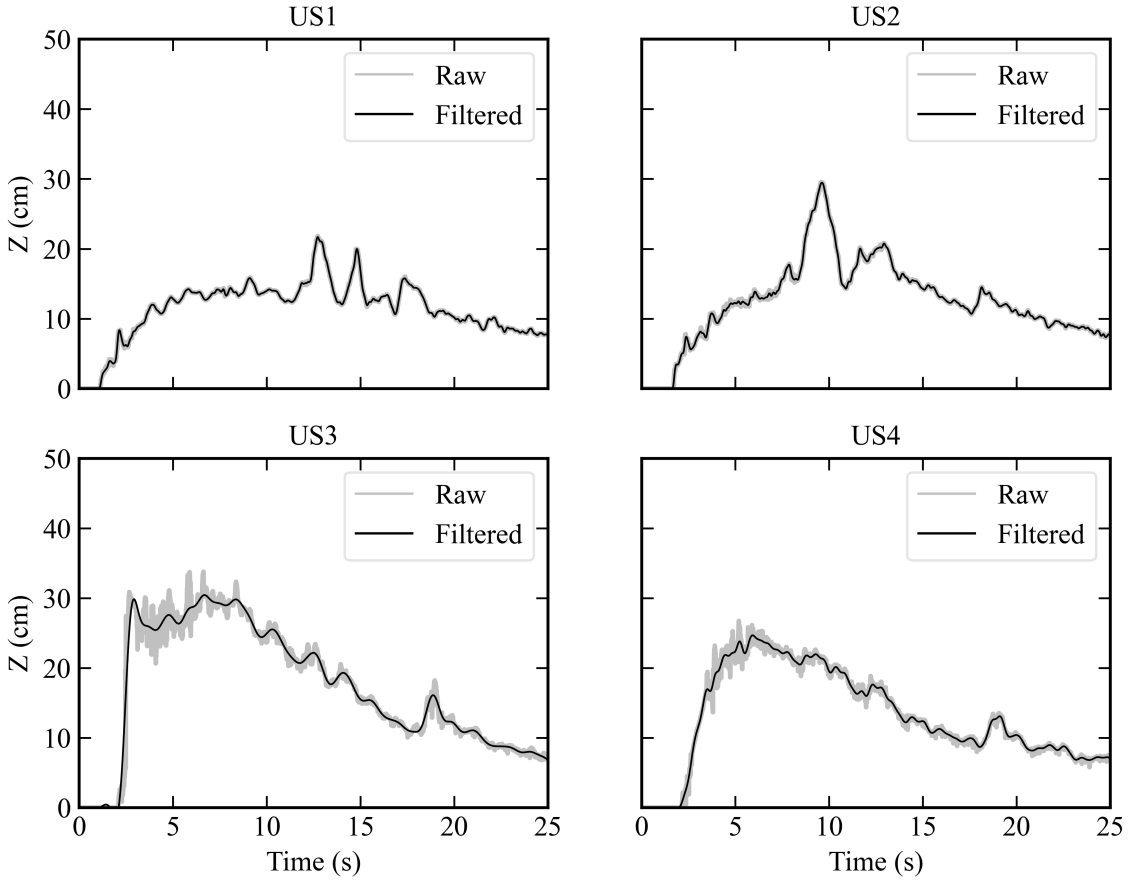

Figure 4.5: Effect of noise filtering applied on the raw collected data for the SW-H1-A1 test

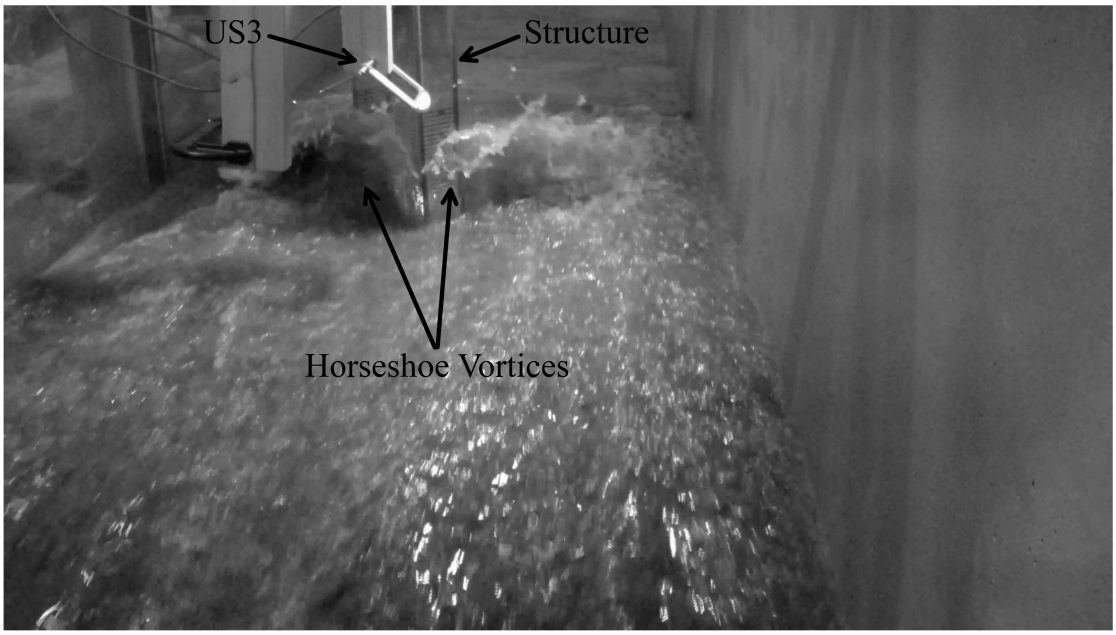

Figure 4.6: Snapshot of the video footage from GoPro1 camera showing the formation of horseshoe vortices in front of the wall

of the gate generates a negative wave propagating upstream from the gate. The free-surface elevation between the leading edge of this negative wave and the bore front is given by

$$\frac{Z}{h_0} = \frac{1}{9}\left(2 - \frac{x}{t\sqrt{g d_0}}\right)^2 \tag{4.3}$$

where Z is the free-surface elevation, x is the distance from the gate, and t is time. Figure 4.8 compares the non-dimensional water surface elevations recorded by US1 for all tests with the analytical solution in non-dimensional form. The results demonstrate good agreement between the two, thereby confirming the reliability of the collected data. The discrepancies observed in the data can be attributed to the fact that the analytical solution was derived for a horizontal bed, whereas the present flume includes an approaching slope immediately downstream of the gate, which influences the flow pattern.

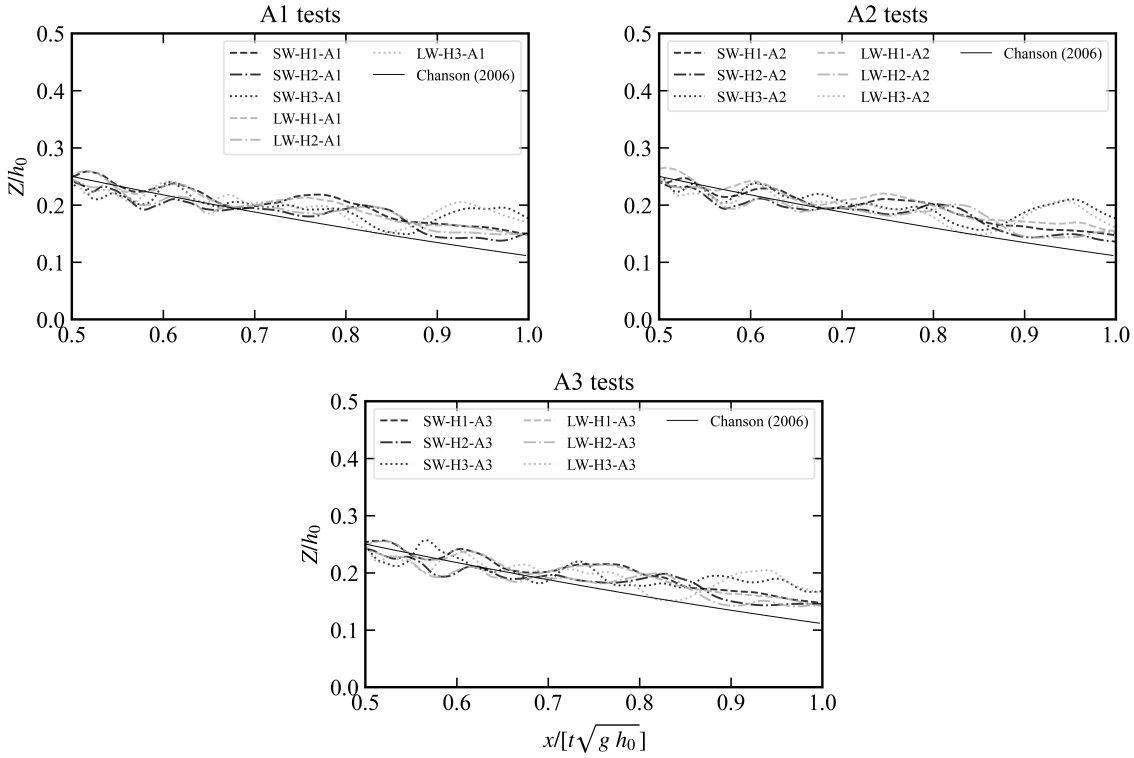

Figure 4.7: Comparison between the non-dimensional bore depth and the analytical solution proposed by Chanson (2006)

Chanson (2006) also proposed the following expression for the flow velocity U over a non-ideal bed with a Darcy friction factor f:

$$\frac{8}{3}\frac{1}{f}\frac{\left(1 - \frac{1}{2}\frac{U}{\sqrt{g h_0}}\right)^3}{\frac{U^2}{g h_0}} = t\sqrt{\frac{g}{h_0}} \tag{4.4}$$

This equation was solved iteratively for U and the resulting values were compared with laboratory measurements, as shown in Figure 4.8. A Darcy friction factor of 0.017 was adopted in this study. However, based on the analysis conducted by Jazaeri et al. (2024) for the same flume, this value may not be applicable to tests with the lowest impoundment depth (h_0 = 0.5

m). Therefore, the results for these cases are excluded from Figure 4.8. The comparison shows very good agreement between the analytical and experimental flow velocities. This agreement is particularly important because the flow velocity plays a critical role in the local scour process through its influence on bed shear stress. Thus, ensuring the reliability of velocity data is essential for subsequent analyses of scour process.

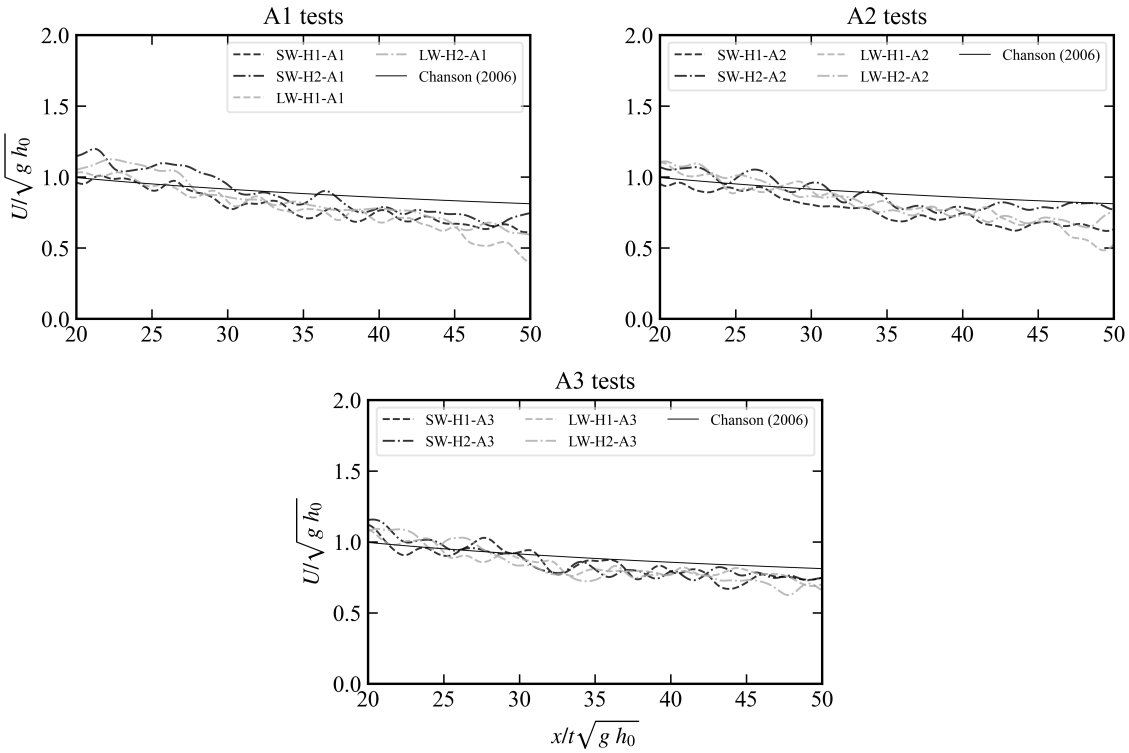

Figure 4.8: Comparison between the non-dimensional bore velocity and the analytical solution proposed by Chanson (2006)

4.3.3 Temporal Evolution of Scour Depth

For each test conducted in this study, the time series of scour depth evolution around the wall was extracted from video snapshots recorded by micro-cameras installed within the wall. Figure 4.9 presents representative snapshots of the SW-H1-A1 test. The scour depth at various locations on the front and side faces of the wall was measured for each video frame using the grid lines drawn on the wall. The maximum scour depth occurred at the upstream corners of the wall from the onset of inundation. This approach enabled analysis of the scour evolution throughout the inundation phase, rather than relying solely on the final scour measurements, which is typically the case in most post-tsunami field survey observations.

The time series of scour depth at the center of the front face and at the upstream corner of the wall, along with the water surface elevation measured at US3, were plotted for all the tests. A key observation stemming from these plots was that the maximum scour depth consistently exceeded the residual (final) scour depth, primarily because of sediment deposition associated with the arrival of secondary bores (Figure 4.10). Consequently, the most critical scour progression occurs during the initial stage of inundation. Therefore, relying solely on scour depths reported in post-tsunami field surveys may be insufficient for developing design guidelines because these values do not necessarily reflect the maximum scour experienced during the event.

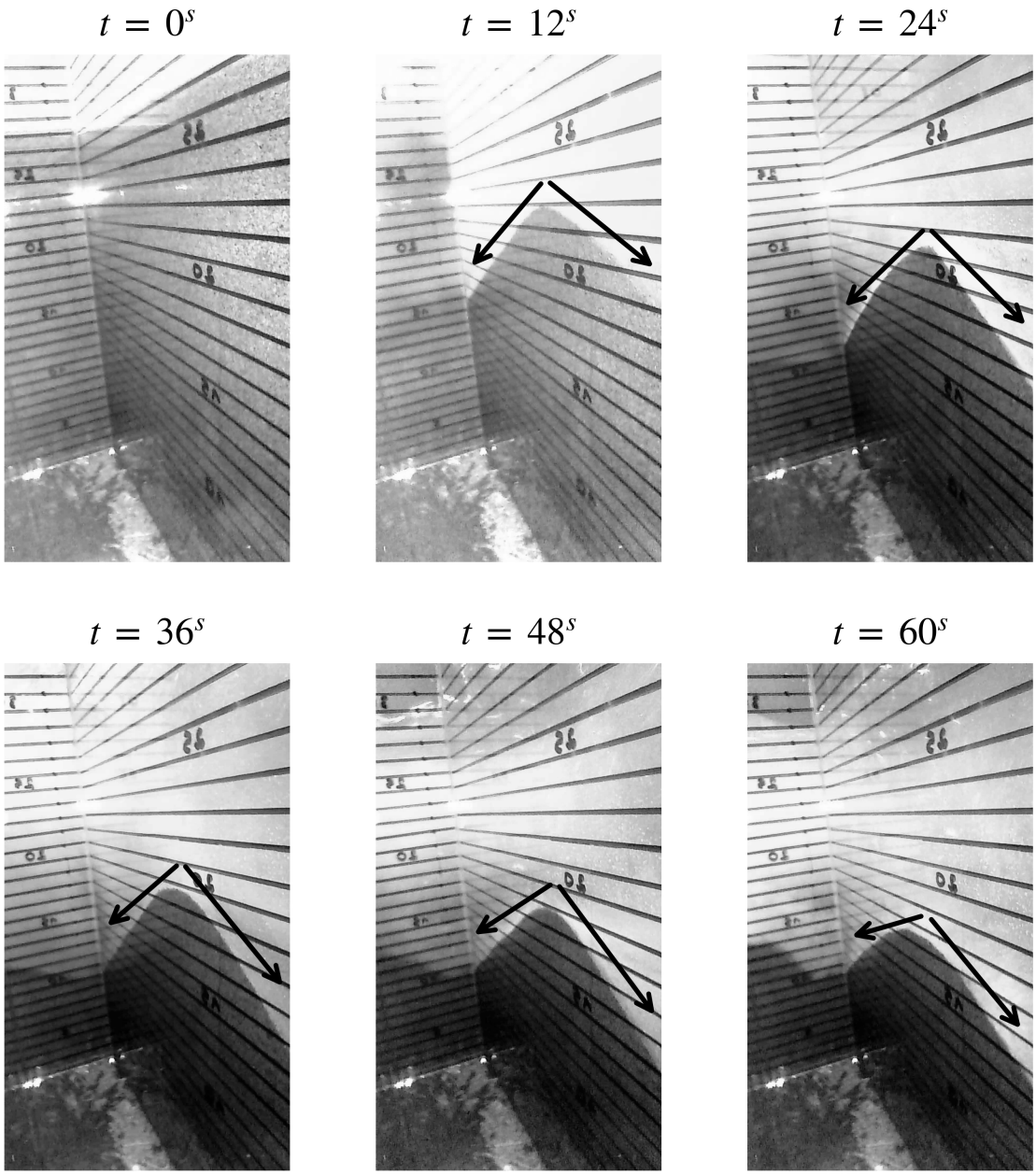

Figure 4.9: Snapshots of the video footage by the wire micro-camera installed within the wall showing the progression of the scour depth at the front and side faces

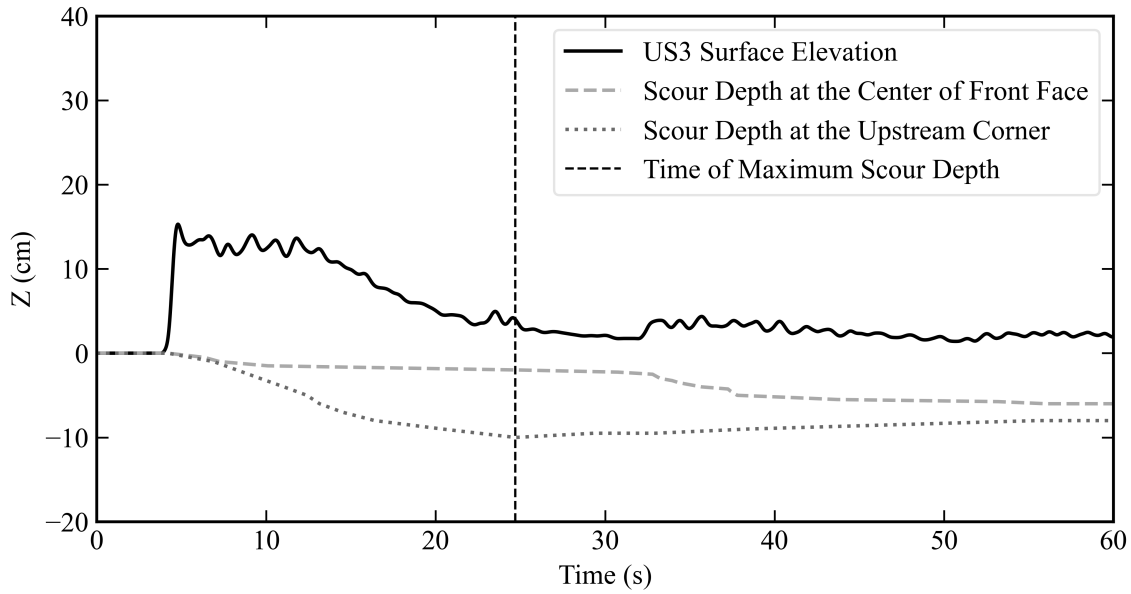

Figure 4.10: Time series of water surface elevation at the location of US3 (solid line), scour depth at the center of the front face (gray dashed line), and scour depth at the upstream corner (dotted line) of the wall together with the time of maximum scour depth (black dashed line at 24.7 s associated with 10 cm scour depth) for the SW-H3-A1 test

4.3.4 Parametric Analysis of the Maximum Scour Depth

Table 4.2 presents the maximum scour depth recorded for each test along with the corresponding time at which it occurred. These maximum values were used to further analyze the influence of various parameters on local scour depth around wall.

To identify general trends, the results were systematically categorized based on key parameters relevant to each analysis, namely, impoundment depth, structural width, and angle. Within each category, the maximum scour depth values from all corresponding tests were averaged to obtain a representative value. For instance, when assessing the influence of impoundment depth at a given orientation, the maximum scour depths from tests with the same impoundment depth and angle but different widths were averaged. This procedure accentuates the dominant patterns associated with the key variables while mitigating the influence of individual test variability.

Figure 4.11 presents the relationship between impoundment depth and maximum scour depth, categorized by structural orientation. As expected, increasing impoundment depth results in deeper scour, reflecting the higher hydraulic energy available to sustain vortex structures and entrain sediment. Across all depths, the wall positioned perpendicular to the flow (0°) consistently produces the deepest scour. This outcome aligns with classical scour theory, where frontal stagnation and lateral flow separation give rise to strong horseshoe vortices that concentrate downflow and enhance sediment excavation at the base of the structure.

The influence of wall rotation becomes more nuanced at varying depths. At the lowest impoundment level (50 cm), the wall aligned parallel to the flow (90°) results in the shallowest scour, likely due to minimal frontal blockage and reduced vortex formation. The scour depth for the 45° orientation was significantly deeper than 90°, but still less than that of the 0° case. As the impoundment depth increases to 60 cm, the difference between the 45° and 90° orientations diminishes, with both producing similar scour depths (15 cm). This convergence suggests that with increased hydraulic energy, the contribution of wake vortices and flow separation near the sides of the wall becomes more comparable to the asymmetric vortices generated by the 45°

Table 4.2: Summary of the maximum scour depth with the associated time for all tests

Short Wall			**Long Wall**		
Name	Time of Maximum Scour Depth (s)	Maximum Scour Depth (cm)	**Name**	Time of Maximum Scour Depth (s)	Maximum Scour Depth (cm)
SW-H1-A1	24.40	-19.0	LW-H1-A1	24.45	-19.5
SW-H2-A1	19.35	-15.5	LW-H2-A1	17.40	-18.5
SW-H3-A1	16.40	-10.0	LW-H3-A1	18.90	-13.0
SW-H1-A2	16.30	-18.0	LW-H1-A2	18.80	-19.0
SW-H2-A2	16.85	-14.0	LW-H2-A2	16.15	-16.0
SW-H3-A2	18.75	-10.5	LW-H3-A2	17.80	-11.5
SW-H1-A3	17.20	-19.5	LW-H1-A3	17.20	-18.0
SW-H2-A3	14.35	-15.0	LW-H2-A3	16.65	-15.0
SW-H3-A3	17.65	-11.75	LW-H3-A3	17.05	-8.0

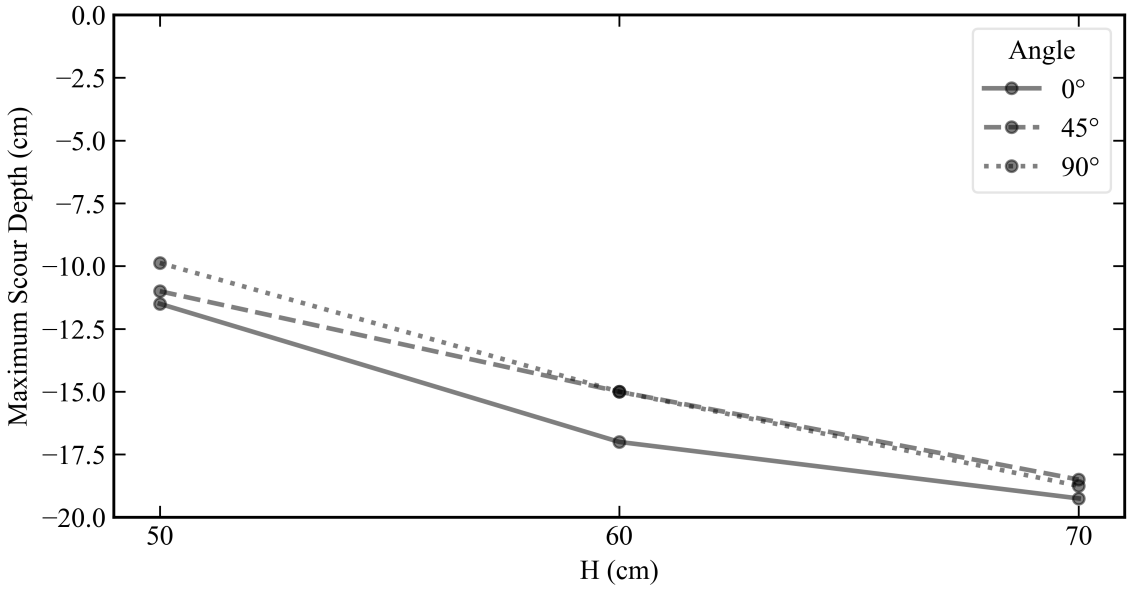

Figure 4.11: Maximum scour depth against impoundment depth categorized by the angle between the flow direction and the wall

case. At 70 cm, the scour depth for the 90° configuration becomes slightly greater than that of 45°, possibly indicating a growing influence of flow separation and vortex formation near the wall's lateral extremities under high-energy conditions. These trends reinforce the understanding that while wall orientation governs the initial vortex formation, its interaction with flow energy significantly modulates the scour response.

Figure 4.12 illustrates the relationship between impoundment depth and maximum scour depth, with data grouped by wall width. For each impoundment depth, the plotted values represent the average of maximum scour depths observed across all wall orientations (0°, 45°, and 90°) for a given width. The results reaffirm that impoundment depth is the principal driver of scour development, with deeper impoundments producing more severe scour due to increased hydraulic energy and sustained vortex activity.

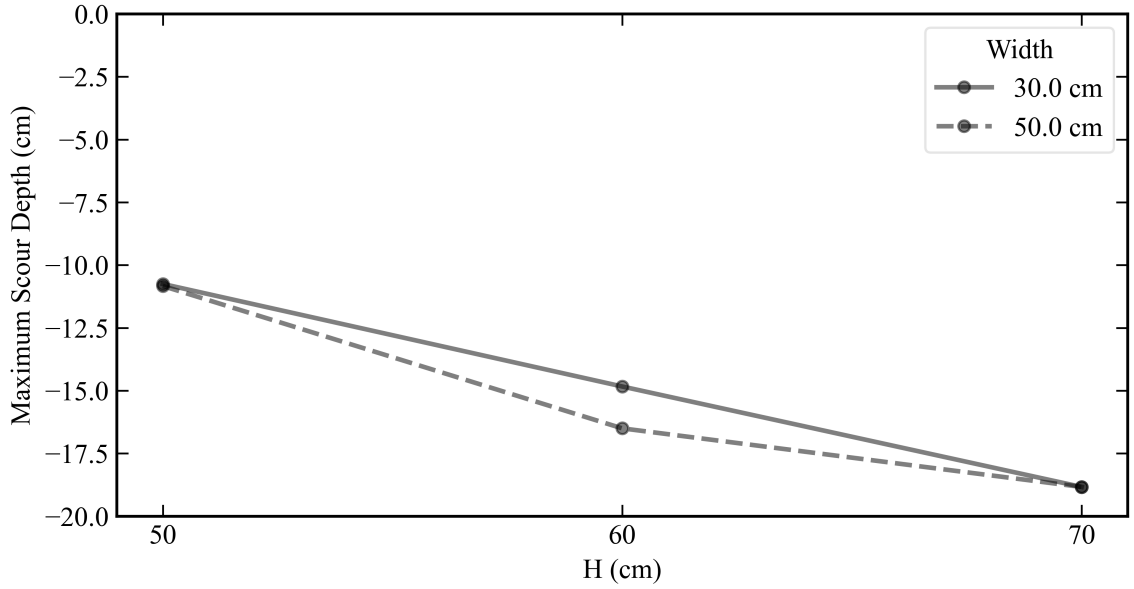

Figure 4.12: Maximum scour depth against impoundment depth categorized by the wall width

Structural width exhibits only a modest influence at 50 cm and 70 cm impoundmene depths, where both widths yield nearly identical scour depths. This suggests that under lower and higher energy conditions, flow dynamics are primarily governed by the available hydraulic forcing, with minimal sensitivity to geometric variations in frontal area. However, at the intermediate impoundment depth of 60 cm, the wider wall (50 cm) results in noticeably deeper scour. This pronounced deviation may reflect a transitional hydraulic regime in which the ratio of flow depth to wall width enhances local flow contraction and intensifies horseshoe vortex development, particularly in configurations that present a broader face to the oncoming flow. Moreover, when scour depths are averaged over all orientations, this condition may coincide with constructive overlap of mechanisms, such as downflow jets, wake-induced separation zones, and vortex impingement, that enhance sediment removal around the base of the wider wall. This highlights the importance of considering compound interactions between wall dimensions and flow intensity when evaluating scour risk.

Figure 4.13 presents the maximum scour depth as a function of wall width, categorized by structural orientation. For each width-angle combination, the scour depths represent the average of maximum values across all impoundment depths (50 cm, 60 cm, and 70 cm). The figure provides insight into how the interaction between width and alignment influences local scour mechanisms.

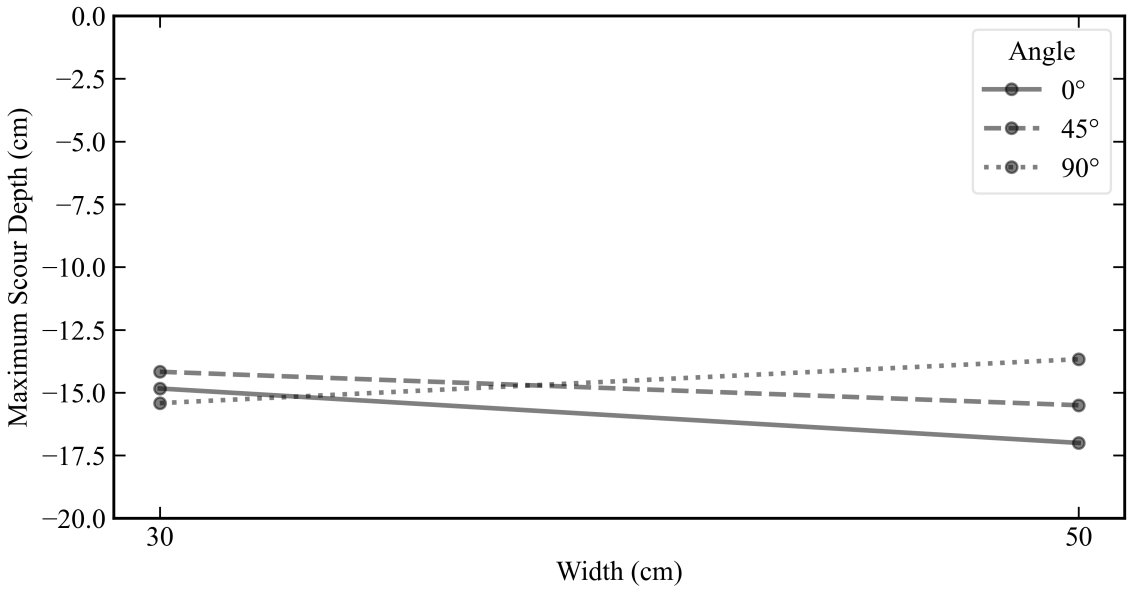

Figure 4.13: Maximum scour depth against wall width categorized by the angle between the flow direction and the wall

For 0° and 45° orientations, where the wall is fully or partially exposed to the incoming flow, increasing the structural width leads to slightly deeper scour. This trend is attributed to enhanced frontal flow obstruction, which promotes stronger flow contraction and intensifies horseshoe vortex formation at the base of the wall. These effects increase the downward and lateral velocity components responsible for sediment entrainment and localized scouring.

In contrast, for the 90° orientation, where the wall is aligned parallel to the flow direction, increasing the width results in shallower scour. This is likely due to the longer sidewall guiding the flow more smoothly, suppressing large-scale separation and reducing the intensity of wake vortices and shear layers near the lateral ends of the wall. Consequently, turbulence-driven sediment transport mechanisms become less effective as width increases in the parallel configuration. This contrasting behavior highlights the critical role of wall–flow alignment in modulating the influence of geometry on local scour processes.

4.3.5 Residual Scour Depth

In addition to the maximum scour depth, the residual scour depth is a critical aspect of the tsunami-induced local scour. During a tsunami event, the structure is subjected to multiple wave impacts of varying energy levels. Highly energetic waves can excavate a scour hole around the structure, whereas less energetic waves may transport sediment from the upstream region and deposit it within the scour hole, thereby reducing its depth. At the same time, slumping of the scour hole slopes can lead to this infill of the scour pit. This process was clearly reflected in the final bathymetry of the sediment section, as captured by the LiDAR scanner, and is illustrated in Figure 4.14.

4.3.6 Comparison with ASCE 7-22 ASCE-7-22 (2022) Standard

To translate the experimental findings into practical applications, the measured scour depths were compared with the design envelope prescribed in ASCE-7-22 (2022), as shown in Figure 4.15. In

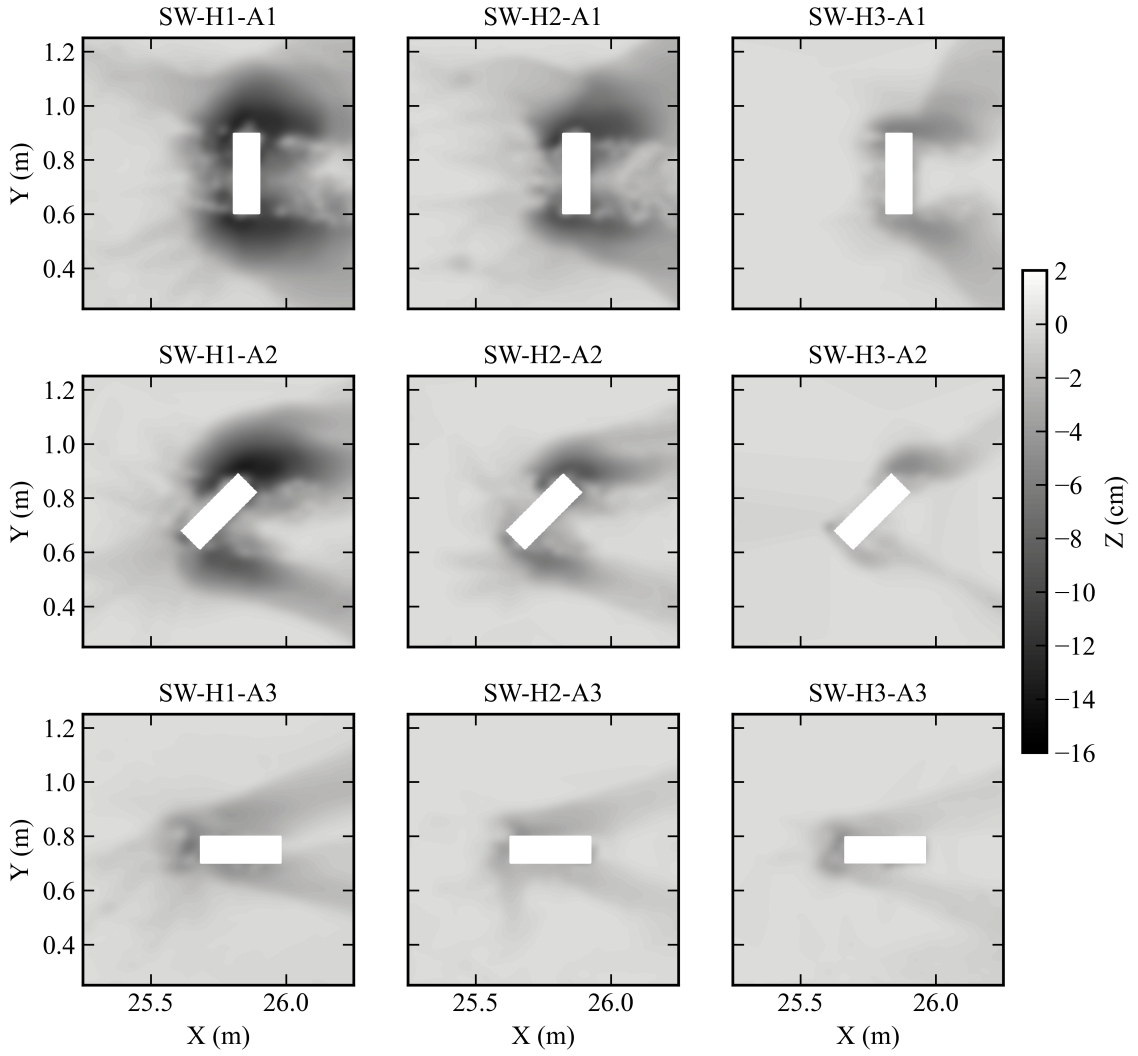

Figure 4.14: Final bathymetry profile of the sediment section obtained from LiDAR scans for all the tests with the short wall

this figure, the horizontal axis represents the Froude number, calculated as the temporal average of the Froude number time series from the beginning of the test up to the moment when the maximum scour depth occurred (as indicated in Table 4.2). In congruence with the prescriptions of the ASCE-7-22 (2022) Chapter 6, the vertical axis shows the maximum scour depth normalized by the projected width of the wall. In the experimental setup, walls oriented parallel to the flow direction (A3 tests) had the smallest projected width exposed to the flow (0.1 m), while those rotated 45 degrees (A2 tests) as well as those perpendicular to the flow (A1 tests) exhibited progressively larger projected widths. Consequently, the normalization procedure yielded larger dimensionless scour depths for the wall parallel to the flow cases. For instance, the points corresponding to LW-H3-A3 and LW-H3-A2 fall outside the prescribed envelope, even though the LW-H3-A1 test, which recorded a deeper absolute scour depth, remains within the acceptable range. These findings indicate that the current formulation of the prescribed envelope may not sufficiently account for the influence of structural orientation and projected width. Therefore, a revision of the standard may be necessary to incorporate additional parameters affecting scour depth and improve the accuracy of foundation design for tsunami-resistant structures.

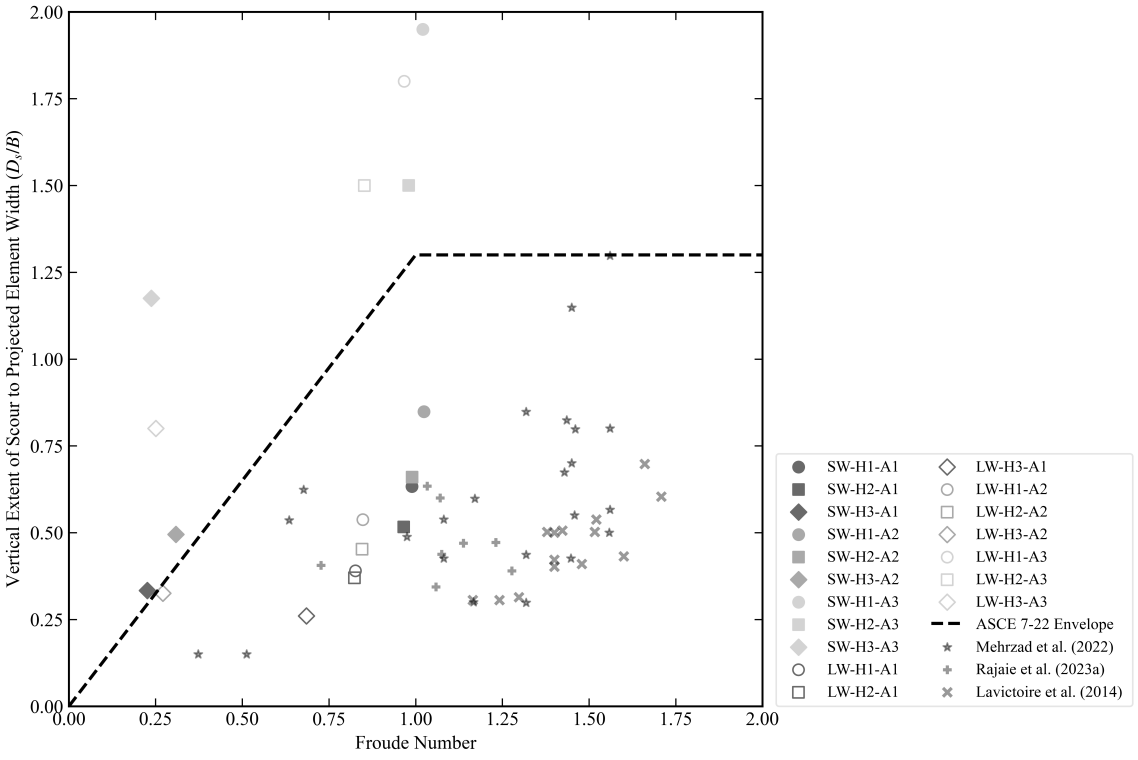

Figure 4.15: Comparison of the results obtained in this study with the envelope prescribed by the ASCE-7-22 (2022) standard

4.4 Discussion and Conclusions

This new study experimentally investigated tsunami-like bore-induced local scour around vertical walls with varying impoundment depths, structural widths, and orientations relative to the flow direction. The findings provide insight into how each of these parameters modulates scour development under highly unsteady, energetic flow conditions representative of tsunami inundation. The most salient findings are summarized below.

4.4.1 Key Finidings

- The impoundment depth, which translated into the depth of the bore, was the dominant factor influencing scour. Increasing the initial impoundment level consistently led to deeper and faster waves and, as such, deeper scour holes. For instance, for walls oriented perpendicular to the flow (0°), the average maximum scour depth increased from 11.5 cm for an impoundment depth of H = 0.5 m to 19.25 cm for H = 0.7 m. This trend reflects the increased hydraulic energy available for sediment entrainment and vortex development due to deeper and faster bores.

- The wall orientation significantly affected scour by controlling the formation and strength of horseshoe vortices. Walls perpendicular to the flow (0°) consistently produced the deepest scour, while rotating them to 90° substantially reduced vortex intensity and associated erosion. For the long wall, the scour depth at 90° was reduced by about 5 cm compared to the 0° case for H = 0.5 m, confirming the protective effect of flow alignment.

- Wall width showed limited influence, except under transitional conditions. For the 0.5 m and 0.7 m impoundment depths, scour depths were nearly identical for the 30 cm and 50 cm long walls. However, at H = 0.6 m, the wider wall produced up to 3 cm deeper scour than the narrow one, possibly due to enhanced flow contraction or horseshoe vortex amplification under intermediate energy levels.

- Residual scour depth was always shallower than the maximum, due to backfilling from sediment-laden secondary bores. This was evident in the time series plots (Figure 4.10) and final bathymetry (Figure 4.14), underscoring the need for time-resolved measurements. Post-tsunami field surveys relying on final scour depth may underestimate peak erosion levels and associated risk when considering it for design.

- Comparison with ASCE-7-22 (2022) showed that normalizing scour depth by projected width can misrepresent structural vulnerability. In several cases, parallel walls (90°), which had smaller projected widths, showed larger normalized scour depths than perpendicular ones despite having shallower absolute scour. This discrepancy suggests that the existing envelope may not fully capture orientation-related effects (Figure 4.15).

4.4.2 Limitations and Future Work

While the results offer valuable insight, the authors acknowledge certain limitations which define the scope of applicability and guide future studies:

- While the experimental matrix included three impoundment depths (0.5 m, 0.6 m, and 0.7 m), three wall orientations (0°, 45°, and 90°), and two wall widths (30 cm and 50 cm), the total number of test cases remained limited to eighteen. Although this configuration enabled a structured parametric investigation, it restricts the statistical robustness of interaction effects between variables. For example, differences observed in scour behavior between short and long walls at the same angle suggest that width–angle–depth interactions may play a significant role, but interpreting such interactions based on a 3×3×2 test matrix remains inherently under-resolved. Additional test cases would allow for better resolution of nonlinearities, statistical validation, and potentially the development of empirical or surrogate models.

- The range of structural widths was limited by blockage ratio constraints. Raudkivi and Ettema (1983) noted that blockage ratios exceeding 33% may induce wall effects that can distort the scour pattern. Accordingly, to avoid such effects, the wall width was capped at 0.5 m in a 1.5 m-wide flume. Broader wall models may induce additional flow confinement and require larger facilities for investigation.

- The sediment layer depth restricted the impoundment height. Deeper scour under higher flow energies could not be tested without risk of flume floor interference. A deeper sediment section would enable safe testing of more extreme tsunami conditions.

- The ADV had to be positioned further upstream of the wall due to turbulence limitations, meaning the recorded velocities may not exactly represent flow conditions at the wall model's base. This may introduce some error in Froude number estimates used in Figure 4.15.

- One of the inherent challenges in experimental sediment transport studies is the difficulty of directly scaling sediment grain size. Unlike geometric or temporal parameters, which can be scaled according to well-established similarity laws (e.g., Froude scaling), sediment cannot be reduced proportionally without introducing cohesion or changing its transport behavior. For instance, applying a 1:25 geometric scale to natural sandy sediments would require using grains so fine that cohesive forces dominate, which no longer represents non-cohesive sediment dynamics. However, Melville and Chiew (1999) proposed that if the ratio of the characteristic structure length to sediment grain diameter exceeds 50, the influence of grain size on local scour becomes negligible. In the present study, this criterion was satisfied in all tests, indicating that a direct scaling of grain size was not required to preserve dynamic similarity in the scour process. Additionally, to establish a realistic relationship between model and prototype time scales, the inundation duration observed in the laboratory was compared with full-scale tsunami conditions. According to Mikami et al. (2012), typical real-world tsunami inundation durations range from 10 to 17.5 minutes. In the present experiments, the inundation time varied from approximately 2 to 3.5 minutes, depending on the impoundment depth. Based on this correspondence, a time scale factor of 1:5 was adopted. Using the Froude similarity law, this implies a geometric length scale factor of 1:25. Accordingly, the prototype-scale impoundment depths represented by the laboratory conditions range from 12.5 m to 17.5 m, which is consistent with observed tsunami wave heights. This confirms the relevance of the experimental setup for modeling real-world tsunami-induced scour scenarios.

- Finally, the flume used a horizontal sediment bed, which precludes examination of scour induced by drawdown flows on sloping terrain. Prior studies by the authors (April-LeQuéré et al., 2022; Schendel et al., 2024) have shown that slope steepness can strongly influence scour patterns, especially on the landward side of structures.

Chapter 5. Numerical Simulation of Local Scour Around Walls Under Unsteady Dam-Break Bores: Benchmarking MIKE3 HD/ST and FLOW-3D with MCDA*

5.1 Introduction

Tsunamis are large waves primarily generated by underwater earthquakes or landslides that propagate toward coastal areas, often causing devastating impacts on coastal infrastructure and communities. For example, the 2004 Indian Ocean Tsunami, which originated near the northern tip of Sumatra Island, Indonesia, resulted in approximately 128,645 fatalities and 37,063 missing persons (Borrero, 2005). Similarly, the 2011 Tohoku Tsunami in Japan caused an estimated 360 billion US dollars in infrastructure damage (Lebreton and Borrero, 2013).

Following such catastrophic events, coastal engineering researchers have carried out extensive field surveys to examine the mechanisms of tsunami-induced structural damage. Post-event investigations of major tsunamis, including the 2004 Indian Ocean, 2010 Chile, 2011 Tohoku, and 2018 Indonesia tsunamis, have documented multiple failure modes. Chock et al. (2013) highlighted the contribution of tsunami wave impact forces to structural failure, and Stolle et al. (2020) emphasized the effects of debris impact on structural stability. However, most forensic engineering post-tsunami field observations consistently identified local scour around structures as one of the dominant failure mechanisms (Kato et al., 2012; Wilson et al., 2012; Palermo et al., 2013; Lim et al., 2015; Krautwald et al., 2021). Therefore, understanding the mechanisms governing local scour around structures and integrating appropriate design provisions into engineering guidelines and standards are essential for enhancing coastal resilience.

Extensive research has been conducted to examine the influence of various parameters on local scour around structures through both experimental investigations and numerical simulations. However, due to the inherent complexity of real-world tsunami generation processes and the challenges associated with accurately reproducing them in laboratory or computational settings, simplified approaches are often employed to approximate tsunami inundation behavior.

Researchers have adopted various methods to simulate tsunami inundation, such as using solitary waves (Kato et al., 2001; Nakamura et al., 2008; Chen et al., 2013; Larsen et al., 2018; Xu and Huang, 2022) and dam-break bores (Imamura et al., 2008; Arnason et al., 2009; Leal et al., 2009; Nouri et al., 2010; Al-Faesly et al., 2012; Wüthrich et al., 2018; Lavictoire et al., 2014; Mehrzad et al., 2022; Rajaie et al., 2023b). Madsen et al. (2008) demonstrated that solitary waves are not an accurate representation of real tsunamis because of their substantially shorter wave periods compared with actual tsunami waves. In contrast, Chanson (2006) compared video recordings of the 2004 Indian Ocean Tsunami with dam-break bores and noted significant similarities between the two, supporting the suitability of dam-break models for simulating tsunami-induced flows.

Although laboratory modelling can capture the inherent complexity and uncertainty of local scouring mechanisms more accurately, it is subject to several limitations. Large scale

*Jazaeri, Seyed Abbas, Nistor, Ioan, Mohammadian, Abdolmajid, and Liu, Xin, *Numerical Simulation of Local Scour Around Walls Under Unsteady Dam-Break Bores: Benchmarking MIKE3 HD/ST and FLOW-3D with MCDA* Journal of Waterways, Ports, Ocean, and Coastal Engineering, ASCE, under review.

experimental facilities capable of minimizing scaling effects are very few, and conducting such experiments is often prohibitively expensive. In contrast, rapid advancements in computational technology have encouraged researchers to increasingly employ numerical modelling. These models are more cost-effective and efficient. However, they frequently depend on simplified assumptions that may limit their ability to fully replicate real-world processes.

Several challenges are inherently associated with the numerical modelling of sediment transport processes. Due to the natural variability and complexity of sediment particles, it is not feasible to reproduce the exact size distribution and spatial arrangement of individual particles within numerical models. Consequently, simplified representative parameters, such as the median grain size (d_{50}), are commonly used, introducing a certain level of approximation in the simulations. Moreover, accurately resolving horseshoe and lateral vortices, which are the primary flow structures responsible for local scour around structures under unsteady flow conditions, requires the implementation of advanced turbulence models to capture their dynamic behavior.

Another major challenge in the numerical modelling of sediment transport lies in selecting an appropriate sediment discharge equation. Numerous empirical formulations have been proposed to estimate bedload, suspended load, or total load sediment discharge, including those by Meyer-Peter and Müller (1948), Engelund and Hansen (1972), Engelund and Fredsøe (1976), Van Rijn (1984a,b, 1993), Nielsen (1992), and the Extended Engelund and Fredsøe equation (Roulund et al., 2005). These formulations are typically derived from laboratory experiments conducted under specific conditions, which limits their general applicability. For example, many were developed for steady-state flow conditions and may not accurately represent sediment transport under unsteady flow scenarios. Additionally, because sediment behavior varies considerably with grain size, these equations are usually valid only within defined sediment size ranges. Consequently, most models include several calibration parameters, such as bedload and suspended load coefficients, that must be adjusted to achieve reliable performance for a given application.

The remainder of this paper is structured as follows. Section 5.2 provides a comprehensive literature review on the numerical modelling of sediment transport around structures. Section 5.3 describes the experimental tests conducted in this study, along with the methodology adopted for numerical simulations. Section 5.4 presents the results analyzed based on numerical simulations, and Section 5.5 discusses these results in detail. Finally, Section 5.6 summarizes the key conclusions of the study, offering guidance for numerical modellers in selecting the most appropriate tool for simulating local scour around walls under unsteady flow conditions.

5.2 Litearture Review

The literature on the numerical modelling of local scour around structures is extensive. However, because the empirical equations for sediment discharge calculations are predominantly based on tests conducted under steady-state conditions, studies employing steady-state scenarios are more prevalent than those involving unsteady conditions. Abdelaziz et al. (2011) investigated the local scour around a circular bridge pier using FLOW-3D developed by Flow Science (2019), utilizing its feature for defining a custom function to incorporate the effect of bed slope on the critical Shields parameter. Ehteram and Mahdavi Meymand (2015) employed SSIMM2 model (Olsen, 1991) to simulate scour around the side piers of a bridge. Baykal et al. (2015) highlighted the importance of including suspended load in sediment transport models for scouring around a circular pier. Omara et al. (2019) utilized FLOW-3D to investigate local scour around bridge piers of various shapes, including circular, rectangular, and square geometries. Fox and Feurich (2019)

also used FLOW-3D to study the local scour around circular and diamond-shaped structures. The novelty of their study was that to reduce the simulation time, they first developed a model without an erodible bed to establish steady-state conditions and subsequently used the results as the initial condition for their local scour simulation. Choufu et al. (2019) studied the local scour around groynes of different sizes using FLOW-3D. Jalal and Hassan (2020) also employed FLOW-3D to study the local scour around a circular bridge pier and conducted a sensitivity analysis on the mesh size. Yang et al. (2021) investigated the local scour around a specific type of bridge pier, known as Tri-USAF, utilizing FLOW-3D. Liu et al. (2022) developed a 3D finite element model to study local scour around two vertical piles with different arrangements.

All aforementioned studies were conducted under steady-state conditions. However, literature on the numerical modelling of sediment transport under unsteady flow conditions is more limited. Ahmad et al. (2018, 2020) employed the REEF3D model (Bihs et al., 2018) to investigate the local scour around a single pier and multiple piers with various arrangements under the effects of breaking waves. Quezada et al. (2018) also utilized the REEF3D model to study the local scour around piles under unsteady and oscillatory flow conditions. Samma et al. (2020) examined scour induced by a wall jet, representing the bottom outlets of dams, downstream of the wall using FLOW-3D. April-LeQuéré et al. (2020) compared the performances of FLOW-3D and Delft3D by Deltares (2025) in simulating local scour around a column installed on a sloped beach. Deng et al. (2022) studied local scour around a new type of bridge pier foundation, referred to as the coconut tree foundation, under wave-current action using FLOW-3D. Margalit et al. (2023) utilized the MIKE3 model developed by the Danish Hydraulic Institute (DHI, 2025) to investigate local scour around a circular bridge pier under combined wave and current action.

However, as mentioned above, because most available empirical equations for calculating sediment discharge were derived under steady-state flow conditions, their applicability to unsteady flow conditions remains uncertain. Consequently, researchers have developed alternative methodologies for sediment transport modelling, which are still under development and require further research. Kim et al. (2014) developed a 3D Lagrangian model to study the local scour around two adjacent cylinders under unsteady flow conditions. Ota et al. (2017) developed a three-dimensional hybrid Eulerian-Lagrangian model to simulate local scour around a weir-type structure by employing an Eulerian approach for the hydrodynamic solver and suspended load movement and a Lagrangian approach for the bed material movement. Cheng et al. (2017) introduced a new approach for simulating sediment transport problems by treating the sediment phase as a non-Newtonian fluid with specific characteristics and employing a multiphase approach for simulating the fluid and sediment phases. This model, known as SedFoam, was implemented within the OpenFOAM framework. Following this development, multiple studies have investigated its application in various cases, including Nagel et al. (2020), who applied this approach to simulate the local scour around a circular pier. Although these Lagrangian and multiphase approaches are grounded in more sophisticated physics, further research is required to fully understand their capabilities, and there remains a preference for utilizing traditional methods.

To the best of authors' knowledge, around walls, no study has assessed the performance of numerical models in simulating local scour under unsteady dam-break bores. Accordingly, the primary objective of this study was to assess the performance of two commonly used numerical tools in simulating the local scour around walls induced by turbulent unsteady dam-break bores. The software packages investigated in this study were MIKE3 Hydrodynamic/Sand Transport (HD/ST) and FLOW-3D. To accomplish this objective, first, a series of experimental tests were conducted in the large Dam-Break Flume of the Water Resources Laboratory at the University of Ottawa, Canada. Next, the numerical experiments were simulated, reproducing these laboratory tests and the numerical results obtained from each software were analyzed in terms of the

hydrodynamic characteristics of dam-break bores and the associated local scour around the wall.

5.3 Methodology

5.3.1 Experimental Setup

To investigate dam-break bore induced local scour around walls, a comprehensive program of experimental tests was conducted in the large Dam-Break Flume at the University of Ottawa, Canada. The flume measures 30.3 m in length, 1.5 m in width, and 1.5 m in height. It comprises several sections, as illustrated in the schematic presented in Figure 5.1. A wall model with dimensions of 0.3 m by 0.1 m, with the longer side perpendicular to the flow direction was installed in a sediment bed. The impoundment depth in the upstream reservoir secured by a rapidly-opening swing gate was 0.7 m. The median grain size (d_{50}) of the sand was 0.11 mm.

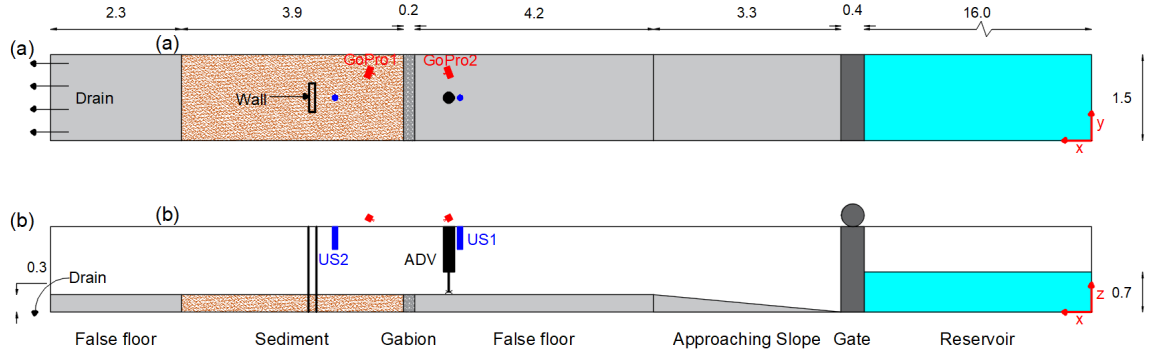

Figure 5.1: (a) Top view and (b) side view schematics of the flume (units in meters, not at scale)

A set of instruments, including two Ultrasonic Sensors (US) and one Acoustic Doppler Velocimeter (ADV) were installed along the flume near the structure to measure various flow characteristics. The positions of these instruments are shown in Figure 5.1. Two GoPro cameras, respectively facing the upstream and downstream sides of the flume, were positioned in the flume to visually capture the general pattern of the flow. Additionally, two wire cameras were installed inside the structure to capture the time evolution of scour depth around the structure. The final (residual) bathymetry of the sediment bed was measured using a Light Detection and Ranging (LiDAR) scanner at the end of each test. One of the important findings of the study was that maximum scour depth occurred at the upstream corner of the wall model. Figure 5.2 shows a snapshot of the sediment section before and after the test.

5.3.2 Numerical Models

Two three-dimensional numerical models were employed to simulate dam-break bore induced local scour around a wall: MIKE3 HD/ST (DHI, 2025) and FLOW-3D (Flow Science, 2019). Both models solve the Navier-Stokes equations, comprising the continuity equation and three non-hydrostatic momentum equations, coupled with sediment-transport and bed-evolution modules, enabling simulation of complex free-surface flows and sediment mobility.

FLOW-3D formulates these equations in Cartesian coordinate systems. Although it only supports regular cubic mesh elements, complex geometries are resolved using the Fractional Area/Volume Obstacle Representation (FAVOR) method proposed by Hirt and Sicilian (1985), which accurately represents solid boundaries within a structured grid. The model also allows

Figure 5.2: Snapshots of the sediment section (a) before and (b) after the test

for nested mesh blocks to refine the resolution near regions of interest. MIKE3 HD/ST, on the other hand, supports both σ and hybrid $\sigma - z$ vertical coordinate systems, enabling flexible specification of layer thicknesses along the depth. In the present study, the σ-coordinate system was adopted because the primary objective was to resolve the terrain elevation and the associated near-bed hydrodynamic and sediment processes. Since σ-coordinates are terrain-following, they naturally align the vertical layers with the bed geometry, making them more suitable for representing the evolving bed profile in the dam-break bore-induced scour problem. As a result, the additional complexity of a hybrid $\sigma - z$ system was not required. In the horizontal plane, it supports both structured and unstructured variable-size meshes.

After conducting a mesh-sensitivity analysis, the optimal horizontal resolutions were selected to balance numerical accuracy and computational efficiency (Table 5.1). It was found that the 0.5 cm refinement in the element size for the gabion and sand section mesh in FLOW-3D increased the simulation time significantly. The average simulation time for the MIKE3 HD/ST models was around 8.5 hours while for the FLOW-3D simulations, with 0.5 cm refinement, it was about 28 hours. Figure 5.3 illustrates the horizontal mesh used in each model. It should be noted that since MIKE3 HD/ST only accepts a single mesh, a triangular transition was required to connect every two quadrilateral mesh areas.

Table 5.1: Horizontal element sizes used in the studied numerical models

Section	**Element Size (cm)**	
	MIKE3 HD/ST	**FLOW-3D**
Reservoir and approaching slope	5×5	
False floor 1	3×3	
Gabion and sand section	1.5×1.5	1.0×1.0
False floor 2	5×5	

Modelling Approach

The numerical investigation comprised three sequential stages, each designed to isolate the effect of a specific modelling component while keeping the others fixed.

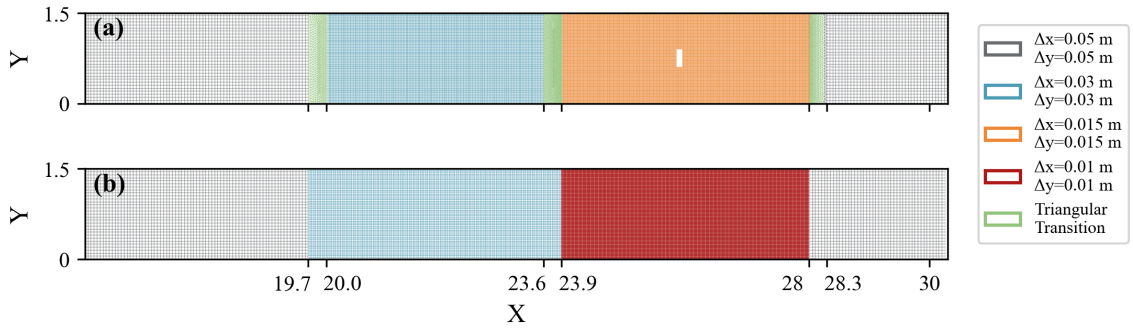

Figure 5.3: Horizontal mesh used in (a) MIKE3 HD/ST and (b) FLOW-3D simulations

- Stage 1: Turbulence closure model sensitivity
- Stage 2: Vertical mesh configuration sensitivity
- Stage 3: Sediment transport model sensitivity

For each software, a baseline configuration was derived from prior studies on local scour around columns, as no previous numerical study has addressed local scour around walls under unsteady flow conditions. Consequently, the present research extends the applicability of existing frameworks to wall geometries subjected to transient dam-break bores. For MIKE3 HD/ST, the base configuration followed the study by Margalit et al. (2023), and for FLOW-3D, the setup of the study by April-LeQuéré et al. (2020) was adopted. Each configuration was subsequently modified to accommodate the wall geometry and the rapidly varying hydrodynamics of dam-break bores. Figure 5.4 summarizes the steps undertaken in this study.

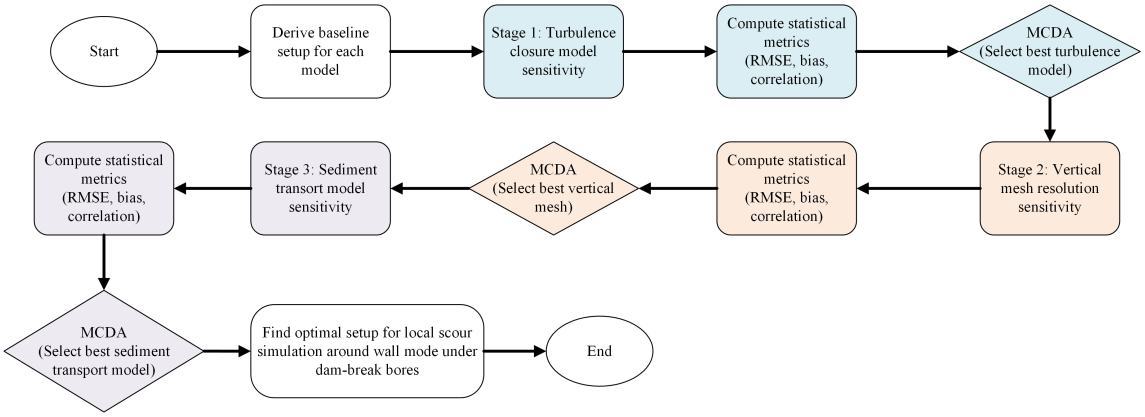

Figure 5.4: Workflow of the three-stage numerical investigation

Stage 1: Turbulence Closure Model Sensitivity

Both MIKE3 HD/ST and FLOW-3D were tested with $k-\varepsilon$, $k-\omega$, and LES turbulence models. For this stage, sediment transport was represented by a fixed baseline equation: Extended Engelund and Fredsøe (Roulund et al., 2005) in MIKE3 HD/ST, according to the study by Margalit et al. (2023), and Nielsen (1992) in FLOW-3D, following the study by April-LeQuéré et al. (2020). The turbulence closure providing the closest agreement with experimental data was retained for the subsequent stages.

Stage 2: Vertical Mesh Configuration Sensitivity

Using the optimal turbulence model identified in Stage 1, vertical-mesh sensitivity tests were performed for both models. The vertical arrangement yielding the best accuracy was adopted for Stage 3. In MIKE3 HD/ST, vertical discretization was represented by 10, 15, and 20 σ-layers, with extremely fine resolution (vertical stretching ratios of 24) near bed and fine resolution near surface (vertical stretching ratios of 4.8) as shown in Figure 5.5.

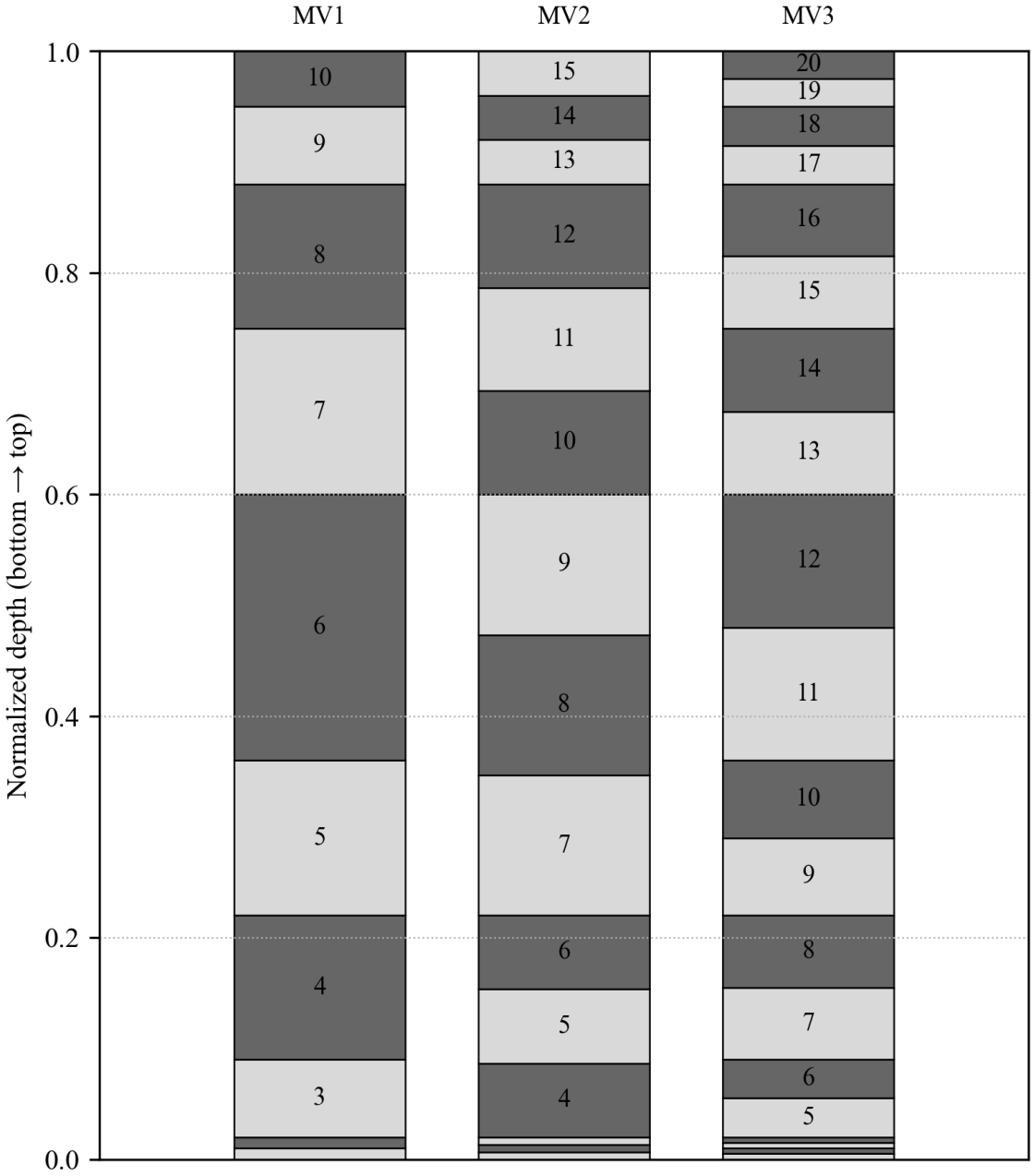

Figure 5.5: Vertical mesh configurations used in MIKE3 HD/ST

In FLOW-3D, a structured Cartesian mesh was used near the wall with an initial uniform vertical resolution of 1 cm. To refine the grid near the bed, a mesh plane was added at the bed elevation (z = 0.3 m), where finer cell heights of 0.75 cm and 0.5 cm were prescribed for the FV2 and FV3 cases, respectively. When a horizontal mesh plane is introduced, FLOW-3D does

not create a separate nested mesh block and instead, it adjusts the cell heights within the same mesh block while keeping the total number of vertical cells constant. The software enforces the specified resolution at the mesh plane location and then increases the cell size linearly away from the plane in both upward and downward directions. The background resolution (1 cm) is recovered halfway between the mesh plane and each boundary. Beyond these transition points, the cells continue to grow gradually such that the total domain height is preserved. As a result, the cells located farther from the bed become slightly larger (1.2 cm for FV2 and 1.5 cm for FV3), which explains the skewed appearance of the upper layers. Figure 5.6 illustrates the three tested vertical resolution profiles and the associated transitions toward the background spacing.

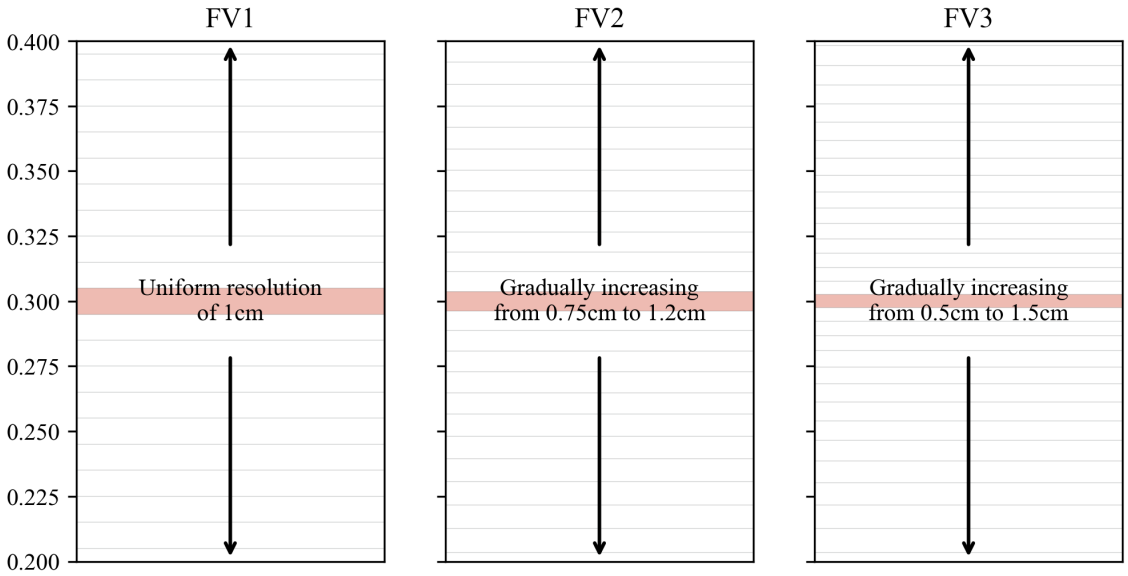

Figure 5.6: Vertical mesh resolutions tested in FLOW-3D

The vertical arrangement yielding the best accuracy was adopted for Stage 3.

Stage 3: Sensitivity to Sediment Transport Equation

With the optimal turbulence model and vertical configuration fixed, both models were tested with multiple bedload sediment-transport formulations. Table 5.2 presents the tested abbreviations used in this study's tests nomenclature for each sediment discharge equation.

Table 5.2: Abbreviations used for each sediment discharge equation used in the tests nomenclature

Sediment Discharge Equation	Abbreviation	Software
Meyer-Peter and Müller (1948)	MPM	MIKE3 HD/ST, FLOW-3D
Engelund and Fredsøe (1976)	EF	MIKE3 HD/ST
Van Rijn (1984a)	VR	MIKE3 HD/ST, FLOW-3D
Nielsen (1992)	N	FLOW-3D
Extended Engelund and Fredsøe (Roulund et al., 2005)	EEF	MIKE3 HD/ST

This stage quantified the influence of sediment-transport formulation on scour evolution under unsteady dam-break conditions.

The Extended Engelund and Fredsøe model (Roulund et al., 2005) is a two-dimensional generalization of the classical one-dimensional formulation of Engelund and Fredsøe (1976), specifically developed for integration into fully three-dimensional hydrodynamic solvers such as MIKE3 HD/ST. This formulation enables the model to resolve sediment motion as a vector quantity influenced by both the magnitude and orientation of the local flow field, while dynamically updating the bed topography through sediment-mass conservation. The two-dimensional nature of this formulation makes it particularly suitable for implementation within three-dimensional hydrodynamic models. Compared with traditional one-dimensional models, it provides a more physically consistent treatment of slope-dependent transport processes and grain mobility under complex flow conditions.

Model Performance Evaluation and Test Naming

A Multi-Criteria Decision Analysis (MCDA) framework (Ishizaka and Nemery, 2013) was used to evaluate and rank the numerical configurations at each stage. MCDA enables multiple performance metrics to be integrated into a single composite score, allowing consistent comparison of model behaviour across hydrodynamic and morphodynamic variables. In this study, five parameters were considered: water-surface elevation at US1 and US2, flow velocity at ADV, and scour depths at the upstream corner and centre of the front face. For each parameter, three statistical metrics were computed: RMSE, bias, and Pearson correlation coefficient (ρ).

To ensure comparability across metrics with different units and scales, each metric was normalized to a dimensionless score between 0 and 1. For RMSE, where lower values indicate better performance, normalization was performed using:

$$\tilde{s}_{m,p,c} = 1 - \frac{s_{m,p,c} - \min(s_{m,p,c})_m}{\max(s_{m,p,c})_m - \min(s_{m,p,c})_m} \tag{5.1}$$

where $s_{m,p,c}$ denotes the score of each model (m), for each parameter (p) using each statistical metric (c) and $\tilde{s}_{m,p,c}$ is the normalized score. It should be noted that in the context of MCDA analysis, the normalization is conducted over the statistical metrics of different scenarios and therefore, the normalized RMSE scores are different from the well-known statistical metric Normalized RMSE (NRMSE).

For the correlation coefficient, where higher values are preferable, normalization was applied as below:

$$\tilde{s}_{m,p,c} = \frac{s_{m,p,c} - \min(s_{m,p,c})_m}{\max(s_{m,p,c})_m - \min(s_{m,p,c})_m} \tag{5.2}$$

For the bias, where the ideal value is zero and deviations in either direction indicate model error, the normalization was performed based on the absolute value of bias as below:

$$\tilde{s}_{m,p,c} = 1 - \frac{|s_{m,p,c}| - \min(|s_{m,p,c}|)_m}{\max(|s_{m,p,c}|)_m - \min(|s_{m,p,c}|)_m} \tag{5.3}$$

The normalized scores for each parameter were then aggregated using equal weights for the three metrics (Equation 5.3.2):

$$\tilde{s}_{m,p} = \frac{1}{3} \sum_{c=1}^{3} \tilde{s}_{m,p,c} \tag{5.4}$$

To reflect the relative importance of each parameter in the context of scour prediction, a weighted aggregation was applied to compute the final performance score for each model as below:

$$S_m = \sum_{p=1}^{5} w_p \tilde{s}_{m,p} \tag{5.5}$$

where w_p denotes the weight assigned to parameter p, with values of 0.15 for the water surface elevations (US1 and US2) and flow velocity (ADV), 0.25 for the scour depth at the center of the front face, and 0.3 for scour depth at the upstream corner of the wall. These weights were particularly chosen to reflect the focus of the study on evaluating the performance of the models in terms of local scour prediction, and more specifically, maximum scour depth at the upstream corner of the wall. The final score S_m represents the overall performance of model m relative to the other models considered at each stage, with higher values indicating better agreement with the experimental observations.

The nomenclature of each test includes four parts. The first component identifies the numerical model, denoted as either M3 for MIKE3 HD/ST or F3 for FLOW-3D. The second component represents the turbulence model, which may be $k\varepsilon$, $k\omega$, or LES. The third part corresponds to the vertical mesh resolution as shown in Figure 5.5 and Figure 5.6. Finally, the fourth specifies the sediment discharge equation employed in the simulation, as defined in Table 5.2.

5.4 Results

5.4.1 Stage 1: Turbulence Model Sensitivity

Three turbulence closures ($k-\varepsilon$, $k-\omega$, and LES), were evaluated in both the MIKE3 HD/ST and FLOW-3D models to assess their ability to reproduce the hydrodynamics and sediment-transport processes induced by the dam-break bore. The analysis focused on two aspects: (1) the accuracy of hydrodynamic predictions and (2) the reproduction of scour evolution around the wall. Figure 5.7 presents the comparison of the numerical simulations with the experimental data for all five parameters.

Hydrodynamic Response

All turbulence models reproduced the overall propagation of the dam-break bore with reasonable accuracy. The numerical model results were exported at 0.5 s intervals over the 60 s simulation. For the hydrodynamic comparison, the 120 numerical data points were resampled to the experimental time (300 Hz sampling frequency) using cubic spline interpolation to ensure a consistent temporal alignment between the datasets. The predicted water-surface elevations at US1 and US2 and the velocity time series at the ADV location captured the rapid bore arrival and subsequent attenuation, with differences in peak timing and amplitude among the turbulence models. At US1, the phase shift between the modelled and measured peak free-surface elevation ranged from 2.3 s to 4.1 s, and the associated amplitude differences ranged from 0.6 cm to 9.7 cm for M3-LES-MV1-EEF simulation. At US2, the phase shift ranged from 2.3 s to 7.3 s, with amplitude differences up to 4.3 cm. At the ADV location, the phase shift was approximately 0.8 s among all cases, and the amplitude discrepancies ranged from 0.07 m/s to 0.38 m/s. Table 5.3 summarizes all statistical metrics. Overall, FLOW-3D exhibited lower RMSE and bias

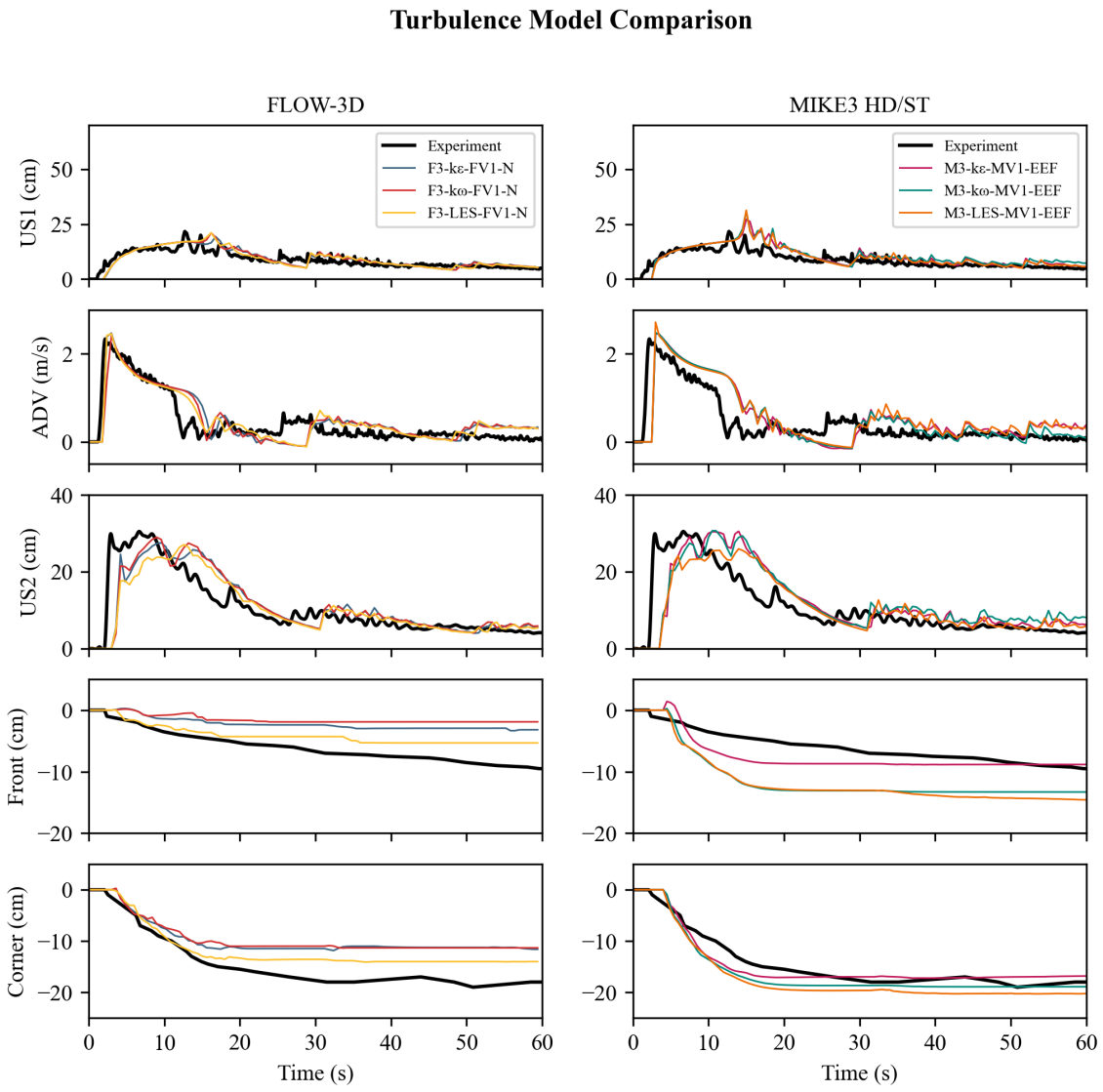

Figure 5.7: Comparison of experimental measurements with numerical simulations for FLOW-3D (left column) and MIKE3 HD/ST (right column) across the three turbulence models, where the rows respectively present the free-surface elevation at US1, velocity at the ADV location, free-surface elevation at US2, scour depth at the centre of the front face, and scour depth at the upstream corner.

values across the hydrodynamic variables, which can be attributed to its VOF-based free-surface capturing method that better resolves large deformations and turbulence-induced fluctuations during bore impact.

Table 5.3: Statistical indicators for the simulations against the experimental hydrodynamics measurements

		FLOW-3D			MIKE3 HD/ST		
		k − ε	**k − ω**	**LES**	**k − ε**	**k − ω**	**LES**
US1	**RMSE (cm)**	2.18	2.33	2.31	3.20	3.49	3.16
	Bias (cm)	0.54	0.58	0.48	1.55	1.87	1.33
	ρ	0.835	0.873	0.879	0.848	0.812	0.842
ADV	**RMSE (m/s)**	0.33	0.33	0.30	0.47	0.45	0.47
	Bias (m/s)	0.06	0.05	0.05	0.13	0.09	0.15
	ρ	0.835	0.823	0.855	0.732	0.753	0.731
US2	**RMSE (cm)**	5.12	5.16	5.25	6.18	6.23	5.82
	Bias (cm)	0.39	0.50	-0.27	1.23	1.54	0.26
	ρ	0.789	0.792	0.766	0.731	0.712	0.715

Scour Evolution

The temporal evolution of scour depth at the upstream corner and front face is presented in Figure 5.7. In FLOW-3D, LES performed the best prediction of scour depth in terms of initial scouring induced by the arrival of bore front, while it was not able to capture the ongoing scour depth evolution after the arrival of the secondary bores at the upstream corner of the wall (around the time 15s). On the other hand, the $k-\varepsilon$ model in MIKE3 HD/ST simulated the scour depth at both the center of the front face and the upstream corner well, although the time to reach the final scour depth at the center of the front face was shorter than the experimental data. Table 5.4 summarizes the statistical metrics for all simulations at the center of the front face and upstream corner of the wall.

Table 5.4: Statistical indicators for the simulations against the experimental sediment transport measurements

		FLOW-3D			MIKE3 HD/ST		
		k − ε	**k − ω**	**LES**	**k − ε**	**k − ω**	**LES**
Front	**RMSE (cm)**	4.08	4.88	2.21	2.12	5.66	5.94
	Bias (cm)	3.76	4.48	1.89	-1.42	-5.16	-5.52
	ρ	0.960	0.898	0.955	0.838	0.864	0.910
Corner	**RMSE (cm)**	5.36	5.48	3.17	1.54	2.04	2.77
	Bias (cm)	4.85	5.02	2.82	-0.08	-1.49	-2.41
	ρ	0.967	0.980	0.980	0.957	0.979	0.978

MCDA-Based Performance Index

The statistical metrics were aggregated for each software, according to the Equations 5.3.2 to 5.3.2, to yield a single performance index S_m. Figure 5.8 presents the normalized statistical metrics for the FLOW-3D simulations obtained using Equations 5.3.2 to 5.3.2. It can be seen that LES turbulence model had the best performance in simulating flow velocity and local scour depths at both locations. In terms of correlation of the scour depths, although it did not get the highest score, but the score is above 90% which shows the model was able to reproduce the same pattern of the scour depth well.

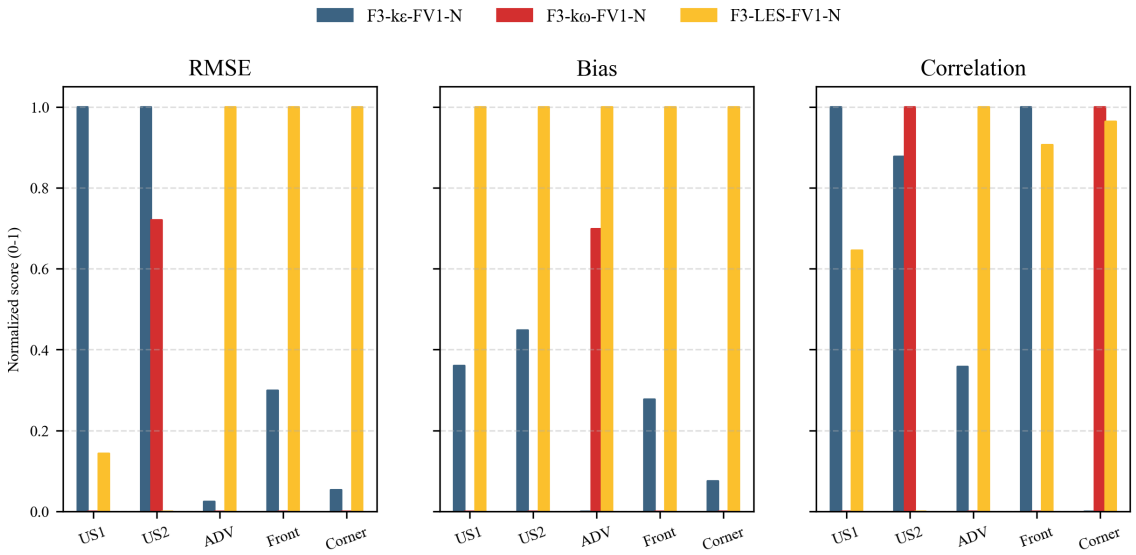

Figure 5.8: Normalized statistical metrics for the FLOW-3D simulations for all parameters

Using the normalized metrics, the aggregated score for each model at each location was calculated using Equation 5.3.2. For this aggregation, all normalized metrics of each model at each location were averaged with equal weights. Figure 5.9 presents the aggregated scores for each model at each location.

Finally, the aggregated normalized score among all locations were averaged using the weights defined in Section 5.3.2 to identify the best performing model. Figure 5.10 shows the results for the FLOW-3D simulations, proving that LES showed the best overall performance in terms of both hydrodynamic and sediment transport simulations of local scour around a wall. Therefore, this turbulence model was selected to be used in the further simulations.

The same methodology was applied to the MIKE3 HD/ST simulations. For the sake of brevity, only the results of the final scores are presented in Figure 5.11. According to the results, the $k-\varepsilon$ turbulence model with the highest score was selected for the next stages simulations in MIKE3 HD/ST. It is noteworthy that the best-performing turbulence model in this study ($k-\varepsilon$) differs from the $k-\omega$ model previously reported in the literature (Margalit et al., 2023) as the most effective for simulating local scour around columns. This outcome underscores the importance of refining numerical scour models according to the geometry of the structure under investigation.

5.4.2 Stage 2: Vertical Mesh Configuration Sensitivity

The selected turbulence models for each software were used in the second stage to analyze the influence of vertical mesh resolution on the simulation results. Three different vertical mesh

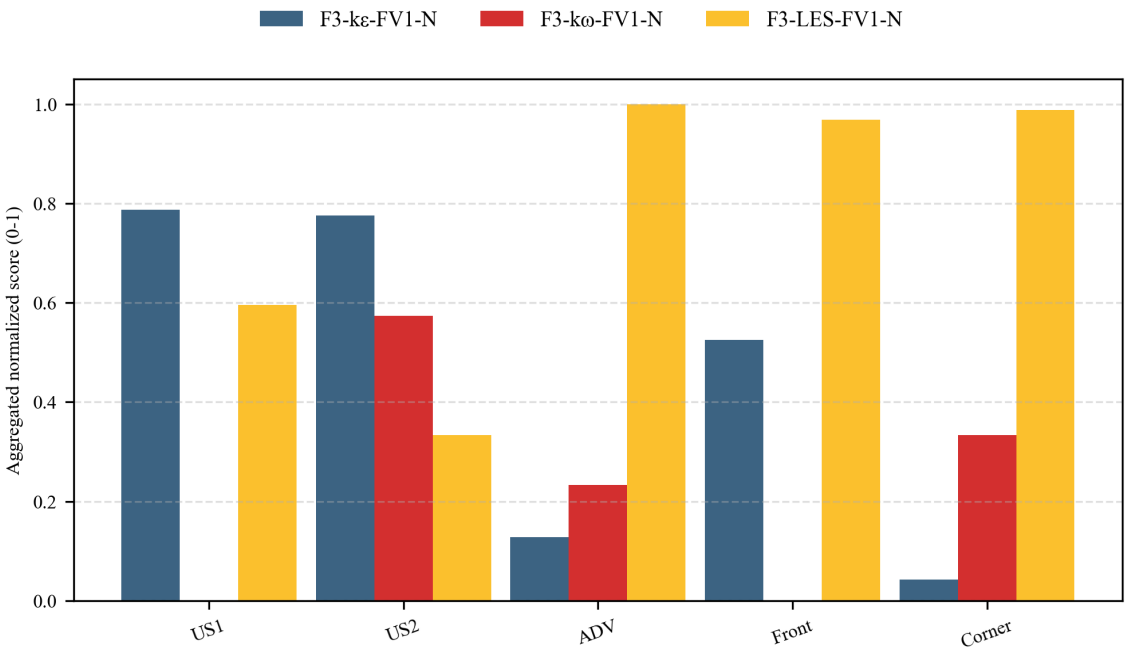

Figure 5.9: Model scores at each location obtained by averaging all normalized statistical metrics for each model and location

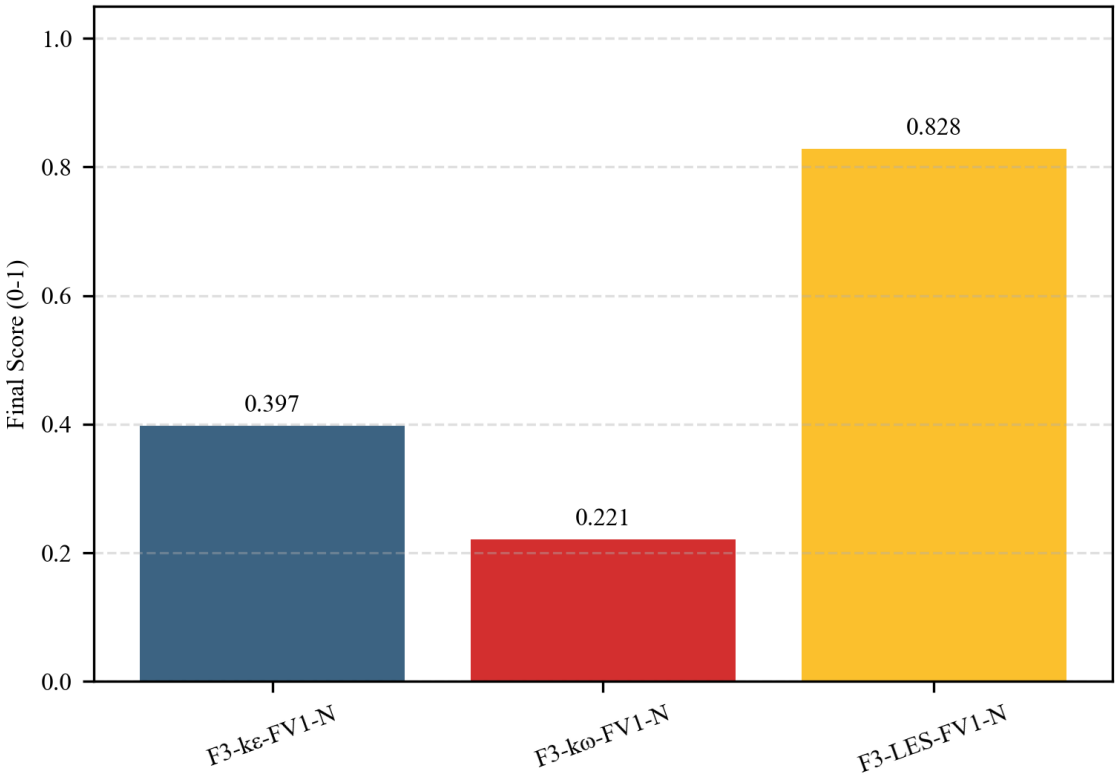

Figure 5.10: Final score of each turbulence model in FLOW-3D simulations

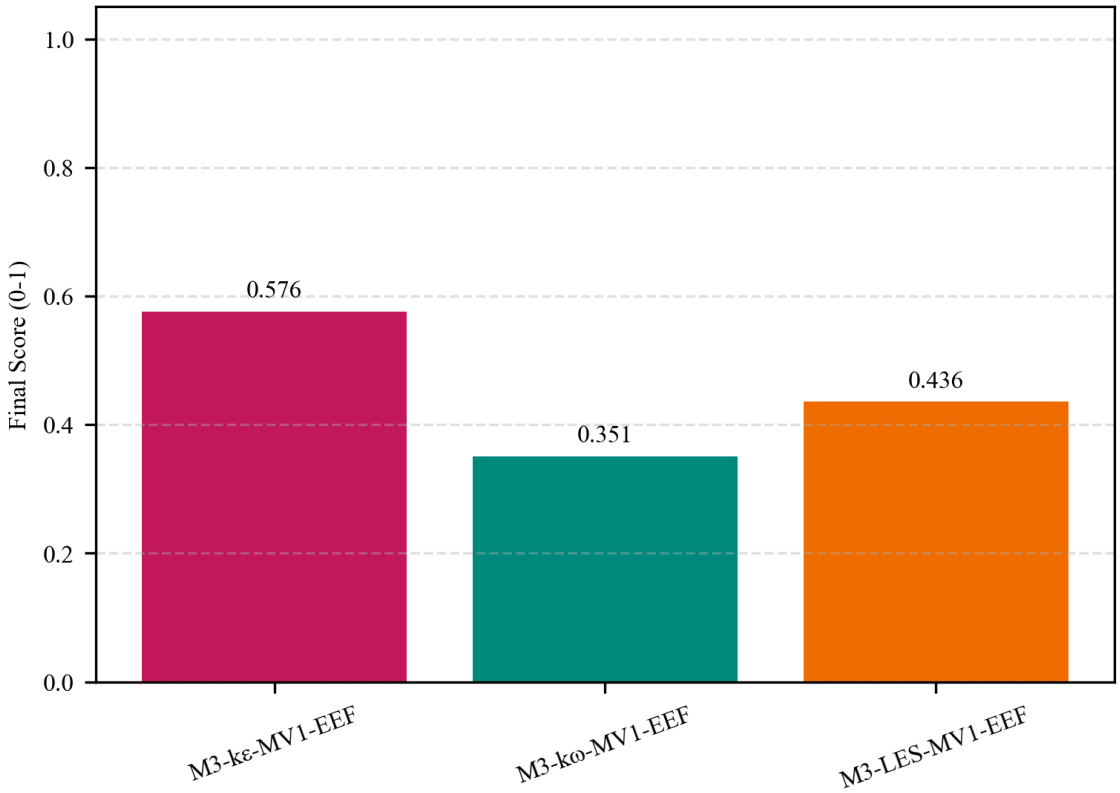

Figure 5.11: Final score of each turbulence model in MIKE3 HD/ST simulations

configurations were tested according to the discretization features available in each solver. For MIKE3 HD/ST, the tested σ-layer distributions were presented in Figure 5.5, and for FLOW-3D the corresponding Cartesian mesh refinements near the bed were shown in Figure 5.6.

Hydrodynamic Response

The results of the vertical mesh sensitivity analysis for both FLOW-3D and MIKE3 HD/ST are presented in Figure 5.12. Overall, both solvers exhibited limited sensitivity of the simulated flow characteristics to vertical mesh refinement. The bore arrival, peak water-surface elevation, and subsequent attenuation were reproduced consistently across all tested configurations with negligible difference.

In FLOW-3D, all three configurations yielded almost identical hydrodynamic responses, with maximum differences of 1% and 2% respectively at US1 and ADV. A minor difference was observed in the initial bore peak at US2, where the flow impacts directly on the wall. Here, a maximum phase shift of four seconds in the timing of the peak among the three simulations was observed, indicating that subtle differences in near-bed momentum transfer and vertical advection affected the exact arrival of the bore front. Beyond this event, the peak attenuation and secondary bores were nearly identical, showing that the finite-volume formulation provides adequate near-bed and free-surface resolution even at the coarsest vertical spacing.

In MIKE3 HD/ST, the results for US1 were nearly identical among the 10-, 15-, and 20-layer meshes, demonstrating numerical consistency in the upstream region. At the ADV location, all configurations reproduced the same velocity peak associated with the initial bore, while the highest-resolution case (20 layers) slightly underpredicted the secondary-bore velocities. At US2, where the bore reflects from and interacts with the wall, all three simulations captured the initial

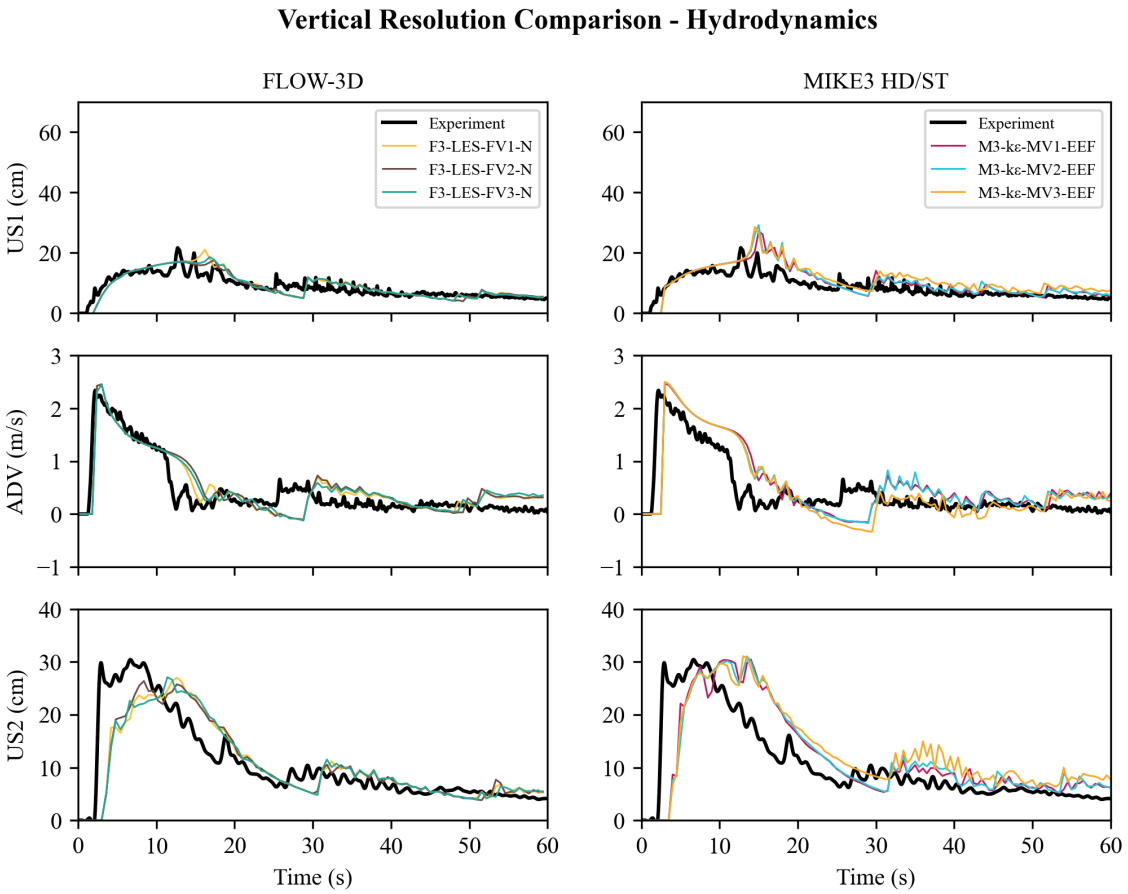

Figure 5.12: Comparison of the hydrodynamic responses for different vertical mesh configurations in FLOW-3D (left column) and MIKE3 HD/ST (right column)

bore with comparable accuracy (less than 0.5% difference in peak surface elevation). However, for the secondary bores the 20-layer mesh produced a modest overestimation of the surface elevation. This behaviour is consistent with known sensitivities of σ-coordinate models, where extremely thin vertical layers can amplify discretization errors in the vertical momentum and turbulence equations, particularly in regions with strong free-surface gradients or recirculation (Mellor et al., 1994; Stelling and Van Kester, 1994).

Overall, the differences observed across vertical resolutions remained minor for both solvers. These findings indicate that the hydrodynamic solutions are numerically robust with respect to vertical discretization.

Scour Evolution

The influence of vertical resolution on the predicted scour evolution is shown in Figure 5.13 for both FLOW-3D and MIKE3 HD/ST. Overall, both solvers reproduced the general pattern of scour development observed in the experiments, though their sensitivity to vertical resolution was more apparent.

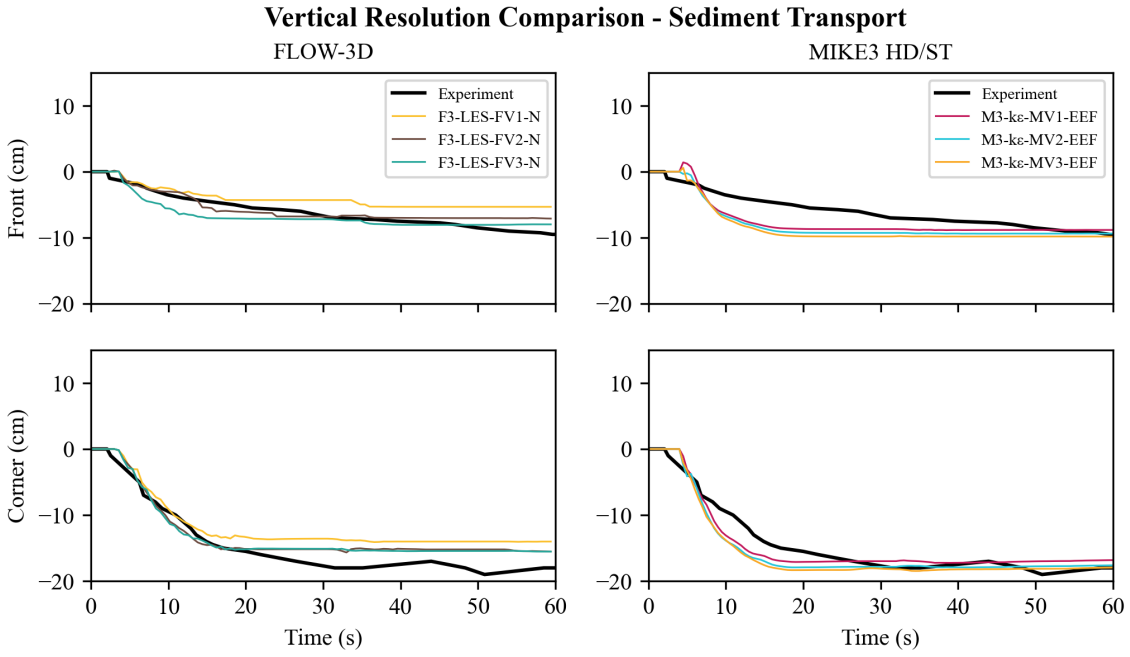

Figure 5.13: Comparison of the local scour depth predictions for different vertical mesh configurations in FLOW-3D (left column) and MIKE3 HD/ST (right column)

In FLOW-3D, the three tested near-bed resolutions (1.0 cm, 0.75 cm, 0.5 cm) produced similar overall scour trends at both the front and corner locations. The coarsest configuration (1 cm) slightly underpredicted the maximum scour depth, while the finest mesh (0.5 cm) overestimated the initial erosion rate immediately after the bore impact. This early-stage over-erosion reflects the model's high responsiveness to near-bed shear stress when the vertical velocity gradient is finely resolved by the LES formulation. These results indicate that FLOW-3D effectively captures the transient erosion mechanism driven by the impinging bore but tends to dissipate sediment transport at later stages as the flow decelerates.

In MIKE3 HD/ST, the predicted scour depths were consistent across the 10-, 15-, and 20-layer configurations, showing minimal mesh dependence. The only noticeable difference occurred during the early phase of scour at the front face, where the coarsest configuration (10

layers) exhibited a small, unrealistic deposition immediately after the bore arrival. This artifact diminished with increasing vertical resolution. Despite the overestimation of the initial scour rate, MIKE3 HD/ST more accurately reproduced the final scour depth than FLOW-3D, indicating that the σ-layer formulation effectively captured the long-term sediment redistribution even when the transient response was damped.

In summary, both models were relatively insensitive to vertical resolution in terms of final scour magnitude, but they differed in their temporal behavior. FLOW-3D more effectively reproduced the rapid initial scour caused by the incoming bore yet slightly underpredicted the final depth, whereas MIKE3 HD/ST captured the long-term equilibrium conditions with higher accuracy but overestimated the initial erosion rate.

MCDA-Based Performance Index

Same MCDA framework similar to the one used in stage 1 simulations was applied to the tests at this stage regarding the vertical mesh configuration. Figure 5.14 presents the final score S_m for the tests in MIKE3 HD/ST. The results showed that increasing the number of vertical layers did not produce a monotonic improvement in MIKE3 HD/ST performance. As illustrated in Figure 5.15, the simulations with finer vertical discretization (15 and 20 layers) exhibited a slight reduction in the peak bed-shear stress at the center of the front face during the arrival of the initial bore. This attenuation reflects the influence of cell-aspect-ratio-driven numerical damping inherent to the implicit solvers. As the number of vertical layers increases while maintaining the same horizontal grid size, the cells become increasingly anisotropic ($\Delta x/\Delta z \gg 1$), which enhances vertical coupling and forces stronger implicit diffusion to maintain numerical stability. The result is a dampened shear-stress response and a weaker near-bed acceleration during the highly transient bore impact. Although the 15-layer configuration produced the lowest peak shear stress, it achieved a higher overall MCDA score than the 20-layer case. This indicates that factors beyond instantaneous shear, such as improved representation of vertical pressure gradients and smoother turbulence dissipation also contributed to its better integrated performance. Overall, the coarser 10-layer mesh provided the best balance between numerical stability and physical fidelity, minimizing excessive damping while maintaining adequate resolution of the vertical velocity gradients driving sediment entrainment.

Figure 5.16 illustrates the results for the FLOW-3D tests. Similar to MIKE3 HD/ST, the influence of numerical damping caused by high cell aspect ratios is evident in FLOW-3D. However, the relatively small differences among the final scores indicate that this model is less sensitive to variations in vertical mesh resolution. This observation further underscores the importance of employing a robust evaluation framework to determine the best-performing scenario, as relying on a single decision metric may be insufficient when comparing complex simulations with closely matched results.

5.4.3 Stage 3: Sediment Transport Sensitivity

The third stage of the numerical analysis investigated the influence of the sediment discharge formulation on the predicted flow and scour characteristics. Both MIKE3 HD/ST and FLOW-3D were evaluated using their respective best-performing turbulence models and vertical mesh configurations obtained from the previous stages. Each model was tested with several empirical sediment discharge equations commonly applied in the modelling of local scour around hydraulic structures. These equations differ in their formulation of bed shear stress dependency and sediment mobility functions and thus are expected to yield different responses under unsteady dam-break forcing.

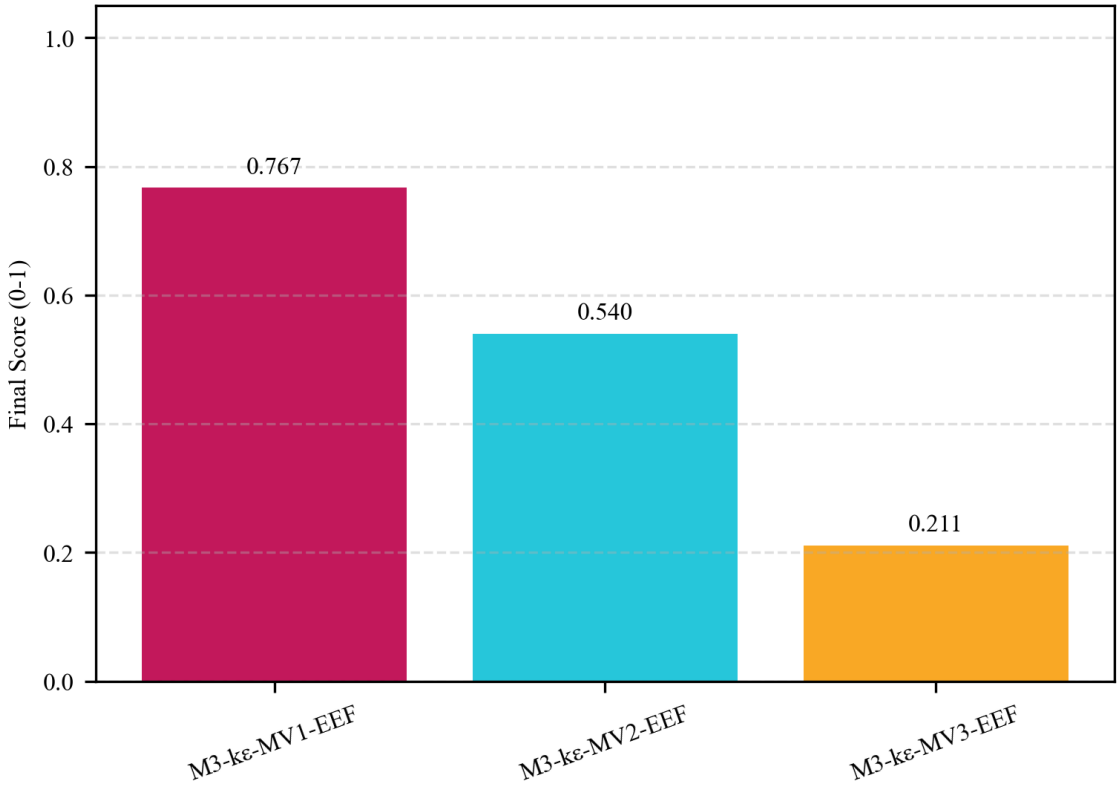

Figure 5.14: Final score S_m calculated for different layer thickness scenarios tested in MIKE3 HD/ST

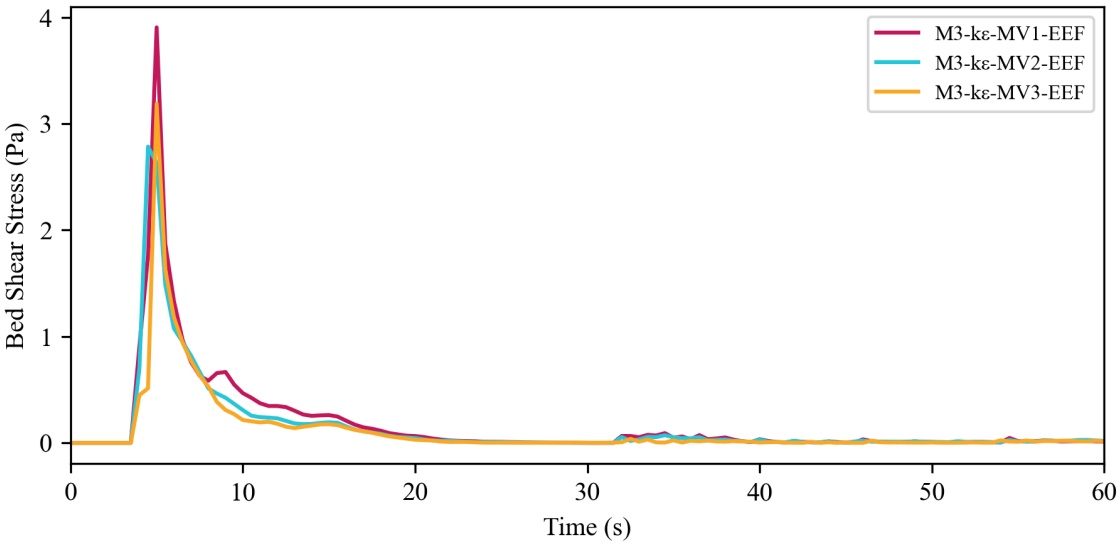

Figure 5.15: Timeseries of the bed shear stress for the three tested vertical mesh configurations in MIKE3 HD/ST

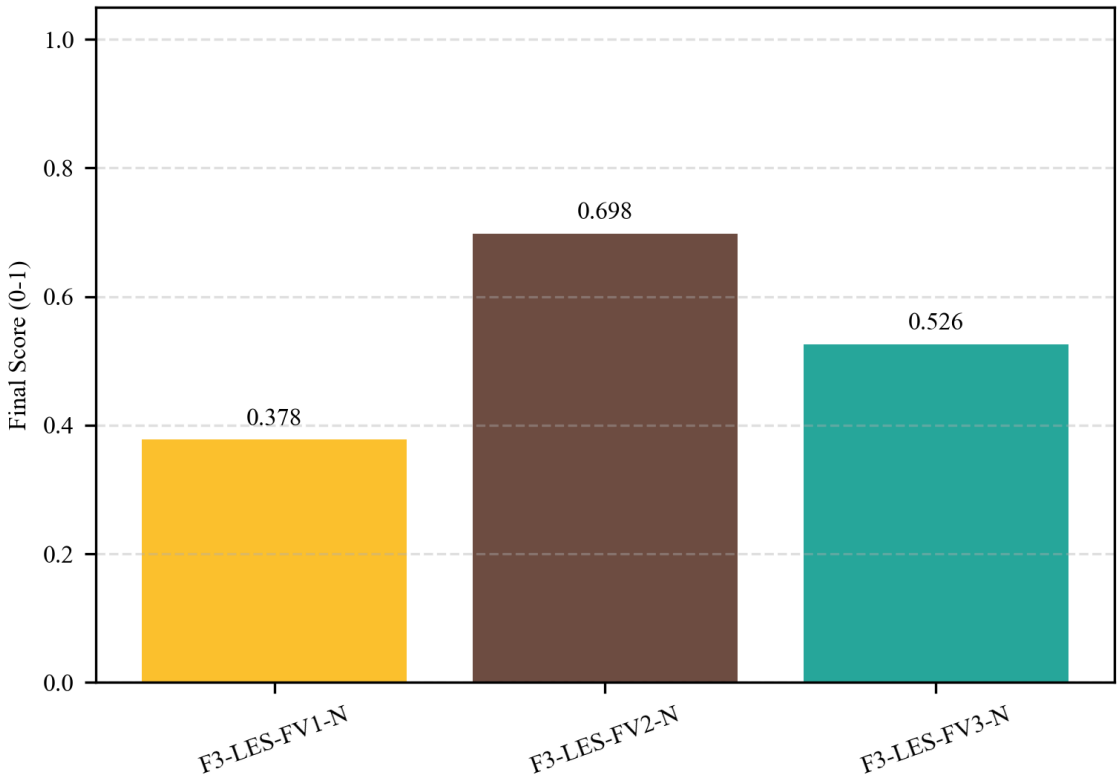

Figure 5.16: Final score S_m calculated for different near bed vertical resolutions tested in FLOW-3D

Hydrodynamic Response

Figure 5.17 compares the hydrodynamic timeseries obtained with the different sediment discharge formulations. FLOW-3D showed very limited sensitivity to the sediment discharge equation for this aspect. The water surface elevations and velocity traces were nearly indistinguishable across Nielsen (1992), Meyer-Peter and Müller (1948), and Van Rijn (1984a), with only a minor deviation at US2, located immediately in front of the wall, during the most turbulent phase of the bore impact. This weak dependence is consistent with FLOW-3D's Cartesian, VOF/LES framework, in which the near-bed shear field, and hence the bore kinematics, are primarily controlled by the resolved turbulence and pressure gradients. The comparatively small bathymetric adjustments that occurred during the short simulation window did not feed back strongly onto the free surface or flow velocity.

In MIKE3 HD/ST, the hydrodynamic signals were also broadly similar among sediment formulations, but a clearer, still modest, sensitivity was evident and increased toward the structure. Differences were smallest at US1, became slightly larger at ADV, and were most visible at US2. This trend reflects stronger morphodynamic-hydrodynamic feedback in the σ-coordinate RANS solver. Changes in predicted bedload flux modified the evolving bed geometry and effective near-bed roughness, which in turn altered local shear and pressure fields most noticeably where the bore impinges and reflects (US2). In other words, the same hydrodynamic solver sees slightly different instantaneous boundary conditions as each sediment discharge equation evolved the bed at a different rate, and that effect is most detectable closest to the wall.

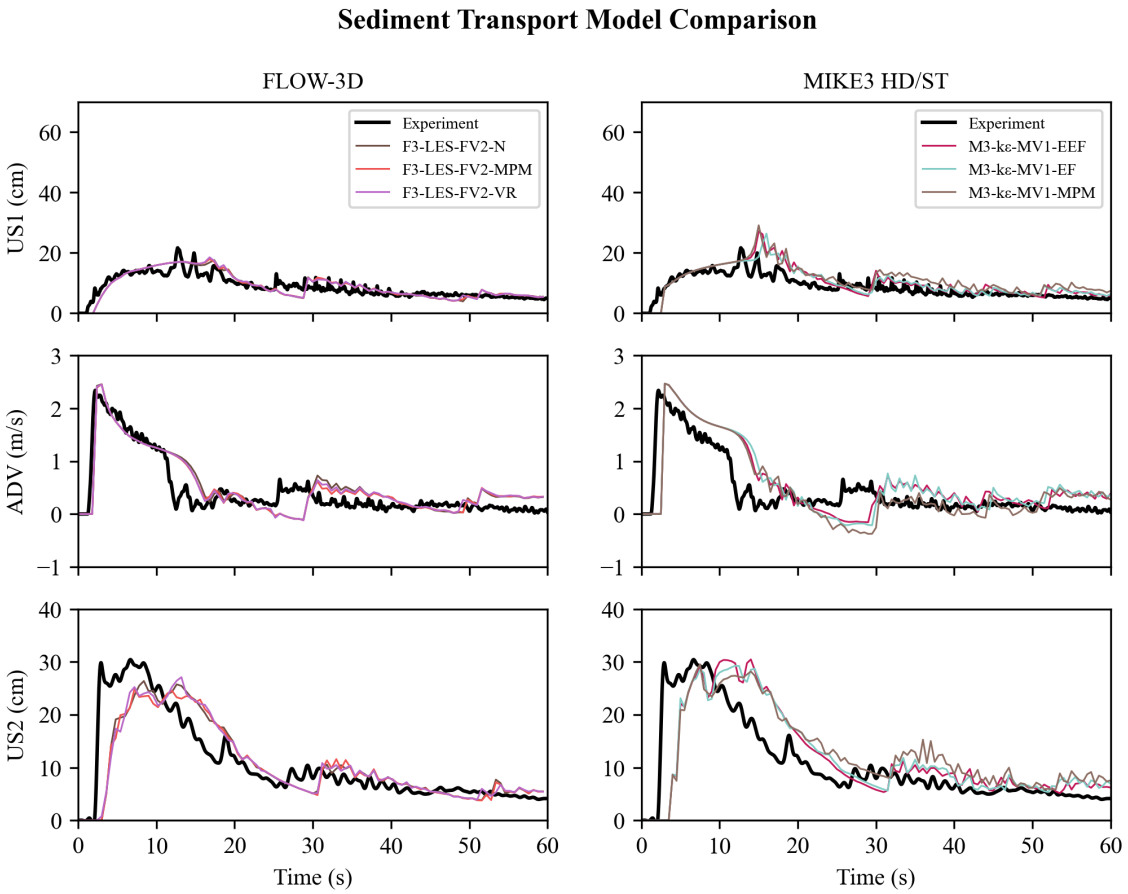

Figure 5.17: Comparison of the hydrodynamic responses for different sediment discharge equations in FLOW-3D (left column) and MIKE3 HD/ST (right column)

Scour Evolution

The predicted temporal evolution of scour depth at the upstream corner and at the center of the front face of the wall is presented in Figure 5.18 for both FLOW-3D and MIKE3 HD/ST. In general, both models captured the characteristic phases of scour development, i.e. rapid erosion following the initial bore impact and subsequent stabilization toward an equilibrium depth, although their sensitivity to the sediment discharge formulation and their temporal accuracy differed.

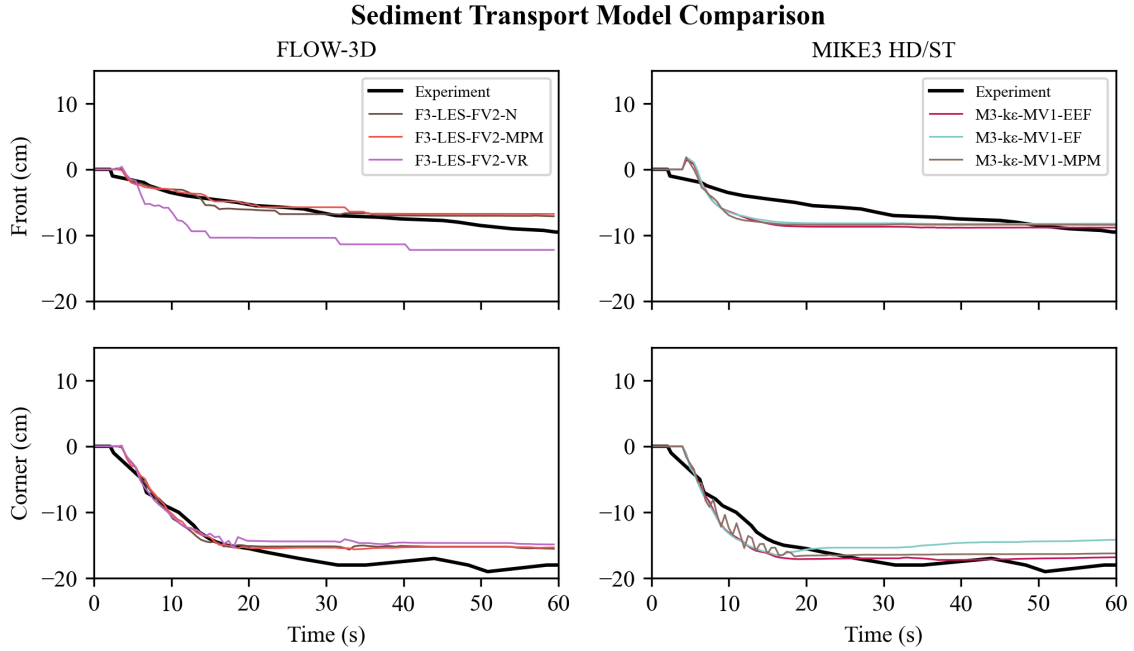

Figure 5.18: Comparison of the local scour depth predictions for different sediment discharge equations in FLOW-3D (left column) and MIKE3 HD/ST (right column)

In FLOW-3D, simulations using the Meyer-Peter and Müller (1948) and Nielsen (1992) formulations produced nearly identical scour-depth curves at both measurement locations. The only significant deviation occurred with the Van Rijn (1984a) equation, which yielded a much deeper scour hole at the front-face gauge. The exaggerated response can be attributed to the strong nonlinear dependence of the Van Rijn (1984a) formulation on the excess Shields parameter and also its inverse relationship to the d_* variable (Equation 5.4.3) which is a representative of the sediment grain size.

$$\mathbf{\Phi} = 0.053 d_*^{-0.3} \left(\frac{\theta}{\theta_c} - 1 \right)^2 .1 \tag{5.6}$$

At the stagnation line in front of the wall, short bursts of high bed shear stress occur. The Van Rijn (1984a) equation exaggerates these short-lived peaks, leading to excessive erosion. In contrast, at the corner where the horseshoe vortex forms, slope corrections to θ_{cr} reduces this exaggeration. As a result, all three formulations produced similar scour depths at the corner, despite differing results at the front face. In FLOW-3D, both the Meyer-Peter and Müller (1948) and Nielsen (1992) formulations captured the early scour development and erosion timing fairly well but underestimated the final equilibrium depth. This suggests that sediment transport gradually weakened as the bore lost energy. This trend aligns with FLOW-3D's dynamic

adjustment of the critical Shields parameter (Soulsby, 1997), which increases over time as the bed steepens and armors, thereby lowering sediment transport capacity in the later stages of the simulation.

In MIKE3 HD/ST, the simulation employing the Van Rijn (1984a) equation could not be completed due to numerical instability during the early stages of bed deformation. The instability likely resulted from the strong nonlinear coupling between the transport term and the σ-layer bedload solver under rapidly varying bed and flow conditions. Therefore, only results from the Extended Engelund-Fredsøe (Roulund et al., 2005), Engelund and Fredsøe (1976), and Meyer-Peter and Müller (1948) formulations are presented.

Among these, the scour evolution at the front face was nearly identical across the three equations, whereas larger differences were observed at the upstream corner. The Meyer-Peter and Müller (1948) simulation exhibited a brief oscillation in scour depth during the arrival of the initial bore but subsequently stabilized and aligned closely with the Extended Engelund-Fredsøe (Roulund et al., 2005) result. The Engelund and Fredsøe (1976) model underpredicted the residual scour depth more than the other two formulations. Compared with FLOW-3D, MIKE3 HD/ST predicted a faster initial scour rate but a more accurate residual (final) depth. This difference can be attributed to their treatment of sediment mobility thresholds. MIKE3 HD/ST employs a fixed critical Shields parameter, while FLOW-3D recalculates it dynamically following Soulsby (1997). The fixed value allows more immediate erosion when the bore impacts the structure but yields more stable long-term behavior as the flow decays.

Overall, both solvers demonstrated limited sensitivity of the scour evolution to the specific sediment discharge equation, except for the Van Rijn (1984a) formulation, which exhibited unrealistic front-face erosion in FLOW-3D and numerical instability in MIKE3 HD/ST. These results highlight the need for caution when applying Van Rijn (1984a) equation to unsteady dam-break flows.

MCDA-Based Performance Index

The final composite scores, shown in Figure 5.19 and Figure 5.20, reflect the overall agreement of each model configuration with the experimental data across all five evaluation parameters. In the FLOW-3D simulations, the Meyer-Peter and Müller (1948) and Nielsen (1992) formulations achieved close composite scores of 0.730 and 0.677, respectively, confirming their comparable predictive capability under unsteady dam-break forcing. In contrast, the Van Rijn (1984a) equation received a substantially lower score (0.164), primarily due to its significant overestimation of the scour depth at the center of the front face. This poor performance is consistent with the earlier discussion, where the nonlinear excess-stress term in the Van Rijn (1984a) formulation led to exaggerated sediment entrainment and unrealistic erosion patterns.

For the MIKE3 HD/ST model, the Extended Engelund-Fredsøe (Roulund et al., 2005) formulation produced the highest overall score (0.761), while the Engelund and Fredsøe (1976) and Meyer-Peter and Müller (1948) equations achieved very close values (0.477 and 0.463, respectively). This higher score confirms the necessity of using two-dimensional sediment discharge equations for local scour simulation around walls under highly turbulent tsunami-like dam-break bores.

Across both solvers, the MCDA results reinforce the qualitative findings from the scour-evolution analyses. The Meyer-Peter and Müller (1948) and Extended Engelund-Fredsøe (Roulund et al., 2005) formulations yielded the most accurate and stable predictions, whereas the Van Rijn (1984a) equation performed poorly in FLOW-3D and proved numerically unstable in MIKE3 HD/ST.

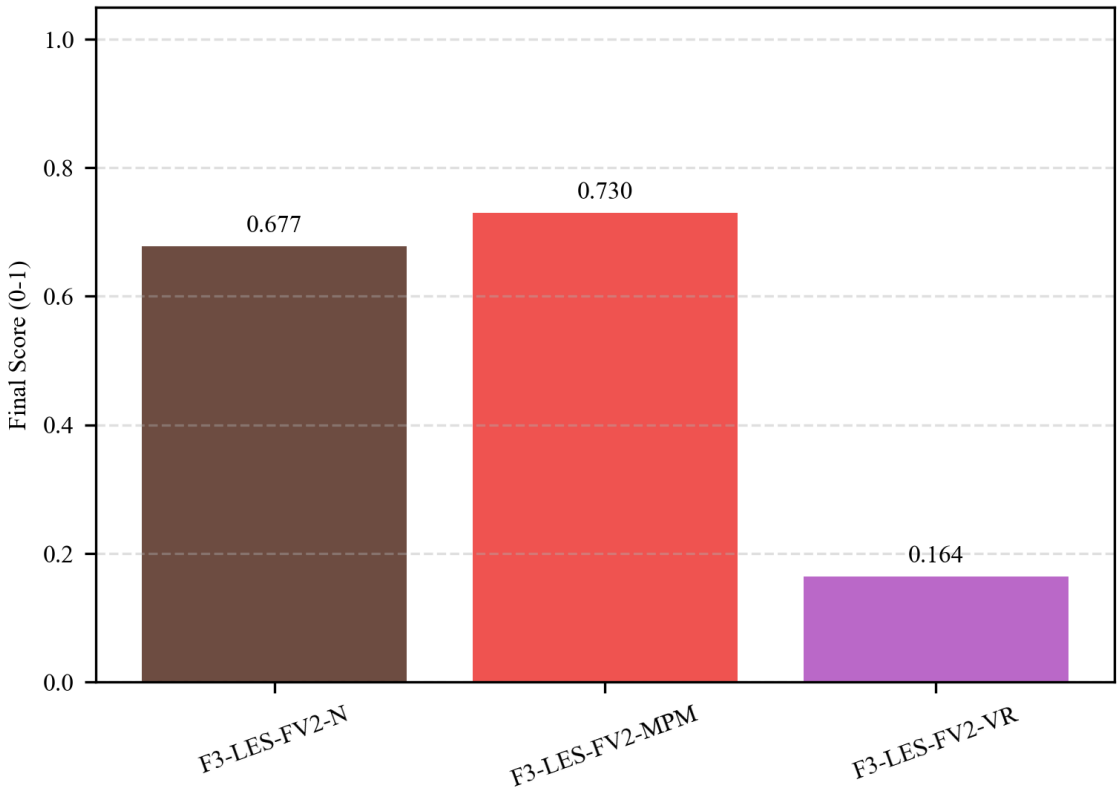

Figure 5.19: Final score S_m calculated for different sediment discharge equations tested in FLOW-3D

5.5 Discussion

5.5.1 Hydrodynamic Response

Although both numerical models accurately reproduced the amplitude and shape of the measured water surface elevations and flow velocity timeseries, they consistently exhibited a phase lag compared to the experimental data. The peak events occurred later in the simulations, indicating a delay in bore arrival at each instrument location. This lag likely arises from the inherent numerical diffusion in the finite-volume discretization and time-stepping schemes which partially smoothed the front edge of the water column in dam-break simulation. The phase lag became more pronounced near US2, where the flow interacted directly with the wall and reflected waves further complicated the local hydrodynamic response.

The comparative analysis revealed that FLOW-3D reproduced the hydrodynamic characteristics more accurately than MIKE3 HD/ST. This can be attributed to the differences in the numerical formulation of the two solvers. FLOW-3D employs a Cartesian finite-volume grid with a VOF free-surface tracking scheme, allowing it to capture sharp discontinuities and strong vertical accelerations associated with the dam-break bore. The use of the LES turbulence model enables explicit resolution of large-scale vortices and transient shear fields near the wall, enhancing the accuracy of bore-structure interactions. In contrast, MIKE3 HD/ST utilizes a σ-coordinate system in which vertical stretching and terrain-following transformations tend to smooth steep gradients, particularly near the free surface and bed. This coordinate system can introduce some level of numerical diffusion, resulting in delayed peaks and reduced amplitudes in water-surface elevation and velocity.

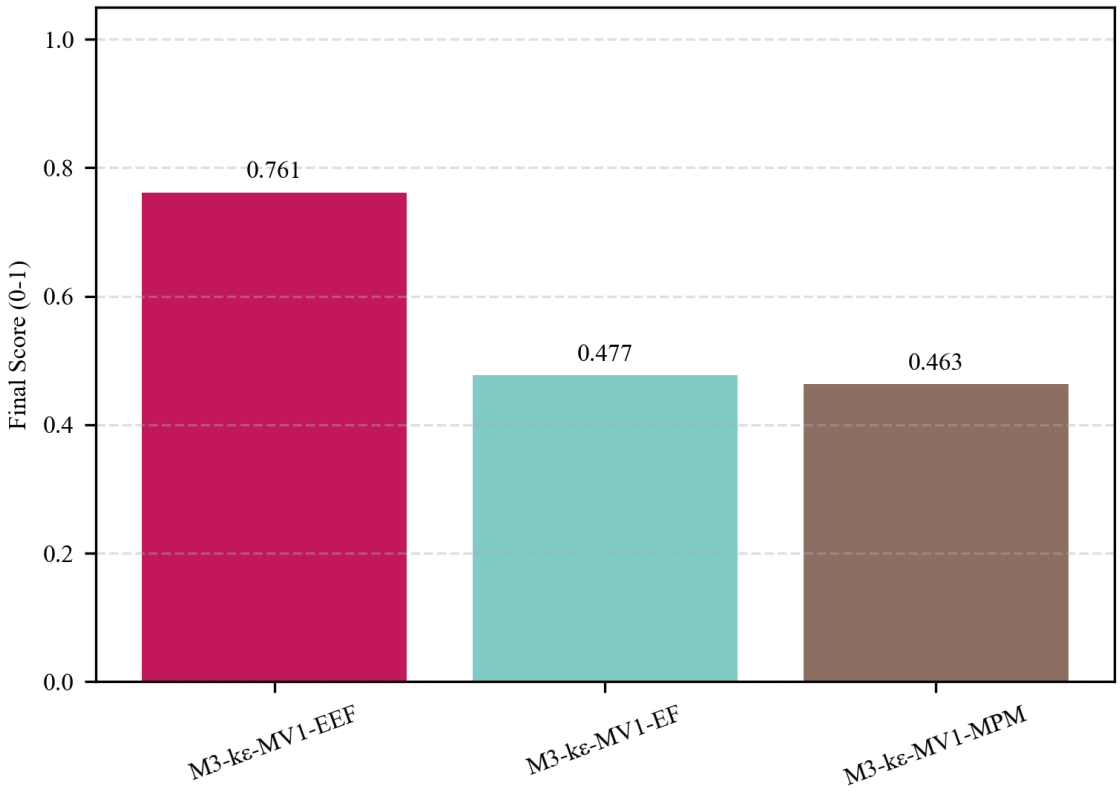

Figure 5.20: Final score S_m calculated for different sediment discharge equations tested in MIKE3 HD/ST

An important finding of this study was that the optimal model configurations for walls differ from those reported for columns. In MIKE3 HD/ST, the best performance for the wall case was obtained using the $k-\varepsilon$ turbulence model, whereas Margalit et al. (2023) identified the $k-\omega$ model as optimal for a circular column. Similarly, in FLOW-3D, the LES configuration produced the best overall performance, whereas April-LeQuéré et al. (2020) found the $k-\varepsilon$ most suitable for simulating flow past a square column. These differences stem from the fundamentally distinct flow-structure interaction mechanisms. Around columns, the flow separates and generates a horseshoe vortex and wake zone, producing nearly axisymmetric turbulence structures that are well represented by two-equation RANS closures such as $k-\omega$. In contrast, flow around a wall is laterally confined, dominated by attached shear layers and impinging jets, which generate highly directional turbulence.

5.5.2 Scour Evolution

Both the experimental and numerical results revealed that the scour process is governed by a rapid initial phase of erosion followed by a quasi-equilibrium stage. In the experiments, this trend was most pronounced at the upstream corner, where the scour depth increased sharply during the arrival of the first bore and then stabilized at an almost constant value. At the center of the front face, the erosion rate was smaller than at the upstream corners but persisted gradually throughout the test, indicating that sediment transport continued at a low intensity after the initial bore impact.

Both numerical models reproduced the “fast-erosion-equilibrium” trend observed in the laboratory tests at the upstream corner of the wall model, but they predicted nearly constant scour

depths once the initial bore had passed. At the center of the front face, both models followed the same fast-erosion-equilibrium pattern, whereas the experimental test showed a slow but continuing erosion. In the experiments, the impinging bore generates the highest instantaneous bed shear stresses, causing most sediment removal during the first few seconds. As the scour hole deepens, the near-bed flow decelerates, which lowers the effective Shields parameter. Moreover, the steepened bed slopes promote armoring and sheltering effects that progressively inhibit further sediment motion. These physical mechanisms contribute to the slow, but continuous erosion recorded in the laboratory, but they are not fully resolved by the numerical models; as a result, subsequent bores propagate over a numerically stabilized bed, producing insufficient shear to restart the gradual erosion observed experimentally.

The absence of continuous erosion at the center of the front face in the numerical results, unlike the gradual scour observed in the laboratory tests, can be explained by the method that both solvers treat sediment motion near the stagnation zone. In the laboratory experiments, the near-bed flow experiences strong downward flow followed by upward deflection, forming a recirculating shear layer rather than a sustained unidirectional current. Although LES in FLOW-3D is, in principle, capable of resolving large coherent structures, the grid resolution used here is insufficient to capture the intermittent turbulent bursts that drive low-magnitude, quasi-steady sediment entrainment. Also, in MIKE3 HD/ST, the $k - \varepsilon$ model smooths these fluctuations due to its inherently more dissipative nature. Furthermore, the static definition of the critical Shields parameter (particularly in MIKE3 HD/ST) limit the capacity to capture the slow, continuous adjustment phase once the main scour hole is formed. Consequently, both models predict an abrupt transition to equilibrium at the center of the front face rather than the gradual deepening recorded in the physical tests.

5.6 Conclusions

In this study, the numerical study on local scour around walls with two modelling software (FLOW-3D and MIKE3 HD/ST) was conducted based on a series of downscaled dam-break experiments. The results and conclusions presented herein reflect the behaviour of these models for the specific case investigated, namely local scour around a wall model induced by unsteady dam-break bores in a controlled laboratory setting. Although the findings offer useful insights, they should be interpreted within the context of this experimental configuration and scope and may serve as an inspiration or guideline for modellers working on similar scour scenarios. The main conclusions are as follows:

- Both FLOW-3D and MIKE3 HD/ST successfully reproduced the principal hydrodynamic and morphodynamic processes associated with dam-break-induced local scour around vertical walls, capturing the rapid initial erosion followed by stabilization of scour depth.
- The hydrodynamic response was predicted more accurately by FLOW-3D owing to its Cartesian VOF formulation and explicit turbulence resolution (LES), whereas the σ-coordinate system of MIKE3 HD/ST introduced mild amplitude damping near the structure.
- The vertical-resolution sensitivity analysis showed that refining the vertical mesh resolution did not monotonically improve results. Excessive refinement led to cell-aspect-ratio-driven implicit damping of near-bed shear stress.

- Van Rijn (1984a) formulation did not simulate the scour evolution under the highly turbulent dam-break bores, which can be attributed to its inverse relationship with the median grain size which results in very large bedload discharges for very fine sand.

- The best-performing model configurations for walls, i.e. $k - \varepsilon$ turbulence model with Extended Engelund and Fredsøe (Roulund et al., 2005) sediment transport model in MIKE3 HD/ST and LES with Meyer-Peter and Müller (1948) sediment transport model in FLOW-3D, differed from those reported for columns in earlier studies. This contrast arises from the fundamentally different turbulence structures and confinement effects governing the two geometries. While flow around columns generates a separated horseshoe vortex system and an axisymmetric wake that is well captured by certain RANS closures, flow around walls is laterally confined and dominated by impinging jets and attached shear layers, producing highly directional and non-axisymmetric turbulence. This difference highlights that numerical configuration and parameterization must be tailored to the structure geometry and flow regime. Directly transferring setups optimized for columns can lead to inaccuracies when applied to walls.

Chapter 6. Conclusions and Recommendations for Future Work

6.1 Conclusions

The thesis presented herein investigated local scour around walls caused by unsteady, tsunami-like dam-break bores, through a comprehensive program of experimental testing and numerical modelling. The experiments specifically examined the influence of the bore characteristics through the generating impoundment depth, the wall width, and the angle between the structure and the flow direction. Based on the findings of this study, the following general conclusions can be drawn:

- Among the three parameters investigated, the bore depth was found to have the greatest influence on local scour depth. This outcome was expected, as a higher bore depth results in bores with greater energy, leading to the formation of deeper scour holes around the wall.
- For both columns and walls, the maximum scour depth consistently occurred at the upstream corner of the structure, irrespective of their width. In the case of a column, the scour depth at the center of its front face was comparable to that measured at the upstream corners. As the wall width increased, the scour depth at the upstream corners became significantly larger than that measured at the center of the front face.
- The width of the wall had minimal impact on the scour depth at the upstream corners, whereas its influence on the scour depth at the center of the front face was significant. Wider walls exhibited a shallower scour depth at the center of the front face. The scouring process at the center of the front face is primarily governed by the impinging bore (jet) in the stagnation region.
- Structures with narrower widths exhibited higher erosion rates at the upstream corners and, consequently, reached their maximum scour depth more rapidly than wider structures.
- The time history of the scour depth at the upstream corners of the structure showed evidence of sediment deposition following the arrival of secondary bores. This observation is significant, as it indicates that the maximum scour depths reported in post-tsunami field surveys may not correspond to the most critical stage of scour development (i.e., maximum scour depth). Therefore, relying solely on scour measurements obtained during field observations to establish design standards and guidelines may be partly inadequate, and, as the present results show, controlled laboratory experiments are necessary to better identify the critical scour depth during tsunami inundation.
- The orientation of the structure relative to the flow direction had a significant influence on the local scouring process by affecting the formation and intensity of the horseshoe and lateral vortices. Walls oriented perpendicular to the flow consistently developed deeper scour holes at the upstream corners than those aligned parallel to the flow. For the longest wall tested in this study, the maximum scour depth, at the upstream corners, in the parallel configuration was approximately 5 cm less than in the perpendicular configuration at an impoundment depth of 0.5 m. This finding suggests that aligning structures parallel to the

incoming flow can have a protective effect by reducing vortex intensity and, consequently, the severity of local scour.

- Comparison of the results with the prescribed envelope in the ASCE-7-22 (2022) standard for estimating local scour depth revealed that normalizing scour depth by the projected width of the structure can misrepresent structural vulnerability. In several cases, the parallel configuration exhibited higher normalized scour depths than the perpendicular configuration, despite having smaller actual scour depths. This overestimation arose solely from the reduced projected width in the parallel configuration.

- Both MIKE3 HD/ST and FLOW-3D models exhibited satisfactory accuracy in simulating local scour around walls under unsteady flow conditions. FLOW-3D exhibited slightly superior performance in reproducing the hydrodynamic characteristics of dam-break bores compared to MIKE3 HD/ST. This improvement can be attributed to the Volume of Fluid (VOF) formulation employed in FLOW-3D, which allows for a more detailed representation of free-surface dynamics and flow behavior.

- Comparison between the numerical simulations of local scour around walls and previous studies on local scour around columns revealed that the best-performing model configurations for columns do not necessarily produce accurate results for walls. This discrepancy arises from the fundamentally different vortex structures involved, i.e. horseshoe and wake vortices around columns versus laterally confined shear layers and impinging jets around walls. This finding highlights the importance of refining numerical models based on the specific geometry of the structure under investigation.

- The vertical mesh sensitivity analysis performed for both MIKE3 HD/ST and FLOW-3D indicated that increasing vertical resolution without a corresponding refinement of the horizontal mesh does not necessarily improve model accuracy. Higher cell aspect ratios were found to increase numerical diffusion and dampening of bed shear stress, the primary driving force for sediment entrainment in numerical models, thereby reducing the accuracy of the predicted scour behavior.

- The Extended Engelund and Fredsøe formulation (Roulund et al., 2005) showed the best performance in predicting local scour depth around walls subjected to tsunami-like dam-break bores. Its superior accuracy can be attributed to its two-dimensional formulation, which accounts for sediment transport in the direction of the flow velocity.

- The bedload discharge equation proposed by Van Rijn (1984a) did not accurately reproduce scour evolution under highly turbulent dam-break bores. This limitation is primarily due to the nonlinear relationship between the instantaneous Shields parameter and the critical Shields parameter, which leads to an exaggerated bedload discharge during short-lived peaks in bed shear stress.

6.2 Recommendations for Future Work

The study presented herein investigated the effects of impoundment depth, wall width, and the orientation between the wall and flow direction on local scour depth under tsunami-like bores. However, the following areas of research are recommended to further enhance the understanding of local scour processes around walls:

- All tests in this study were performed under dry-bed conditions. However, conducting experiments on wet-bed (saturated soil) conditions is essential to better understand the effects of successive tsunami inundations on local scour around walls in coastal regions.
- The tests conducted in this study were performed over a horizontal bed and the effects of sloped bed on the local scour around wall models was not considered. Moreover, this study did not account for the influence of the tsunami drawdown phase on local scour development. Previous studies (April-LeQuéré et al., 2022; Schendel et al., 2024) on columns have shown that the drawdown phase can induce considerable erosion, particularly on the shoreward side of the structure. Hence, it is recommended that future experiments be conducted over sloped beds to better understand the effects of drawdown on scour hole evolution around walls.
- In the present study, an ADV was positioned upstream of the structure due to its limitations in measuring flow velocity within highly turbulent regions near the wall. Moreover, the ADV records velocity at a single point, which restricts spatial resolution. Therefore, it is recommended that future experiments employ more advanced instruments, such as Ultrasonic Velocity Profiler (UVP), to obtain higher-resolution velocity measurements closer to the structure and to better characterize the flow variations in its vicinity.
- Due to time constraints, this study examined only three wall widths and three orientations between the structure and the flow direction. While the findings contribute to understanding the influence of these parameters on local scour development, conducting additional tests with a broader range of configurations would provide a more comprehensive assessment of their effects.
- The vertical mesh sensitivity analysis in this study was performed using a single horizontal mesh resolution. However, simultaneous refinement of both horizontal and vertical meshes may improve the accuracy of local scour simulations. Therefore, it is recommended that future studies investigate the combined effects of horizontal and vertical mesh refinement on model performance.
- More advanced numerical CFD modelling using more sophisticated models such as OpenFOAM could be explored to enhance the accuracy of simulating local scour around walls under unsteady flow conditions.

Bibliography

Abdelaziz, S., Bui, M. D., and Rutschmann, P. (2011). Numerical investigation of flow and sediment transport around a circular bridge pier. In *Proceedings of 34th IAHR World Congress*, Brisbane, Australia.

Ahmad, N., Bihs, H., Myrhaug, D., Kamath, A., and Arntsen, Ø. A. (2018). Three-dimensional numerical modelling of wave-induced scour around piles in a side-by-side arrangement. *Coastal Engineering*, 138:132–151.

Ahmad, N., Kamath, A., and Bihs, H. (2020). 3D numerical modelling of scour around a jacket structure with dynamic free surface capturing. *Ocean Engineering*, 200:107104.

Al-Faesly, T., Palermo, D., Nistor, I., and Cornett, A. (2012). Experimental Modeling of Extreme Hydrodynamic Forces on Structural Models. *International Journal of Protective Structures*, 3(4):477–505.

Amini, A., Melville, B. W., Ali, T. M., and Ghazali, A. H. (2012). Clear-Water Local Scour around Pile Groups in Shallow-Water Flow. *Journal of Hydraulic Engineering*, 138(2):177–185.

April-LeQuéré, P. (2022). *Scouring Around Multiple Structures in Extreme Flow Conditions*. PhD thesis, University of Ottawa.

April-LeQuéré, P., Nistor, I., and Mohammadian, A. (2020). Numerical Modeling of Tsunami-Induced Scouring around a Square Column: Performance Assessment of FLOW-3D and Delft3D. *Journal of Coastal Research*, 36(6):1278 – 1291. Publisher: Coastal Education and Research Foundation.

April-LeQuéré, P., Nistor, I., and Mohammadian, A. (2021). Effect of Lateral Spacing of Structures on Tsunami-Induced Scour. *Journal of Coastal Research*, 37(4).

April-LeQuéré, P., Nistor, I., Mohammadian, A., Schimmels, S., Schendel, A., Goseberg, N., Welzel, M., Krautwald, C., and Stolle, J. (2022). Hydrodynamics and Associated Scour around a Free-Standing Structure Due to Turbulent Bores. *Journal of Waterway, Port, Coastal, and Ocean Engineering*, 148(5):04022013.

Aránguiz, R., Esteban, M., Takagi, H., Mikami, T., Takabatake, T., Gómez, M., González, J., Shibayama, T., Okuwaki, R., Yagi, Y., Shimizu, K., Achiari, H., Stolle, J., Robertson, I., Ohira, K., Nakamura, R., Nishida, Y., Krautwald, C., Goseberg, N., and Nistor, I. (2020). The 2018 Sulawesi tsunami in Palu city as a result of several landslides and coseismic tsunamis. *Coastal Engineering Journal*, 62(4):445–459.

Arnason, H., Petroff, C. M., and Yeh, H. (2009). Tsunami Bore Impingement onto a Vertical Column. *Journal of disaster research*, 4:391–403.

ASCE-7-22 (2022). Tsunami Loads and Effects. In *Minimum Design Loads and Associated Criteria for Buildings and Other Structures (ASCE 7-22)*, volume 1. American Society of Civil Engineers, Reston, Virginia.

Baykal, C., Sumer, B. M., Fuhrman, D. R., Jacobsen, N. G., and Fredsøe, J. (2015). Numerical investigation of flow and scour around a vertical circular cylinder. *Philosophical Transactions of the Royal Society A: Mathematical, Physical and Engineering Sciences*, 373(2033):20140104.

Beg, M. (2010). Characteristics of Developing Scour Holes around Two Piers Placed in Transverse Arrangement. In *Scour and Erosion*, pages 76–85, San Francisco, California, United States. American Society of Civil Engineers.

Bihs, H., Heveling, K., and Kamath, A. (2018). REEF3D:NSEWAVE, A THREE-DIMENSIONAL NON-HYDROSTATIC WAVE MODEL ON A FIXED GRID. *Coastal Engineering Proceedings*, (36):8.

Blasius, H. (1913). Das Aehnlichkeitsgesetz bei Reibungsvorgängen in Flüssigkeiten. In Verein deutscher Ingenieure, editor, *Mitteilungen über Forschungsarbeiten auf dem Gebiete des Ingenieurwesens*, pages 1–41. Springer Berlin Heidelberg, Berlin, Heidelberg.

Bordbar, A., Sharifi, S., and Hemida, H. (2021). Investigation of the flow behaviour and local scour around single square-shaped cylinders at different positions in live-bed. *Ocean Engineering*, 238:109772. Publisher: Elsevier BV.

Borrero, J. C. (2005). Field Survey of Northern Sumatra and Banda Aceh, Indonesia after the Tsunami and Earthquake of 26 December 2004. *Seismological Research Letters*, 76(3):312–320.

Borrero, J. C., Cronin, S. J., Latu'ila, F. H., Tukuafu, P., Heni, N., Tupou, A. M., Kula, T., Fa'anunu, O., Bosserelle, C., Lane, E., Lynett, P., and Kong, L. (2023). Tsunami Runup and Inundation in Tonga from the January 2022 Eruption of Hunga Volcano. *Pure and Applied Geophysics*, 180(1):1–22.

Bryant, E. (2001). *Tsunami: The Underrated Hazard*, volume 1 of *Springer Praxis Books*. Springer Berlin Heidelberg, Berlin, Heidelberg, 1 edition.

Butterworth, S. (1930). On the Theory of Filter Amplifiers. *Experimental Wireless and the Wireless Engineer*, 7:536–541.

CCH (2013). Article 11- Regulations Within Flood Hazard Districts and Development Adjacent to Drainage Facilities. In *City and County of Honolulu (CCH) Building Code*, pages 115–120. City and County of Honolulu, Honolulu , Hawaii.

Chanson, H. (2006). Tsunami Surges on Dry Coastal Plains: Application of Dam Break Wave Equations. *Coastal Engineering Journal*, 48(4):355–370. Publisher: Taylor & Francis.

Chauchat, J., Cheng, Z., Nagel, T., Bonamy, C., and Hsu, T.-J. (2017). SedFoam-2.0: a 3-D two-phase flow numerical model for sediment transport. *Geoscientific Model Development*, 10(12):4367–4392.

Chen, J., Huang, Z., Jiang, C., Deng, B., and Long, Y. (2013). Tsunami-induced scour at coastal roadways: a laboratory study. *Natural Hazards*, 69(1):655–674.

Cheng, Z., Hsu, T.-J., and Calantoni, J. (2017). SedFoam: A multi-dimensional Eulerian two-phase model for sediment transport and its application to momentary bed failure. *Coastal Engineering*, 119:32–50.

Chock, G., Robertson, I. N., Kriebel, D. L., Francis, M., and Nistor, I. (2013). *Tohoku, Japan, Earthquake and Tsunami of 2011: performance of structures under tsunami loads*. American Society of Civil Engineers, Reston, Virginia.

Choufu, L., Abbasi, S., Pourshahbaz, H., Taghvaei, P., and Tfwala, S. (2019). Investigation of Flow, Erosion, and Sedimentation Pattern around Varied Groynes under Different Hydraulic and Geometric Conditions: A Numerical Study. *Water*, 11(2):235.

Chuang, W.-L., Chang, K.-A., Kaihatu, J., Cienfuegos, R., and Mokrani, C. (2020). Experimental study of force, pressure, and fluid velocity on a simplified coastal building under tsunami bore impact. *Natural Hazards*, 103(1):1093–1120.

Deltares (2025). Delft3D Flexible Mesh.

Deng, X., He, S., and Cao, Z. (2022). Numerical investigation of the local scour around a coconut tree root foundation under wave-current joint actions. *Ocean Engineering*, 245:110563.

Depstech (2021). DS300 Industrial Endoscope User Manua. User Manual C.01.006.00153V02, Depstech, Shenzhen, China.

Devi, G. and Kumar, M. (2022). Chapter 29 - last century evolution in local scour measuring techniques. In Zakwan, M., Wahid, A., Niazkar, M., and Chatterjee, U., editors, *Water Resource Modeling and Computational Technologies*, volume 7 of *Current Directions in Water Scarcity Research*, pages 513–529. Elsevier.

DHI (2025). MIKE3 HD and ST.

Díaz, M. J. C., Fernández-Nieto, E. D., and Ferreiro, A. M. (2008). Sediment transport models in Shallow Water equations and numerical approach by high order finite volume methods. *Computers & Fluids*, 37(3):299–316.

Dissanayaka, K. D. C. R. and Tanaka, N. (2023). Scour around the single emergent cylinder due to subcritical and supercritical approach flow conditions. *ISH Journal of Hydraulic Engineering*, 0(0):1–16. Publisher: Taylor & Francis.

Ehteram, M. and Mahdavi Meymand, A. (2015). Numerical modeling of scour depth at side piers of the bridge. *Journal of Computational and Applied Mathematics*, 280:68–79.

Elliott, K. R. and Baker, C. J. (1985). Effect of Pier Spacing on Scour Around Bridge Piers. *Journal of Hydraulic Engineering*, 111(7):1105–1109.

Engelund, F. and Fredsøe, J. (1976). A Sediment Transport Model for Straight Alluvial Channels. *Hydrology Research*, 7(5):293–306.

Engelund, F. and Hansen, E. (1972). *A monograph on sediment transport in alluvial streams*. Teknisk forlag, Copenhagen, 3. rev. ed edition. OCLC: 925867092.

Ettema, R., Melville, B. W., and Barkdoll, B. (1998). Scale Effect in Pier-Scour Experiments. *Journal of Hydraulic Engineering*, 124(6):639–642.

FEMA-P-55 (2011). *Coastal Construction Manual (FEMA P-55)*, volume II. Federal Emergency Management Agency, 4 edition.

FEMA-P-646 (2019). *Guidelines for Design of Structures for Vertical Evacuation from Tsunamis (FEMA P-646)*, volume 1. Federal Emergency Management Agency, 3 edition.

Flow Science (2019). FLOW-3D HYDRO.

Fox, B. and Feurich, R. (2019). CFD Analysis of Local Scour at Bridge Piers. In *Proceedings of the SEDHYD 2019 Conference*, volume 2, Reno, Nevada, USA.

Fritz, H. M. and Borrero, J. C. (2006). Somalia Field Survey after the December 2004 Indian Ocean Tsunami. *Earthquake Spectra*, 22(3S):219–233.

Fritz, H. M., Borrero, J. C., Synolakis, C., and Yoo, J. (2006). 2004 Indian Ocean tsunami flow velocity measurements from survivor videos. *Geophysical Research Letters*, 33(24):2006GL026784.

Fuhrman, D. R., Baykal, C., Mutlu Sumer, B., Jacobsen, N. G., and Fredsøe, J. (2014). Numerical simulation of wave-induced scour and backfilling processes beneath submarine pipelines. *Coastal Engineering*, 94:10–22.

Fujii, N., Ikeno, M., Sakikiyama, T., Matsuyama, M., Takao, M., and Mukohara, T. (2009). Hydraulic Experiment on Flow and Topography Change in Harbor due to Tsunami and Its Numerical Simulation. *Journal of Japan Society of Civil Engineers, Ser. B2 (Coastal Engineering)*, 65(1):291–295.

Ghobarah, A., Saatcioglu, M., and Nistor, I. (2006). The impact of the 26 December 2004 earthquake and tsunami on structures and infrastructure. *Engineering Structures*, 28(2):312–326.

GoPro, Inc. (2018). HERO7 Black User Manual. User manual 130-26422-000, GoPro Inc., San Mateo, California, USA.

Goseberg, N., Wurpts, A., and Schlurmann, T. (2013). Laboratory-scale generation of tsunami and long waves. *Coastal Engineering*, 79:57–74.

Harish, S., Sriram, V., Schüttrumpf, H., and Sannasiraj, S. A. (2022). Tsunami-like Flow-Induced Forces on the Landward Structure behind a Vertical Seawall with and without Recurve Using OpenFOAM. *Water*, 14(13).

Hirt, C. W. and Sicilian, J. M. (1985). A Porosity Technique for the Definition of Obstacles in Rectangular Cell Meshes. Washington, DC.

Hottinger Brüel & Kjær GmbH (2025). MX1601B Universal Amplifier – Data Sheet. Technical Datasheet B03882, Hottinger Brüel & Kjær GmbH (HBK), Darmstadt, Germany.

Hu, Z. and Li, Y. P. (2025). Full-scale tsunami-induced scour around a circular pile with three-dimensional seepage. *Coastal Engineering*, 197:104676.

Hu, Z., Qi, W.-G., and Li, Y. P. (2025). The Role of Dynamic Seepage Response in Sediment Transport and Tsunami-Induced Scour. *Journal of Geophysical Research: Oceans*, 130(3):e2024JC021084.

Hur, D.-S., Nakamura, T., and Mizutani, N. (2007). Sand suction mechanism in artificial beach composed of rubble mound breakwater and reclaimed sand area. *Ocean Engineering*, 34(8-9):1104–1119.

Hurtado-Herrera, M., Uh Zapata, M., Hammouti, A., Pham Van Bang, D., Zhang, W., and Nguyen, K. D. (2024). Numerical investigation of the scour around a diamond- and square-shaped pile in a narrow channel. *Ocean Engineering*, 309:118374. Publisher: Elsevier BV.

Iizuka, H. and Matsutomi, H. (2000). Damage due to the flooding flow of tsunami. In *Proceedings of Coastal Engineering, JSCE*, pages 381–385. Japan Society of Civil Engineers.

Imamura, F., Goto, K., and Ohkubo, S. (2008). A numerical model for the transport of a boulder by tsunami. *Journal of Geophysical Research: Oceans*, 113(C1).

Ishizaka, A. and Nemery, P. (2013). *Multi-Criteria Decision Analysis: Methods and Software*. Wiley, 1 edition.

Islam, S. U., Zhou, C. Y., Shah, A., and Xie, P. (2012). Numerical simulation of flow past rectangular cylinders with different aspect ratios using the incompressible lattice Boltzmann method. *Journal of Mechanical Science and Technology*, 26(4):1027–1041.

Iwai, S. and Goto, K. (2021). Threshold flow depths to move large boulders by the 2011 Tohoku-oki tsunami. *Scientific Reports*, 11(1):13434.

Jacobsen, N. G. (2011). *A Full Hydro- and Morphodynamic Description of Breaker Bar Development*. PhD thesis, Technical University of Denmark.

Jaffe, B. E., Borrero, J. C., Prasetya, G. S., Peters, R., McAdoo, B., Gelfenbaum, G., Morton, R., Ruggiero, P., Higman, B., Dengler, L., Hidayat, R., Kingsley, E., Kongko, W., Lukijanto, Moore, A., Titov, V., and Yulianto, E. (2006). Northwest Sumatra and Offshore Islands Field Survey after the December 2004 Indian Ocean Tsunami. *Earthquake Spectra*, 22(3_suppl):105–135.

Jalal, H. K. and Hassan, W. H. (2020). Three-dimensional numerical simulation of local scour around circular bridge pier using Flow-3D software. *IOP Conference Series: Materials Science and Engineering*, 745:012150.

Jayaratne, M. P. R., Nicholas, M., Ghodoosipour, B., Mugnaini, S., Nistor, I., and Shibayama, T. (2018). TSUNAMI-INDUCED HYDRODYNAMICS AND SCOUR AROUND STRUCTURES. *Coastal Engineering Proceedings*, 1(36):currents.5.

Jayaratne, M. P. R., Premaratne, B., Adewale, A., Mikami, T., Matsuba, S., Shibayama, T., Esteban, M., and Nistor, I. (2016). Failure Mechanisms and Local Scour at Coastal Structures Induced by Tsunami. *Coastal Engineering Journal*, 58(4):1640017–1–1640017–38. Publisher: Taylor & Francis.

Jazaeri, S. A., Nistor, I., Mohammadian, A., and Liu, X. (2024). A critical review on the tsunami-induced scour around structures. *Coastal Engineering Journal*, pages 1–28.

Jordan, C., Jayaratne, M. P. R., Mugnaini, S., and Nicholas, M. (2019). TSUNAMI INDUCED SCOUR ON STRUCTURES. In *Coastal Sediments 2019*, pages 2521–2532, Tampa/St. Petersburg, Florida, USA. WORLD SCIENTIFIC.

Kato, F., Sato, S., and Yeh, H. (2001). Large-Scale Experiment on Dynamic Response of Sand Bed Around a Cylinder Due to Tsunami. In *Coastal Engineering 2000*, pages 1848–1859, Sydney, Australia. American Society of Civil Engineers.

Kato, F., Suwa, Y., Watanabe, K., and Hatogai, S. (2012). MECHANISMS OF COASTAL DIKE FAILURE INDUCED BY THE GREAT EAST JAPAN EARTHQUAKE TSUNAMI. *Coastal Engineering Proceedings*, 1(33):structures.40.

Kawachi, I., Aida, J., Hikichi, H., and Kondo, K. (2020). Disaster resilience in aging populations: lessons from the 2011 Great East Japan earthquake and tsunami. *Journal of the Royal Society of New Zealand*, 50(2):263–278.

Khosronejad, A., Kang, S., and Sotiropoulos, F. (2012). Experimental and computational investigation of local scour around bridge piers. *Advances in Water Resources*, 37:73–85. Publisher: Elsevier BV.

Kihara, N., Arikawa, T., Asai, T., Hasebe, M., Ikeya, T., Inoue, S., Kaida, H., Matsutomi, H., Nakano, Y., Okuda, Y., Okuno, S., Ooie, T., Shigihara, Y., Shoji, G., Tateno, T., Tsurudome, C., and Watanabe, M. (2021). A physical model of tsunami inundation and wave pressures for an idealized coastal industrial site. *Coastal Engineering*, 169:103970.

Kihara, N., Fujii, N., and Matsuyama, M. (2012). Three-dimensional sediment transport processes on tsunami-induced topography changes in a harbor. *Earth, Planets and Space*, 64(10):787–797.

Kim, H. S., Nabi, M., Kimura, I., and Shimizu, Y. (2014). Numerical investigation of local scour at two adjacent cylinders. *Advances in Water Resources*, 70:131–147.

Kiraga, M. and Popek, Z. (2020). On local scouring downstream small water structures. *PeerJ*, 8:e10282.

Kirkoz, M. S. (1983). Breaking and run-up of long waves, tsunamis: their science and engineering. In *Tsunamis: their science and engineering*, endai-Ofunato-Kamaishi, Japan. Terra Scientific Pub.

Krautwald, C., Stolle, J., Robertson, I., Achiari, H., Mikami, T., Nakamura, R., Takabatake, T., Nishida, Y., Shibayama, T., Esteban, M., Goseberg, N., and Nistor, I. (2021). Engineering Lessons from September 28, 2018 Indonesian Tsunami: Scouring Mechanisms and Effects on Infrastructure. *Journal of Waterway, Port, Coastal, and Ocean Engineering*, 147(2).

Larsen, B. E., Arbøll, L. K., Kristoffersen, S. F., Carstensen, S., and Fuhrman, D. R. (2018). Experimental study of tsunami-induced scour around a monopile foundation. *Coastal Engineering*, 138:9–21.

Larsen, B. E., Fuhrman, D. R., Baykal, C., and Sumer, B. M. (2017). Tsunami-induced scour around monopile foundations. *Coastal Engineering*, 129:36–49.

Lauber, G. and Hager, W. H. (1998). Experiments to dambreak wave: Horizontal channel. *Journal of Hydraulic Research*, 36(3):291–307.

Lavictoire, A., Nistor, I., and Rennie, C. (2014). Local scour around structures due to hydraulic bores. Halifax.

Leal, J. G. A. B., Ferreira, R. M. L., and Cardoso, A. H. (2009). Maximum Level and Time to Peak of Dam-Break Waves on Mobile Horizontal Bed. *Journal of Hydraulic Engineering*, 135(11):995–999.

Lebreton, L. C.-M. and Borrero, J. C. (2013). Modeling the transport and accumulation floating debris generated by the 11 March 2011 Tohoku tsunami. *Marine Pollution Bulletin*, 66(1-2):53–58.

Lee, S. O. and Sturm, T. W. (2009). Effect of Sediment Size Scaling on Physical Modeling of Bridge Pier Scour. *Journal of Hydraulic Engineering*, 135(10):793–802.

Leica Geosystems AG (2019). Leica ScanStation P50 Datasheet. Technical Datasheet 869145, Leica Geosystems AG, Heerbrugg, Switzerland.

Li, J., Kong, X., Yang, Y., Deng, L., and Xiong, W. (2022). CFD investigations of tsunami-induced scour around bridge piers. *Ocean Engineering*, 244:110373.

Li, J., Kong, X., Yang, Y., Hu, J., and Jin, R. (2023). Numerical Modeling of Solitary Wave-Induced Flow and Scour around a Square Onshore Structure. *Journal of Marine Science and Engineering*, 11(1):198. Publisher: MDPI AG.

Lim, G., Premaratne, B., Jayaratne, M. P. R., Marriott, M., and Shibayama, T. (2015). Comparison of Failure Mechanisms of Coastal Structures due to the 2004 Indian Ocean and 2011 Tohoku Tsunami Events. In *6th International Conference on Structural Engineering and Construction Management*, pages 72–79.

Liu, M.-m., Wang, H.-c., Tang, G.-q., Shao, F.-f., and Jin, X. (2022). Investigation of local scour around two vertical piles by using numerical method. *Ocean Engineering*, 244:110405.

Liu, P. L.-F., Yeh, H., and Synolakis, C. E. (2008). BENCHMARK PROBLEMS. In *Advances in Coastal and Ocean Engineering*, volume 10, pages 223–230. WORLD SCIENTIFIC.

Liu, X., Li, J.-H., Wang, Y.-Z., Qiu, X., Li, J.-H., and Liu, Y.-L. (2025). Experimental study of the flow around a near-wall rectangular cylinder. *Experiments in Fluids*, 66(8):157.

Lozano-Durán, A., Giometto, M. G., Park, G. I., and Moin, P. (2020). Non-equilibrium three-dimensional boundary layers at moderate Reynolds numbers. *Journal of Fluid Mechanics*, 883:A20.

Madsen, P. A., Fuhrman, D. R., and Schäffer, H. A. (2008). On the solitary wave paradigm for tsunamis. *Journal of Geophysical Research: Oceans*, 113(C12).

Maqtan, R., Yusuf, B., and Hamzah, S. B. (2018). Physical Modeling of Landward Scour Due to Tsunami Bore Overtopping Seawall. *MATEC Web of Conferences*, 203:01003.

Margalit, J., Mandviwalla, X., Roulund, A., and Kærgaard, K. (2023). Efficient 3D Numerical Modelling of Clear and Live bed Scour in Waves and Current. In *Proceedings of the 11th International Conference on Scour and Erosion*, Copenhagen, Denmark. Internation Society for Soil Mechanics and Geotechnical Engineering.

Masaya, R., Suppasri, A., Yamashita, K., Imamura, F., Gouramanis, C., and Leelawat, N. (2020). Investigating beach erosion related with tsunami sediment transport at Phra Thong Island, Thailand, caused by the 2004 Indian Ocean tsunami. *Natural Hazards and Earth System Sciences*, 20(10):2823–2841.

Massa Products Corporation (2023). M5000 Ultrasonic Sensor Datasheet. Datasheet 150423, Massa Products Corporation, Hingham, MA, USA.

Matsutomi, H. and Okamoto, K. (2010). Inundation flow velocity of tsunami on land. *Island Arc*, 19(3):443–457.

McGovern, D., Allsop, W., Rossetto, T., and Chandler, I. (2023). Large-scale experiments on tsunami inundation and overtopping forces at vertical sea walls. *Coastal Engineering*, 179:104222.

McGovern, D., Todd, D., Rossetto, T., Whitehouse, R., Monaghan, J., and Gomes, E. (2019). Experimental observations of tsunami induced scour at onshore structures. volume 152, page 103505.

Mehrzad, R., Nistor, I., and Rennie, C. (2016). Experimental modeling of supercritical flows induced erosion around structures.

Mehrzad, R., Nistor, I., and Rennie, C. (2022). Scour Mechanics of a Tsunami-Like Bore around a Square Structure. *Journal of Waterway, Port, Coastal, and Ocean Engineering*, 148(1).

Mellor, G. L., Ezer, T., and Oey, L.-Y. (1994). The Pressure Gradient Conundrum of Sigma Coordinate Ocean Models. *Journal of Atmospheric and Oceanic Technology*, 11(4):1126–1134.

Melville, B. W. and Chiew, Y.-M. (1999). Time Scale for Local Scour at Bridge Piers. *Journal of Hydraulic Engineering*, 125(1):59–65.

Meyer-Peter, E. and Müller, R. (1948). Formulas for Bed-Load transport. Technical Report TKJ3000, TU Delft, Netherlands.

Mikami, T., Shibayama, T., Esteban, M., and Matsumaru, R. (2012). Field Survey of the 2011 Tohoku Earthquake and Tsunami in Miyagi and Fukushima Prefectures. *Coastal Engineering Journal*, 54(1):1250011–1–1250011–26.

Mitobe, Y., Adityawan, M. B., Tanaka, H., Kawahara, T., Kurosawa, T., and Otsushi, K. (2014). EXPERIMENTS ON LOCAL SCOUR BEHIND COASTAL DIKES INDUCED BY TSUNAMI OVERFLOW. *Coastal Engineering Proceedings*, 1(34):sediment.62.

Mori, N., Takahashi, T., Yasuda, T., and Yanagisawa, H. (2011). Survey of 2011 Tohoku earthquake tsunami inundation and run-up. *Geophysical Research Letters*, 38(7).

Murty, T. S. (1977). *Seismic sea waves: tsunamis*. Bulletin of the Fisheries Research Board of Canada ; 198. Dept. of Fisheries and the Environment, Fisheries and Marine Service : available from Print. and Pub. Supply and Services Canada, Ottawa.

Nagel, T., Chauchat, J., Bonamy, C., Liu, X., Cheng, Z., and Hsu, T.-J. (2020). Three-dimensional scour simulations with a two-phase flow model. *Advances in Water Resources*, 138:103544.

Nakamura, T., Kuramitsu, Y., and Mizutani, N. (2008). Tsunami Scour Around a Square Structure. *Coastal Engineering Journal*, 50(2):209–246. Publisher: Taylor & Francis.

Nielsen, P. (1992). *Coastal bottom boundary layers and sediment transport*. Number v. 4 in Advanced series on ocean engineering. World Scientific, Singapore ; River Edge, N.J.

Nistor, I., Palermo, D., Nouri, Y., Murty, T., and Saatcioglu (2009). Tsunami-Induced Forces on Structures. In *Handbook of Coastal and Ocean Engineering*, pages 261–286. WORLD SCIENTIFIC.

Nortek AS (2018). The Comprehensive Manual for Velocimeters. User manual N3015–30, Nortek AS, Rud, Norway.

Nouri, Y., Nistor, I., Palermo, D., and Cornett, A. (2010). Experimental Investigation of Tsunami Impact on Free Standing Structures. *Coastal Engineering Journal*, 52(1):43–70. Publisher: Taylor & Francis.

Okada, T., Sugano, T., Ishikawa, T., Ohgi, T., Takai, S., and Hamabe, C. (2005). Structural Design Methods of Buildings for Tsunami Resistance (SMBTR). Design Guideline, The Building Center of Japan, Japan.

Olsen, M. J., Cheung, K. F., YamazakI, Y., Butcher, S., Garlock, M., Yim, S., McGarity, S., Robertson, I., Burgos, L., and Young, Y. L. (2012). Damage Assessment of the 2010 Chile Earthquake and Tsunami Using Terrestrial Laser Scanning. *Earthquake Spectra*, 28(1_suppl1):179–197.

Olsen, N. R. B. (1991). *A three-dimensional numerical model for simulation of sediment movements in water intakes*. PhD Thesis, University of Trondheim, The Norwegian Institute of Technology.

Omara, H., Elsayed, S. M., Abdeelaal, G. M., Abd-Elhamid, H. F., and Tawfik, A. (2019). Hydromorphological Numerical Model of the Local Scour Process Around Bridge Piers. *Arabian Journal for Science and Engineering*, 44(5):4183–4199.

Ota, K., Sato, T., Nakagawa, H., and Kawaike, K. (2017). Three-Dimensional Simulation of Local Scour around a Weir-Type Structure: Hybrid Euler-Lagrange Model for Bed-Material Load. *Journal of Hydraulic Engineering*, 143(4):04016096.

Palermo, D., Nistor, I., Saatcioglu, M., and Ghobarah, A. (2013). Impact and damage to structures during the 27 February 2010 Chile tsunami. *Canadian Journal of Civil Engineering*, 40(8):750–758.

Qi, W., Gao, F., Han, X., and Gong, Q. (2012). Local Scour And Pore-water Pressure Around a Monopile Foundation Under Combined Waves And Currents. volume All Days.

Quezada, M., Tamburrino, A., and Niño, Y. (2018). Numerical simulation of scour around circular piles due to unsteady currents and oscillatory flows. *Engineering Applications of Computational Fluid Mechanics*, 12(1):354–374.

Rahman, M. A., Tanaka, N., and Reheman, N. (2021). Experimental study on reduction of scouring and tsunami energy through a defense system consisting a seaward embankment followed by vertically double layered vegetation. *Ocean Engineering*, 234:108816.

Rajaie, M., Azimi, A. H., Nistor, I., and Rennie, C. D. (2023a). Experimental Investigations of the Impact of Tsunami-Like Hydraulic Bores on a Square Vertical Structure. I: Pore Pressure Variations. *Journal of Waterway, Port, Coastal, and Ocean Engineering*, 149(1):04022027.

Rajaie, M., Azimi, A. H., Nistor, I., and Rennie, C. D. (2023b). Experimental Investigations of the Impact of Tsunami-Like Hydraulic Bores on a Square Vertical Structure. II: Local Scour. *Journal of Waterway, Port, Coastal, and Ocean Engineering*, 149(1):04022028.

Raudkivi, A. J. and Ettema, R. (1983). Clear-Water Scour at Cylindrical Piers. *Journal of Hydraulic Engineering*, 109(3):338–350.

Richmond, B., Szczuciński, W., Chagué-Goff, C., Goto, K., Sugawara, D., Witter, R., Tappin, D. R., Jaffe, B., Fujino, S., Nishimura, Y., and Goff, J. (2012). Erosion, deposition and landscape change on the Sendai coastal plain, Japan, resulting from the March 11, 2011 Tohoku-oki tsunami. *Sedimentary Geology*, 282:27–39.

Ritter, A. (1892). Die Fortpflanzung der Wasserwellen. *Vereine Deutcher Ingenieure Zeitswchrift*, 36:947–954.

Robertson, I. N., Paczkowski, K., Riggs, H. R., and Mohamed, A. (2013). Experimental Investigation of Tsunami Bore Forces on Vertical Walls. *Journal of Offshore Mechanics and Arctic Engineering*, 135(2):021601.

Rossetto, T., Peiris, N., Pomonis, A., Wilkinson, S. M., Re, D. D., Koo, R., and Gallocher, S. (2007). The Indian Ocean tsunami of December 26, 2004: observations in Sri Lanka and Thailand. *Natural Hazards*, 42(1):105–124.

Roulund, A., Sumer, B. M., Fredsoe, J., and Michelsen, J. (2005). Numerical and experimental investigation of flow and scour around a circular pile. *Journal of Fluid Mechanics*, 534:351–401. Publisher: Cambridge University Press.

Saatcioglu, M., Ghobarah, A., and Nistor, I. (2006). Performance of Structures in Indonesia during the December 2004 Great Sumatra Earthquake and Indian Ocean Tsunami. *Earthquake Spectra*, 22(3_suppl):295–319.

Samma, H., Khosrojerdi, A., Rostam-Abadi, M., Mehraein, M., and Cataño-Lopera, Y. (2020). Numerical simulation of scour and flow field over movable bed induced by a submerged wall jet. *Journal of Hydroinformatics*, 22(2):385–401.

Sato, S. and Okuma, S. (2014). DESTRUCTION MECHANISM OF COASTAL STRUCTURES DUE TO THE 2011 TOHOKU TSUNAMI IN THE SOUTH OF FUKUSHIMA. *Coastal Engineering Proceedings*, 1(34):75.

Schendel, A., Schimmels, S., Welzel, M., April-LeQuéré, P., Mohammadian, A., Krautwald, C., Stolle, J., Nistor, I., and Goseberg, N. (2024). Spatiotemporal Scouring Processes around a Square Column on a Sloped Beach Induced by Tsunami Bores. *Journal of Waterway, Port, Coastal, and Ocean Engineering*, 150(3):04024005.

Shafiei, S., Melville, B. W., Shamseldin, A. Y., Watts, M. J., and Hoffman, T. G. (2015). Experimental Investigation of Tsunami Bore Induced Scour around Structures. page 7, Auckland, New Zealand.

Song, Y., Xu, Y., Ismail, H., and Liu, X. (2022). Scour modeling based on immersed boundary method: A pathway to practical use of three-dimensional scour models. *Coastal Engineering*, 171:104037.

Soulsby, R. (1997). 9. Bedload transport. In *Dynamics of marine sands*, pages 156–170. Thomas Telford Publishing, London.

Stahlmann, A. (2013). Numerical and Experimental Modeling of Scour at Foundation Structures for Offshore Wind Turbines. volume All Days.

Stelling, G. S. and Van Kester, J. A. T. M. (1994). On the approximation of horizontal gradients in sigma co-ordinates for bathymetry with steep bottom slopes. *International Journal for Numerical Methods in Fluids*, 18(10):915–935.

Stolle, J., Ghodoosipour, B., Derschum, C., Nistor, I., Petriu, E., and Goseberg, N. (2019). Swing gate generated dam-break waves. *Journal of Hydraulic Research*, 57(5):675–687.

Stolle, J., Krautwald, C., Robertson, I., Achiari, H., Mikami, T., Nakamura, R., Takabatake, T., Nishida, Y., Shibayama, T., Esteban, M., Nistor, I., and Goseberg, N. (2020). Engineering lessons from the 28 September 2018 Indonesian tsunami: debris loading. *Canadian Journal of Civil Engineering*, 47(1):1–12.

Straub, L. G. (1934). Effect of channel-contraction works upon regimen of movable bed-streams. *Eos, Transactions American Geophysical Union*, 15(2):454–463.

Sugawara, D., Takahashi, T., and Imamura, F. (2014). Sediment transport due to the 2011 Tohoku-oki tsunami at Sendai: Results from numerical modeling. *Marine Geology*, 358:18–37.

Sumer, B. M., Whitehouse, R. J. S., and Tørum, A. (2001). Scour around coastal structures: a summary of recent research. *Coastal Engineering*, 44(2):153–190.

Sun, X., Luo, T., Wang, L., Wang, H., Song, Y., and Li, Y. (2019). Numerical simulation of gas recovery from a low-permeability hydrate reservoir by depressurization. *Applied Energy*, 250:7–18.

Synolakis, C. and Bernard, E. N. (2006). Tsunami science before and beyond Boxing Day 2004. *Philosophical Transactions of the Royal Society A: Mathematical, Physical and Engineering Sciences*, 364(1845):2231–2265.

Synolakis, C., Deb, M. K., and Skjelbreia, J. E. (1988). The anomalous behavior of the runup of cnoidal waves. *Physics of Fluids*, 31(1):3–5.

Synolakis, C., Okal, E., and Bernard, E. (2005). The Megatsunami of December 26, 2004. *The Bridge*, 35(2):26–35.

Tadepalli, S. and Synolakis, C. (1994). The run-up of N-waves on sloping beaches. *Proceedings of the Royal Society of London. Series A: Mathematical and Physical Sciences*, 445(1923):99–112.

Takahashi, T., Shuto, N., Imamura, F., and Asai, D. (2001). Modeling Sediment Transport due to Tsunamis with Exchange Rate between Bed Load Layer and Suspended Load Layer. In *Coastal Engineering 2000*, pages 1508–1519, Sydney, Australia. American Society of Civil Engineers.

Tanioka, Y., Yamanaka, Y., and Nakagaki, T. (2022). Characteristics of the deep sea tsunami excited offshore Japan due to the air wave from the 2022 Tonga eruption. *Earth, Planets and Space*, 74(1):61.

Tonkin, S., Francis, M., and Bricker, J. (2013). Limits on Coastal Scour Depths due to Tsunami. In *International Efforts in Lifeline Earthquake Engineering*, pages 671–678. American Society of Civil Engineers.

Tonkin, S., Yeh, H., Kato, F., and Sato, S. (2003). Tsunami scour around a cylinder. *Journal of Fluid Mechanics*, 496:S0022112003006402. Publisher: Cambridge University Press.

Tregnaghi, M., Marion, A., and Coleman, S. (2009). Scouring at bed sills as a response to flash floods. *Journal of Hydraulic Engineering*, 135(6):466–475.

Triatmadja, R., Hijah, S. N., and Nurhasanah, A. (2011). Scouring Around Coastal Structures Due to Tsunami Surge.

Tsuji, Y., Namegaya, Y., Matsumoto, H., Iwasaki, S.-I., Kanbua, W., Sriwichai, M., and Meesuk, V. (2006). The 2004 Indian tsunami in Thailand: Surveyed runup heights and tide gauge records. *Earth, Planets and Space*, 58(2):223–232.

Van Rijn, L. C. (1984a). Sediment Transport, Part I: Bed Load Transport. *Journal of Hydraulic Engineering*, 110(10):1431–1456.

Van Rijn, L. C. (1984b). Sediment Transport, Part II: Suspended Load Transport. *Journal of Hydraulic Engineering*, 110(11):1613–1641.

Van Rijn, L. C. (1993). *Principles of sediment transport in rivers, estuaries and coastal seas: Part I*. Aqua Publications, Amsterdam.

Virtanen, P., Gommers, R., Oliphant, T. E., Haberland, M., Reddy, T., Cournapeau, D., Burovski, E., Peterson, P., Weckesser, W., Bright, J., Van Der Walt, S. J., Brett, M., Wilson, J., Millman, K. J., Mayorov, N., Nelson, A. R. J., Jones, E., Kern, R., Larson, E., Carey, C. J., Polat, İ., Feng, Y., Moore, E. W., VanderPlas, J., Laxalde, D., Perktold, J., Cimrman, R., Henriksen, I., Quintero, E. A., Harris, C. R., Archibald, A. M., Ribeiro, A. H., Pedregosa, F., Van Mulbregt, P., SciPy 1.0 Contributors, Vijaykumar, A., Bardelli, A. P., Rothberg, A., Hilboll, A., Kloeckner, A., Scopatz, A., Lee, A., Rokem, A., Woods, C. N., Fulton, C., Masson, C., Häggström, C., Fitzgerald, C., Nicholson, D. A., Hagen, D. R., Pasechnik, D. V., Olivetti, E., Martin, E., Wieser, E., Silva, F., Lenders, F., Wilhelm, F., Young, G., Price, G. A., Ingold, G.-L., Allen, G. E., Lee, G. R., Audren, H., Probst, I., Dietrich, J. P., Silterra, J., Webber, J. T., Slavič, J., Nothman, J., Buchner, J., Kulick, J., Schönberger, J. L., De Miranda Cardoso, J. V., Reimer, J., Harrington, J., Rodríguez, J. L. C., Nunez-Iglesias, J., Kuczynski, J., Tritz, K., Thoma, M., Newville, M., Kümmerer, M., Bolingbroke, M., Tartre, M., Pak, M., Smith, N. J., Nowaczyk, N., Shebanov, N., Pavlyk, O., Brodtkorb, P. A., Lee, P., McGibbon, R. T., Feldbauer, R., Lewis, S., Tygier, S., Sievert, S., Vigna, S., Peterson, S., More, S., Pudlik, T., Oshima, T., Pingel, T. J., Robitaille, T. P., Spura, T., Jones, T. R., Cera, T., Leslie, T., Zito, T., Krauss, T., Upadhyay, U., Halchenko, Y. O., and Vázquez-Baeza, Y. (2020). SciPy 1.0: fundamental algorithms for scientific computing in Python. *Nature Methods*, 17(3):261–272.

Wilson, R., Davenport, C., and Jaffe, B. (2012). Sediment scour and deposition within harbors in California (USA), caused by the March 11, 2011 Tohoku-oki tsunami. *Sedimentary Geology*, 282:228–240.

Wüthrich, D., Pfister, M., Nistor, I., and Schleiss, A. J. (2018). Experimental Study of Tsunami-Like Waves Generated with a Vertical Release Technique on Dry and Wet Beds. *Journal of Waterway, Port, Coastal, and Ocean Engineering*, 144(4):4018006.

Xu, C. and Huang, Z. (2022). An Experimental Study of Characteristics of Solitary-Wave-Induced Scour Around a Pile Breakwater with a Discussion on Effects of the Distance between Piles. *Journal of Earthquake and Tsunami*, 16(03):2240002.

Xu, C., Huang, Z., and Yao, Y. (2019). A wave-flume study of scour at a pile breakwater: Solitary waves. *Applied Ocean Research*, 82:89–108.

Yamashita, K., Sugawara, D., Takahashi, T., Imamura, F., Saito, Y., Imato, Y., Kai, T., Uehara, H., Kato, T., Nakata, K., Saka, R., and Nishikawa, A. (2016). Numerical Simulations of Large-Scale Sediment Transport Caused by the 2011 Tohoku Earthquake Tsunami in Hirota Bay, Southern Sanriku Coast. *Coastal Engineering Journal*, 58(4):1640015–1–1640015–28.

Yang, Q., Yu, P., and Liu, H. (2021). CFD modelling of local scour around Tri-USAF in sand with different arrangements under steady current. *Ocean Engineering*, 235:109359.

Yoshii, T., Tanaka, S., and Matsuyama, M. (2018). Tsunami inundation, sediment transport, and deposition process of tsunami deposits on coastal lowland inferred from the Tsunami Sand Transport Laboratory Experiment (TSTLE). *Marine Geology*, 400:107–118.

Yu, T., Li, Y., Chen, X., and Tang, J. (2022). Experimental study on wave- and current-induced scour around an anti-deposition permeable breakwater. *Ocean Engineering*, 257:111565.

Zarrati, A. R., Gholami, H., and Mashahir, M. (2004). Application of collar to control scouring around rectangular bridge piers. *Journal of Hydraulic Research*, 42(1):97–103. Publisher: Informa UK Limited.

Zhang, W., Zapata, M. U., Bai, X., Pham-Van-Bang, D., and Nguyen, K. D. (2020). Three-dimensional simulation of horseshoe vortex and local scour around a vertical cylinder using an unstructured finite-volume technique. *International Journal of Sediment Research*, 35(3):295–306.

Zhang, Y., Chen, G., Hu, J., Chen, X., Yang, W., Tao, A., and Zheng, J. (2017). Experimental study on mechanism of sea-dike failure due to wave overtopping. *Applied Ocean Research*, 68:171–181.

Zhang, Y., Menghao, Z., Shengqi, J., Feifei, W., and Songping, L. (2025). Experimental and numerical investigations of scours around a rectangular pile cap using a horseshoe-shaped collar. *AQUA — Water Infrastructure, Ecosystems and Society*, 74(4):321–334. Publisher: IWA Publishing.